Gems & Gemology

Winter 2023
Volume LIX

The Quarterly Journal of the Gemological Institute of America

Texas Topaz
Bohemian Garnet in Early Glass Objects
Field Report on Slovak Opal
Beryl Inclusions Chart

GEMS & GEMOLOGY

Winter 2023
VOLUME 59, No. 4


p. 419


p. 464

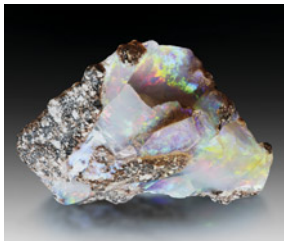
p. 471


p. 492


p. 501


p. 511

Editorial

Feature Articles

Field Reports

Charts

Regular Features

GEMS & GEMOLOGY®

gia.edu/gems-gemology

Customer Service
(760) 603-4200
gandg@gia.edu

Subscriptions
Copies of the current issue may be purchased for $29.95 plus shipping. Subscriptions are $79.99 for one year (4 issues) in the U.S. and $99.99 elsewhere. Canadian subscribers should add GST. Discounts are available for renewals, group subscriptions, GIA alumni, and current GIA students. To purchase print subscriptions, visit store.gia.edu or contact Customer Service. For institutional rates, contact Customer Service.

Database Coverage
Gems & Gemology's impact factor is 2.6, according to the 2022 Journal Citation Reports by Clarivate Analytics (issued June 2023). *G&G* is abstracted in Thomson Reuters products (Current Contents: Physical, Chemical & Earth Sciences and Science Citation Index—Expanded, including the Web of Knowledge) and other databases. For a complete list of sources abstracting *G&G*, go to gia.edu/gems-gemology, and click on "Publication Information."

Manuscript Submissions
Gems & Gemology, a peer-reviewed journal, welcomes the submission of articles on all aspects of the field. Please see the Author Guidelines at gia.edu/gems-gemology or contact the Managing Editor. Letters on articles published in *G&G* are also welcome. Please note that Field Reports, Lab Notes, Gem News International, Micro-World, Colored Stones Unearthed, Diamond Reflections, Charts, and In the Spotlight are not peer-reviewed sections but do undergo technical and editorial review.

Gems & Gemology is published quarterly by the Gemological Institute of America, a nonprofit educational organization for the gem and jewelry industry.

Postmaster: Return undeliverable copies of *Gems & Gemology* to GIA, The Robert Mouawad Campus, 5345 Armada Drive, Carlsbad, CA 92008.

Our Canadian goods and service registration number is 126142892RT.

About the Cover

Texas topaz, the state's official gemstone, is valued for its natural blue color. Discovered in 1904, the 925 ct crystal on the cover was formerly displayed in the state capitol building and is now part of the Hamman Gem and Mineral Gallery at the University of Texas at Austin. The 13.8 ct round topaz has a Lone Star cut, faceted to display the five-point star of the state flag. Courtesy of Cub Root (Form to Feeling, Austin, Texas). Photos by Blanca Espinoza.

Printing is by L+L Printers, Carlsbad, CA.

GIA World Headquarters The Robert Mouawad Campus 5345 Armada Drive Carlsbad, CA 92008 USA

ISSN 0016-626X

Texas Topaz, Slovak Opal, a Beryl Inclusions Chart, and More

Welcome to the Winter 2023 edition of *Gems & Gemology*! This issue brings an exciting conclusion to the volume year with three feature articles, a field report, a colorful new inclusions chart, and the return of the *Colored Stones Unearthed* column along with our other regular columns.

Our first article explores a prized gemstone from the United States: Texas topaz, sought after for its domestic provenance and rare natural blue color. Dr. Roy Bassoo and coauthors begin with a historical account of topaz from Mason County, Texas, followed by discussion of its geologic origin, compositional characteristics, manufacture, and significance to the gem trade. In addition, the authors seek to provide a basis for determining geographic provenance.

"...a prized gemstone from the United States: Texas topaz, sought after for its domestic provenance and rare natural blue color."

Next, Dr. Karl Schmetzer and fellow researchers investigate a technique for setting cut garnets on glass objects, invented by Claudius vom Creutz of Nuremberg in the late sixteenth century. Examining two glass vessels at museums in Germany, the authors analyze the stones decorating the objects and the methods used to attach them.

Petrified tree fern from northeast China is the topic of our next article. A team led by Ying Yan reports on the gemological properties, chemical composition, and appearance of this material, which displays a beautiful pattern and is being used in intricate carvings in China.

Our fourth article, a field report from Dr. Peter Semrád, presents the revival of Slovak opal mining. It provides a brief history of mining in the area and details on geology and mineralogy, followed by coverage of recent mining activity, production, and marketing.

To close out our features, GIA researchers led by Nathan Renfro and John I. Koivula offer a captivating look at the internal features of beryl, with a foldout chart featuring 30 remarkable photomicrographs. Laminated versions of the chart, along with the six other inclusion charts in the series—emerald, sapphire, ruby, diamond, opal, and spinel—are available at store.gia.edu.

G&G's regular columns continue to provide the latest gemological findings. Noteworthy updates from GIA laboratories are summarized in *Lab Notes*, including an HPHT-treated laboratory-grown diamond featuring dramatic color zoning, an antique Indian-style headdress decorated with seed pearls, and a rare faceted thomsonite. *Micro-World* showcases the inner landscapes of gemstones with striking hollandite crystals in a Brazilian amethyst, a stress halo resembling a butterfly in a natural diamond, a metal sulfide crystal suspended in a padparadscha sapphire, and more. *Colored Stones Unearthed* returns in this issue, covering the formation and mining of gemstones from sedimentary rocks. Finally, highlights from the *Gem News International* section include reports on pyritized triceratops fossils from South Dakota, training for artisanal diamond miners in Liberia, and a recent discovery of blue amblygonite-montebrasite from Rwanda.

We hope you enjoy the latest edition of *Gems & Gemology*!

Duncan Pay | Editor-in-Chief | dpay@gia.edu

Topaz from Mason County, Texas

Roy Bassoo, Diane Eames, Matthew F. Hardman, Kenneth Befus, and Ziyin Sun

Gem-quality naturally blue topaz occurs in Mason County, Texas. Known as "Texas topaz," this gem is highly sought after in the United States because of its domestic provenance and rare natural blue color. To date, no studies have identified gemological or compositional characteristics that could distinguish Texas topaz from topaz sourced elsewhere. This study provides a historical account of topaz from Mason County and discusses its geologic origin, compositional characteristics, manufacture, and significance to the gem trade. A total of 83 alluvial topaz crystals from Mason County were analyzed using standard gemological testing; Fourier-transform infrared, ultraviolet/visible/near-infrared, and Raman spectroscopic techniques; and laser ablation–inductively coupled plasma–mass spectrometry to gather gemological and geochemical data. Most Texas topaz is colorless, though some is light blue or brown. A small percentage of the blue stones displayed a saturated bodycolor. Color zoning was often visible and became more noticeable with luminescent excitation. Ultraviolet luminescence at 225 nm excitation revealed green to blue luminescent growth bands and rarely red luminescent growth bands. Topaz crystals from Mason County are not often free of inclusions. When present, multiphase melt and fluid inclusions contain carbon dioxide. Mineral inclusions include albite, anorthite, quartz, muscovite, pseudobrookite, and columbite-tantalite. Machine learning algorithms were applied to fingerprint the trace element composition of the samples. Trace concentrations of phosphorus, scandium, titanium, iron, gallium, germanium, niobium, tin, tantalum, and tungsten best constrained the formation and provenance of Texas topaz. For gemologists, these trace elements can also aid in assessing the geographic provenance because most Texas topaz presents a distinct trace element composition. This work demonstrates the potential effectiveness of machine learning and statistical modeling in gemstone provenance determination. These can be powerful tools in conjunction with traditional gemological discrimination techniques.

Topaz is an orthorhombic nesosilicate with the general chemical formula $Al_2SiO_4F_2$. It can form from fluorine- and lithium-rich, peraluminous (aluminum-rich and calcium-poor), and highly fractionated silicic melts or gases geologically associated with rhyolites, pegmatites, or hydrothermal-greisen rocks (Burt et al., 1982; Congdon and Nash, 1988; Payette and Martin, 1990; Menzies, 1995; Zhang et al., 2002; Marshall and Walton, 2007; Gauzzi et al., 2018; Gauzzi and Graça, 2018). In pegmatites, topaz is found alongside quartz, feldspar, muscovite, and accessory tourmaline and fluorite (Pollard et al., 1989). In greisens, which are granitic rocks altered by internal magmatic fluids, topaz is also associated with rare metal deposits of tantalum, niobium, tungsten, lithium, tin, and molybdenum (Burt et al., 1982; Manning and Hill, 1990; Taylor, 1992; Raimbault et al., 1995; Charoy and Noronha, 1996; Williams-Jones et al., 2000).

In Brief

- This study discusses the history, geologic origin, compositional characteristics, manufacture, and significance within the trade of naturally blue Texas topaz.
- Trace concentrations of tin and tungsten in Texas topaz and the presence of cassiterite and scheelite in the region suggest possible greisen ore mineralization in Mason County, Texas.
- Machine learning and statistical modeling of topaz trace element data from worldwide sources demonstrate their utility in assisting with gemstone provenance determination.

Globally sourced gem and fine mineral specimens of topaz are prized for their luster, clarity, hardness, and wide range of colors, including orange, pink, and blue. Whereas most topaz is colorless, certain growth

See end of article for About the Authors and Acknowledgments.
Gems & Gemology, Vol. 59, No. 4, pp. 414–431,
http://dx.doi.org/10.5741/GEMS.59.4.414

Figure 1. A fine 925 ct crystal that was formerly displayed in the Texas State Capitol and sat on the governor's desk in 1969 when the legislature adopted blue Texas topaz as the state gem. This specimen was found in 1904 and now resides in the Hamman Gem and Mineral Gallery in the Department of Earth and Planetary Sciences at the University of Texas at Austin (catalog no. B0344). Photo by Blanca Espinoza.

environments induce defects and impurities that create color centers. In the case of pink to violet colors, Cr^{3+} acts as a chromophore, substituting for Al^{3+}. A combination of oxygen-to-metal charge transfer and radiation-induced color centers can modify pink to violet material to orange Imperial topaz (Gaft et al., 2003; Schott et al., 2003; Taran et al., 2003). Oxygen hole center defects produce brown or blue colors, though the possibility of additional defects causing blue color remains uncertain (Krambrock et al., 2007; Rossman, 2011). Pronounced blue colors can also be created or enhanced through irradiation and heat treatments (Simmons, 2007). Colorless topaz was first irradiated to create a blue color in 1957 (Pough, 1957). Artificially irradiated and heat treated blue topaz subsequently entered the market in the late 1970s, and its popularity and low cost eventually made it the most commonly irradiated gemstone on the market (Nassau and Prescott, 1975; Crowningshield, 1981; Nassau, 1985). This treatment became so widespread that any blue topaz in today's market is assumed to have been irradiated (Rossman, 2011).

Considering the prevalence of artificially blue topaz, the naturally blue topaz from Mason County, Texas, is significant (figure 1). Indeed, faceters of Texas topaz understand that treating this gemstone could render it indistinguishable from those found in other locations. In Mason County, as with most geographic occurrences, colorless topaz is the most common. However, faint blue to sky blue hues can be relatively uncommon. Pink, brown, and gray colors are rare (figure 2).

Topaz was first collected in Mason County in the late 1800s, long before the first reported accounts of topaz treatment (Meyer, 1913; Leiper, 1951). By the 1950s, Texas topaz had become important in the regional gem trade (White, 1960; Towner, 1968, 1969; Browne, 1982). The timing is anecdotally linked to World War II, when scientists moved to the American Southwest for the nuclear weapons program and engaged in recreational mineral hunting on weekends and holidays. This led to the formation of gem and mineral groups and increased rockhounding and gem faceting in the region. Topaz from Mason County be-

Figure 2. Rough topaz from Mason County analyzed in this study, showing the range of color of this material. The large blue specimen weighs 188 ct. Photo by Emily Lane; courtesy of Diane Eames.

came the most commonly used gemstone in faceting competitions at Texas gem and mineral shows. In 1969, the state legislature adopted Mason County blue topaz as the official state gemstone, introducing the "Texas topaz" label.

Texas topaz remained in the hobbyist realm until the early 2000s, when Diane Eames and Brad Hodges established Gems of the Hill Country, a jewelry store in the town of Mason. From this rural platform they built a successful niche jewelry business centered on locally sourced and manufactured Texas topaz pieces (figure 3). Gems of the Hill Country supplied both local and national markets with jewelry showcasing Texas topaz. Their advertising campaign significantly elevated the prestige of Texas's state gemstone.

Because of its local provenance, topaz from Texas has a much higher regional value than similarly colored topaz from other localities worldwide. The most sought-after stones exhibit a saturated blue color. Price varies with the saturation of blue color and the cut quality. Early in the twentieth century, faceters used the Portuguese cut to create stones with deep pavilions to intensify the pale colors. Today most of this topaz is faceted in the Lone Star cut (box A) or variations thereof. Blue or brown color zones are placed in the culet to intensify the perceived color (King Jr., 1961).

Establishing the provenance of Texas topaz has posed a challenge in the regional gem trade. Buyers are wary of intentional or inadvertent substitution of low-value foreign topaz for high-value local material. This article presents a gemological and analytical

Figure 3. Faceted Texas topaz specimens with brown, blue, and green bodycolors, ranging from 0.62 to 9.34 ct. Texas topaz has been sought after for its naturally occurring blue color. Photo by Brad Hodges; courtesy of Diane Eames.

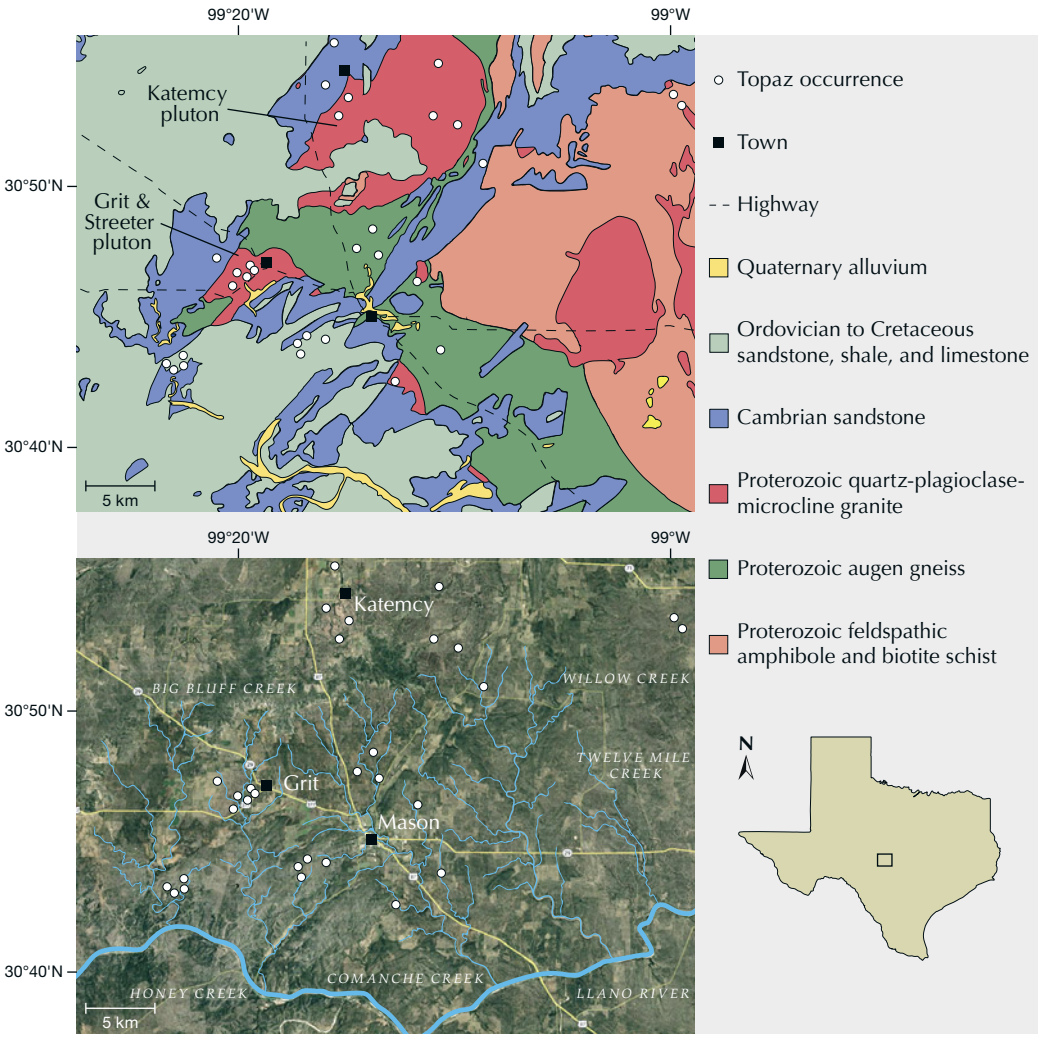

Figure 4. Geologic map (top) and aerial view (bottom) of the Mason County area in Texas, showing known locations where topaz has been collected in alluvium. While many Texas topaz occurrences have been discovered historically, these maps document those that have been published (Leiper, 1951; Towner, 1968, 1969; Fechenbach, 1984). The geologic map is modified from the Geologic Database of Texas (https://txpub.usgs.gov/txgeology).

study of Texas topaz to augment the various worldwide databases of colored stone deposits. Trace element compositions for topaz from Mason County are presented, along with a demonstration of how machine learning can assist with the geographic provenance determination of Texas topaz.

GEOLOGY AND MINING

Texas topaz crystallizes from niobium-yttrium-fluorine (NYF) pegmatites that are genetically and spatially associated with granites in the Llano Uplift in central Texas. The Llano Uplift is a 9000 km^2 exposure of Proterozoic igneous and metamorphic rocks from the Grenville orogen that are 1.0 to 1.3 billion years old (Mosher et al., 2008). Topaz can be found in pegmatites throughout the Llano Uplift; however, nearly all gem-quality material is derived from the granitic Grit, Streeter, and Katemcy plutons in the western Llano Uplift (White, 1960; Towner, 1969; Reed, 1999; Barker and Reed, 2010). The source granites have very low strontium concentrations and zirconium/hafnium ratios, suggesting that extreme fractional crystallization rather than partial melting led to their formation (Barker and Reed, 2010; Collins, 2008). The topaz-producing granites intrude the Proterozoic Packsaddle schist, Valley Springs gneiss, and/or other granite plutons. When not exposed, they are mostly overlain by the Middle Cambrian Hickory sandstone member of the Riley Sandstone formation, Cretaceous Edwards limestones, and quaternary alluvium (figure 4).

Euhedral topaz crystallizes in sub-meter-diameter vugs within relatively small meter- to decameter-long pegmatites, which tend to be gradational with the host granites (White, 1960). Pegmatite vugs also contain microcline, albite, and "books" of biotite, fluorite, and quartz embedded within a clay matrix (Meyer, 1913; Leiper, 1951; Hoover, 1992). Topaz has

BOX A: CUTTING OF TEXAS TOPAZ

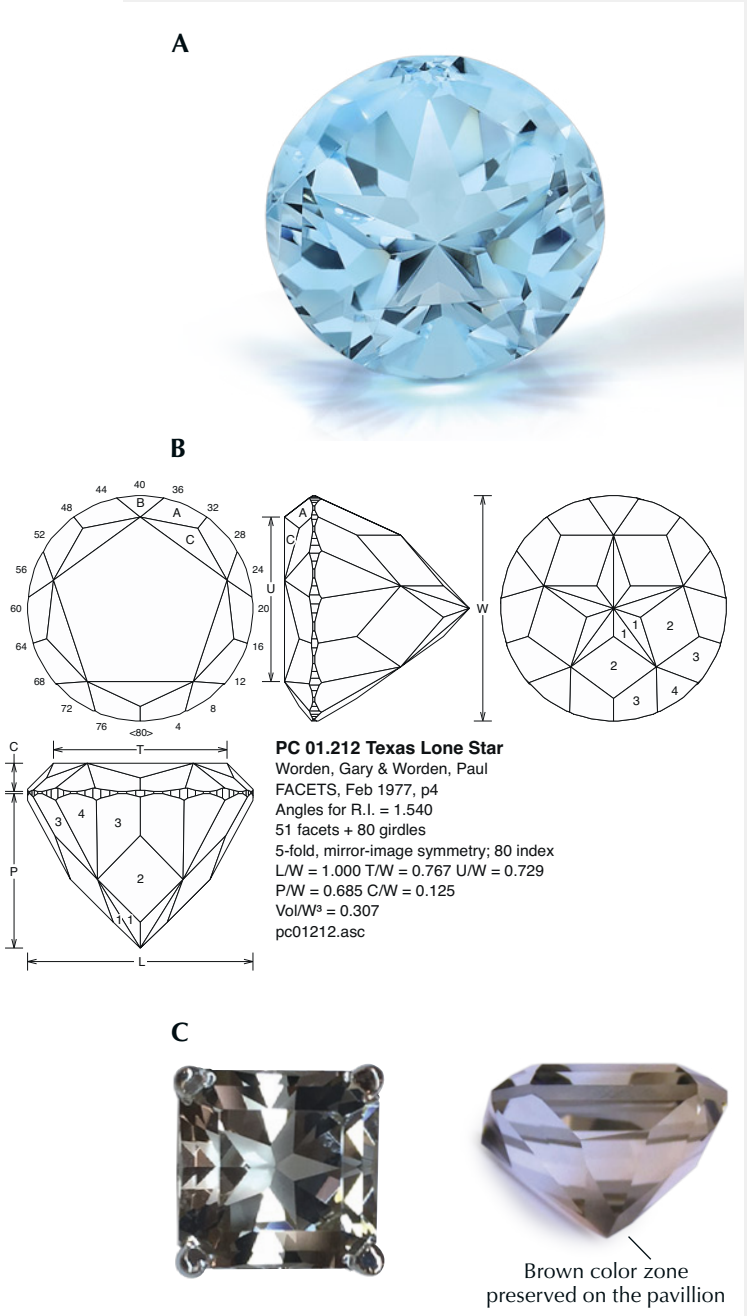

Figure A-1. A: 14.5 mm round 13.8 ct topaz from Mason County, Texas. Photo by Blanca Espinoza; courtesy of Form to Feeling. B: Facet design for Lone Star cut (from the open database at http://www.facetdiagrams.org). C: A cut topaz with brown color zones deliberately positioned along the pavilion to display a brownish bodycolor in the table view. Photos by Brad Hodges.

Topaz is popular with American faceters for its perfect basal cleavage plane. To prevent breakage during faceting and scratches during polishing, a gem cutter must avoid placing the table along the cleavage plane. Chips along the girdle may indicate that the cleavage plane is parallel to the girdle, which is also undesirable. The strongest color saturation in topaz occurs parallel to the *c*-axis. Therefore, faceters cannot simply orient the stone away from potential weakness associated with the basal cleavage without sacrificing color. To optimize color and avoid structural weakness, faceters attempt to cut topaz so that the table is ~7° off the cleavage plane, an orientation that minimizes fractures and accentuates color. A Texas topaz faceted with a 0.5 micron polish and a correctly oriented cleavage plane can achieve subadamantine luster and deeply saturated color, both of which contribute to its appeal.

The development of the Lone Star cut (figure A-1, A) distinguished Texas topaz as a regionally unique and desirable gemstone. The facets on its pavilion produce a large five-point star visible through the table, a shape reminiscent of the star in the Texas state flag. The pavilion of the traditional Lone Star cut represents up to 80% of the stone's total depth, making it unsuitable for rings and earrings. Alternative versions have a pavilion that accounts for 60–65% of the total depth, and these have become popular. Most are cut as round gems, but fancy Lone Star variations have also been developed.

Several Texas faceters have contributed to the design and popularity of the Lone Star cut. Gary Worden and Paul Worden of San Angelo are credited as the original designers (Worden, 1977; see figure A-1, B). Additional star cuts were developed by hobbyist faceters. The most influential were Charles Covill and Robert Strickland, both of Austin, who developed many variations and freely shared their designs with other gem cutters.

The commercial development of Lone Star cut Texas topaz initially relied on independent hobby cutters mainly selling their work in the town of Mason. With the opening of the retail store Gems of the Hill Country in 2007, manufacturing shifted to a commercial scale. Cofounders Diane Eames and Brad Hodges sourced, faceted, and designed Texas topaz jewelry pieces, providing a retail avenue for the state gem. Acquiring topaz from local rock hounds, ranchers, and topaz enthusiasts, Gems of the Hill Country expanded its inventory of gem-quality blue, pink, and brown topaz (figure A-1, C). Gems of the Hill Country has since closed, but the founders still maintain a large inventory of Texas topaz. During its decade-plus run, Gems of the Hill Country not only sold Texas topaz to buyers in the United States, Germany, and the United Kingdom but also founded and participated in Texas Topaz Day in Mason from 2008 to 2012, celebrating Texas topaz with a public mineral hunt on local topaz-bearing ranches. These efforts elevated the awareness and prestige of Texas topaz and "American-made" gemstones and jewelry.

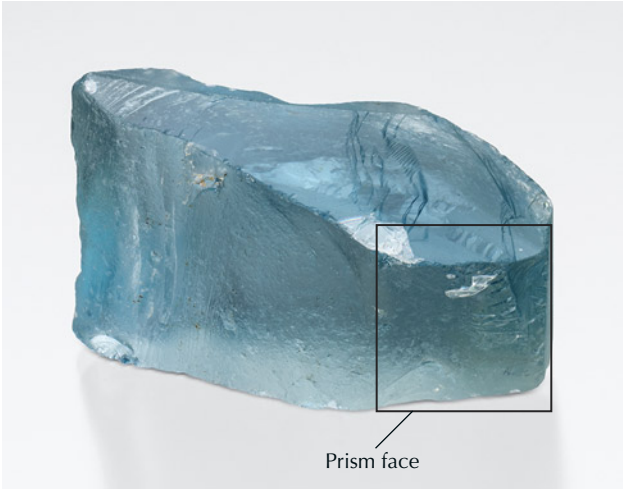

Figure 5. Example of a waterworn topaz with terminations and prism faces with narrow grooves and etchings in a 188 ct specimen. Photo by Emily Lane; courtesy of Diane Eames.

only rarely been extracted directly from vuggy pegmatites of Mason County granites through small hard-rock mining operations. Primary topaz extracted from these pegmatite vugs typically presents as rhombic to square and singly terminated prisms. As shown in figure 1 and figure 5, terminations and prism faces may display narrow grooves and etchings (White, 1960).

The vast majority of Texas topaz has been recovered from alluvial drainages, specifically along creeks and rivers south and east of the Katemcy pluton. These localized drainages sometimes correspond with the trend of pegmatites. Liberated alluvial topaz accumulates within potholes, depressions, and other structural traps where stream velocities slow, causing the high-density topaz (~3.5 g/cm^3) to settle (figure 6, top). Some alluvial topaz remains euhedral yet frosted, but most are well rounded and abraded. Corundum, including ruby, has occasionally been found within topaz-bearing alluvium, though it likely did not form alongside topaz. The original economic target for prospectors in Mason County was cassiterite, a tin ore mineral (Leiper, 1951; Sparks, 1968). Alluvial topaz is also found in the Middle Cambrian Hickory Sandstone Formation (White, 1960; Sparks, 1968; Fechenbach, 1984; Barnes et al., 1992; Collins, 2008). The occurrence of alluvial topaz in both Holocene and Middle Cambrian sedimentary rocks suggests a protracted history of erosion and deposition across millions of years.

Mining in central Texas has a rich history that began with the Spanish conquistadors searching for riches, including gold and the famed Seven Cities of Cibola. In 1893, George Kunz published the first report of topaz in Texas (Kunz, 1893). At that time, pegmatites in the Llano Uplift were being carefully assessed for their economic potential, as some hosted exceptional minerals containing rare earth elements.

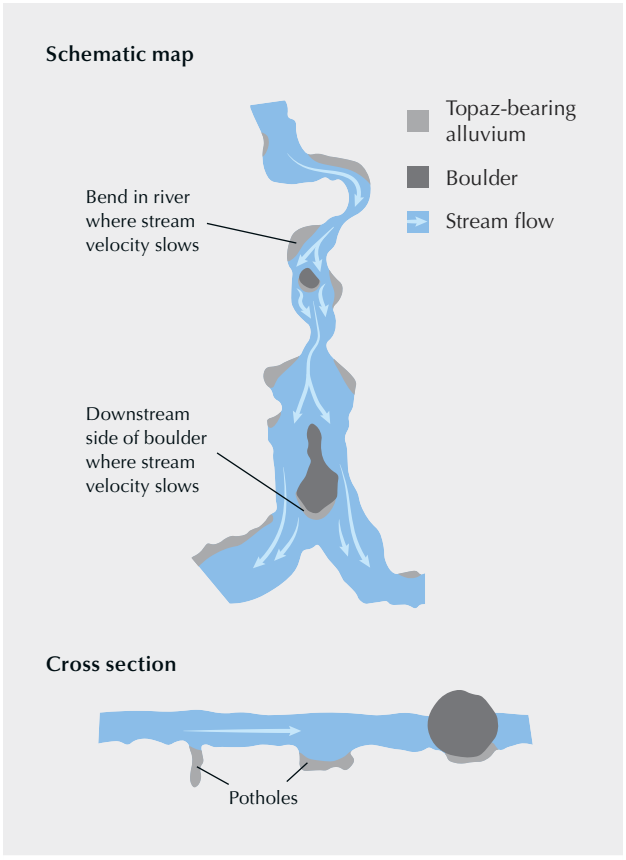

Figure 6. Top: Schematic map and cross section views of representative locations where alluvial topaz accumulates along a river or stream. Modified from Fechenbach (1984). Bottom: Dalan Hargrave (background) and Diane Eames (foreground) sieving gravels for topaz. Photo by Brad Hodges.

Thomas Edison's Piedmont Mining Company purchased the Barringer Hill pegmatite deposit to acquire rare earth minerals such as gadolinite, which were critical for filaments in the emerging technology of light bulbs (Smith, 2008). This acquisition did not involve topaz, however, as the rare earth pegmatites tended to occur in the eastern Llano Uplift and gem-quality topaz was found much farther to the west. Economic interest in the topaz-bearing pegmatites was later fueled by the search for economic tin deposits because of their association with cassiterite (Meyer, 1913).

Prospecting for topaz in Mason County has primarily been a seasonal activity by part-time local artisanal miners and recreational rock hounds (e.g., Browne, 1982; International Labour Organisation, 1999; Hinton, 2005). Prospectors sift gravels along waterways on public lands or local ranches such as the Seaquist or Lindsay ranches that allow prospecting for a daily fee (figure 6, bottom). The most productive sites are placers at the contact between bedrock and stream deposits. When prospective locations for alluvial topaz are determined, the sediment is disaggregated and passed through sieves. Published anecdotes refer to placer "pockets" containing dozens of stones larger than 1 cm in diameter and others with multiple waterworn crystals ranging from 8 to 926 ct. Mason County has produced topaz crystals and alluvial stones weighing less than 1 ct up to approximately 6800 ct, which is the largest topaz ever recovered in North America (Leiper, 1951; White, 1960; Towner, 1968, 1969; Sparks, 1968; Sinkankas, 1997). Historically, the average size recovered by artisanal and recreational prospectors has been between 1 and 10 ct. Decades of targeted placer mining on publicly accessible tracts of land have considerably depleted these deposits, as the authors can attest to after many laborious hours digging in Mason County drainages.

Topaz is still found today but in far lesser abundance than in earlier decades. Many areas that appear untouched today were likely excavated by past miners and have subsequently been refilled with gravels during flooding events. Rounded and abraded topaz may be mistaken for quartz. However, topaz can be accurately identified by its habit, cleavage, coloration, clarity, frosted appearance, and high density. Prospectors in the past sometimes carried bromoform or other heavy liquids to isolate the heavier topaz from the lighter quartz (Towner, 1968, 1969). Most prospectors work during the day, but others use UV flashlights at night to find strongly luminescent specimens.

MATERIALS AND METHODS

A total of 71 rough Texas topaz specimens were loaned to GIA for study by author DE, and an additional 12 rough samples were loaned to GIA by the Barron Gem and Mineral collection in the Department of Earth and Planetary Sciences at the University of Texas at Austin. Topaz specimens from other global localities were sourced from GIA's colored stone reference collection and are summarized in table 1. These samples are of D-type and E-type origin according to GIA's classification scheme for degree of confidence of origin (Vertriest et al., 2019). These 379 samples total are from Australia (8), Brazil (89), Colombia (47), Germany (3), Guyana (107), Japan (1), Mexico (40), Namibia (3), Nigeria (5), Pakistan (4), Russia (9), Sri Lanka (4), the United States (excluding Texas, 30), and Zimbabwe (29). Topaz samples with Texas listed as their origin are confirmed to be from Texas. The authors acknowledge that mineral specimens not sourced from Texas might be ambiguous in origin, and we consider the nuances in their trace element concentrations beyond the scope of this study. Instead, this study presents a potential use of machine learning to assist specifically in provenance determinations of Texas topaz.

Morphology, optical character, inclusion species, and composition of Texas topaz were assessed using various gemological, spectroscopic, and analytical methods. We also calculated specific gravity by measuring the mass in air and the mass submerged in water using a Mettler AM100 scale. A Gem Instruments Duplex II refractometer was used to measure refractive index. Surface fluorescence images were acquired using a DiamondView ultraviolet imaging system with a flash lamp source, an incident wavelength of ~225 nm, and an exposure time of approximately 5 s. Visible/near-infrared (Vis-NIR) absorption spectra were collected with a PerkinElmer Lambda 950 UV-Vis spectrophotometer in the 200–1000 nm range, with 1 nm spectral resolution at 77 K. Bulk Fourier-transform infrared (FTIR) spectra were collected using a Thermo Scientific Nicolet iN10 FTIR spectrometer equipped with an XT-KBr beam splitter and a mercury-cadmium-telluride (MCT) detector operating with a 4× beam condenser. FTIR analyses were performed across the 675–4000 cm^{-1} range in cooled transmission mode using a 200 × 200 µm aperture, 64 to 128 scans, and a spectral resolution of 4 cm^{-1}. Raman spectra of topaz-hosted inclusions were collected with a Thermo Scientific DXR Raman microscope equipped with a 532 nm laser operating at 8 mW, a ~2 µm spot, and a high-resolution grating (1800

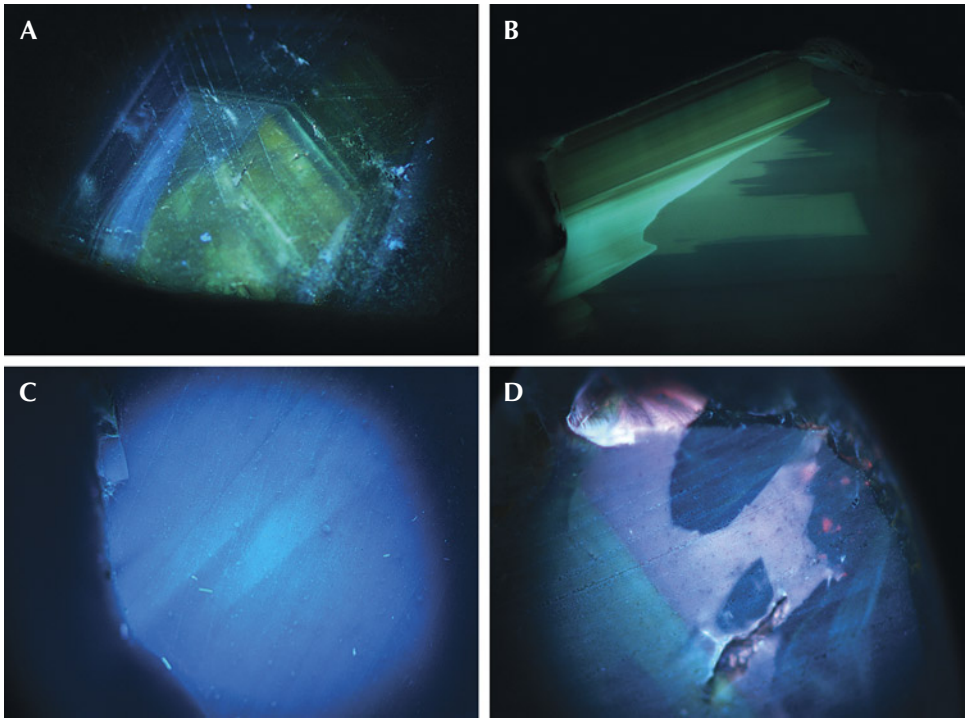

Figure 7. Representative UV luminescence images of Texas topaz acquired using ~225 nm excitation. Note the red luminescent zones in a topaz sample with elevated levels of chromium (image D). Images by Roy Bassoo; field of view ~15 mm.

lines/mm). Inclusion identity was confirmed with Raman spectra by matching peak positions and heights of the inclusions' spectra with those in the RRUFF spectral database (Lafuente et al., 2016).

Trace element concentrations were measured by laser ablation–inductively coupled plasma–mass spectrometry (LA-ICP-MS) using a Thermo Fisher iCAP Qc ICP-MS, coupled to an Elemental Scientific Lasers NWR213 laser ablation system with a frequency-quintupled Nd:YAG laser (213 nm wavelength with 4 ns pulse width). Ablation was carried out with 55 µm spot sizes, a fluence of 8–10 J/cm^2, repetition rates of 20 Hz, and dwell times of 35 s. The isotope ^{29}Si was used as an internal standard at 152854 ppmw, which is a representative average silicon ppmw content of topaz (Agangi et al., 2014, 2016; Gauzzi et al., 2018). United States Geological Survey glass standards GSD-1G and GSE-1G and National Institute of Standards and Technology (NIST) glass standard SRM 610 were used as external standards. Concentrations are reported as ppm throughout this article. Conversion factors are determined by factory-set parameters of Thermo Scientific's Qtegra software (Version 2.10.3324.131).

In this study, we calibrated a random forest machine learning model (Breiman, 2001) to predict topaz provenance using trace element compositions. This classification model calculated the probability of a single topaz specimen originating from Mason County, Texas. To calibrate this model, two outcome classes were defined: (1) topaz derived from Texas and (2) topaz derived from all other worldwide localities. For detailed information about the parameters used for model calibration, see appendix 1 (www.gia.edu/doc/winter-2023-texas-topaz-appendix1.pdf).

RESULTS

Gemological and Spectroscopic Characteristics. This study examined 83 topaz samples from Mason County ranging in size from 4 to 189 ct, with a mean weight of 21 ct. All of these samples were rounded and abraded and either colorless (47%), blue (50%), or yellowish brown (3%). Of the blue topaz, 75% were very light blue and 19% were light blue with saturated blue color zones. In some instances, this blue color can be desaturated by sunlight (Leiper, 1951). Only 6% of the Texas topaz samples had the deeply saturated blue bodycolor or color zones shown in figure 1. We measured a mean specific gravity of 3.55 ± 0.17 and a mean refractive index of 1.620 ± 0.001 and range from 1.615–1.625. The samples also had a vitreous luster and a white streak.

When exposed to ultraviolet luminescence, the Texas topaz displayed blue and/or green luminescent bodycolor and growth bands (figure 7, A–C). One sample showed red luminescent growth bands (figure 7D), which are known to be caused by Cr^{3+} impurities, which may impart a pink bodycolor (Petrov et

TABLE 1. Summary of trace element concentrations (in ppmw) of topaz measured by LA-ICP-MS.

Locality	Tectonic environment[a]	No. of measurements[b]		P	Sc	Ti	V	Cr	Fe	Ga	Ge	Nb	Sn	Ta	W
U.S. (Texas)	Orogen	180	Min	bdl[c]	1.5	bdl	bdl	bdl	bdl	1.02	12.3	bdl	bdl	bdl	bdl
			Max	589	4.4	209	40.21	99.6	193	17.50	223.7	4.36	2.4	4.100	0.98
			Median	14	3.4	8	bdl	bdl	35	5.57	68.3	0.03	bdl	0.010	bdl
			MAD[d]	7	0.3	4	—	—	24	1.64	23.4	0.03	—	0.010	—
Australia	Orogen	15	Min	bdl	2.1	2	bdl	bdl	10	1.89	12.3	bdl	bdl	bdl	bdl
			Max	153	3.5	44	18.76	4.1	132	9.31	336.3	0.60	1.4	0.050	2.90
			Median	26	3.0	10	bdl	bdl	68	5.46	32.4	0.01	bdl	0.010	bdl
			MAD	15	0.4	5	—	—	33	1.18	8.6	0.01	—	0.010	—
Brazil	Shield	200	Min	bdl	1.3	2	bdl	bdl	bdl	0.40	3.7	bdl	bdl	bdl	bdl
			Max	690	7.7	195	133.65	565.4	4032	25.72	976.2	4.58	19.4	4.240	13.83
			Median	19	2.5	14	9.30	54.7	34	4.25	31.3	bdl	bdl	bdl	bdl
			MAD	10	1.0	11	13.78	81.1	23	4.20	28.0	—	—	—	—
Colombia	Shield	98	Min	bdl	1.6	3	bdl	bdl	bdl	1.74	47.2	bdl	bdl	bdl	bdl
			Max	316	2.8	45	0.70	2.1	105	12.16	239.6	4.08	3.6	15.060	0.72
			Median	34	2.3	10	bdl	bdl	44	4.28	99.9	0.04	bdl	0.020	bdl
			MAD	34	0.4	5	—	—	10	1.49	13.9	0.03	—	0.015	—
Germany	Extended crust	6	Min	12	2.8	8	5.36	4.7	18	0.72	8.1	bdl	bdl	bdl	bdl
			Max	265	3.3	90	20.96	103.4	92	14.48	129.9	0.51	0.4	0.120	0.32
			Median	60	3.3	35	12.28	61.5	25	1.92	62.9	bdl	bdl	bdl	bdl
			MAD	63	0.1	28	7.17	29.2	9	0.96	59.3	—	—	—	—
Guyana	Shield	165	Min	bdl	1.5	11	bdl	bdl	bdl	1.90	6.6	bdl	bdl	bdl	bdl
			Max	3378	130.0	19767	108.00	217.3	1709	52.25	202.0	72.60	32.2	10.320	83.18
			Median	411	8.1	89	0.28	bdl	32	7.21	33.9	0.93	0.2	0.310	0.37
			MAD	421	7.0	84	0.42	—	19	2.88	13.0	1.32	0.3	0.460	0.49
Japan	Orogen	2	Min	46	3.0	2	bdl	0.4	10	5.00	19.2	0.02	0.4	0.010	bdl
			Max	54	3.2	7	bdl	0.4	15	5.77	72.9	0.03	0.6	0.020	0.06
			Median	50	3.1	5	bdl	0.4	12	5.39	46.0	0.03	0.5	0.015	0.03
			MAD	6	0.2	3	—	0.0	4	0.57	39.8	0.01	0.1	0.007	0.04
Mexico	Orogen	80	Min	bdl	2.9	24	bdl	bdl	65	2.71	13.4	0.41	bdl	0.050	0.26
			Max	146	35.3	372	0.69	27.5	2024	41.34	38.1	199.00	4.0	24.330	26.84
			Median	17	5.8	104	0.16	bdl	251	8.75	26.1	2.76	0.2	0.680	1.05
			MAD	5	1.0	35	0.08	—	76	2.41	3.5	1.56	0.2	0.520	0.56
Namibia	Shield	6	Min	12	2.4	1	bdl	bdl	bdl	2.59	44.9	bdl	bdl	bdl	bdl
			Max	93	3.0	16	0.15	bdl	26	8.67	160.9	0.06	bdl	0.010	0.07
			Median	14	2.7	9	bdl	bdl	23	3.27	89.8	bdl	bdl	0.010	bdl
			MAD	3	0.2	9	—	—	4	0.60	63.4	—	—	—	—
Nigeria	Shield	10	Min	bdl	2.6	2	bdl	bdl	21	1.41	18.5	bdl	bdl	bdl	bdl
			Max	106	5.1	198	0.50	6.4	227	9.10	269.0	3.55	bdl	0.470	3.03
			Median	33	3.3	4	bdl	bdl	47	2.00	34.6	0.02	bdl	0.005	bdl
			MAD	26	0.4	3	—	—	30	0.47	12.6	0.02	—	0.007	—

TABLE 1 (continued). Summary of trace element concentrations (in ppmw) of topaz measured by LA-ICP-MS.

Locality	Tectonic environment[a]	No. of measurements[b]		P	Sc	Ti	V	Cr	Fe	Ga	Ge	Nb	Sn	Ta	W
Pakistan	Orogen	10	Min	bdl	2.3	9	bdl	0.4	bdl	1.17	12.2	bdl	bdl	bdl	bdl
			Max	24	3.0	150	44.13	108.2	13	3.61	184.1	0.05	1.0	0.010	0.14
			Median	11	2.8	43	22.44	62.4	bdl	1.62	18.1	bdl	bdl	bdl	bdl
			MAD	10	0.3	40	14.15	53.3	—	0.60	8.1	—	—	—	—
Russia	Orogen	18	Min	11	2.2	6	bdl	bdl	bdl	0.24	0.4	bdl	bdl	bdl	bdl
			Max	954	3.7	121	688.05	1326.8	56	7.06	18.8	0.03	bdl	0.010	0.10
			Median	23	3.0	14	115.95	257.6	bdl	1.17	5.4	bdl	bdl	bdl	bdl
			MAD	10	0.2	10	123.00	277.5	—	0.97	4.9	—	—	—	—
Sri Lanka	Shield	8	Min	bdl	1.9	3	bdl	bdl	bdl	1.68	8.2	bdl	bdl	bdl	bdl
			Max	75	2.9	17	24.78	72.0	138	10.19	123.9	0.15	bdl	0.050	0.08
			Median	bdl	2.4	10	bdl	bdl	35	7.41	83.8	0.05	bdl	bdl	0.04
			MAD	—	0.5	4	—	—	32	3.13	52.8	0.05	—	—	—
U.S. (California)	Orogen	5	Min	10	2.5	2	bdl	bdl	bdl	1.13	243.7	bdl	bdl	bdl	bdl
			Max	30	2.9	20	bdl	bdl	bdl	7.13	420.4	0.08	bdl	0.320	bdl
			Median	13	2.7	3	bdl	bdl	bdl	3.44	373.7	bdl	bdl	0.020	bdl
			MAD	13	2.7	3	—	—	—	3.44	46.7	—	—	0.020	—
U.S. (Colorado)	Orogen	2	Min	48	1.8	3	bdl	bdl	35	1.35	71.6	bdl	bdl	bdl	bdl
			Max	72	2.0	3	0.08	bdl	36	1.83	77.0	bdl	bdl	bdl	bdl
			Median	—	—	—	—	—	—	—	—	—	—	—	—
			MAD	—	—	—	—	—	—	—	—	—	—	—	—
U.S. (Indiana)	Shield	2	Min	192	2.4	12	0.09	bdl	90	11.33	76.5	0.06	bdl	0.030	0.22
			Max	216	2.6	16	0.11	bdl	106	12.86	81.2	0.08	0.3	0.040	0.23
			Median	—	—	—	—	—	—	—	—	—	—	—	—
			MAD	—	—	—	—	—	—	—	—	—	—	—	—
U.S. (Utah)	Orogen	50	Min	bdl	1.9	10	bdl	bdl	35	1.39	8.9	bdl	bdl	bdl	bdl
			Max	142	23.9	996	26.88	191.4	1631	18.52	47.9	96.15	4.5	16.910	40.06
			Median	17	4.1	140	0.14	bdl	226	4.88	19.5	1.76	bdl	0.250	0.46
			MAD	7	0.8	43	0.05	—	92	2.23	2.8	1.33	—	0.210	0.45
Zimbabwe	Shield	58	Min	bdl	1.3	bdl	bdl	bdl	bdl	0.26	138.6	bdl	bdl	bdl	bdl
			Max	322	2.7	42	0.81	59.2	331	4.62	1308.0	0.68	8.7	1.230	0.19
			Median	98	2.4	4	bdl	bdl	bdl	2.86	724.0	0.02	bdl	0.035	bdl
			MAD	107	0.2	3	—	—	—	1.02	484.1	0.03	—	0.037	—
Detection limit (ppmw)				9	0.1	1	0.06	0.3	7	0.02	0.4	0.01	0.2	0.004	0.03

[a]*Classes derived from Simmons et al. (2012).*
[b]*Includes replicate analyses. Please see appendix 1.*
[c]*bdl = below detection limit*
[d]*MAD = median absolute deviation*

al., 1977; Taran et al., 1994, 2003). Only 4% of the analyzed topaz were inert or showed no luminescence response. The UV, visible, and infrared absorbance spectroscopic characteristics of Texas topaz were documented (figure 8). Absorption in the ultraviolet to visible spectrum found that 74% of the ana-

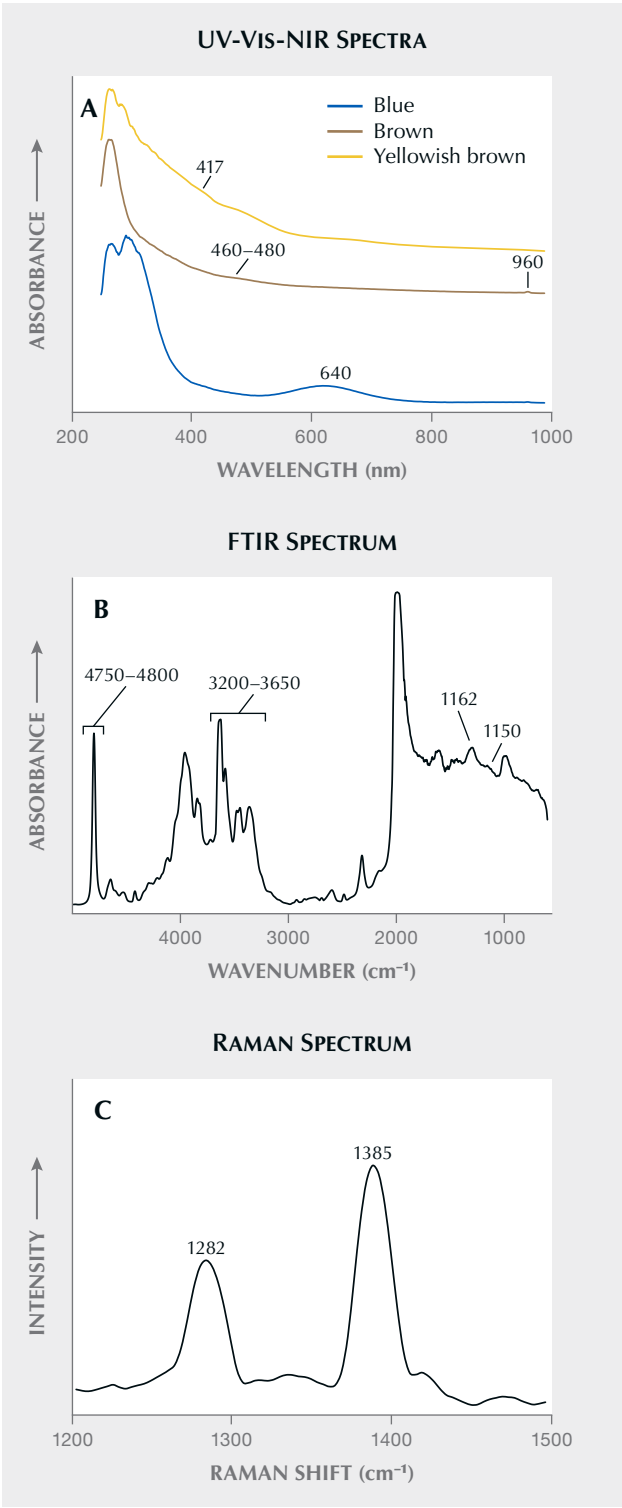

Figure 8. Representative UV-Vis-NIR, FTIR, and Raman spectra collected from 54 Texas topaz samples. The UV-Vis-NIR spectra were selected based on the prominence of the 417 nm, 460–480 nm, and 960 nm absorbances. The spectra are nonpolarized for the anisotropic topaz. Spectra are offset vertically for clarity. The Raman spectrum shows peaks related to CO_2.

lyzed Texas topaz had a small broad band at 640 nm (figure 8A). This feature has previously been attributed to an oxygen hole center that is strongly associated with the preservation of blue color (Krambrock et al., 2007). About 17% of the samples displayed a small broad band in the 460–480 nm range, likely associated with a temperature-sensitive oxygen hole center that causes brown color (Petrov, 1983; Aines and Rossman, 1986; Souza et al., 2006). Topaz with a broad 640 nm band sometimes has a 460–480 nm band, suggesting the two may be related. Small absorption bands at 417 nm occurred in 6% of the examined Texas topaz and indicate the presence of yellow color (Rossman, 2011). The defects responsible for the 417 nm absorption may be caused by a combination of a trapped-electron and oxygen hole centers (Schott et al., 2003; Gaft et al., 2005).

Each sample had a small absorbance peak at 960 nm, possibly an overtone of a hydroxyl (OH) group. Each topaz also had a large absorbance in the 230–305 nm range, likely produced by an Al=Si=O structure, which is an absorbance feature also observed in spodumene (Bonventi et al., 2012). Infrared absorbance in the 800–1050 cm^{-1} range is caused by vibrations of the SiO_4 tetrahedra, while observed absorbances near 1150 and 1162 cm^{-1} are commonly attributed to Al-OH and Al-O-H bonds within topaz (Londos et al., 1992; Prasad and Gowd, 2003; figure 8B). Absorbances observed in all samples occurring at 3200–3650 cm^{-1} and 4750–4800 cm^{-1} represented hydroxyl stretching vibrations (Aines and Rossman, 1986; Shinoda and Aikawa, 1997; Prasad and Gowd, 2003). Typically, OH substitutes for fluorine according to a temperature-dependent relationship in which higher OH correlates with crystallization at lower temperatures of 300–600°C compared to magmatic topaz formed at 600–800°C (Soufi, 2021 and references therein). No calibrations exist between IR absorbance and OH content in topaz, and therefore we did not establish absolute OH or fluorine content in Texas topaz. Regardless, most gem-quality topaz has high fluorine and low OH concentrations (G. Rossman, pers. comm., 2023), and the topaz-bearing pegmatites in Mason County host significant amounts of the fluorine-rich mineral fluorite (CaF_2).

Texas topaz is not typically free of inclusions. Only about 10% of the material is suitable for faceting when considering size, depth of color, color zoning, and inclusions. We occasionally observed multiphase fluid and melt inclusions, some containing bubbles of carbon dioxide. Among the mineral inclusions identified with Raman were albite,

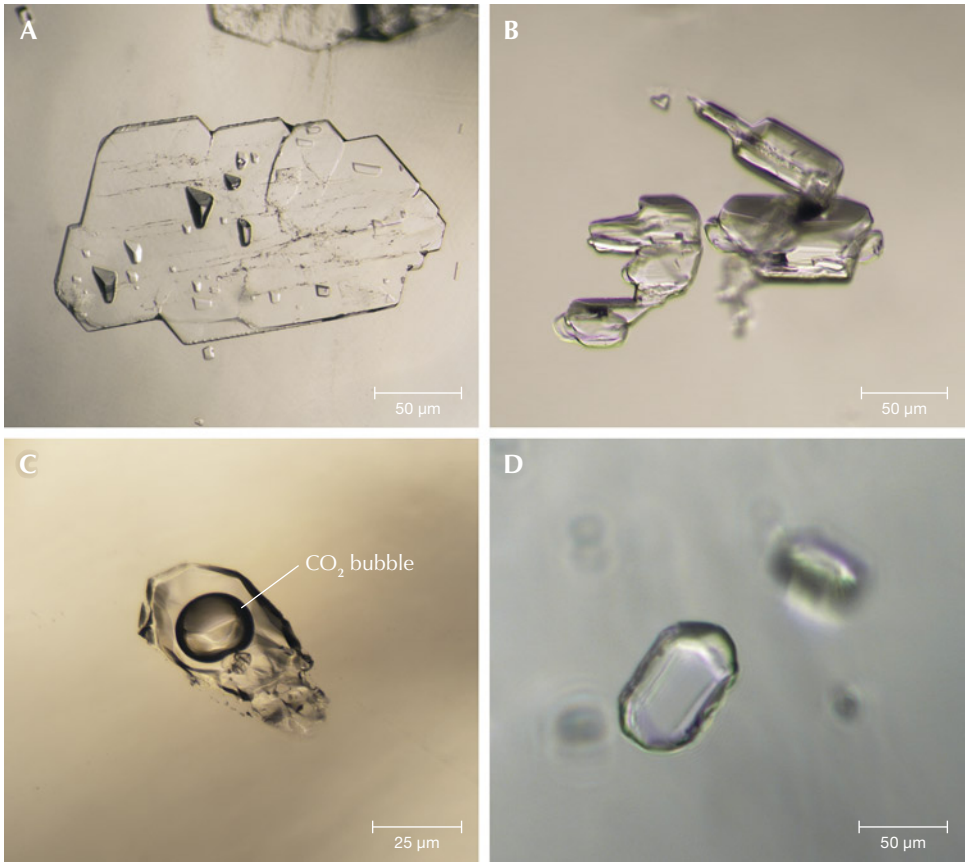

Figure 9. Examples of mineral and fluid inclusions found in Texas topaz: anorthosite (A), albite (B), fluid and melt inclusions (C), and quartz (D). Photomicrographs by Roy Bassoo.

anorthite, quartz, muscovite, pseudobrookite, rutile, and columbite-tantalite group minerals (figure 9). Most Texas topaz is alluvial and has been rounded by weathering. The waterworn samples had the fewest inclusions, which is expected because weathering in an alluvial environment would preferentially remove the poorer-quality stones by erosive attrition. For this reason, alluvial stones yield relatively flawless gemstones when faceted (Leiper, 1951).

Visual inspection and spectroscopic measurements revealed that Texas topaz shares many characteristics with topaz found in other localities globally. This study did not determine any defining characteristics or spectroscopic fingerprint to distinguish or differentiate Texas topaz.

Major and Trace Element Compositions. The major oxide composition of Texas topaz showed little deviation from that expected for $Al_2SiO_4(F,OH)_2$, with Al_2O_3 and SiO_2 accounting for 55.3 ± 0.4 wt.% and 31.8 ± 2.3 wt.%, respectively. The fluorine content of Texas topaz ranges from 19 to 21 wt.% (Collins, 2008), which suggests it may have formed from transitional pegmatite to hydrothermal processes (e.g., Foord et al., 1990; Soufi, 2021 and references therein). Minor oxide concentrations of FeO, MnO, and CaO were low, ranging from below detection limits to 0.3 wt.%. These major and minor element concentrations do not allow a clear distinction of Texas topaz from other global sources.

To test whether the trace element composition of Texas topaz has a characteristic identity, we measured trace elements in the samples. Germanium, iron, titanium, gallium, scandium, and phosphorus were detected consistently but at low concentrations (<600 ppm). Niobium, tantalum, tungsten, and tin were infrequently detected and when detected had very low concentrations (<5 ppm) (table 1). Similarly, the potential chromophore chromium was detected in only six samples but had a mean concentration of 27 ± 24 ppm.

Simple inspection of the trace element concentrations revealed limited diagnostic criteria. As expected with pegmatites, evidence of crystallization from highly fractionated fluids was present. Specifically, the niobium/tantalum (Nb/Ta) ratio of <5 served as a marker of mineralization in granitic rocks and can track increasing fractionation. This ratio likely reflects the magmatic to hydrothermal transition where tantalum is much less soluble than niobium in highly

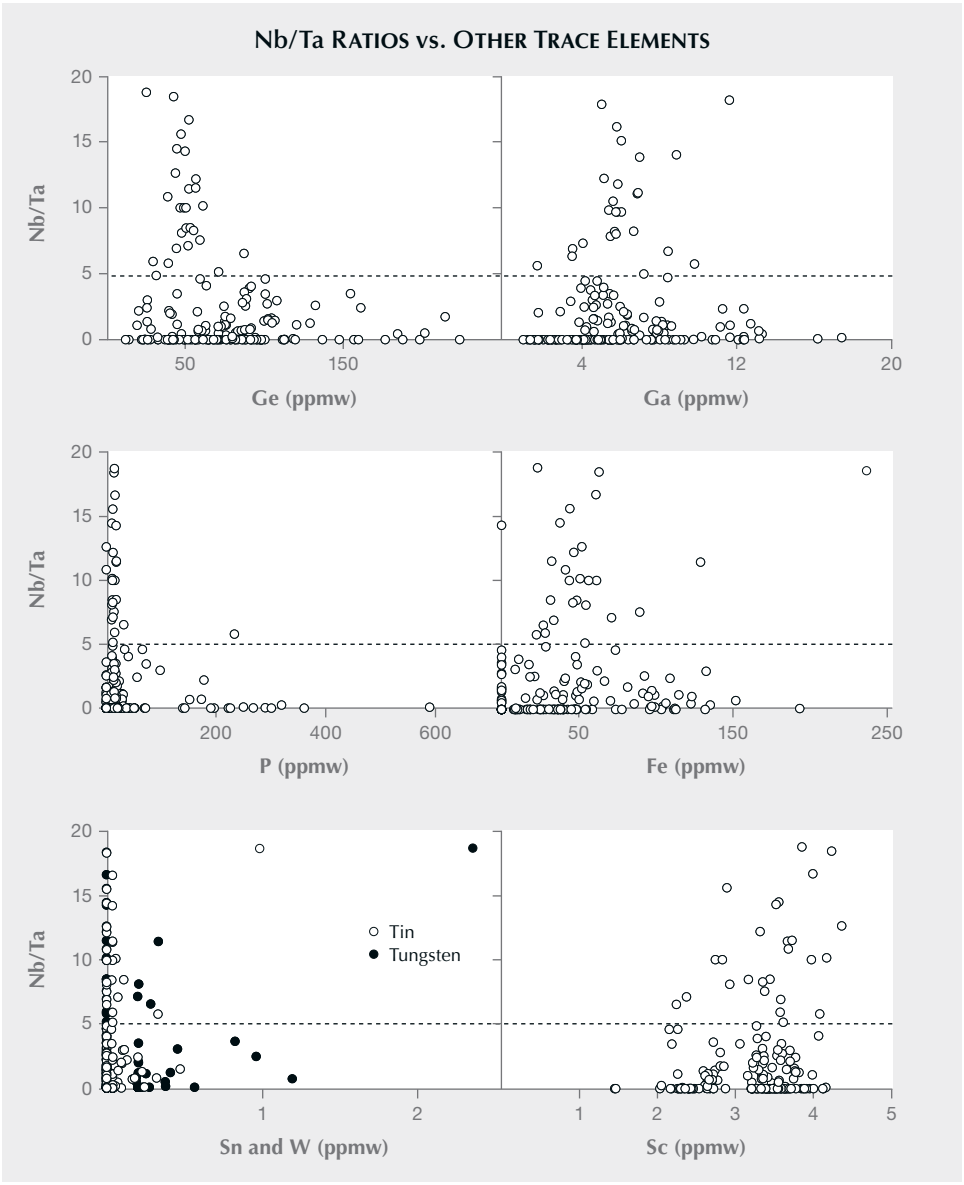

Figure 10. Nb/Ta ratios vs. germanium, gallium, phosphorus, iron, tin, tungsten, and scandium concentrations in Mason topaz. The dashed line indicates Nb/Ta ratios of ~5 (see Ballouard et al., 2016).

fractionated aqueous solutions (Zaraisky et al., 2010; Ballouard et al., 2016). Although the Nb/Ta ratio is normally applied to whole-rock analyses, germanium, gallium, phosphorus, tin, tungsten, and iron of the topaz samples showed increasing concentrations correlating with low Nb/Ta ratios (figure 10). Furthermore, most samples had gallium contents <20 ppm, but germanium ranged from 10 to 235 ppm. Such values are associated with topaz crystallization from pegmatites and greisens, consistent with the local Mason County geology (Duck, 1986; Breiter et al., 2013). Scandium concentration decreased with increasing fractionation, suggesting that scandium was incorporated into thortveitite or zinnwaldite during early crystallization of the host granite (Bianchi et al., 1988; Hreus et al., 2021). The concentrations of tin and tungsten were <3 ppm and notably low. However, the highly incompatible nature of tin and tungsten and the presence of cassiterite and scheelite in the region may collectively suggest greisen ore mineralization in Mason County (Paige, 1911; Meyer, 1913; Pollard et al., 1989). Indeed, previous geochemical studies suggest that topaz may indicate rare metal mineralization of pegmatites (Agangi et al., 2014, 2016).

The trace element concentrations of Texas topaz did not offer a readily accessible statistical or graphical signature for determining its origin. However, recent advances in machine learning as applied to trace

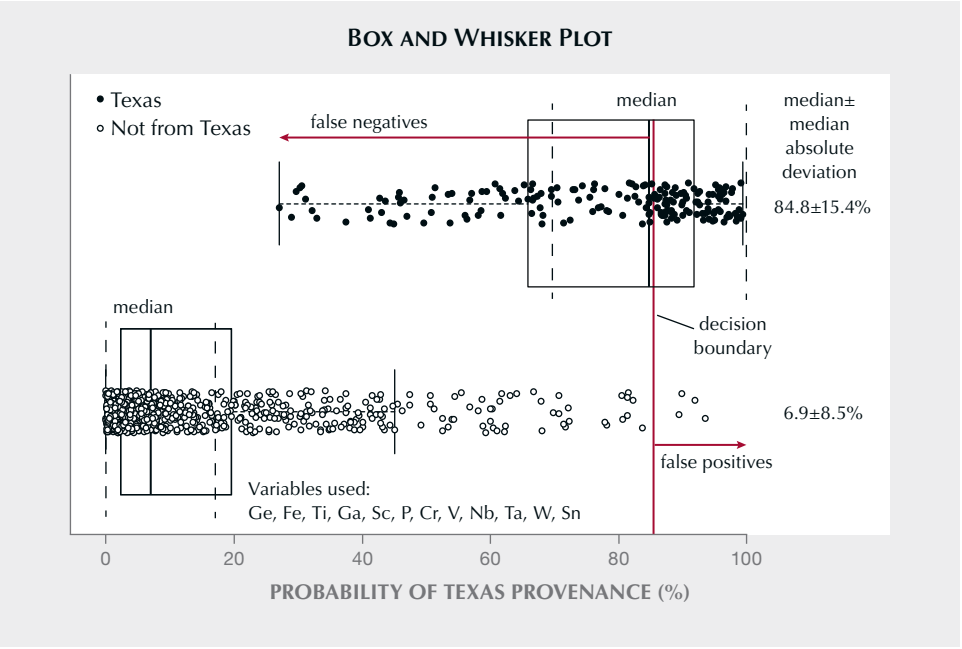

Figure 11. Box and whisker plot for the probability of Texas provenance for all topaz in this study, determined by the random forest machine learning method. Thick black vertical lines correspond to the median value, boxes correspond to the interquartile range (IQR), and horizontal dashed lines correspond to "whiskers" and extend 1.5× beyond the IQR. Samples with probabilities beyond the whiskers are considered outliers. The median absolute deviations are shown as vertical dashed lines.

element concentrations are a promising new tool for determining gemstone provenance. This approach is not without precedent for gemstones (e.g., Blodgett and Shen, 2011; Luo et al., 2015). We hypothesized that machine learning using the random forest statistical method could provide a robust probability of a specific topaz specimen being sourced from Mason County, Texas (Breiman, 2001). The effectiveness of machine learning depends in part on the size of the database available for model calibration, where larger datasets improve the effectiveness of the machine learning method. In this study, the authors compiled a new trace element dataset for 461 topaz samples, with 83 of known Texas provenance. However, it must be noted that Texas topaz are D-type and E-type samples according to GIA's origin classification scheme and were not obtained by sampling *in situ* (Vertriest et al., 2019).

To calibrate this model, the concentrations of germanium, iron, titanium, gallium, scandium, phosphorus, chromium, vanadium, niobium, tantalum, tungsten, and tin were used as variables. Each topaz could be assigned a pseudo-probability value by considering the proportion of the trees in the random forest model that "vote" for each outcome. Classification probability ranges from 0 to 100%, with higher probabilities indicating an increased likelihood of Texas provenance. One outcome was labeled "Texas" and the other "Not from Texas." The most significant trace elements for the Texas provenance were scandium, titanium, germanium, and chromium. An 85% decision boundary or classification value, above and below which one classifies a sample into different groups, was selected. Choosing the position of the decision boundary is user-determined and essential for making reliable provenance determinations (see appendix 1). Using these criteria, most topaz from Texas plotted with a very high likelihood of Texas origin (figure 11). Only ~12% of the 83 known Texas topaz samples were assigned a provenance other than Texas, or a "False Negative." These "False Negative" samples may correspond to populations that differ compositionally from the majority of Texas topaz. Regarding the overlap of probability, we find that some topaz from other locations has a higher probability of being derived from Texas, suggesting some degree of compositional similarity. This is expected in natural systems that have a continuum of compositional variability. However, analyzing additional Mason County samples will enable the model to better predict the provenance for these topaz compositions.

Importantly, 7% of the topaz from the global dataset were incorrectly classified as from Texas. These "False Positives" would be misidentified as "Texas" using the current machine learning approach. Samples from Namibia, Nigeria, Australia, and from California and Indiana in the United States were the most common false positives, with probabilities for Texas provenance of approximately 73%, 62%, 65%, 55%, and 70%, respectively (table 2). The ambiguity in our machine learning results was

TABLE 2. Median probabilities (±1σ)[a] or likelihood of topaz from other global locations being derived from Texas.

Locality	Tectonic environment[b]	No. of samples	Median probability of Texas provenance (%)
Germany	Extended crust	6	9 ± 9
Australia	Orogen	15	65 ± 28
Japan	Orogen	2	44 ± 7
Mexico	Orogen	80	3 ± 6
Pakistan	Orogen	10	6 ± 3
Russia	Orogen	18	1 ± 1
U.S. (California)	Orogen	5	55 ± 19
U.S. (Indiana)	Orogen	2	69 ± 2
Zimbabwe	Orogen	58	10 ± 6
Brazil	Shield	198	7 ± 5
Colombia	Shield	98	21 ± 12
Guyana	Shield	165	4 ± 3
Namibia	Shield	6	73 ± 8
Nigeria	Shield	10	62 ± 17
Sri Lanka	Shield	8	34 ± 19
U.S. (Colorado)	Shield	2	39 ± 4
U.S. (Utah)	Shield	50	3 ± 7

[a]*Includes replicate analyses. Please see appendix 1.*
[b]*Classes derived from Simmons et al. (2012).*

caused by fewer specimens from those locations. Larger sample sizes lead to more representative datasets. Greater sampling is required for populations where the compositional variation is larger. By acquiring more samples, we can better characterize the full compositional range of that suite of samples. For example, for populations of topaz with a smaller compositional range, fewer samples will be required to fully characterize the compositions of topaz from that locality. Indeed, countries with large numbers of topaz samples in this study, such as Brazil, Guyana, Colombia, Zimbabwe, and Mexico, had the lowest probabilities of Texas provenance, ranging from 3 to 21%.

These findings indicate that most Texas topaz have sufficiently distinct trace element compositions that allow them to be geochemically differentiated from topaz those in other global localities. Increased certainty in assigning provenance could be accomplished by also considering factors such as hue and saturation, fluorescence color, infrared and UV-Vis-NIR spectra, and inclusion suites (e.g., Palke et al., 2023). The machine learning model can also help identify deposits with similar geologic settings. The high predicted probability of similarity between Texas topaz and that from other U.S. locations and Australia may also indicate that they formed in similar geological conditions, resulting in the overlapping trace element compositions observed. Future studies of trace elements of tin and tungsten in topaz could improve our understanding of the geologic conditions leading to the formation of rare metal ore deposits, for example. Indeed, trace element compositions in colored stones better reflect the geologic environment in which they formed rather than their geographic origin (e.g., McClure et al., 2019).

CONCLUSIONS

Trace element compositions suggest topaz is derived from greisens and pegmatites. Furthermore, the presence of tin- and tungsten-bearing minerals such as cassiterite and scheelite, respectively, in the region

Figure 12. This 1,296 ct topaz crystal with a blue rim was recovered in Mason County, Texas. Photo by Ken Larsen; courtesy of the Smithsonian Institution Collection.

may collectively suggest greisen ore mineralization in Mason County. Topaz found in Mason County, Texas, has gemological characteristics that make it appealing for the gem trade (figure 12) and of particular commercial value throughout the state of Texas. However, misrepresentation often goes along with increased value. By combining trace element composition analysis with novel machine learning methods, origin determination for topaz could be possible. Better prediction of topaz provenance requires abundant sampling, especially from localities where current sampling is limited. This study has shown that trace element composition can be combined with traditional gemological observations to estimate a probability of Texas provenance. The inherent gemological value of Texas topaz is elevated by its domestic provenance, cementing its place among other highly prized gemstones from the United States.

ABOUT THE AUTHORS

Dr. Roy Bassoo is formerly a postdoctoral research associate at GIA in Carlsbad, California. Diane Eames is a GIA graduate gemologist and jeweler. Dr. Kenneth Befus is a gem and mineral curator at the Jackson School of Geosciences at University of Texas at Austin. Dr. Matthew F. Hardman is a research scientist at GIA in Carlsbad, California. Ziyun Sun is a senior research associate at GIA in Carlsbad, California.

ACKNOWLEDGMENTS

We sincerely thank Rose Tozer of GIA's Richard T. Liddicoat Gemological Library and Information Center for guiding us to excellent historical documents referring to Texas topaz. We also thank Dr. Aaron Palke for his technical feedback in the drafting of this article, Maxwell Hain for his philosophical contributions, Dr. Rhiana Elizabeth Henry for her proofreading, and the peer reviewers for feedback that improved the content of this article.

REFERENCES

Agangi A., Kamenetsky V.S., Hofmann A., Przybyłowicz W., Vladykin N.V. (2014) Crystallisation of magmatic topaz and implications for Nb-Ta-W mineralisation in F-rich silicic melts – The Ary-Bulak ongonite massif. *Lithos*, Vol. 202-203, pp. 317–330, http://dx.doi.org/10.1016/j.lithos.2014.05.032

Agangi A., Gucsik A., Nishido H., Ninagawa K., Kamenetsky V.S. (2016) Relation between cathodoluminescence and trace-element distribution of magmatic topaz from the Ary-Bulak massif, Russia. *Mineralogical Magazine*, Vol. 80, No. 5, pp. 881–899, http://dx.doi.org/10.1180/minmag.2016.080.023

Aines R.D., Rossman G.R. (1986) Relationships between radiation damage and trace water in zircon, quartz, and topaz. *American Mineralogist*, Vol. 71, No. 9-10, pp. 1186–1193.

Ballouard C., Poujol M., Boulvais P., Branquet Y., Tartèse R., Vigneresse J-L. (2016) Nb-Ta fractionation in peraluminous granites: A marker of the magmatic-hydrothermal transition. *Geology*, Vol. 44, No. 3, pp. 231–234, http://dx.doi.org/10.1130/G37475.1

Barker D.S., Reed R.M. (2010) Proterozoic granites of the Llano Uplift, Texas: A collision-related suite containing rapakivi and topaz granites. *Geological Society of America Bulletin*, Vol. 122, No. 1-2, pp. 253–264, http://dx.doi.org/10.1130/B26451.1

Barnes V.E., Hartmann B.M., Scranton D.F. (1992) Geologic Map of Texas: scale 1:500,000. Bureau of Economic Geology. University of Texas, Austin.

Bianchi R., Pilati T., Diella V., Gramaccioli C.M., Mannucci G. (1988) A re-examination of thortveitite. *American Mineralogist*, Vol. 73, No. 5-6, pp. 601–607.

Blodgett T., Shen A.H. (2011) Application of discriminant analysis in gemology: Country-of-origin separation in colored stones and distinguishing HPHT-treated diamonds. *G&G*, Vol. 47, No. 2, p. 145.

Bonventi W., Isotani S., Albuquerque A.R.P. (2012) Color dependence on thickness in topaz crystal from Brazil. *Advances in Condensed Matter Physics*, article no. 873804, http://dx.doi.org/10.1155/2012/873804

Breiman L. (2001) Random forests. *Machine Learning*, Vol. 45, pp. 5–32.

Breiter K., Gardenová N., Vaculovič T., Kanický V. (2013) Topaz as an important host for Ge in granites and greisens. *Mineralogical Magazine*, Vol. 77, No. 4, pp. 403–417, http://dx.doi.org/10.1180/minmag.2013.077.4.01

Browne V. (1982) Topaz in the Lone Star state. *Jewelry Making Gems and Minerals*, Vol. 531, pp. 16–18.

Burt D.M., Sheridan M.F., Bikun J.V., Christiansen E.H. (1982) Topaz rhyolites; distribution, origin, and significance for exploration. *Economic Geology*, Vol. 77, No. 8, pp. 1818–1836, http://dx.doi.org/10.2113/gsecongeo.77.8.1818

Charoy B., Noronha, F. (1996) Multistage growth of a rare-element, volatile-rich microgranite at Argemela (Portugal). *Journal of Petrology*, Vol. 37, No. 1, pp. 73–94, http://dx.doi.org/10.1093/petrology/37.1.73

Collins A. (2008) Chemical and optical discriminators for Mason topaz. Undergraduate senior honors thesis, University of Texas, Austin.

Congdon R.D., Nash W.P. (1988) High-fluorine rhyolite: An eruptive pegmatite magma at the Honeycomb Hills, Utah. *Geology*, Vol. 16, No. 11, pp. 1018–1021, http://dx.doi.org/10.1130/0091-7613(1988)016%3C1018:HFRAEP%3E2.3.CO;2

Crowningshield R. (1981) Irradiated topaz and radioactivity. *G&G*, Vol. 17, No. 4, pp. 215–217.

Duck J.J. (1986) Investigation of factors controlling the partitioning of trace germanium and gallium between topaz and quartz. PhD thesis, University of Pittsburgh.

Fechenbach M.F. (1984) Trapping the crafty topaz. *Jewelry Making Gems and Minerals*, Vol. 558, pp. 55–57.

Foord E.E., Jackson L.L., Taggart J.E., Crock J.G., King T.V.V. (1990) Environment of crystallization of topaz as inferred from crystal chemistry and infrared spectra. In *Abstracts of the 15th General Meeting of the International Mineralogical Association Proceedings*, pp. 306–307, Beijing.

Gaft M., Nagli L., Reisfeld R., Panczer G., Brestel M. (2003) Time-resolved luminescence of Cr^{3+} in topaz $Al_2SiO_4(OH,F)_2$. *Journal of Luminescence*, Vol. 102-103, pp. 349–356, http://dx.doi.org/10.1016/S0022-2313(02)00532-X

Gaft M., Reisfeld R., Panczer G. (2005) *Modern Luminescence Spectroscopy of Minerals and Materials*. Springer Berlin, Heidelberg, 356 pp.

Gauzzi T., Graça L.M. (2018) A cathodoluminescence-assisted LA-ICP-MS study of topaz from different geological settings. *Brazilian Journal of Geology*, Vol. 48, No. 01, pp. 161–176, http://dx.doi.org/10.1590/2317-4889201820170127

Gauzzi T., Graça L.M., Lagoeiro L., de Castro Mendes I., Queiroga G.N. (2018) The fingerprint of imperial topaz from Ouro Preto region (Minas Gerais state, Brazil) based on cathodoluminescence properties and composition. *Mineralogical Magazine*, Vol. 82, No. 4, pp. 943–960, http://dx.doi.org/10.1180/minmag.2017.081.078

Hinton J.J. (2005) *Communities and Small-Scale Mining: An Integrated Review for Development Planning*. CASM, Washington, DC.

Hoover D.B. (1992) *Topaz*. Butterworth-Heinemann Ltd., London.

Hreus S., Výravský J., Cempírek J., Breiter K., Galiová M.V., Krátký O., Šešulka V., Škoda R. (2021) Scandium distribution in the world-class Li-Sn-W Cínovec greisen-type deposit: Result of a complex magmatic to hydrothermal evolution, implications for scandium valorization. *Ore Geology Reviews*, Vol. 139, Part A, article no. 104433, http://dx.doi.org/10.1016/j.oregeorev.2021.104433

International Labour Organization (1999) Social and labour issues in small-scale mines. Report at the Tripartite Meeting on Social and Labour Issues in Small-Scale Mines, ILO, Geneva.

King Jr. E.A. (1961) Texas gemstones. Bureau of Economic Geology, Report of Investigations, No 42. The University of Texas at Austin, Austin, Texas.

Krambrock K., Ribeiro L.G.M., Pinheiro M.V.B., Leal A.S., Menezes M.Â de B.C., Spaeth J.-M. (2007) Color centers in topaz: Comparison between neutron and gamma irradiation. *Physics and Chemistry of Minerals*, Vol. 34, pp. 437–444, http://dx.doi.org/10.1007/s00269-007-0160-z

Kunz G.F. (1893) Notes on topaz from Texas. *New York Academy of Science Transactions*, Vol. 12, p. 96.

Lafuente B., Downs R.T., Yang H., Stone N. (2016) The power of databases: The RRUFF project. In T. Armbruster and R.M. Danisi, Eds., *Highlights in Mineralogical Crystallography*, pp. 1–29. W. de Gruyter GmbH, Berlin.

Leiper H. (1951) Texas blue topaz. *Lapidary Journal*, Vol. 5, No. 1, pp. 98–102.

Londos C.A., Vassilikou-Dova A., Georgiou G., Fytros L. (1992) Infrared studies of natural topaz, *Physica Status Solidi A*, Vol. 133, No. 2, pp. 473–479, http://dx.doi.org/10.1002/pssa.2211330231

Luo Z., Yang M., Shen A.H. (2015) Origin determination of dolomite-related white nephrite through iterative-binary linear discriminant analysis. *G&G*, Vol. 51, No. 3, pp. 300–311, http://dx.doi.org/10.5741/GEMS.51.3.300

Manning D.A.C., Hill P.I. (1990) The petrogenetic and metallogenetic significance of topaz granite from the southwest England orefield. In H.J. Stein and J.L. Hannah, Eds., *Orebearing Granite Systems; Petrogenesis and Mineralizing Processes*, Vol. 246, Geological Society of America, Boulder, Colorado, http://dx.doi.org/10.1130/SPE246-p51

Marshall D., Walton L. (2007) Topaz. In L.A. Groat, Ed., *Geology of Gem Deposits*. Mineralogical Association of Canada Short Course Series, Vol. 37, pp. 161–168.

McClure S.F., Moses T.M, Shigley J.E. (2019) The geographic origin dilemma. *G&G*, Vol., 55, No. 4, pp. 457–462.

Menzies M.A. (1995) The mineralogy, geology and occurrence of

topaz. *Mineralogical Record*, Vol. 26, No. 1, pp. 5–53.
Meyer L.C. (1913) Topaz and stream tin in Mason County, Texas. *Engineering and Mining Journal*, Vol. 95, pp. 511–512.
Mosher S., Levine J.S.F., Carlson W.D. (2008) Mesoproterozoic plate tectonics: A collisional model for the Grenville-aged orogenic belt in the Llano uplift, central Texas. *Geology*, Vol. 36, No. 1, pp. 55–58, http://dx.doi.org/10.1130/G24049A.1
Nassau K. (1985) Altering the color of topaz. *G&G*, Vol. 21, No. 1, pp. 26–34, http://dx.doi.org/10.5741/GEMS.21.1.26
Nassau K., Prescott B.E. (1975) Blue and brown topaz produced by gamma irradiation. *American Mineralogist*, Vol. 60, No. 7-8, pp. 705–709.
Paige S. (1911) Mineral resources of the Llano-Burnet region, Texas, with an account of the Precambrian geology. U.S. Department of the Interior, Bulletin 450.
Palke A., Renfro N., Hapeman J.R., Berg R.B. (2023) Gemological characterization of Montana sapphire from the secondary deposits at Rock Creek, Missouri River, and Dry Cottonwood Creek. *G&G*, Vol. 59, No. 1, pp. 2–45, http://dx.doi.org/10.5741/GEMS.59.1.2
Payette C., Martin R.F. (1990) Melt inclusions in the quartz phenocrysts of rhyolites from Topaz and Keg Mountains, Thomas Range, Utah. *Geological Society of America Special Papers*, Vol. 246, pp. 89–102.
Petrov I. (1983) Paramagnetische Zentren in Topas. PhD thesis, Heidelberg University, Germany.
Petrov I., Beredinski W., Bank H. (1977) Bestrahlte gelbe und rotbraune Topase and ihre Erkennung. *Zeitschrift der Deutschen Gemmologischen Gesellschaft*, Vol. 26, No. 3, pp. 148–151.
Pollard P.J., Taylor R.G., Tate N.M. (1989) Textural evidence for quartz and feldspar dissolution as a mechanism of formation for Maggs pipe, Zaaiplaats tin mine, South Africa. *Mineralium Deposita*, Vol. 24, No. 3, pp. 210–218, http://dx.doi.org/10.1007/BF00206444
Pough F.H. (1957) The coloration of gemstones by electron bombardment. *Zeitschrift der Deutschen Gesellschaft für Edelsteinkunde*, Vol. 20, p. 71.
Prasad P.S.R., Gowd T.N. (2003) FTIR spectroscopic study of hydroxyl ions in natural topaz. *Journal Geological Society of India*, Vol. 61, pp. 202–208.
Reed R.M. (1999) Emplacement and deformation of late syn-orogenic, Grenville-age granites in the Llano Uplift, Central Texas. PhD thesis, University of Texas, Austin.
Raimbault L., Cuney M., Azencott C., Duthou J.-L., Joron J.L. (1995) Geochemical evidence for a multistage magmatic genesis of Ta-Sn-Li mineralization in the granite at Beauvoir, French Massif Central. *Economic Geology*, Vol. 90, No. 3, pp. 548–576, http://dx.doi.org/10.2113/gsecongeo.90.3.548
Rossman G.R. (2011) The color of topaz. In *Topaz: Perfect Cleavage*. ExtraLapis English. No. 14. Lithographie, LLC, Denver, Colorado, pp. 79–85.
Schott S., Rager H., Schürmann K., Taran M. (2003) Spectroscopic study of natural gem quality "Imperial"-topazes from Ouro Preto, Brazil. *European Journal of Mineralogy*, Vol. 15, No. 4, pp. 701–706, http://dx.doi.org/10.1127/0935-1221/2003/0015-0701
Shinoda K., Aikawa N. (1997) IR active orientation of OH bending mode in topaz. *Physics and Chemistry of Minerals*, Vol. 24, No. 8, pp. 551–554, http://dx.doi.org/10.1007/s002690050071
Simmons W.B. (2007) Gem-bearing pegmatites. In L.A. Groat, Ed., *Geology of Gem Deposits*. Mineralogical Association of Canada Short Course Series, Vol. 37, pp. 169–206.
Simmons W.B., Pezzotta F., Shigley J.E., Beurlen H. (2012) Granitic pegmatites as sources of colored gemstones. *Elements*, Vol. 8, No. 4, pp. 281–287, http://dx.doi.org/10.2113/gselements.8.4.281
Sinkankas J. (1997) *Gemstones of North America, Volume 3*. Geoscience Press, Inc., Tucson, Arizona.
Smith A.E. (2008) The Baringer Hill pegmatite, Llano County, Texas. *The Backender's Gazette*, September, pp. 6–18.
Soufi M. (2021) Origin and physical-chemical control of topaz crystallization in felsic igneous rocks: Contrasted effect of temperature on its OH–F substitution. *Earth Science Reviews*, Vol. 213, article no. 103467, http://dx.doi.org/10.1016/j.earscirev.2020.103467
Souza D.N., Fernandes de Lima J., Valerio M.E.G., Caldas L.V.E. (2006) Thermally stimulated luminescence and EPR studies on topaz. *Applied Radiation and Isotopes*, Vol. 64, No. 8, pp. 906–909, http://dx.doi.org/10.1016/j.apradiso.2006.03.006
Sparks D. (1968) The Texas topaz fields. *Gems and Minerals*, Vol. 367, pp. 20–25.
Taran M.N., Langer K., Platonov A.N., Indutny V. (1994) Optical absorption investigation of Cr^{3+} ion-bearing minerals in the temperature range 77-797 K. *Physics and Chemistry of Minerals*, Vol. 21, No. 6, pp. 360–372, http://dx.doi.org/10.1007/BF00203294
Taran M.N., Tarashchan A.N., Rager H., Schott St., Schürmann K., Iwanuch W. (2003) Optical spectroscopy study of variously colored gem-quality topazes from Ouro Preto, Minas Gerais, Brazil. *Physics and Chemistry of Minerals*, Vol. 30, No. 9, pp. 546–555, http://dx.doi.org/10.1007/s00269-003-0356-9
Taylor R.P. (1992) Petrological and geochemical characteristics of the Pleasant Ridge zinnwaldite-topaz granite, southern New Brunswick, and comparisons with other topaz-bearing felsic rocks. *Canadian Mineralogist*, Vol. 30, No. 3, pp. 895–921.
Towner J.M. (1968) A topaz hunt in Mason County, Texas. *Lapidary Journal*, September, pp. 780–785.
——— (1969) Bigger and better topaz in Mason County. *Lapidary Journal*, August, pp. 700–705.
Vertriest W., Palke A.C., Renfro N.D. (2019) Field gemology: Building a research collection and understanding the development of gem deposits. *G&G*, Vol. 55, No. 4, pp. 490–511, http://dx.doi.org/10.5741/GEMS.55.4.490
White J.W. (1960) Topaz-bearing pegmatites and gem topaz in the Llano Uplift, Texas. Master's thesis, University of Texas, Austin.
Williams-Jones A.E., Samson I.M., Olivo G.R. (2000) The genesis of hydrothermal fluorite-REE deposits in the Gallinas Mountains, New Mexico. *Economic Geology*, Vol. 95, No. 2, pp. 327–341, http://dx.doi.org/10.2113/gsecongeo.95.2.327
Worden P.W. Jr. (1977) Lone Star. *Facets*, February, p. 4.
Zaraisky G.P., Korzhinskaya V., Kotova N. (2010) Experimental studies of Ta_2O_5 and columbite–tantalite solubility in fluoride solutions from 300 to 550°C and 50 to 100 MPa. *Mineralogy and Petrology*, Vol. 99, pp. 287–300, http://dx.doi.org/10.1007/s00710-010-0112-z
Zhang R.Y., Liou J.G., Shu J.F. (2002) Hydroxyl-rich topaz in high-pressure and ultrahigh-pressure kyanite quartzites, with retrograde woodhouseite, from the Sulu terrane, eastern China. *American Mineralogist*, Vol. 87, No. 4, pp. 445–453, http://dx.doi.org/10.2138/am-2002-0408

Bohemian Garnets as Decorative Materials for Glass Vessels from the Late Sixteenth to Early Eighteenth Centuries

Karl Schmetzer, Hans Albert Gilg, and Hans-Jörg Ranz

The decorative craft of setting cut garnets on colorless or yellow glass vessels was invented by Claudius vom Creutz in the Imperial City of Nuremberg circa 1591. The legal context surrounding development of the technique can be traced through details set forth in imperial privileges (which were similar in effect to modern patents) from 1591, 1653, and 1714, and in relevant historical literature, particularly in books summarizing decisions of the Nuremberg administration and the imperial administration in Prague and Vienna.

Two glass vessels in the collections of the Bavarian National Museum in Munich and the Passau Glass Museum (Passau, Germany) are adorned with red stones using a technique attributed to Creutz. These were examined at the museums using a portable X-ray fluorescence analyzer, and it was found that rose-cut Bohemian garnets were affixed by layers of reddish brown or yellow lead glass to the bodies of the engraved glass goblets. This process entailed using heat to melt the lead glass, which simultaneously heated the garnets and the glass objects to temperatures below melting point. A second glass goblet from the Passau collection was decorated with red glass stones imitating Bohemian garnets.

Garnet-glass doublets, also designated as garnet-topped doublets, are known to most gemologists. These doublets consist of a thin layer or slice of almandine garnet fused to a body of colored glass. The color of the glass pavilion (e.g., green, blue, or yellow) dominates the color of the composite stone, and the red color of the garnet slice, representing the crown, has only little influence upon the doublet's coloration (Michel, 1926; Webster, 1964; Webster and Anderson, 1983). Such materials appeared in large quantities on the market in the 1920s but, according to Burdet (1925), were already being produced in the 1840s in the French Jura north of Geneva.

The present study describes another composite of glass and garnet, which was produced from the end of the sixteenth century to the first decades of the eighteenth century—more than two centuries before the manufacture of "modern" garnet-glass doublets started. In particular, this article describes the history and production of a composite consisting of faceted Bohemian garnets attached to glass goblets and glass beakers for decoration.

The Bavarian National Museum in Munich houses such a lidded goblet (figure 1), decorated with faceted red stones, described as garnets by Rückert (1982). It is stated that the goblet was donated to the museum's collection in 1960 from the estate of the Munich medical doctor Heinrich Brauser (1872–1959). The goblet was purchased by Brauser in 1926 from a Munich art gallery; for more details on Brauser and his glass collection, see Rückert (1962) and Pfeiffer (1977).

The goblet shows an engraving of a hunting scene with two hunters and several animals in a forest and is dated, based on the hunters' attire and the rose cuts of the garnets, to the 1630s or 1640s. Rückert (1982) also mentions that the decoration of glass objects with garnet is originally related to the Nuremberg artisan Claudius vom Creutz, who had, according to Rückert, obtained an imperial privilege for this technique in the first decade of the seventeenth century. Clues to the goblet's origin in Nuremberg and the

See end of article for About the Authors and Acknowledgments.
Gems & Gemology, Vol. 59, No. 4, pp. 432–449,
http://dx.doi.org/10.5741/GEMS.59.4.432

Figure 1. Lidded goblet from the collection of the Bavarian National Museum in Munich, embellished with red Bohemian garnets. Inventory no. 60/74, height 17.7 cm. Photo by Bastian Krack; courtesy of Bavarian National Museum in Munich.

process developed by Creutz are also given by other authors (Bernt, 1950; Fuchs, 1959; Meyer-Heisig, 1963). In contrast, Żelasko (2014) dates the lidded goblet from the Munich collection to 1655 and assigns its origin to glassworks in Lower Silesia (now Poland), but without a detailed substantiation of this new provenance. Żelasko (2014) also incorrectly identified the red decorative materials as glass imitations, when they were in fact red garnets.

In an anthology of artists and craftspersons related to the Imperial City of Nuremberg (Grieb, 2007a), Claudius vom Creutz (also "von Creutz," "Kreutz," "Creuz," or "de la Croix" in various documents) is listed as a gemstone cutter and horologist. It is mentioned that he trained several cutters in Nuremberg, and he is described in a portrait (figure 2) as the first garnet setter (*Cranaten Sezer*) in that city. The index of artistic crafts in Grieb (2007b) mentions within the group of gemstone cutters, seal engravers, and goldsmiths several professions that still exist such as diamond cutter, ruby cutter, and garnet cutter, but also "garnet rose setter," a craft that is obsolete.

The present article seeks to elucidate the use of red Bohemian garnet to decorate glass objects, a technique invented by Creutz in the latter sixteenth century. Furthermore, the authors present a brief overview of Creutz and the imperial privileges granted to him and his successors. Such imperial privileges are compara-

Figure 2. Portrait of gem cutter Claudius vom Creutz, designated as the first garnet setter in the city of Nuremberg. Copper engraving by Johann Paul Zieger, Nuremberg, seventeenth century. Courtesy of the Germanic National Museum in Nuremberg (signature MP 5071, Kapsel-Nr. 72).

Figure 3. Extraction and processing of Bohemian garnets in the nineteenth century: (1) digging at the surface, (2) retrieving garnet-bearing soil or gravel from deeper levels and sieving, (3) washing to remove soil, (4) sorting, (5) cutting, (6) polishing, and (7) a view of the cutting table. From Gareis (1884).

ble to modern patents. However, these privileges were granted by grace of the emperor rather than by general law and were specific to each invention and inventor. For this study, the method applied for attaching garnets to the glass substrate was also examined by microscopic and analytical techniques and is explained with the help of these results.

The use of Bohemian garnet for jewelry and other decorative objects is known since the migration period in Europe from about 400 to 600 CE (e.g., Quast and Schüssler, 2000; Gilg et al., 2015). Most garnets originate from secondary deposits, where they can be easily removed from the garnet-bearing soil or gravel. The methods for digging and cutting at the end of the nineteenth century (illustrated in figure 3) appear to be more or less identical to the techniques applied in the centuries before.

CLAUDIUS VOM CREUTZ

Sources. Two main sources review original documents related to events in the life of Creutz: the decisions of the council of the Imperial City of Nuremberg

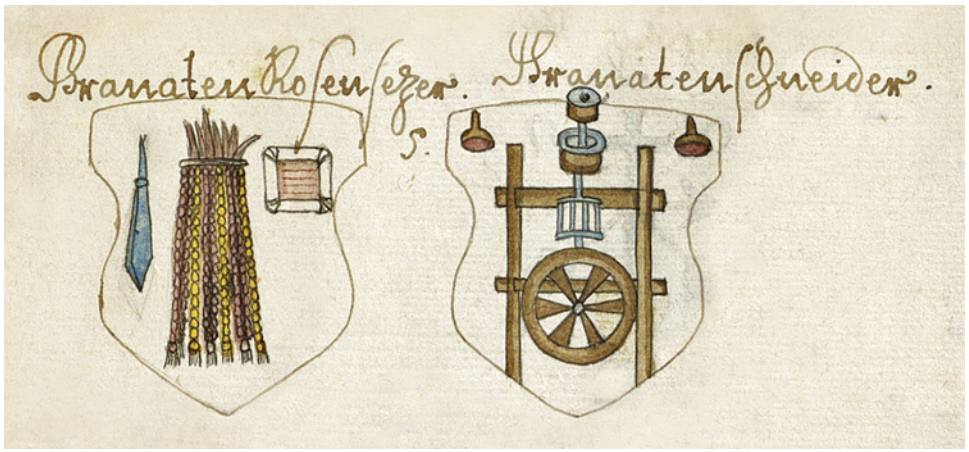

Figure 4. Coat of arms for the crafts of the "garnet rose setter" (left) and "garnet cutter," from the handwritten descriptions of all crafts in the Imperial City of Nuremberg around 1700. From Von Ursprung und Herkom[m]en samt Beschreibung aller Hand Wercker in der Stadt Nürnberg *(ca. 1700). Courtesy of the Germanic National Museum in Nuremberg (signature Merkel Hs 2° 981).*

(Hampe, 1904) and the yearbooks of the art historical collections of the imperial family (Graf zu Trautmannsdorff-Weinsberg, 1889, 1894; Graf von Abensberg und Traun, 1898). An anonymous compilation of all crafts in Nuremberg at the time (*Von Ursprung und Herkom[m]en samt Beschreibung aller Hand Wercker in der Stadt Nürnberg*, ca. 1700) dedicates one page (see figure 4) to Creutz and the professions of garnet rose setter and garnet cutter. Two handwritten copies of the treatise are kept in different archives in Nuremberg (see also a second copy of the book, titled *Von Ankunft und Herkommen aller Handwerker, so in der Stadt und Landwehr Nürnberg wohnhaft*, 1719). A file of Creutz's privileges with documents from 1591 to 1600 is kept in the Austrian State Archives in Vienna.[1] Further dates from his life are found in Thieme (1913) and on the "Astronomy in Nuremberg" website (www.astronomie-nuernberg.de).

In Brief

- Rose-cut Bohemian garnets were attached as decorative materials to the surfaces of engraved glass vessels by thin layers of low-melting-point lead glass.
- The technique was invented around 1590 by Claudius vom Creutz in Nuremberg and continued to be used through the first decades of the eighteenth century.
- Legal rights governing use of the technique, known as privileges, were granted to citizens of Nuremberg by Emperor Rudolf II and his successors.

Summary of Events (see table 1 and Schmetzer et al., 2024). The first document to mention Creutz in the Imperial City of Nuremberg is dated 1572 and refers to a textile merchant. A first marriage was reported in the same year, and a second is known from 1588. Creutz was Calvinist, and several documents mention that he descended and migrated from France, though his place and date of birth are unknown.

TABLE 1. History of garnet setting on glass objects.

1572	C. vom Creutz is mentioned as a textile merchant in the city of Nuremberg
1584, 1588, 1589	Various privileges of the city of Nuremberg are granted to Creutz
1591	The privilege of Emperor Rudolf II is granted to Creutz
1598	Privileges of the city of Nuremberg are extended
1600	The privilege of Emperor Rudolf II is extended
1604	Death of Creutz
1610s to 1620s	Transfer of the imperial privilege to V. Fischer, whose son J.T. Fischer later sells the rights to G. Schürstab (all from Nuremberg)
1653	Renewal of the privilege by Emperor Ferdinand III to G. Schürstab
1714	Renewal of the privilege by Emperor Karl VI to J.J. Vogel and J.P. Rotgängel of Nuremberg
1720	Five master craftspersons are still working in Nuremberg as garnet rose setters

[1]File: Creutz Claudius, Nürnberg, erhält das Privileg böhmische Granaten zu färben und zu schneiden (1591). Signature: AT-OeStA/HHStA RHR Grat Feud Gewerbe-, Fabriks- und Handlungsprivilegien 2-2-14.

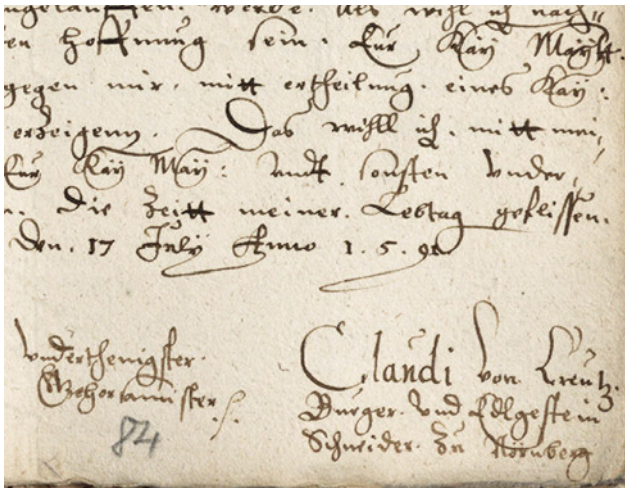

Figure 5. Signature from the petition of Creutz, "citizen and gem cutter from Nuremberg," to Emperor Rudolf II. The petition is dated July 17, 1591. Courtesy of the Austrian State Archives in Vienna (see footnote 1).

In 1584, Creutz applied for a privilege related to a tool for cutting Bohemian garnets, which was granted by the Nuremberg Council. At the time, the issue of local privileges by a city was an exception in the history of laws, at least in Germany. A further privilege was issued in 1588 for the cutting of rock crystal and jasper. The technical details of these inventions and their advancements to the state of art are unknown. A third local privilege, issued in 1589, referred to the "setting of rose cut garnets."

In May 1591, Creutz petitioned Emperor Rudolf II (1552–1612, r. 1576–1612), residing in Prague, to grant a privilege for the same topic (figure 5). The application mentions four steps of production: cutting, composing, setting, and melting (i.e., attaching by melting an intermediate lead glass fixation layer) of Bohemian garnets on colorless or yellowish glass. Further details about the technique are not given, but it is mentioned that examples of embellished glasses accompanied the petition. The privilege was granted by grace of the Holy Roman Emperor in August 1591 for a term of eight years.

Between 1598 and 1600, Creutz petitioned the Nuremberg Council and the emperor for extensions of his privileges, and the Nuremberg Council also intervened on his behalf at Prague. Extensions were granted from the Nuremberg Council in 1598 and the emperor in 1600, whereby Creutz was even able to extend the privilege to his wife and sons and to include a cutting tool.

Creutz educated several apprentices in his techniques for cutting and setting garnets. If these apprentices wanted to work independently, they could attain licenses against payment. Creutz took action several times against infringements of his rights, and Nuremberg craftspersons who copied his art and techniques were forced to pay penalties (Pohlmann, 1961).

It is said that Creutz became wealthy from his craft but died poor due to an extravagant lifestyle. After his death in 1604, his privileges were transferred to his three underage sons and their rights were exercised by their guardians, according to numerous documents from 1605 to 1611.

SUCCESSORS OF CREUTZ

Sources. A file containing documents about the extension of Creutz's privilege to Georg Schürstab in 1653 is available from the Austrian State Archives in Vienna,[2] and a document related to this legal act is preserved at the Germanic National Museum in Nuremberg[3] (figure 6). A further extension was issued in 1714 for Johann Jacob Vogel and Johann Paul Rotgängel. The file for this act is found in the Austrian State Archives in Vienna,[4] and a related document is kept in the Historical Archives of the City of Nuremberg[5] (figure 7).

Summary of Events (see table 1 and Schmetzer et al., 2024). After Creutz's death, the rights were transferred to Valentin Fischer, who had been taught the technique of cutting and setting garnets by Creutz. Upon Fischer's death in 1621, the rights were inherited by his son Johann Thomas Fischer, who sold the privilege to Georg Schürstab at Nürnberg. In 1653, the privilege was renewed by Emperor Ferdinand III (1608–1657, r. 1637–1657). A further extension of the privilege was issued by Emperor Karl VI (1685–1740, r. 1711–1740) for Johann Jacob Vogel and Johann Paul Rotgängel in 1714.

The detailed text of the imperial privilege from 1714 shows a broad application to all glass objects

[2]File: Schürstab Georg zu Nürnberg, erhält Privileg Böhmische Granaten zu versetzen (1653). Signature: AT-OeStA/HHStA RHR Grat Feud Gewerbe-, Fabriks- und Handlungsprivilegien 9-2-9.

[3]File: Privileg für Georg Schürstab (1653). Signature: SB-URO Or. Perg. Dated October 1, 1653.

[4]File: Vogel Johann Jakob und Rothgängel Johann Paul erhalten Privileg die böhmischen Granaten zu schneiden, zu versetzen und zu verkaufen (1714). Signature: AT-OeStA/HHStA RHR Grat Feud Gewerbe-, Fabriks- und Handlungsprivilegien 11-2-3.

[5]File: Kaiserliches Privileg Vogel/Rothgängel von (1714). Signature: A 1 Nr. 1714-06-10 GF.

Figure 6. Emperor Ferdinand III's privilege for Georg Schürstab, 1653. Courtesy of the Germanic National Museum in Nuremberg (see footnote 3).

decorated with Bohemian garnet, including their production and commercial distribution. The privilege was valid for all principalities and imperial cities within the Holy Roman Empire. All princes, dignitaries, and officials were requested to uphold the rights of privilege holders. Penalties for infringements of these rights were also quoted. Such rights could be transferred to all descendants or heirs of the owners.

Figure 7. First page of the privilege of Emperor Karl VI for Johann Jacob Vogel and Johann Paul Rotgängel, 1714. Courtesy of the Historical Archive of the City of Nuremberg (see footnote 5).

Figure 8. Lidded goblet from the collection of the Bavarian National Museum, embellished with red Bohemian garnets. Inventory no. 60/74, height 17.7 cm. Photos by Bastian Krack; courtesy of Bavarian National Museum in Munich.

It is mentioned that the privilege was intended to deter the production of objects of low quality.

If we compare the various texts of documents issued from the late sixteenth to early eighteenth centuries, it is worth mentioning that the description of the technique applied is almost identical to Creutz's original wording, and no further technical details were added in later applications or privileges. Within these descriptions, no details are provided on how the faceted Bohemian garnets were affixed to the glass substrate.

In 1720, there were still five master craftspersons with the title of "garnet rose setter" working in Nuremberg, but this profession became extinct in the second half of the eighteenth century (Gatterer, 1790). The decline of garnet setting on glassware coincided with the decline of the art of glass engraving in Nuremberg, as described by Hampe (1919).

MATERIALS AND METHODS

Glass goblets and beakers embellished with Bohemian garnets are extremely rare. We are aware of the sample owned by the Bavarian National Museum, inventory no. 60/74 (figure 1 and figure 8; see Rückert, 1982; Żelasko, 2014) and a glass beaker preserved in the Passau Glass Museum, inventory no. Hö 67867 (figure 9). This beaker was described by Żelasko (2014) as originating from glassworks in Lower Silesia and dated to 1655. The beaker was purchased in 1993 at an art auction, according to Peter Höltl from the Passau Glass Museum. The decoration of the Munich goblet originally consisted of 60 red stones on the body and 45 red stones on the lid, while the decorative pattern of the Passau beaker featured 44 red stones. These two decorated and engraved glass objects were examined in the present study.

Another glass goblet associated with the technique developed by Creutz (Stehlíková, 2004) is preserved in the Czech National Museum in Prague, but this example was not available for examination.

The Passau Glass Museum also houses numerous examples of goblets and beakers set with red (and also green) decorative materials, some of which are rose-cut red glass imitations of garnet. For comparison, we selected one of these samples, a lidded goblet, inventory no. Hö 71145 (figure 10), which was attributed by Żelasko (2014) to glassworks in Lower Silesia and dated to the first quarter of the eighteenth century.

The three decorated glass vessels were examined on the museum premises in Munich and Passau. In an initial visual inspection, we numbered each garnet and the positions of missing decorative materials

Figure 9. Beaker from the collection of the Passau Glass Museum, decorated with red Bohemian garnets. Inventory no. Hö 67867, height 9.8 cm. Photos courtesy of P. Höltl, Passau Glass Museum.

Figure 10. Lidded goblet from the collection of the Passau Glass Museum, embellished with red and green imitation stones made of lead glass. Inventory no. Hö 71145, height 8.5 cm. Photo courtesy of P. Höltl, Passau Glass Museum.

on photos of the glass objects, noting particularly the gem cutting styles (see figures 8 and 9). Next, the three samples were chemically analyzed using a portable Bruker Tracer III-SD energy-dispersive X-ray fluorescence (EDXRF) analyzer (figures 11 and 12). The instrument is equipped with a rhodium anode, a silicon drift detector with a resolution of 147 eV at 10,000 cps, and a portable vacuum pump system. The spot size of the primary beam is about 2 × 3 mm. We used two analytical conditions for the measurement. The first setup, with an accelerating voltage of 15 kV and a beam current of 25 µA under vacuum, was used to analyze the light elements of interest (magnesium to iron; note that sodium cannot be detected with this method and could also be present in the glasses). The second setup was used for the ex-

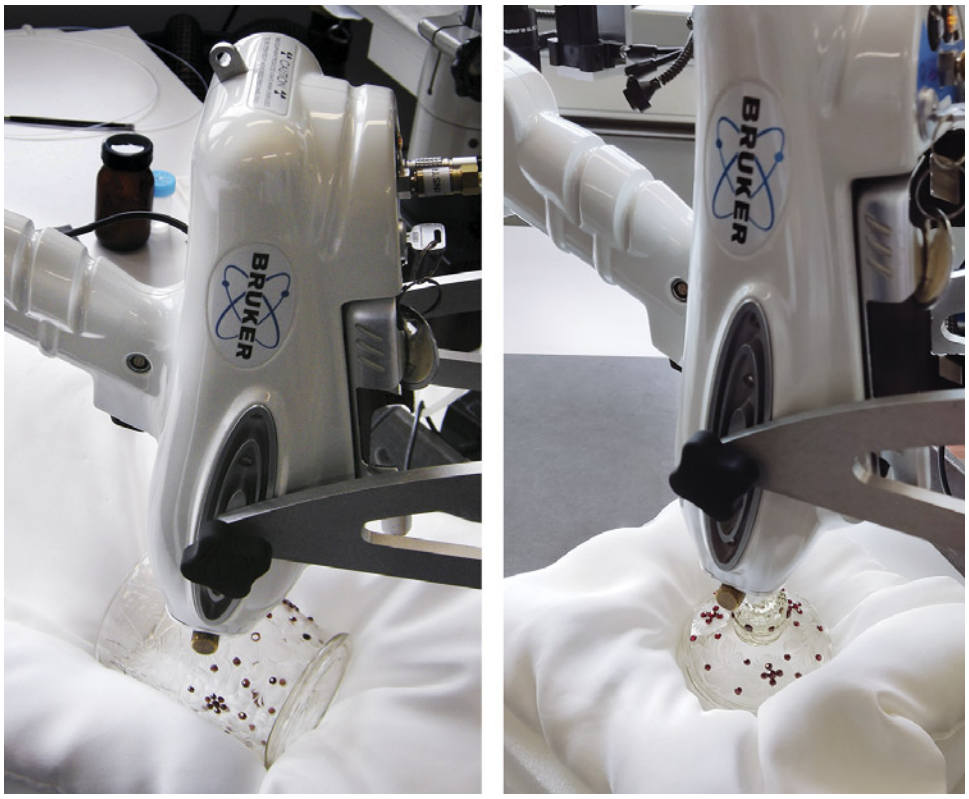

Figure 11. Examination of the lidded goblet in the research and conservation rooms of the Bavarian National Museum using a portable X-ray fluorescence analyzer. Photos by K. Schmetzer.

amination of heavier elements with 40 kV and 30 µA using a yellow filter (thicknesses of 0.001 mil titanium and 0.012 mil aluminum) that eliminated the weak Bragg peaks in the spectra. The acquisition time was 30 seconds for each spectrum. We measured twelve garnets in Munich and eight garnets in Passau, as well as three red glass imitation stones on the goblet from Passau (figure 10).

In some areas of the glass objects, the red decorative materials were lost, but residues of a reddish brown (Munich) or yellow (Passau) fixation layer were left behind. Therefore, we were able to perform a three-part series of examinations, in which the primary X-ray beam was directed at (1) the glass goblets or beaker alone, (2) the glass and residues of the fixation layers, and (3) the glass and the fixation layers

Figure 12. Examination of the beaker (left) and the lidded goblet (right) in the exhibition rooms of the Passau Glass Museum using a portable X-ray fluorescence analyzer. Photos by K. Schmetzer.

together with the red decorative materials. Three to four such rounds of examination were performed for all three engraved glass vessels.

In addition to X-ray fluorescence analysis, we examined the garnets, the fixation layer, and the underlying glass of the Munich goblet using Olympus BX51 and Leica M205 C microscopes and a portable Enwave EZRaman-N-785-B spectrometer. The spectrometer works with a fiber-optic system; the laser wavelength applied was 785 nm at an energy of 300 mW, with a measurement range from 100 to 3300 cm^{-1} and a spectral resolution of 7 cm^{-1}. The acquisition time was 50 seconds for each spectrum, and we always averaged 10 measurements. Again, several series of Raman spectra were obtained for (1) the glass goblet alone, (2) the glass and residues of the fixation layers, and (3) the glass and the fixation layers together with the red decorative materials. We analyzed the same spots that had been measured by EDXRF.

Finally, to test the Munich goblet's reddish brown fixation layers for stability and the presence of organic materials, these layers were brought into contact with a hot needle and examined microscopically. Again we examined the same spots measured by EDXRF.

RESULTS

Examination of the Lidded Goblet in Munich. *Engraved Glass Body*. A microscopic examination of the lidded goblet from the Munich collection showed that the edges of the glass engraving are slightly rounded. This resembles previous observations made on engraved glasses that have been heat treated after engraving, commonly known as fire polishing of glass.

Decoration. The decoration of this goblet consists of transparent rose-cut stones of either groups of 4 mm stones surrounded by 3 mm stones or single 3 mm

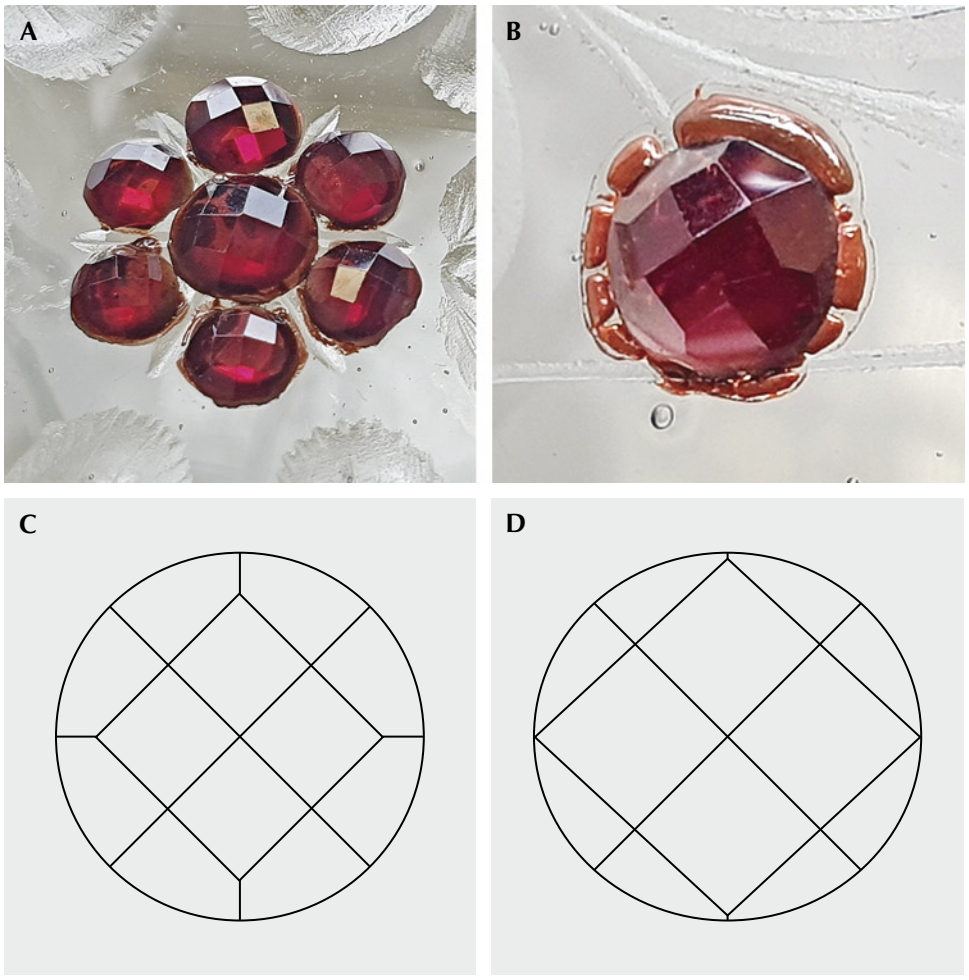

Figure 13. A and B: Rose-cut garnets decorating the lidded goblet from the collection of the Bavarian National Museum. The diameters are 4 mm (center stone) and 3 mm (surrounding stones) in A and 3 mm in B; photos by H.A. Gilg. C: Diagram of the most common cut observed for the garnets in Munich. D: A small proportion of the garnets showed somewhat larger central squares.

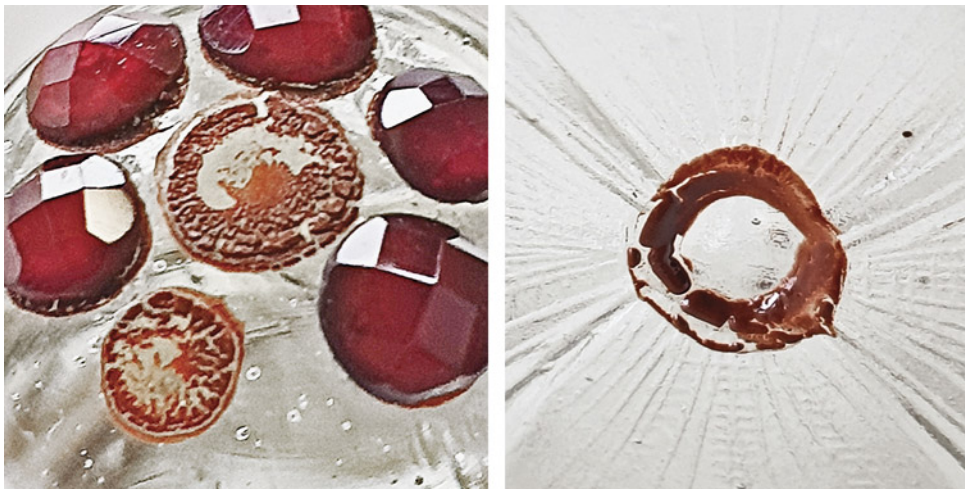

Figure 14. Residues of the reddish brown fixation layer on the glass substrate of the lidded goblet in Munich; the diameters of the reddish brown residual materials measure 4 and 3 mm (left, center and bottom, respectively) and 3 mm (right). Photos by H.A. Gilg.

stones (figure 13, A and B). The cut of all the stones was identical, with four-fold symmetry—i.e., four square facets in the center, each adjacent to four outer quadrilateral facets (figure 13, A–C). In general, the girdles of the rose-cut stones were rounded. Three stones showed an identical cut but different facet proportions, with relatively large central squares and relatively small outer facets (figure 13D). No inclusions or indications of heat treatment were observed in the red decorative materials at the magnification applied (up to 100×).

Fixation Layer. On the surface of this goblet, especially at locations with missing red decorative garnets, we observed residual masses of a reddish brown substance that was partly transparent and partly opaque (figure 14). The residual material showed an uneven distribution on the surface of the underlying glass substrate. The same reddish brown substance was also observed between the rim of the red decorative stones and the underlying glass (figure 13B), especially in views from the interior of the beaker through the vessel's glass wall. It seemed as if this material was ejected from a gap between the glass substrate of the goblet and the red decorative stones.

Microscopic examination showed details of such flow structures (figure 15, A and B). At most locations, the thickness of the reddish brown layer was quite variable, with a somewhat uneven color intensity (figure 15C). This impression was caused not only by the variable thickness of the layer but also by small opaque particles unevenly dispersed within this layer. The same observation was made at locations where red decorative stones remained (figure 16). The reddish brown layers as a whole showed no reaction upon contact with a hot needle, which indicates that no organic volatile matter was part of the residual fixation layers.

Raman Analysis. The Raman spectra of the rose-cut stones showed, especially in comparison with standard spectra of Bohemian chromium pyropes (from

Figure 15. A and B: Microscopic images of the reddish brown fixation layer on the glass substrate of the lidded goblet in Munich showing flow structures. C: Within the groundmass of lead glass, small hematite particles are finely dispersed. Photomicrographs by H.-J. Ranz; fields of view 3.5 mm (A), 0.9 mm (B), and 1.8 mm (C).

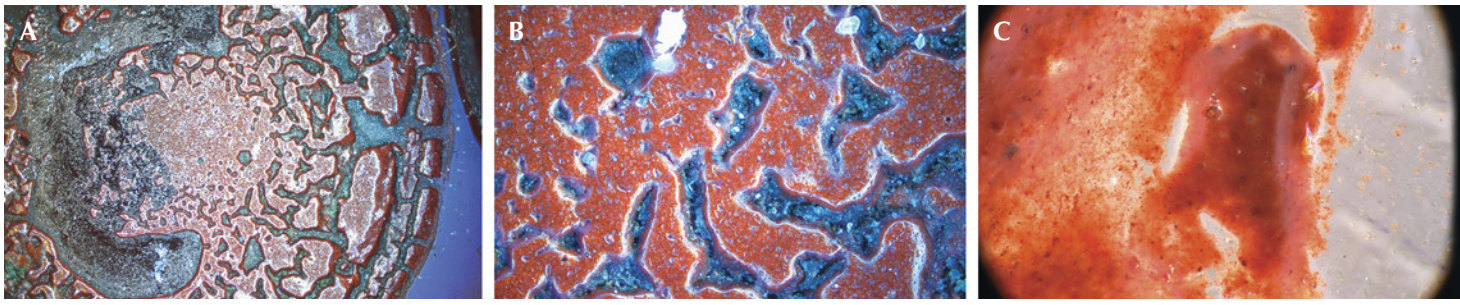

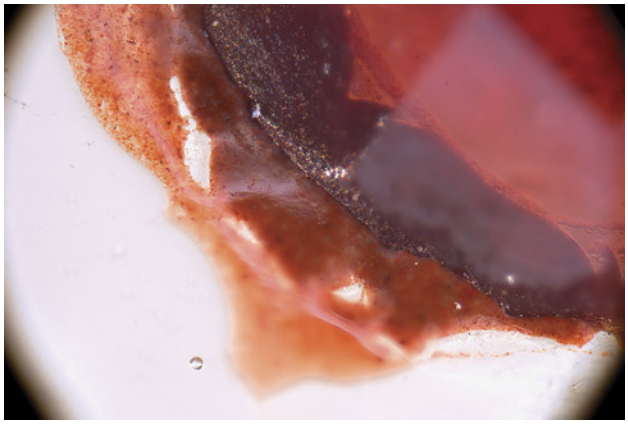

Figure 16. Decorative Bohemian garnet fixed to the colorless glass substrate of the lidded goblet in Munich. The reddish brown fixation layer is found in the gap between the garnet and the glass substrate, but also on the glass substrate outside of the garnet. Photomicrograph by H.-J. Ranz; field of view 4.47 mm.

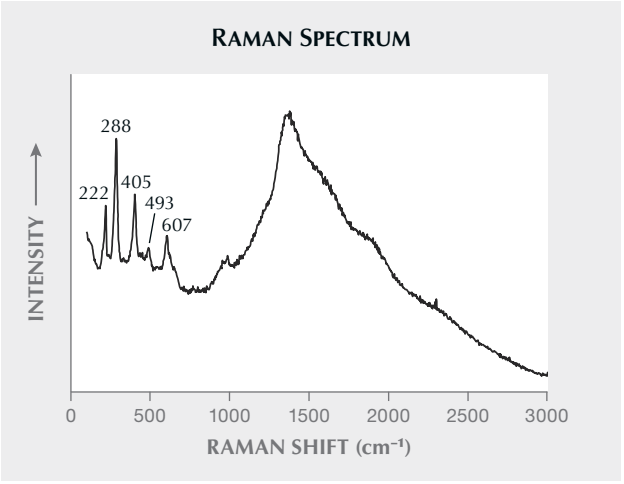

Figure 18. Raman spectrum of the reddish brown fixation layer on the Munich glass substrate. The different maxima (labeled) were assigned to finely dispersed hematite particles; the broad maximum at 1500 cm^{-1} is also observed in the Raman spectrum of the underlying glass substrate without any additional fixation layer or garnet.

the Bohemian Midlands, in the collections of the authors) taken with the same instrument, that all red stones measured were titanium-bearing chromium pyrope (figure 17; see Gilg and Gast, 2016). Furthermore, Raman spectroscopy revealed that the fixation layers contain hematite (figure 18), recognized by the irregularly distributed reddish brown opaque particles seen in the microscope.

Figure 17. Raman spectrum of a Bohemian pyrope on glass and a spectrum of a standard sample of Bohemian garnet. The broad maximum at 1500 cm^{-1} is also observed in the Raman spectrum of the underlying glass substrate without any additional fixation layer or garnet.

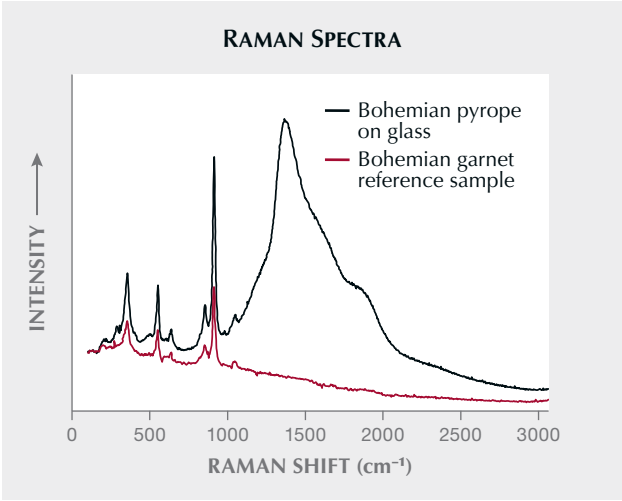

X-Ray Fluorescence Analysis. The X-ray fluorescence spectra recorded from all three vessels showed no significant differences for each vessel between various locations examined on the same decorated glass. This indicates the use of a uniform substance as the fixation layer and a uniform material applied on top of this substance for embellishment.

The spectra of the glass of the engraved goblet from Munich show the signals of silicon, potassium, and calcium as main components and traces of aluminum, phosphorus, titanium, manganese, iron, copper, zinc, strontium, rubidium, and zirconium (figure 19). Compared to this potassium-calcium-glass, the fixation layer was distinguished by additional characteristic lines of lead and iron and weaker lines of tin and copper. In addition, the red decorative material shows an enrichment of magnesium, aluminum, titanium, chromium, and iron.

Examination of the Beaker in Passau. *Decoration*. This beaker shows red rose-cut garnets with a diameter of 3 mm each (figure 20, left). The cutting style is identical to the rose cuts observed in the Munich lidded goblet, with slightly different proportions—i.e., somewhat larger central squares compared to the outer quadrilateral facets (figure 20, right).

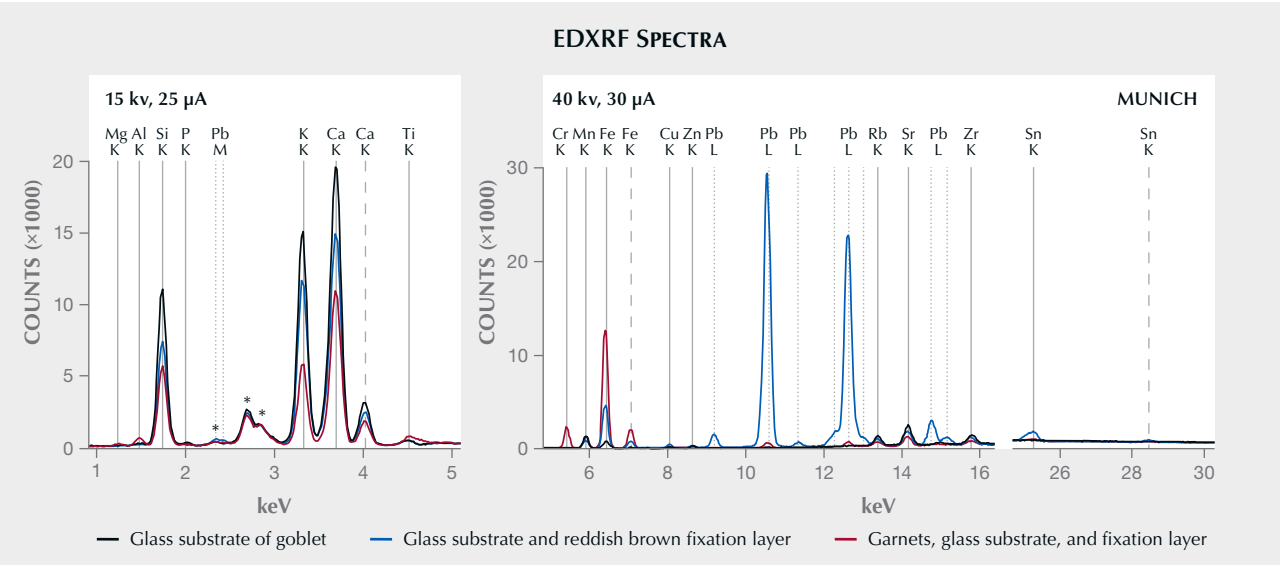

Figure 19. EDXRF spectra of the lidded goblet from the Bavarian National Museum. The spectra were recorded with two different experimental setups: 15 kV and 25 µA (left) and 40 kV and 30 µA (right). Solid gray lines indicate the positions of Kα X-ray lines, dashed gray lines represent the positions of Kβ X-ray lines, and dotted gray lines represent the positions of L and M X-ray lines. The peaks labeled with an asterisk originate from the X-ray tube (Rh) and from the collimator (Pd).

Fixation Layer. The beaker from the Passau glass collection also showed some residual material of a fixation layer. These masses, in contrast to the fixation layer observed on the Munich lidded goblet, were an intense yellow and showed an uneven, roughened undulating surface with a bubble-like texture (figure 21).

X-Ray Fluorescence Analysis. The spectra from the beaker from the Passau Glass Museum again revealed the presence of a potassium-calcium glass. In the yellow fixation layer, the elements lead, tin, copper, and antimony were also present (figure 22). Compared to the spectra of the glass substrate with the fixation layer, the red faceted rose-cut stones indicate an enrichment of magnesium, aluminum, titanium, chromium, and iron.

Examination of the Lidded Goblet in Passau. *Decoration and Fixation Layer*. This goblet, decorated with red and green glass imitation stones, showed no fixation layer between the decoration and the underlying glass substrate.

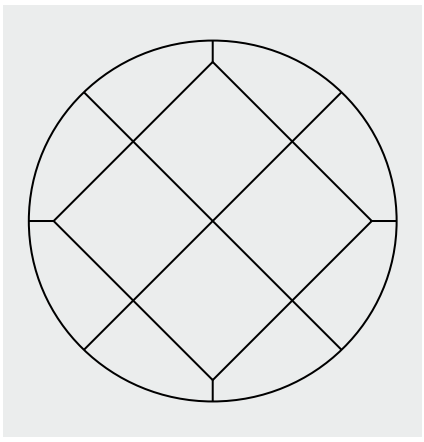

Figure 20. Left: Rose-cut garnets decorating the beaker from the collection of the Passau Glass Museum, 3 mm in diameter. Photo by H.A. Gilg. Right: Diagram of the common cut observed for the garnets in Passau.

Figure 21. Residues of the yellow fixation layer on the glass substrate of the beaker in Passau showing an uneven surface with a bubble-like texture; the yellow residual materials measure about 3 mm in diameter. Photos by H.A. Gilg.

X-Ray Fluorescence Analysis. This vessel was different from the other two samples examined. Again, the spectra (not given here) characterize a potassium-calcium glass, but with an enrichment of arsenic. Compared to the underlying glass, the red decorative glass materials show an enrichment only of lead.

DISCUSSION

Identification of Materials. The examined glass vessels consist of potassium-calcium glasses, which are typical for the seventeenth and eighteenth centuries (see Wedepohl, 2003). The hot needle test applied to the reddish brown fixation layer of the Munich lidded goblet and the absence of characteristic C-H vibration lines in the Raman spectrum indicate that no organic components were present in the residues of the fixation layer. In contrast, the Raman spectrum combined with the microscopic examination shows the presence of small hematite particles, which are responsible for the coloration of this layer that was consequently identified as a hematite-bearing lead glass.

According to their actual weight percentage of lead oxide, lead glasses reveal a melting point in the range of 700°–800°C, compared to a melting point of "ordinary" potassium-calcium glasses at about 1100°C (Wedepohl, 2003; Stern and Gerber, 2004). For the red decorative stones, a fixation layer of lead glass with a lower melting point was obviously applied, which did not affect or damage the underlying

Figure 22. EDXRF spectra of the beaker from the Passau Glass Museum. The spectra were recorded with two different experimental setups: 15 kV and 25 µA (left) and 40 kV and 30 µA (right). Solid gray lines indicate the positions of Kα X-ray lines, dashed gray lines represent the positions of Kβ X-ray lines, and dotted gray lines represent the positions of L and M X-ray lines. The lines labeled with an asterisk originate from the X-ray tube (Rh) and from the collimator (Pd).

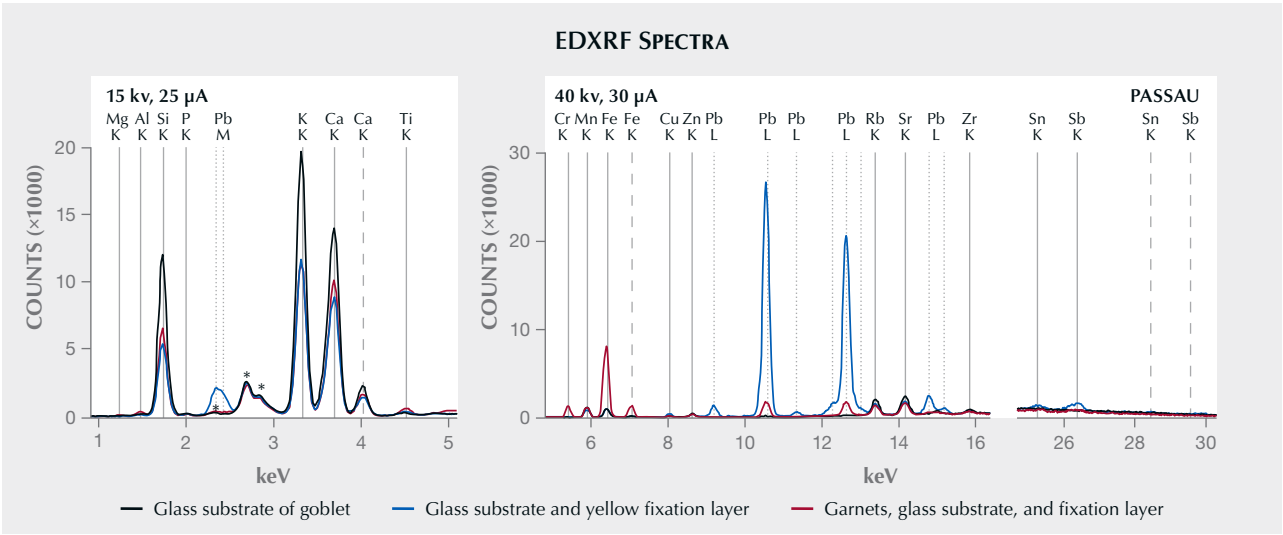

glass substrate or the decorative material. This result also applies to the Passau beaker, which shows the application of a yellow lead glass as the fixation layer. The coloration of the reddish brown lead glass layer in the Munich goblet is due to admixtures of small particles of hematite pigments. The yellow coloration of the lead glass layer in the Passau beaker is assumed to be due to the observed traces of tin- and antimony-bearing pigments. Such pigments, in general, are responsible for a yellow coloration of historical glasses (Wedepohl, 2003). Without hematite, the lead glass in the Munich goblet would most likely also show a yellow coloration, but in that case the presence of hematite is dominant for its reddish brown coloration, and the yellow color component is not visible.

The red decorative stones on the surface of the lidded goblet from Munich and the beaker from Passau were identified as Bohemian pyrope. The X-ray fluorescence spectra show—compared to the spectra of the underlying glass substrate and the lead glass fixation layer—an enrichment of magnesium and aluminum, two of the main components of pyrope (silicon is always present in the glasses and a silicon peak is always seen in the spectra of all materials examined). In addition, the spectra of the red stones show an enrichment of titanium and iron and especially chromium, which is considered the main color-causing trace element of red Bohemian pyrope garnet (Amthauer, 1976; Gilg et al., 2015; for a recent summary of properties of Bohemian garnet, see Hanus et al., 2022).

The red decorative materials applied to the lidded goblet in Passau were identified as lead glass.

Production Techniques. The results described above offer some clues to Creutz's original production technique. Theoretically, there are many possible methods for placing red garnets on glass substrates, but many of these would not produce the properties determined for the glass vessels in Munich and Passau. Consequently, we are only discussing the technique and its variations that are consistent with the results of the visual and chemical examination of the samples.

For the decoration of engraved glass vessels, rosecut Bohemian garnets were attached with a fixation layer to the outer surface of the underlying glass substrates. At the end of the manufacturing process, after cooling of the heated goblet or beaker, the final fixation layer consisted of a lead glass with a lower melting point than that of the main glass body. In order to hide the fixation layer in the Munich example, finely grained hematite particles (or other iron-bearing oxides or hydroxides that turned to hematite after heating) were added to the lead glass, imitating the coloration of Bohemian pyrope.

It has been known for centuries that it is possible to anneal pyrope at an elevated temperature range of about 700°–800°C without decomposition. This knowledge was publicly available since at least the late seventeenth century in the famous book by Kunckel (1689) about glass technology. According to more recent studies, the structure of Bohemian pyrope is stable to at least 1000°C (Zboril et al., 2003).

For the attachment of garnets to the main glass substrate, it can be assumed that finely ground lead glass frit, possibly with an admixture of finely ground hematite, was mixed with water or with an organic binder such as gum arabic or tragacanth, which have been used for pigments since the Middle Ages. After drying of the intermediate fixation layer between the garnets and the glass, the garnets would be placed in the desired positions on the glass body. After heat treatment of the complete glass body and melting of the fixation layer, the organic binder would completely escape by oxidation and vaporization, leaving a lead glass layer with melted or blister structures (for this production step, see Brepohl, 1983).

A variant of this scenario is to add a binder to finely ground lead glass frit and cover the flat base of the garnet roses with that mixture. After the garnets have been prepared with such a layer and that layer has dried, placing them on a heated glass body would cause the dried fixation layer to melt after evaporation of the binder, in that way fixing the garnets upon cooling. Further variants are conceivable, especially if we consider the different textures of the residual fixation layers of the vessels preserved in Munich and Passau.

The steps described for such a production process are consistent with the four steps mentioned in the privileges of Creutz and his successors:

1. Cutting and faceting of the garnets
2. Connecting the garnets with a mixture of lead glass and a binder
3. Setting the garnets on the glass substrate
4. Melting the mixture of lead glass and binder by heat treatment

The difference between the two variants described is based upon the method of melting the fixation layer, a mixture of finely grained lead glass and a binder. The two alternatives are:

- Heating the glass body of the goblet or beaker together with the intermediate fixation layer and the garnets, after the fixation layer had dried between the glass substrate and the garnets
- Heating the glass body of the goblet or beaker to melt the fixation layer already adhered to the rose-cut garnets

Obviously, different artisans applied different recipes for the mixture used as a fixation layer, and these recipes were closely guarded trade secrets. The temperatures applied for the melting processes might have varied according to the artist, and even the same artist could have worked with slightly different temperatures, if we consider the ability to measure and adjust temperatures in the seventeenth century. These slightly different production processes allow us to understand some properties of the final products such as the different coloration of the final fixation layer on the surface of the Munich lidded goblet and the Passau beaker. The glass objects, their engraving, and their subsequent embellishment could have been produced by different craftspersons in Nuremberg or elsewhere.

CONCLUSIONS

The documents available in archives in Vienna and Nuremberg indicate the use of a process to decorate glass substrates with rose-cut Bohemian garnets from the end of the sixteenth century to the first decades of the eighteenth century. This process was invented and developed by Claudius vom Creutz in Nuremberg, who first obtained privileges from the Imperial City of Nuremberg and later from Emperor Rudolf II. Glass objects produced with this technique are extremely rare, but two glass vessels preserved in museums in Munich and Passau were available for examination.

On the lidded goblet from the Munich museum and the beaker in Passau, Bohemian garnets are attached by a fixation layer, consisting of lead glass with admixtures, that was melted by careful heating processes. A third glass vessel examined, a lidded goblet in Passau, proved to have rose-cut glass, not garnets. It is unknown whether glass objects other than goblets and beakers were decorated with Bohemian garnets. Such objects would also fall within the wording used within the imperial privileges to describe the process. The nature of "garnet doublets" mentioned in inventories in the late seventeenth and early eighteenth centuries (Brackenhofer, 1683; *Museum Wolffianum*, 1714) is unclear. In the seventeenth century, "doublets" generally consisted of an upper and lower part of the same stone, with a colored layer in between (*Praktisches Handbuch für Künstler...*, 1793).

These two glass vessels from Munich and Passau were prepared with the same type of production technique, which is clearly revealed by the examination of the samples. The most common feature is the fixation layer of lead glass in between the garnets and the glass substrate of the vessels. The chemical differences between the two layers and the presence of an admixture of hematite in the fixation layer of the lidded goblet in Munich indicate different manufacturers and possibly production in different cities or locations.

Żelasko (2014) mentioned invoices for glasses decorated with garnets, which were produced in Lower Silesia in the seventeenth century. This indicates that the method was also applied in regions or cities beyond Nuremberg. It is documented that infringements of the privileges of Creutz were pursued in Nuremberg, but it is unknown whether the privileges were also effective in distant areas of the Holy Roman Empire with industrial glassworks.

ABOUT THE AUTHORS

Dr. Karl Schmetzer is an independent researcher living in Petershausen, near Munich. Dr. Hans Albert Gilg is a professor at the Chair of Engineering Geology, Technical University of Munich, Germany. Hans-Jörg Ranz is a staff member at the conservation department of the Bavarian National Museum in Munich.

ACKNOWLEDGMENTS

The authors are grateful to Peter Höltl and staff members of the Passau Glass Museum for permission to examine the glass beaker and lidded goblet from the collection and for their assistance during our time at the museum. We are also grateful to Dr. Annette Schommers and Isabel Wagner for their assistance during our work on the premises of the Bavarian National Museum in Munich. Raman spectroscopy in Munich was performed by Dr. Markus Roos of the Bavarian State Office for Monument Protection. Dr. A. Schommers is also thanked for a critical review of the manuscript.

REFERENCES

Amthauer G. (1976) Kristallchemie und Farbe chromhaltiger Granate. *Neues Jahrbuch für Mineralogie Abhandlungen*, Vol. 126, No. 2, pp. 158–186.

Bernt W. (1950) *Altes Glas*. Prestel Verlag, Munich, p. 56.

Brackenhofer E. (1683) *Musaeum Brackenhofferianum: das ist ordentliche Beschreibung aller, so wohl natürlicher als kunstreicher Sachen, welches sich in weyland Hrn. Eliae Brackenhoffers, gewesenen Dreyzehners bey hiesiger Statt Straßburg, hinterlassenen Cabinet befinden*. Johann Wespern, Straßburg, p. 23.

Brepohl E. (1983) *Kunsthandwerkliches Emaillieren*, 3rd ed. VEB Fachbuchverlag, Leipzig, p. 31.

Burdet G. (1925) *Étude historique sur la pénétration et le développement de l'industrie lapidaire sur le plateau de Septmoncel et dans la région de Saint-Claude*. Morez, France, p. 57.

Fuchs L.F. (1959) Zum Tode Dr. Heinrich Brausers. *Weltkunst*, Vol. 29, No. 24, p. 23.

Gareis A. (1884) Die Granatindustrie in Böhmen. *Illustrierte Welt*, Vol. 32, No. 5, pp. 51–52.

Gatterer C.W. (1790) *Technologisches Magazin*, Erster Band, Erstes und Zweytes Stück. Andreas Seyler, Memmingen, p. 185.

Gilg H.A., Gast N. (2016) Determination of titanium content in pyrope by Raman spectroscopy. *Journal of Raman Spectroscopy*, Vol. 47, No. 4, pp. 486–491, http://dx.doi.org/10.1002/jrs.4838

Gilg H.A., Gast N., Hyršl J. (2015) Chromium pyropes from Bohemia: Characterization and identification in archaeological and historical jewellery. In *Mineral Resources in a Sustainable World, Proceedings of the 13th Biennial SGA Meeting, Nancy, France, 24–27 August 2015*, Vol. 4, pp. 1301–1304.

Graf von Abensberg und Traun H., Ed. (1898) *Jahrbuch der Kunsthistorischen Sammlungen des allerhöchsten Kaiserhauses*, Vol. 19, Part II, F. Tempsky, Prague; F. Tempsky, Vienna; G. Freytag, Leipzig, 198 pp.

Graf zu Trauttmansdorff-Weinsberg F., Ed. (1889) *Jahrbuch der Kunsthistorischen Sammlungen des allerhöchsten Kaiserhauses*, Vol. 10, Verlag von Adolf Holzhausen, Vienna, 429 pp.

——— (1894) *Jahrbuch der Kunsthistorischen Sammlungen des allerhöchsten Kaiserhauses*, Vol. 15, Part II, F. Tempsky, Prague; F. Tempsky, Vienna; G. Freytag, Leipzig, 215 pp.

Grieb M.H., Ed. (2007a) *Nürnberger Künstlerlexikon*, Vol. 1. K.G. Saur Verlag, Munich, p. 234.

——— (2007b) *Nürnberger Künstlerlexikon*, Vol. 4. K.G. Saur Verlag, Munich, pp. 1806–1807.

Hampe T. (1904) *Nürnberger Ratsverlässe über Kunst und Künstler im Zeitalter der Spätgotik und Renaissance [Decisions of the Council of the Imperial City of Nuremberg]. II. Band 1571-1618*. Karl Graeser & Kie., Vienna; B.G. Teubner, Leipzig, 541 pp.

——— (1919) *Das Altnürnberger Kunstglas und seine Meister*. Verlag von Duncker & Humblot, Munich and Leipzig, pp. 36–41.

Hanus R., Hladký P., Vyskočilová G. (2022) Ulrike Sophie von Levetzow's jewels collection: Identification and restoration. *International Journal of Conservation Science*, Vol. 13, No. 2, pp. 367–380.

Kunckel J. (1689) *Ars vitraria experimentalis: Oder vollkommene Glasmacher-Kunst*. Verlegung Christoph Riegels, Frankfurt and Leipzig, pp. 275, 440.

Meyer-Heisig E. (1963) Caspar Lehmann. Ein Beitrag zur Frühgeschichte des deutschen Glasschnittes. *Anzeiger des Germanischen Nationalmuseums*, Vol. 1963, pp. 116–131.

Michel H. (1926) *Nachahmungen und Verfälschungen der Edelsteine und Perlen und ihre Erkennung*. Verlag von Ulr. Mosers Buchhandlung, Graz, pp. 18–19.

Museum Wolffianum (1714) Gottfried Rothen, Leipzig, p. 61.

Pfeiffer W. (1977) Vorwort. In S. Baumgärtner, *Gläser: Antike, Mittelalter, Neuere Zeit: Museum der Stadt Regensburg, Katalog der Glassammlung Sammlung Brauser*. Corona-Verlag, Karlsruhe, p. 5.

Pohlmann H. (1961) The inventor's right in early German law. *Journal of the Patent Office Society*, Vol. 43, No. 2, pp. 121–139.

Praktisches Handbuch für Künstler, aus dem Englischen nach der zwoten verbesserten und vermehrten Ausgabe übersetzt und mit Anmerkungen versehen [Practical Manual for Artists, Translated from English, Expanded and Revised] (1793) Zweyter Teil. Waltherische Hofbuchhandlung, Dresden, pp. 428–433.

Quast D., Schüssler U. (2000) Mineralogische Untersuchungen zur Herkunft der Granate merowingerzeitlicher Cloisonnéarbeiten. *Germania*, Vol. 78, pp. 75–96.

Rückert R. (1962) Gläser aus der Sammlung Dr. Brauser im Bayerischen Nationalmuseum. *Münchner Jahrbuch der bildenden Kunst*, Vol. 13, pp. 238–248.

——— (1982) *Die Glassammlung des Bayerischen Nationalmuseums München*. Vol. II. Hirmer Verlag, Munich, pp. 180–181.

Schmetzer K., Gilg H.A., Ranz H.-J. (2024) Das Granatrosensetzen - ein fast vergessenes Nürnberger Kunsthandwerk. *Gemmologie: Zeitschrift der Deutschen Gemmologischen Gesellschaft* (in print).

Stehlíková D. (2004) *The Bohemian Garnet*. Mucha Museum Ltd. in collaboration with the National Museum in Prague, p. 13.

Stern W.B., Gerber Y. (2004) Potassium-calcium glass: New data and experiments. *Archaeometry*, Vol. 46, No. 1, pp. 137–156, http://dx.doi.org/10.1111/j.1475-4754.2004.00149.x

Thieme U., Ed. (1913) *Allgemeines Lexikon der bildenden Künstler von der Antike bis zur Gegenwart*. Vol. 8. E.A. Seemann Verlag, Leipzig, p. 104.

Von Ursprung und Herkom[m]en samt Beschreibung aller Hand Wercker in der Stadt Nürnberg [Origin and Description of All Crafts in the City of Nuremberg] (ca. 1700) Germanic National Museum in Nuremberg collection. Signature: Merkel Hs 2° 981.

Von Ankunft und Herkommen aller Handwerker, so in der Stadt und Landwehr Nürnberg wohnhaft [Origin and Description of All Crafts in the City of Nuremberg] (1719) Historical Archive of the City of Nuremberg. Signature: B 12 Nr. 62.

Webster R. (1964) Composite stones. *Journal of Gemmology*, Vol. 9, No. 5, pp. 160–176.

Webster R., Anderson B.W. (1983) *Gems: Their Sources, Descriptions, and Identification*, 4th ed. Butterworths, London, pp. 460–462.

Wedepohl K.H. (2003) *Glas in Antike und Mittelalter: Geschichte eines Werkstoffs*. E. Schweizerbart'sche Verlagsbuchhandlung, Stuttgart, pp. 5–30.

Zboril R., Mashlan M., Barcova K., Walla J., Ferrow E., Martinec P. (2003) Thermal behaviour of pyrope at 1000 and 1100°C: mechanism of Fe^{2+} oxidation and decomposition model. *Physics and Chemistry of Minerals*, Vol. 30, No. 10, pp. 620–627, http://dx.doi.org/10.1007/s00269-003-0355-x

Żelasko S. (2014) *Barock und Rokoko im Hirschberger Tal: Stein- und Glasschnitt 1650-1780*. Glasmuseum Passau, pp. 11–12, 23, 112–113.

A Unique Petrified Tree Fern from Northeast China

Ying Yan, Xiao-Yan Yu, Han-Yue Xu, and Zhi-Rong Xie

A unique petrified tree fern displaying distinct patterns was recently discovered in northeast China, attracting considerable interest. This study provides a comprehensive set of data for this material obtained through standard gemological testing, petrographic observation, scanning electron microscopy, energy-dispersive spectroscopy, electron probe microanalysis, and Raman spectroscopy. The petrified tree fern exhibits colors ranging from golden yellow to brown, with additional variations caused by iron oxides. Chalcedony is the primary mineral component, while the presence of metastable moganite gives chalcedony its fibrous nature, contributing to the delicate structure of the samples. The surface pattern originates from plant structures preserved during silicification, further confirming the samples belong to the extinct Cretaceous period tree fern *Tempskya* sp.

Petrified wood is the fossilized remains of ancient trees that have undergone a process occurring over millions of years (Nowak et al., 2005; Yoon and Kim, 2008; Kim et al., 2010). During this process, dissolved SiO_2 infiltrates the organic matter of buried trees, causing the precipitation of various crystalline siliceous minerals along the wood fiber cells. As a consequence, silicified fossils with preserved woody structures are formed (Murata, 1940; Rößler, 2000; Mustoe, 2008; Yu, 2016). However, most petrified wood is not of gem quality, lacking the necessary beauty and luster (Saminpanya, 2015).

Since 2010, a unique tree fern fossil recovered from riverbeds and secondary placers in northeast China has captured the attention of botanists (Cheng and Liu, 2017; Yang et al., 2018). This unusual tree fern, *Tempskya*, is the only genus in the family Tempskyaceae and occurred only in the Cretaceous (box A). These petrified tree fern fossils are composed of polycrystalline quartz. With its distinct patterns, this material has drawn the interest of gem collectors in the area (Xu, 2021). Lapidary artists value specimens for their use in cabochons, beads, and carvings (figure 1). As local jewelers recognized the worth of this material, they began to incorporate it into souvenirs and polished collectible items, adding to the appreciation of petrified tree fern (Pakhomova et al., 2020).

Figure 1. Chalcedony petrified tree fern is carved as an ornamental gem material. This 60 × 40 mm dragon carving has a uniform texture and bright color. Photo by Hai-Long Wang.

See end of article for About the Authors and Acknowledgments.
Gems & Gemology, Vol. 59, No. 4, pp. 450–465,
http://dx.doi.org/10.5741/GEMS.59.4.450

Box A: Botany of Petrified Tree Fern

Tree ferns, members of the Cyatheales order, constitute a captivating and ancient group of ferns distinguished by their unique and primitive traits. These remarkable ferns stand apart from their botanical counterparts in several ways (Large and Braggins, 2004):

1. *Trunk-like stems:* Living tree ferns are primarily recognized for their upright, trunk-like stems, which resemble the trunks of trees. These stems can grow to considerable heights, and they are a defining feature of these ferns.
2. *Large compound leaves:* At the top of their tall stems, tree ferns display large and elaborate compound leaves. These leaves consist of numerous leaflets arranged in a feather-like or palmate fashion, giving them a distinctive and attractive appearance.
3. *Primitive nature:* Tree ferns are considered relatively primitive in the plant kingdom. Their status as "living fossils" and the distinctive features of their stems and growth habits make tree ferns a captivating subject of study in the field of botany.

Tempskya, an extinct genus of tree ferns, thrived during the Cretaceous period and has left fossils in both the Northern and Southern hemispheres (Tidwell et al., 2010). Unlike living tree ferns, *Tempskya* was characterized by short, slender underground stems or rhizomes with diminutive leaves (figure A-1). Its growth habit, distinct from any contemporary fern or living plant, consisted of multiple conjoined dichotomous branching stems enmeshed within roots to form a "false trunk" (Martínez and Olivo, 2015). The "false trunk" was composed of rhizomes modified to grow vertically and embedded in a dense mantle of adventitious roots. The trunk cross sections produced an attractive pattern of light and dark tissues originating from the vascular system of stem and leaf traces (figure A-2). During the process of silicification, the tree fern underwent a transformation that left the stone with a beautiful pattern of color and texture.

Figure A-1. Tempskya *sp. reconstruction. Illustration by Matteo De Stefano/MUSE; courtesy of MUSE - Science Museum of Trent in cooperation with Wikimedia Italia.*

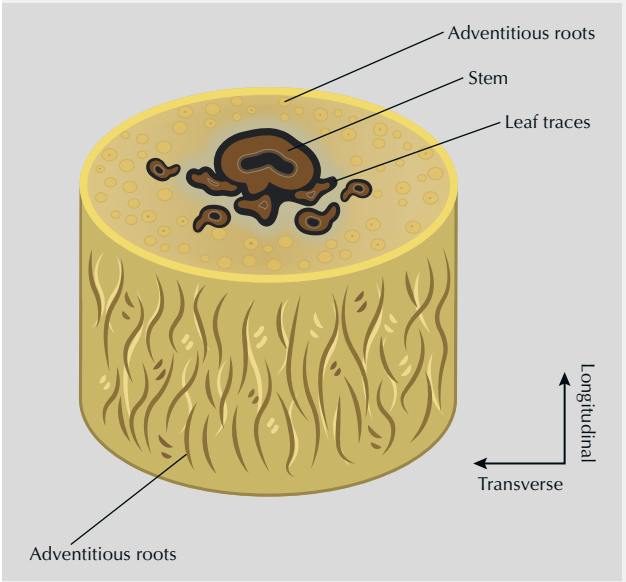

Figure A-2. Anatomy of petrified tree fern Tempskya *sp. The longitudinal and transverse sections of the trunk produce unique patterns of light and dark tissues originating from the vascular system of the stem, adventitious roots, and leaf traces. Within the realm of botany, a plant's vascular system is the assemblage of conducting tissues and associated supportive fibers that transport nutrients and fluids throughout the plant body. Illustration by Ying Yan.*

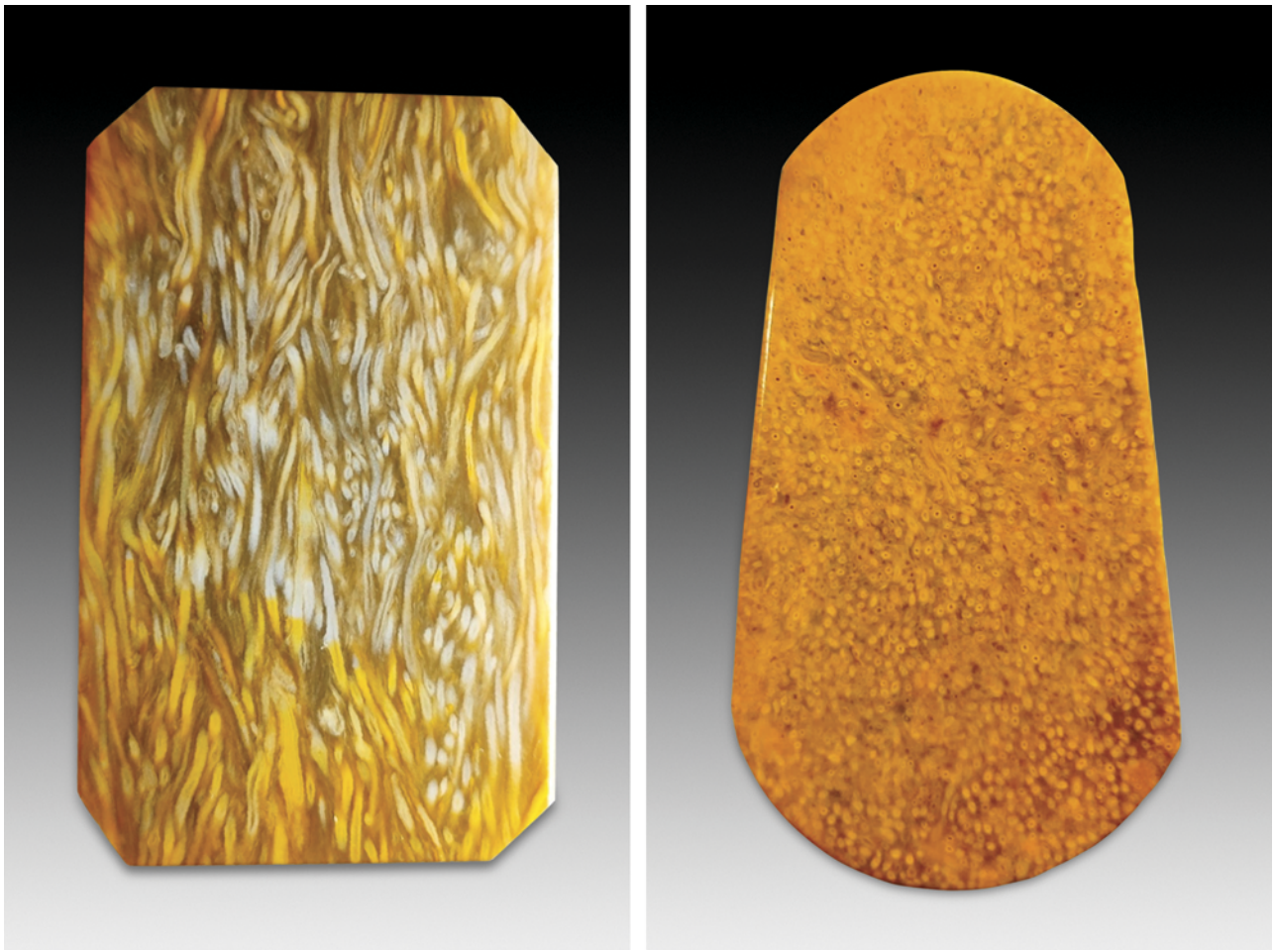

Figure 2. These polished slabs of petrified tree fern with an attractive golden yellow color show two different unusual plant textures that are typical of fine Chinese material. The entangled adventitious roots form a vivid pattern in a longitudinal section (left, 55 × 35 mm). Many adventitious roots have a circular shape in cross section (right, 40 × 25 mm). Photos by Hai-Long Wang.

Petrified tree fern possesses desirable qualities as a gem material, characterized by its refined texture and preserved plant patterns (figure 2). Previous studies have focused primarily on paleogeography, paleoclimatology, and mineralogical aspects of petrified tree fern (Rößler, 2000; Witke et al., 2004), leaving its gemological significance largely unexplored, particularly with regard to microstructural analysis. The resemblance between petrified tree fern and tiger's-eye (Holden, 2003) raises the need for accurate separation (figure 3). In view of these considerations, this study provides a comprehensive analysis of the microstructure and mineral composition of petrified tree fern.

MATERIALS AND METHODS

Six studied petrified tree fern samples (S1–S6) were procured from the gem market in Qiqihar, Heilongjiang Province, China. These specimens were originally collected by local villagers from fluvial deposits near the village of Henan, Keshan County, in Heilongjiang Province in the northern Songliao Basin (figure 4). The Songliao Basin is a Mesozoic-Cenozoic

In Brief

- Petrified tree fern displays a typical golden yellow to brown color and distinct plant structures such as stems, adventitious roots, and leaf traces.
- The plant patterns preserved during silicification indicate the specimens in this study belonged to the extinct Cretaceous tree fern *Tempskya* sp.
- Fibrous chalcedony is the primary mineral contributing to the delicate structure of petrified tree fern.

Figure 3. Brownish yellow tiger's-eye sold in the jewelry market in Wuhan, China, is identified incorrectly as petrified tree fern. The tiger's-eye is in the cross pattern and in the upper right, alongside various other products sold at the market. Photo by Ying Yan.

intracratonic basin across the Heilongjiang, Jilin, and Liaoning provinces of northeast China. One of the most prolific oil sedimentary basins in China, it is considered a long-lived terrestrial basin preserving a nearly complete Cretaceous sedimentary record (Yang et al., 2018). The Cretaceous strata in the basin are rich in biological fossils (Gao and Song, 1994; Kong et al., 2006). A discovery there in 2017 of a new species of tree fern fossil, *Tempskya zhangii*, has shed light on the paleogeographic environment of the Songliao Basin during the Cretaceous period (Yang et al., 2018).

The rough samples were rounded chunks covered with gray-white and brownish yellow weathering crust, indicating that the fossils had been transported by water over a long distance to their current sites (figure 5). The six samples were ground into polished slabs in the transverse direction (figure 6). Additionally, a sample of tiger's-eye with an appearance similar to that of petrified tree fern was procured from

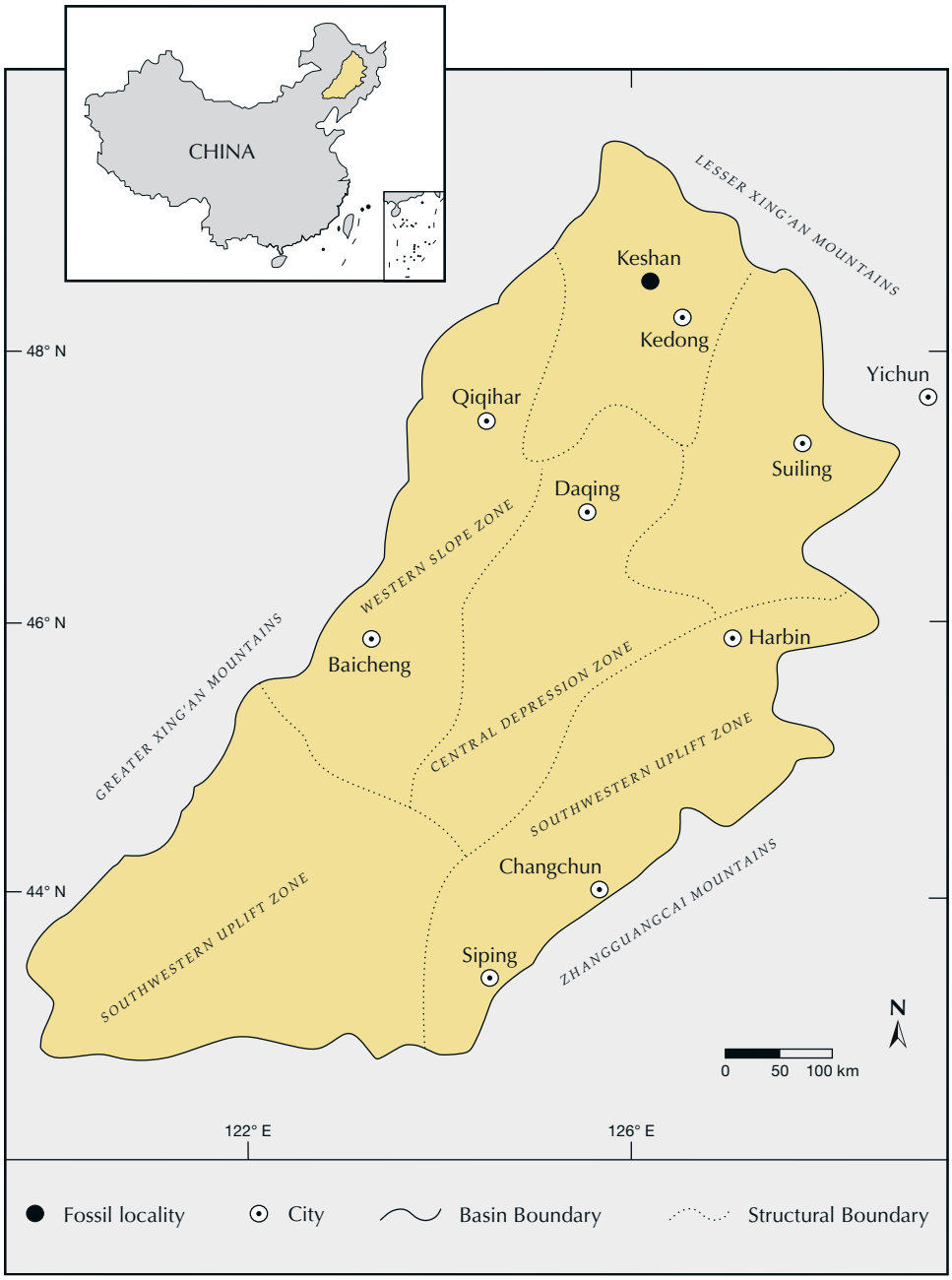

Figure 4. This map of Songliao Basin of northeast China shows fossil localities and major structure zones. Modified from Cheng and Liu (2017).

the jewelry market in Wuhan for gemological and visual comparisons (figure 7).

The six petrified tree fern samples and the one tiger's-eye sample were examined using standard gemological methods including visual observation, refractive index measurement, fluorescence reaction observation under long-wave (365 nm) and short-wave (254 nm) UV, and hydrostatic specific gravity testing.

The samples were prepared as thin sections both perpendicular and parallel to the plant texture direction, labeled as transverse and longitudinal, respectively. These sections were examined using an Olympus BX51 petrographic microscope. Scanning electron microscopy (SEM) was used to observe fractures in randomized directions of the petrified tree fern samples, performed by JEOL JSM-7800F. Working voltage and working distance were 15 kV and 10 mm, respectively. Energy-dispersive spectrometry (EDS) (Oxford X-Max 50) element mapping allowed the observation of chemical variation within the same regions.

Figure 5. The six rough samples of petrified tree fern from northeast China investigated in this work, ranging from 135.50 to 332.13 g. Photos by Han-Yue Xu.

Chemical composition was determined at the MNR Key Laboratory of Metallogeny and Mineral Assessment, Institute of Mineral Resources, Chinese Academy of Geological Science in Beijing. The analy-

Figure 6. The six petrified tree fern samples cut in the transverse direction and analyzed for this study (3.2–4.1 cm in length and 1.6–2.5 cm in width). Photos by Han-Yue Xu.

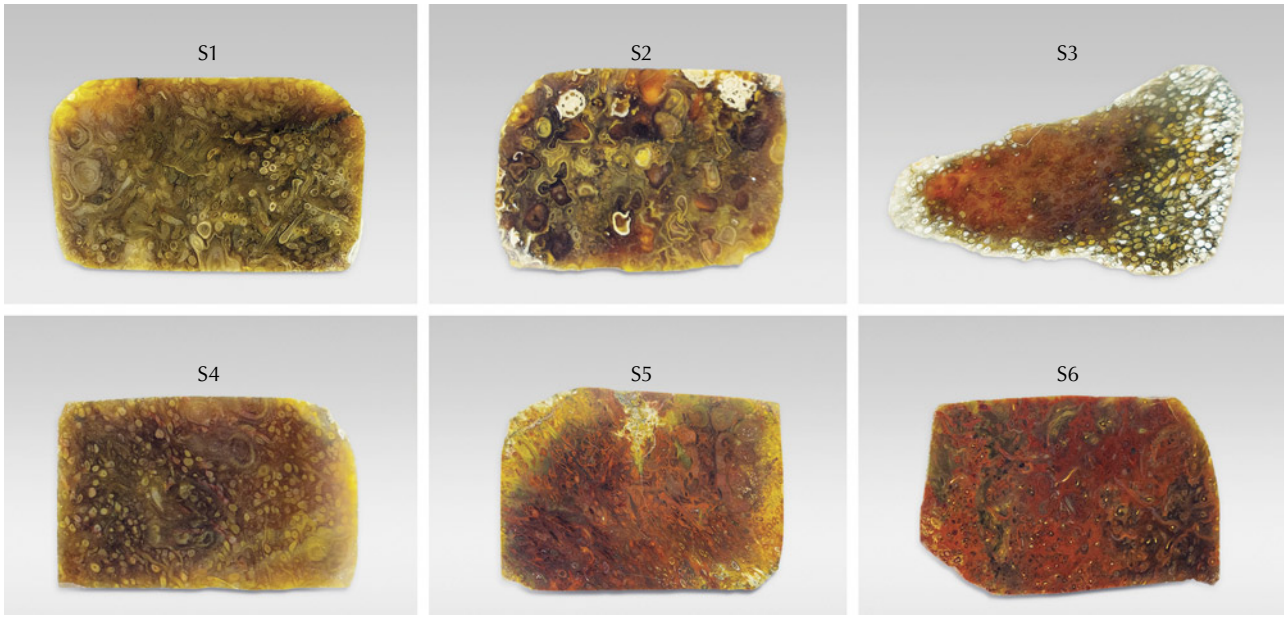

Figure 7. This polished specimen of tiger's-eye (3.5 × 1.6 mm, 14.57 g) exhibits a golden yellow coloration similar to that of petrified tree fern. Photo by Ying Yan.

sis was performed with a JEOL JXA-8230 electron probe microanalyzer (EPMA) equipped with four wavelength-dispersive spectrometers. The sections were coated with an approximately 20 nm thin conductive carbon film prior to analysis. Accelerating voltage, beam current, and spot size were 15 kV, 20 nA, and 5 µm, respectively. Jadeite (silicon, aluminum), hematite (iron), rutile (titanium), potassium feldspar (potassium), and wollastonite (calcium) were used as standards. Data were corrected online using a modified ZAF correction procedure.

Raman spectra were recorded using a Horiba HR-Evolution Raman micro spectrometer with an argon-ion laser operating at 532 nm excitation between 1800 and 100 cm^{-1} and accumulating up to three scans.

RESULTS

Gemological Properties and Visual Appearance. The gemological properties of the six petrified tree fern samples are compared to the single tiger's-eye sample in table 1. All of the samples displayed golden yellow to brown colors, but red impurities were observed in regions of samples S5 and S6. All petrified tree fern samples had a refractive index of 1.53–1.54 with specific gravity varying from 2.60 to 2.63. Their luminescence was inert under long-wave and short-wave UV radiation.

The polished surface of the petrified tree fern highlighted the internal structure of the plant, which differed from the parallel fiber structure found in tiger's-eye. Three representative samples with distinctive internal textures of tree fern were selected for visual examination (figure 8). The unique surface patterns consisted of plant stems, adventitious roots, and leaf traces, appearing striped in a longitudinal section or irregularly rounded in a transverse section. The plant texture of sample S5 was entirely red, with tubular stems, dense adventitious roots, leaf bases,

Figure 8. The structures of samples S1 (A), S2 (B), and S5 (C) observed under visible light. A is a longitudinal cross section view; B and C are transverse cross section views. Photomicrographs by Han-Yue Xu; field of view 2.0 mm.

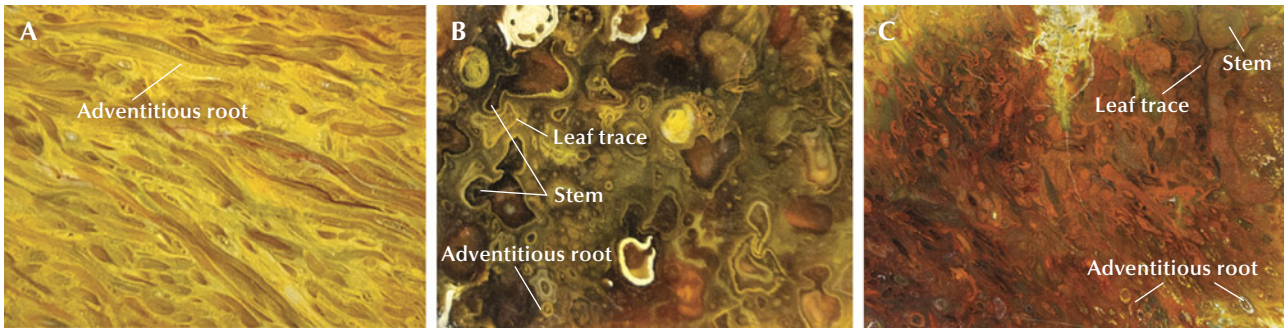

TABLE 1. Gemological properties of petrified tree fern and tiger's-eye from China.

Property	Petrified tree fern	Tiger's-eye
Color	Golden yellow, brown, and red band; gray-white regolith on the surface	Golden yellow to brown
Diaphaneity	Translucent to opaque	Opaque
Refractive index[a]	1.53–1.54	1.54
Specific gravity	2.60–2.63	2.60
Long-wave UV	Inert	Inert
Short-wave UV	Inert	Inert
Textural features observed in visible light	Individual stems, adventitious roots, and leaf traces give the petrified specimens a unique appearance	The lustrous golden brown band exhibits radiant chatoyancy in polished sections

[a]*Determined using the spot method.*

and a clear entanglement. Conversely, tiger's-eye is characterized by lustrous golden brown bands that display banded chatoyancy (figure 9).

Figure 9. Chatoyancy in a polished section of tiger's-eye. A characteristic of this gem is the local variability in the orientation of the cat's-eye, causing different bands of reflected light when rotated relative to a point light source. Photomicrograph by Ying Yan; field of view 1.3 mm.

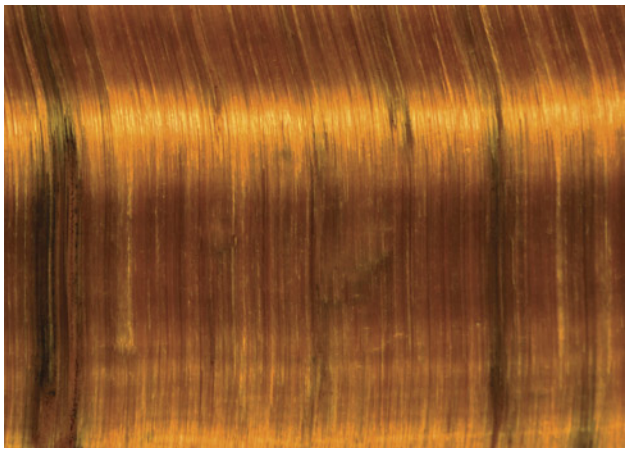

Microstructure. A polarizing microscope further revealed a well-preserved wood grain structure in the petrified tree fern samples. Individual stems were tubular and contained pith, vascular strands, xylem (the primary vascular tissue, which transports water and dissolved minerals from the roots to the leaves), and a cortex (figure 10A). The cortex was three-layered (figure 10B); the middle cortex had thick wall cells, while the outer and inner cortex were relatively thin. The pith was composed of thin wall cells that were elliptical in cross section. Each leaf trace had a single spindle-shaped vascular bundle (specialized tissues that run through and carry water and nutrition to different parts of the plant). The adventitious root was small in diameter, and the xylem was differentiated into two zones. The outer cortex consisted of large parenchyma cells. In contrast, the inner cortex was composed of thin wall cells (figure 10C). The solid, compact trunk was composed of stems embedded in a matrix of adventitious roots that were independent and intertwined with other roots (figure 10D).

Mineralogically, the microcrystalline structure of petrified tree fern is diverse. Thin sections showed that samples were silicified by replacement, and

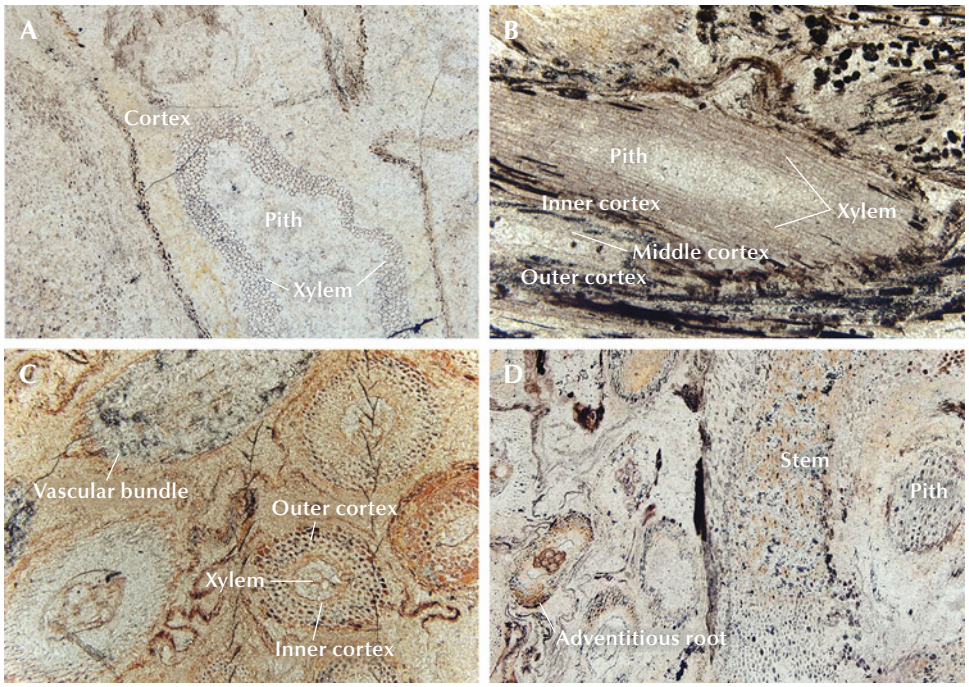

Figure 10. Typical plant structure characteristics of petrified tree fern under plane-polarized light. A: In a cross section of S2, a stem segment shows cortex, xylem, and pitch. B: In a longitudinal section of S3, the stem, a visible three-layered cortex, and pith are surrounded by xylem. C: Details of the diarchal xylem and the outer and inner cortex of an adventitious root in S4. D: A cross section of S5 shows a comparison of stem and adventitious root structure. Adventitious roots are small in diameter and appear curved, round, or oval. Photomicrographs by Han-Yue Xu; fields of view 0.48 mm (A, B, and D) and 0.36 mm (C).

chalcedony ± microcrystalline quartz made up more than 95% of their content. The quartz particles were rarely euhedral, mainly presenting as irregular microcrystals (less than 10 μm in diameter) and fibrous chalcedony spherulites (100–200 μm in diameter). The quartz particles were grayish white under plane-polarized light. According to Li (2016), wood fiber is the plant tissue component that is most resistant to decomposition and recrystallization, making it hard to mineralize. We therefore conclude that brownish yellow wood fiber structures are partly preserved in the petrified tree fern (figure 11A), but the decom-

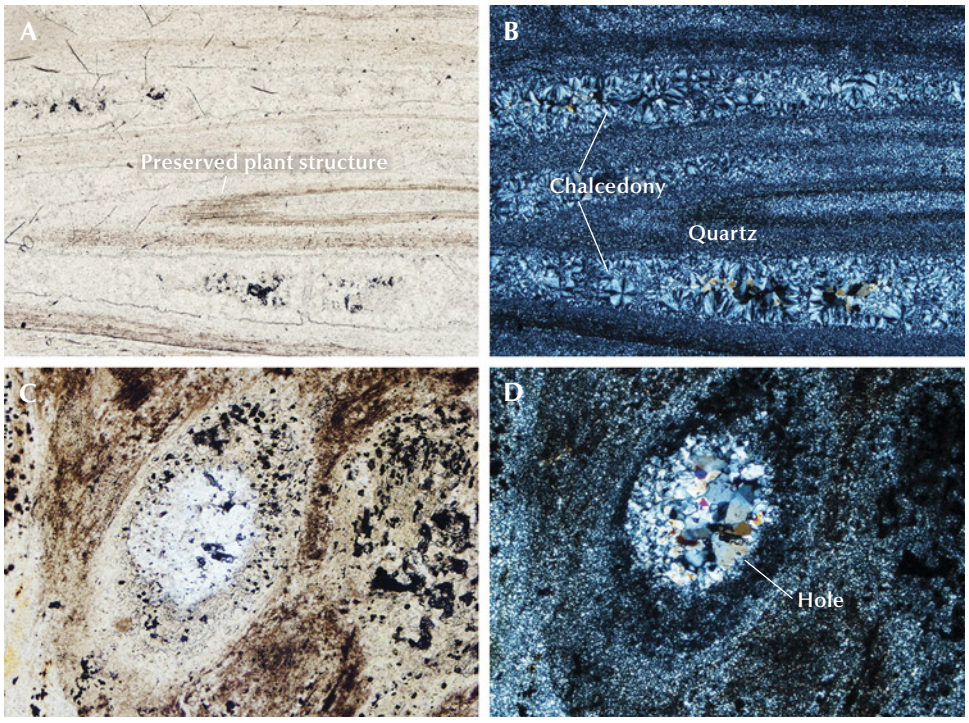

Figure 11. Photomicrographs of petrified tree fern taken with a polarizing microscope. A: Plane-polarized light reveals the preserved yellow-brown plant structure in S2. B: Cross-polarized light shows that the vein is filled with a mixture of chalcedony and microcrystalline quartz. C: A hollow structure image of sample S4 under plane-polarized light. D: Cross-polarized light reveals that subhedral quartz crystals precipitated in the hole, while fine-grained quartz surrounded the hole. Photomicrographs by Han-Yue Xu; fields of view 0.55 mm (A and B) and 0.43 mm (C and D).

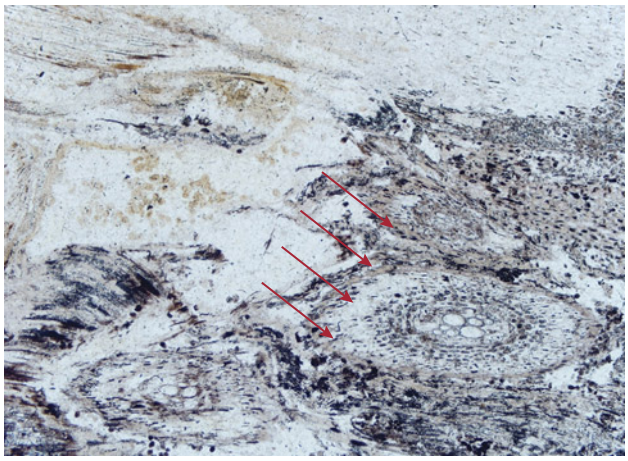

Figure 12. In sample S5, the plant structure features become more evident closer to the regolith, following the direction of the arrows. Photomicrograph by Han-Yue Xu; field of view 0.8 mm.

posed part of the plant structure filled with chalcedony (figure 11B). In general, fossilization occurs when quartz has precipitated on the wall cells of samples, while chalcedony forms in open spaces such as vessels and veins (Hassan, 2017). As shown in figure 10B, fine-grained quartz filled in areas where woody structures were retained in the plant stems and roots. Conversely, radiating fibrous chalcedony crystallized in veins. Moreover, the subhedral quartz crystals were present in hollow structures such as vessels, veins, and holes (figure 11, C and D), while fine-grained quartz surrounded the hole.

In addition, the plant structure was more evident near the shell of the petrified tree fern (figure 12) due to surface weathering. This weathering leads to fine crystalline decomposition and recrystallization of silica along the woody texture, reducing transparency and enhancing the distinct wood structure. The secondary regolith of the samples exhibited a wide distribution of yellow and red minerals that are associated with the woody structure (figure 13). However, the coloration is mainly affected by various minerals present during the weathering process.

SEM imaging revealed three distinct quartz textures in sample S4. The first texture consisted of cryptocrystalline quartz particles of 1 μm in diameter, grown in layers. The second was characterized by euhedral equant quartz crystals with particle diameters ranging from 1 to 5 μm (figure 14A), filling voids and partially visible due to a rhombohedral fracture surface. The first and second textures were both granular structures with low transparency. Conversely, the third texture contained semitranslucent regions composed of chalcedony fibers measuring approximately 5–10 μm in length. Figure 14B illustrates the structural characteristics of fibrous chalcedony. Most of the silica particles in the samples consisted of fine-grained quartz and chalcedony, with euhedral particles being less common.

The occurrence of vascular bundle structures on certain fracture surfaces mainly indicated atypical growth textures. Dense, oriented fibrous chalcedony formed around the pore wall. In the cross section of

Figure 13. Impurity minerals surrounded by the weathered shell of S5 and S6, respectively. Left: These yellow color iron compounds were not positively identified by Raman spectroscopy. Right: Hematite was identified using Raman analysis. Photomicrographs by Han-Yue Xu; fields of view 0.10 mm (left) and 0.48 mm (right).

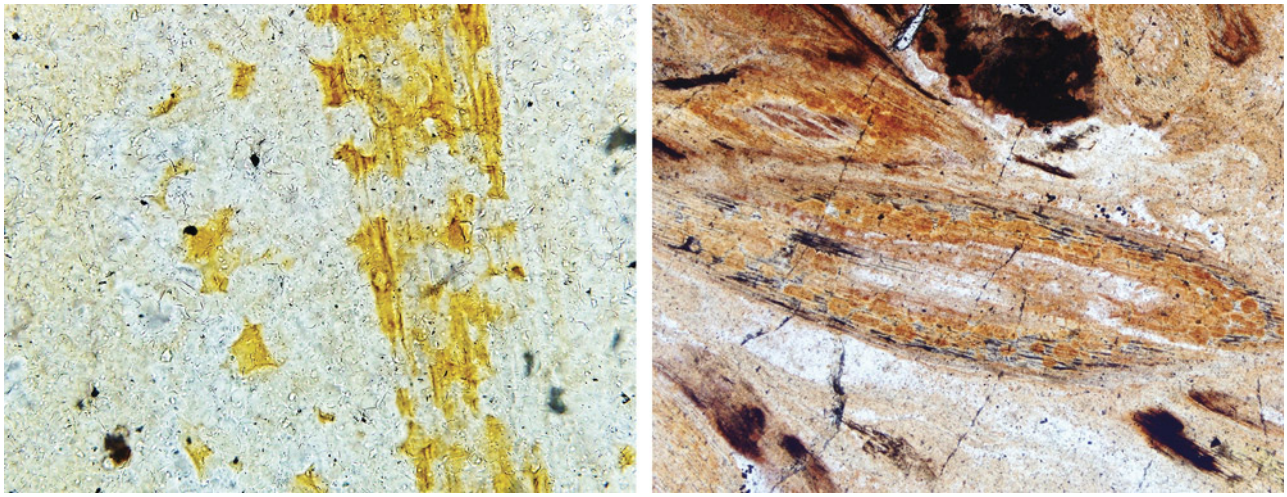

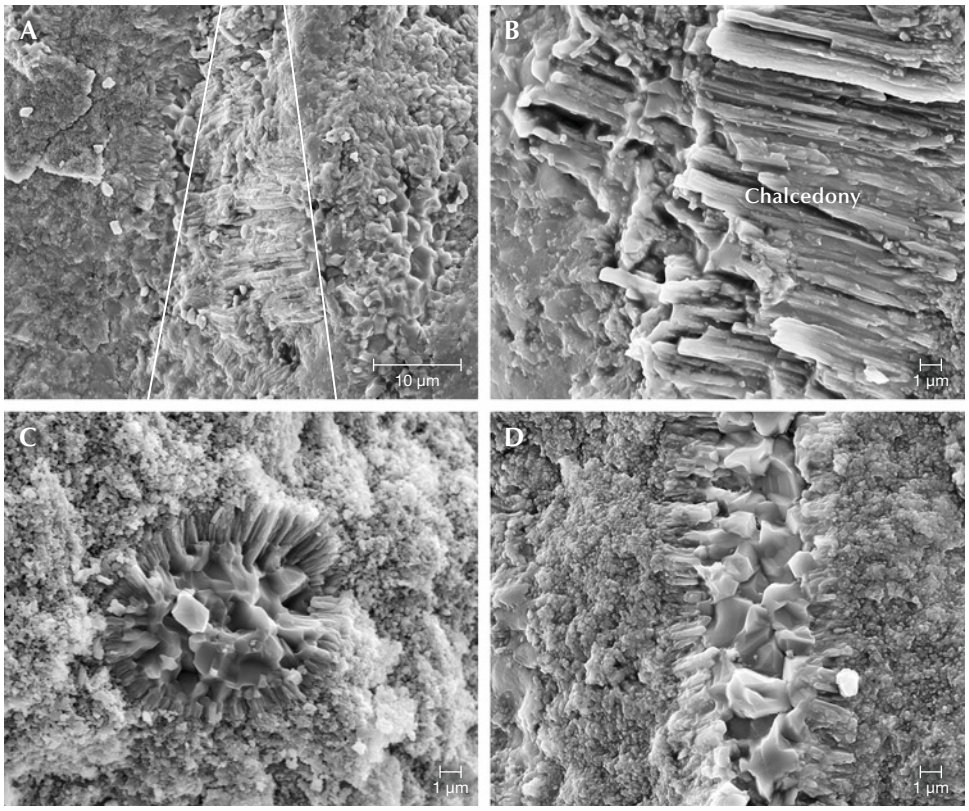

Figure 14. SEM images of petrified tree fern sample S4. A: From left to right, the contrast of mineral particle morphology between fine-grained quartz and fibrous quartz is indicated by the white lines. B: Details of the fibrous chalcedony in image A. C: The silica occurs as radial arms, as shown in cross section. D: In a longitudinal section, the minerals show a parallel arrangement, with the crystals appearing to develop from the outside to the inside.

sample S4, a radial arrangement of fibers was evident (figure 14C). The vascular bundle structure showed a parallel arrangement in a longitudinal section (figure 14D). The agate-like geode growth structure suggests a silicification sequence from the outside (Scurfield and Segnit, 1984). After the SiO_2 solution or colloid enters the vascular bundle cell or duct, quartz crystals grow in an oriented pattern around the cell wall. Crystal particles become progressively larger toward the center, displaying well-defined faces, which suggests that quartz had space for growth during formation, and crystals appeared to develop inward from the exterior.

Element Mapping and Chemical Composition. In a backscattered electron image, a long columnar-shaped impurity in sample S6 can be seen in stark contrast to the host material (figure 15A). Element

Figure 15. Element mapping of sample S6 using SEM-EDS. A: A long square columnar disseminated mineral showing high contrast. B: Element mapping of the sample for silicon, iron, oxygen, calcium, and carbon.

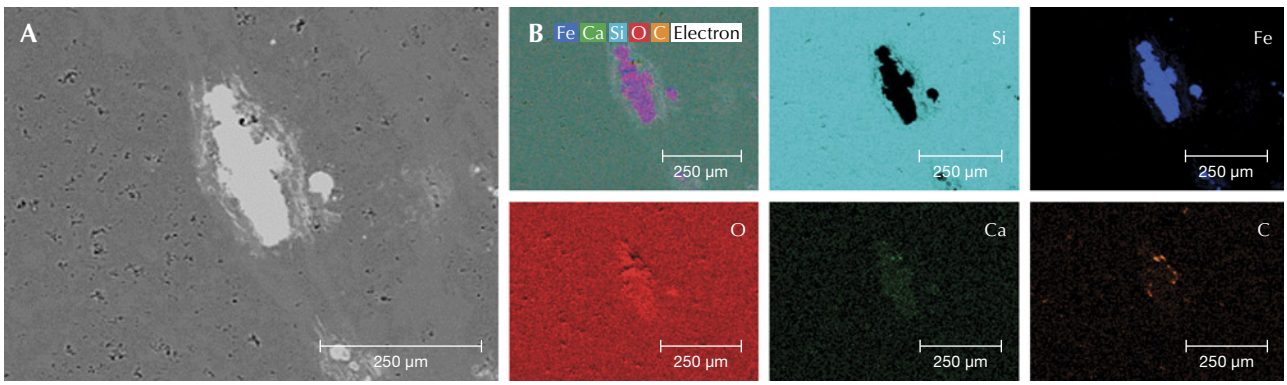

TABLE 2. Chemical composition (in wt.%) of petrified tree fern, obtained by EPMA.

Spot no.	SiO_2	Al_2O_3	FeO	TiO_2	K_2O	CaO	Total
1	99.43	0.16	0.30	0.05	0.02	0.02	99.98
2	97.94	0.10	0.01	0.02	0.02	0.01	98.10
3	98.82	0.02	0.05	0.02	0.02	0.03	98.96
4	98.68	0.16	0.14	0.13	0.01	0.02	99.14
5	99.31	0.18	0.05	0.05	0.03	0.03	99.65
Detection limit (wt.%)	0.008	0.008	0.009	0.024	0.005	0.006	

mapping revealed that the petrified tree fern matrix mainly contained silicon and oxygen, while the impurity minerals primarily consisted of iron and oxygen (figure 15B). Iron in the form of hematite is most likely the cause of color. At the same time, the boundary between the impurity minerals and the matrix contained a small amount of carbon corresponding to the residual carbonaceous matter in petrified wood (Li, 2016).

The backscattered electron image of the petrified tree fern shows a smooth surface. Five random spots on representative sample S1 were analyzed by EPMA. The results in table 2 agree well with the element mapping data, mainly containing SiO_2 (97.94–99.43 wt.%) and a few impurity elements. This confirms that there is no clear difference in the position and composition of distinct plant textures in petrified tree fern.

Raman Spectroscopy. Raman spectroscopy was used to detect other phases that might be present in the samples (Kingma and Hemley, 1994). Figure 16 reveals that the Raman spectrum of petrified tree fern sample S2 is characterized by quartz mixed with moganite, indicated by the peak at 503 cm^{-1} (Heaney and Post, 1992; Hardgrove and Rogers, 2013). The Raman shifts present in petrified tree fern and tiger's-eye occur predominantly at 127, 209, 262, 357, 402, and 465 cm^{-1}, corresponding to quartz. Specifically, the scattering peak at 465 cm^{-1} is sharp and strong, related to the typical Si–O bending vibration of quartzite. Two peaks near 127 and 209 cm^{-1} correspond to the rotational or translational vibration of SiO_4. Absorptions with very weak intensity at 262, 357, and 402 cm^{-1} are characteristic Raman scattering peaks for quartz.

DISCUSSION

The petrified tree fern examined in this study displayed golden yellow to brown colors, with color variations attributed to the presence of iron oxides,

Figure 16. The Raman spectrum of petrified tree fern sample S2 shows dominantly quartz (Q) peaks with a moganite (M) peak at 503 cm^{-1}. Tiger's-eye shows the same quartz peaks but lacks the moganite peak. Spectra are offset vertically for clarity.

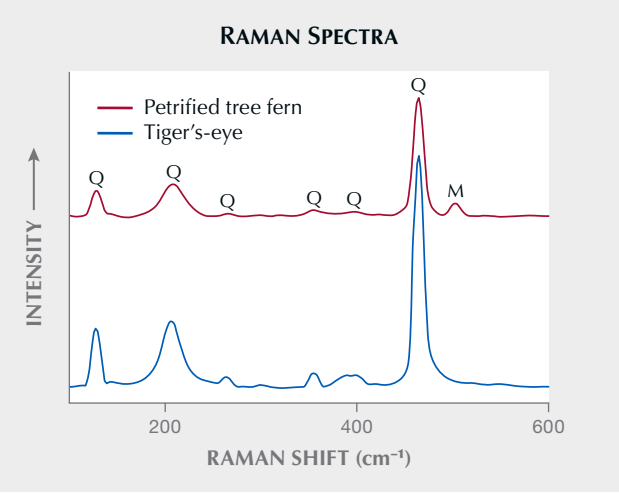

particularly hematite. Most samples were translucent to opaque, with deeper tones. Figure 12 shows the color-banded specimens resulting from the absorption of iron-bearing solutions along the wood grain. This observation suggests that the wood retains a degree of permeability (Mustoe and Acosta, 2016). Furthermore, the red and yellow exterior zones in the samples and the element mapping of iron oxide impurity minerals provide evidence that ferric oxide infiltrated the wood during the later stages of diagenesis (Saminpanya, 2016). Weathering during this process caused decomposition and subsequent recrystallization of cryptocrystalline quartz along the wood grain, reducing transparency and making the woody structure more visible (Stein, 1982; Li, 2016).

The unique characteristics of the six samples analyzed in this study, including the three-layered cortex, distinctive pith composition, the single fusiform vascular bundle, and the presence of stems embedded within an adventitious root matrix, indicated a connection to the Cretaceous tree fern *Tempskya* sp. (Clifford and Dettmann, 2005). Tree ferns are large, woody ferns that resemble trees and have trunk-like structures with fronds. The starting material of a tree fern, rather than a true tree, represents a notable variation within ordinary petrified wood.

Petrified tree fern and tiger's-eye, both being forms of quartz, bear notable similarities in appearance and physical properties. Standard gemological properties are insufficient to distinguish between them, which has led to some confusion within the jewelry market. When examined in cross section, the adventitious roots of petrified tree fern exhibited a distinct oval pattern (figure 17A), while tiger's-eye displayed a mosaic of fibrous bundles on end (figure 17B). These two patterns are very similar when viewed with the unaided eye.

In tiger's-eye, crocidolite and columnar quartz grow simultaneously from opposing crack walls toward the center of the vein during a crack-seal process. The metasomatism only occurs when oxidizing fluids break down the crocidolite to hematite and goethite (Heaney and Fisher, 2003). Fibers of crocidolite are encased within columnar quartz and when grown parallel to each other (figure 17D) (Hu and Heaney, 2010). The formation of petrified wood, on the other hand, occurs under highly specific conditions (Pakhomova et al., 2020). Early research suggested that the petrification process is often associated with volcanic activity (Murata, 1940). Fallen or still upright trees become buried by volcaniclastics due to intense geological activity (Flörke et al., 1982). Ballhaus et al. (2012) observed that trees

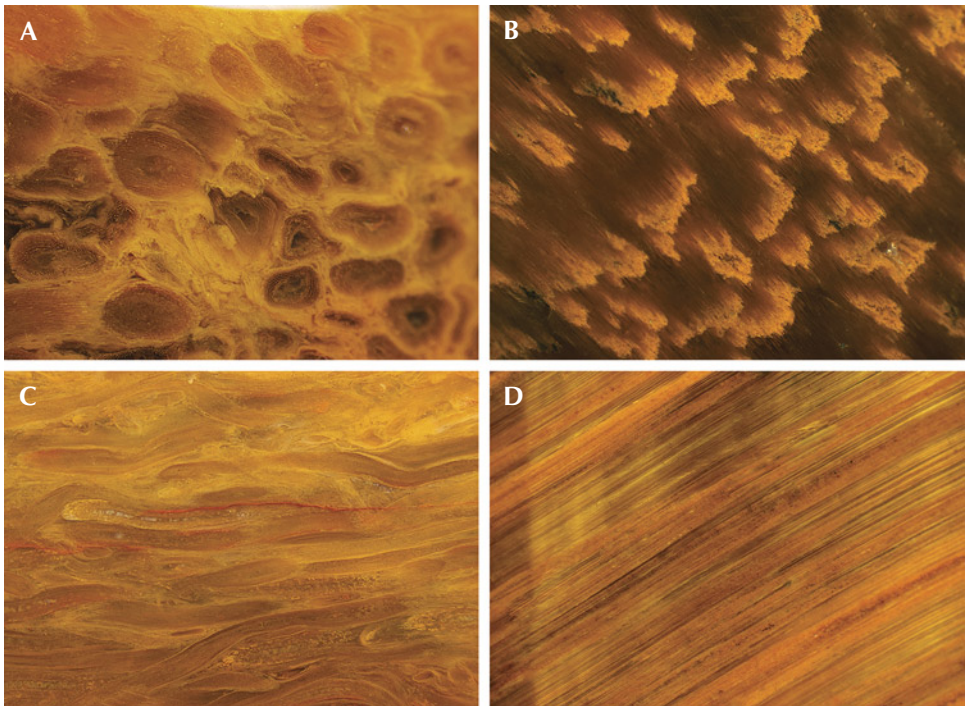

Figure 17. Comparison of surface pattern similarities between petrified tree fern and tiger's-eye. A: Adventitious roots were confined to a shallow surface layer in the cross section of sample S1. B: Under reflected light, a cross section of tiger's-eye shows tufted ends of crocidolite bundles encased within quartz. C: Adventitious roots show a relatively well-preserved circular texture in a longitudinal section. D: Tiger's-eye is characterized by a parallel fiber structure in a longitudinal section, and a silky luster is seen in polished sections. Photomicrographs by Ying Yan; fields of view 0.5 mm (A), 0.7 mm (B), 1.0 mm (C), and 1.2 mm (D).

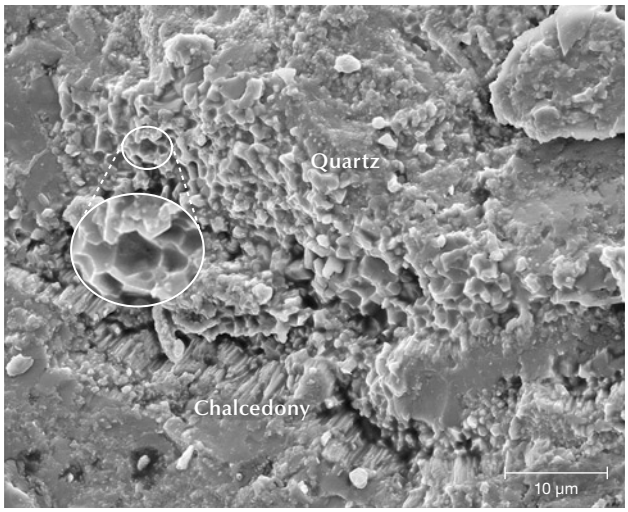

Figure 18. An SEM image of sample S3 reveals well-formed quartz particles approximately 5 µm in diameter, with a hexagonal cross section left by a fracture. Fibrous chalcedony is observed at the border transition.

exhibit a clear propensity to absorb silica from hydrothermal fluids. Over time, the minerals crystallize, preserving the original structure and morphology of the organism in a fossilized form. The primary source of silica in this process is derived from ash silts (Saminpanya, 2015). Silica is considered the most active material for petrifying wood (Scurfield and Segnit, 1984). Through this process, petrified tree fern can preserve intricate patterns of fern fronds and the overall structure of the tree fern with remarkable detail (figure 17C). Therefore, the distinct silicification processes of petrified tree fern and tiger's-eye result in unique structures and surface patterns, enabling their differentiation through careful macroscopic observation.

Buurman (1972) categorized the mineralization of wood into four processes: silicification, carbonation, phosphate accumulation, and sulfide accumulation. Among these, silicification involving quartz minerals is the most prevalent. Petrified tree fern has a chemical composition of SiO_2, and there was no significant difference in chemical composition observed among the six different samples from this study, indicating that the specimens were thoroughly silicified. Quartz plays a crucial role in preserving the cell walls, resulting in the predominantly microcrystalline quartz composition of the preserved plant structures (Dietrich et al., 2013). Cell lumina, on the other hand, are filled with cryptocrystalline silica, specifically fibrous chalcedony, occupying the areas where plant structures have disappeared. Previous studies have confirmed that the fibrous character of chalcedony may arise from various forms of silica, including moganite as a metastable phase often found in fibrous chalcedony (Hassan, 2017; Mustoe, 2023). Raman spectroscopy was used to provide further evidence of constituent phases, enabling clearer identification of moganite in petrified tree fern (Heaney and Post, 1992; Götze et al., 1998). Furthermore, the Raman spectrum of tiger's-eye lacks the signal of moganite, which might be a way to distinguish petrified tree fern from tiger's-eye.

Additionally, highly crystalline quartz exhibits a hexagonal columnar growth (figure 18). An essential preservation characteristic is the presence of open vessels that provide space for the formation of well-developed quartz after the surrounding tissue has been silicified. The quartz filling this open space results from a separate mineralization event that occurred after dissolved silica levels dropped (Mustoe, 2023). However, the large particle size and rough edges of crystalline quartz in petrified wood cause light to be reflected and refracted internally, resulting in limited transparency (Lei, 2010). Conversely, fibrous chalcedony, the primary mineral commonly found in petrified tree fern, contributes to a delicate structure and enhances transparency (Miladinović et al., 2016; Lei, 2022). Therefore, the plant pattern filled with crystalline quartz can be more clearly distinguished from the surrounding chalcedony portions. In China, chalcedony petrified tree fern is highly valued as a lapidary material and ornamental stone, with high-quality specimens sought for the creation of carvings (figure 19).

CONCLUSIONS

Petrified tree fern from northeast China exhibited colors ranging from golden yellow to brown, with additional variations attributed to the presence of iron oxides. These specimens possessed distinct plant structures such as stems, adventitious roots, and leaf traces, resulting in a unique appearance. Although standard gemological testing proved insufficient in distinguishing petrified tree fern from tiger's-eye, differences could be observed in their surface patterns, chatoyancy, and Raman spectra.

SEM-EDS and EPMA analyses confirmed the thorough silicification of the petrified tree fern samples, revealing a predominant SiO_2 composition

Figure 19. Pixiu dragon carvings are sought after in China and elsewhere; this piece carved in petrified tree fern measures approximately 35 × 20 mm. Photo by Hai-Long Wang.

across various plant structures. Additionally, SEM and Raman spectroscopy identified chalcedony as the primary mineral component in petrified tree fern. The fibrous texture of chalcedony is induced by the presence of metastable moganite, contributing to the delicate structure observed. This material is remarkable for its beautiful pattern, representing an intriguing fusion of botany and gemology.

ABOUT THE AUTHORS

Ying Yan (2009210031@email.cugb.edu.cn) is a PhD candidate, and Dr. Xiao-Yan Yu (yuxy@cugb.edu.cn, corresponding author) is a professor of gemology and mineralogy, at the School of Gemmology, China University of Geosciences in Beijing. Han-Yue Xu and Zhi-Rong Xie are postgraduate students at the School of Gemmology, China University of Geosciences in Beijing.

ACKNOWLEDGMENTS

The authors gratefully acknowledge support from China Geological Survey grant DD20190379-88 and would like to thank Dr. Ye-Ming Cheng for the meaningful discussion on botany. The authors are grateful for the insightful peer reviews of Dr. George Mustoe and Dr. Peter Heaney.

REFERENCES

Ballhaus C., Gee C.T., Bockrath C., Greef K., Mansfeldt T., Rhede D. (2012) The silicification of trees in volcanic ash - An experimental study. *Geochimica et Cosmochimica Acta*, Vol. 84, No. 1, pp. 62–74, http://dx.doi.org/10.1016/j.gca.2012.01.018

Buurman P. (1972) *Mineralization of Fossil Wood*. Rijksmuseum van Geologie en Mineralogie, Leiden.

Cheng Y.M., Liu F.X. (2017) The first discovery of Cretaceous cyatheaceae stem fossils in China. *Acta Geoscientica Sinica*, Vol. 38, No. 2, pp. 135–143.
Clifford H.T., Dettmann M.E. (2005) First record from Australia of the Cretaceous fern genus *Tempskya* and the description of a new species, *T. judithae*. *Review of Palaeobotany and Palynology*, Vol. 134, No. 1-2, pp. 71–84, http://dx.doi.org/10.1016/j.revpalbo.2004.12.001
Dietrich D., Lampke T., Rößler R. (2013) A microstructure study on silicified wood from the Permian Petrified Forest of Chemnitz. *Paläontologische Zeitschrift*, Vol. 87, No. 3, pp. 397–407, http://dx.doi.org/10.1007/s12542-012-0162-0
Flörke O.W., Köhler H.B., Langer K., Tönges I. (1982) Water in microcrystalline quartz of volcanic origin: Agates. *Contributions to Mineralogy and Petrology*, Vol. 80, No. 4, pp. 324–333.
Gao R.Q., Song Z.C. (1994) Study on Early Cretaceous palynological assemblage in deep Songliao Basin. *Acta Palaeontologica Sinica*, Vol. 33, No. 6, pp. 659–675 [in Chinese].
Götze J., Nasdala L., Kleeberg R., Wenzel M. (1998) Occurrence and distribution of "moganite" in agate/chalcedony: A combined micro-Raman, Rietveld, and cathodoluminescence study. *Contributions to Mineralogy and Petrology*, Vol. 133, No. 1, pp. 96–105, http://dx.doi.org/10.1007/s004100050440
Hardgrove C., Rogers A.D. (2013) Thermal infrared and Raman microspectroscopy of moganite-bearing rocks. *American Mineralogist*, Vol. 98, No. 1, pp. 78–84, http://dx.doi.org/10.2138/am.2013.4152
Hassan K.M. (2017) Mineralogical and geochemical signatures of silicified wood from the petrified forest, New Cairo, Egypt. *Canadian Mineralogist*, Vol. 55, No. 2, pp. 317–332, http://dx.doi.org/10.3749/canmin.1600089
Heaney P.J., Fisher D.M. (2003) New interpretation of the origin of tiger's-eye. *Geology*, Vol. 31, No. 4. pp. 323, http://dx.doi.org/10.1130/0091-7613(2003)031%3C0323:NIOTOO%3E2.0.CO;2
Heaney P.J., Post J.E. (1992) The widespread distribution of a novel silica polymorph in microcrystalline quartz varieties. *Science*, Vol. 255, No. 5043, pp. 441–443, http://dx.doi.org/10.1126/science.255.5043.441
Holden C. (2003) Tiger's eye: Looks are deceiving. *Science*, Vol. 300, No. 5617, p. 245.
Hu K.F., Heaney P.J. (2010) A microstructural study of pietersite from Namibia and China. *G&G*, Vol. 46, No. 4, pp. 280–286, http://dx.doi.org/10.5741/GEMS.46.4.280
Kim K.W., Yoon C.J., Kim P.G., Lee M.B., Lim J.H. (2010) Fine structure and X-ray microanalysis of silicified woods from a Tertiary basin Pohang, Korea by scanning electron microscopy. *Micron*, Vol. 40, pp. 519–525, http://dx.doi.org/10.1016/j.micron.2009.04.006
Kingma K.J., Hemley R.J. (1994) Raman spectroscopic study of microcrystalline silica. *American Mineralogist*, Vol. 79, pp. 269–273.
Kong H., Chen C.R., Dang Y.M., Yang J.G., Huang Q.H., Zhao C.B. (2006) Review of three Cretaceous biota in Songliao Basin. *Acta Palaeontologica Sinica*, No. 3, pp. 416–424.
Large M.F., Braggins J.E. (2004) *Tree Ferns*. Timber Press, Portland, Oregon.
Lei F.F. (2010) Mineral characteristics and gemological economic evaluation of petrified wood from Burma. Master's thesis, Guilin University of Technology [in Chinese].
——— (2022) Analysis of the influence of mineralogical characteristics of silicified wood on transparency. *Journal of Suihua University*, Vol. 42, No. 5, pp. 156–160 [in Chinese].
Li Y.T. (2016) Study on microstructure and mineralogy characteristics of petrified wood from Qitai, Xinjiang and Pagan, Myanmar. Master's thesis, China University of Geosciences, Beijing [in Chinese].
Martínez L.C.A., Olivo M.S. (2015) *Tempskya* in the Valanginian of South America (Mulichinco Formation, Neuquén Basin, Argentina)—Systematics, palaeoclimatology and palaeoecology. *Review of Palaeobotany and Palynology*. Vol. 219, pp. 116–131, http://dx.doi.org/10.1016/j.revpalbo.2015.04.002
Miladinović Z., Simić V., Jelenković R., Ilić M. (2016) Gemstone deposits of Serbia. *Geologica Carpathica*, Vol. 67, No. 3, pp. 211–222, http://dx.doi.org/10.1515/geoca-2016-0014
Murata K.J. (1940) Volcanic ash as a source of silica for the silicification of wood. *American Journal of Science*, Vol. 238, No. 8, pp. 586–596.
Mustoe G.E. (2008) Mineralogy and geochemistry of late Eocene silicified wood from Florissant Fossil Beds National Monument, Colorado. In H.W. Meyer and D.M. Smith, Eds., *Special Papers of the Geological Society of America*, Vol. 435, pp. 127–140, http://dx.doi.org/10.1130/2008.2435(09)
——— (2023) Silicification of wood: An overview. *Minerals*, Vol. 13, No. 2, article no. 206, http://dx.doi.org/10.3390/min13020206
Mustoe G.E., Acosta M. (2016) Origin of petrified wood color. *Geoscience*, Vol. 6, No. 2, article no. 25, http://dx.doi.org/10.3390/geosciences6020025
Nowak J., Florek M., Kwiatek W., Lekki J., Chevallier P., Zieba E., Mestres N., Dutkiewicz E.M., Kuczumow A. (2005) Composite structure of wood cells in petrified wood. *Materials Science and Engineering*, Vol. 25, pp. 119–130, http://dx.doi.org/10.1016/j.msec.2005.01.018
Pakhomova V., Solyanik V., Fedoseev D., Kultenko S.Y., Tishkina V.B., Gusarova V.S. (2020) Gem News International: Occurrence of petrified woods in the Russian Far East: Gemology and origin. *G&G*, Vol. 56, No. 2, pp. 306–308.
Rößler R. (2000) The late Paleozoic tree fern Parsonius- an ecosystem unto itself. *Review of Palaeobotany and Palynology*. Vol. 119, No. 1-2, pp. 143–159.
Saminpanya S. (2015) Gem News International: Thai-Myanmar petrified woods. *G&G*, Vol. 51, No. 3, pp. 337–339.
——— (2016) Trace elements and mineral chemistry of silicified wood from Thailand: Colours and elemental distribution. *Australian Journal of Earth Sciences*, Vol. 63, No. 7, pp. 873–884, http://dx.doi.org/10.1080/08120099.2016.1251492
Scurfield G., Segnit E.R. (1984) Petrifaction of wood by silica minerals. *Sedimentary Geology*, Vol. 39, pp. 149–167, http://dx.doi.org/10.1016/0037-0738(84)90048-4
Stein C.L. (1982) Silica recrystallization in petrified wood. *Journal of Sedimentary Research*, Vol. 52, No. 4, pp. 1277–1282, http://dx.doi.org/10.1306/212F8116-2B24-11D7-8648000102C1865D
Tidwell W.D., Ash S.R., Britt B.B. (2010) Oldest known dicotyledonous lianas from the early late Cretaceous of Utah and New Mexico, USA. In C.T. Gee, Ed., *Plants in Mesozoic Time: Morphological Innovations, Phylogeny, Ecosystems*. Indiana University Press, Bloomington, Indiana, pp. 271–291.
Witke L., Götze J., Rößler R., Dietrich D., Marx G. (2004) Raman and cathodoluminescence spectroscopic investigations on Permian fossil wood from Chemnitz – A contribution to the study of the permineralisation process. *Spectrochimica Acta Part A: Molecular and Biomolecular Spectroscopy*, Vol. 60, No. 12, pp. 2903–2912, http://dx.doi.org/10.1016/j.saa.2003.12.045
Xu H.Y. (2021) Mineralogy and structure characteristics of silicified tree fern from Heilongjiang. Master's thesis, China University of Geosciences, Beijing [in Chinese].
Yang X.N., Liu F.X., Cheng Y.M. (2018) A new tree fern stem, *Tempskya zhangii* sp. nov. (Tempskyaceae) from the Cretaceous of northeast China. *Cretaceous Research*, Vol. 84, No. 1, pp. 188–199, http://dx.doi.org/10.1016/j.cretres.2017.11.016
Yoon C.J., Kim K.W. (2008) Anatomical descriptions of silicified woods from Madagascar and Indonesia by scanning electron microscopy. *Micron*, Vol. 39, No. 7, pp. 825–831, http://dx.doi.org/10.1016/j.micron.2007.12.011
Yu X.Y. (2016) *Colored Gemology*, 2nd ed. Geological Publishing House, Beijing [in Chinese].

Slovak Opal: A New Life for a Historical Gem

Peter Semrád

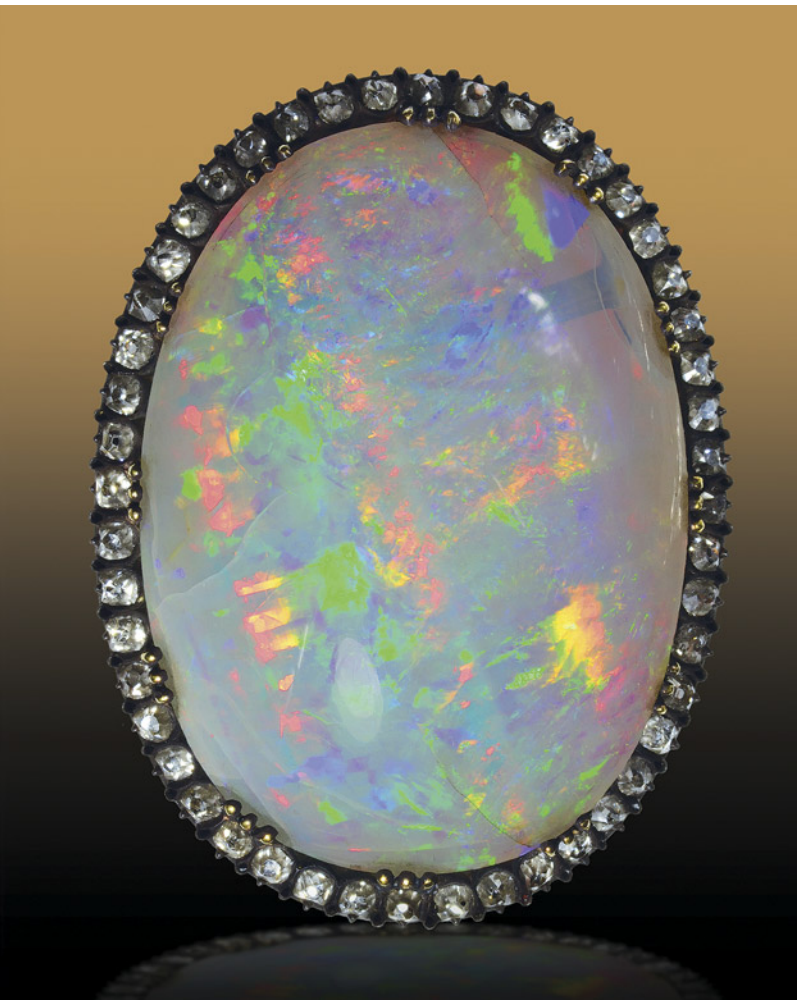

Figure 1. A silver brooch containing a large Slovak opal (77 ct, 34.5 × 25 × 13 mm) and 48 diamonds. The opal was initially purchased for Louis XVIII's personal collection. In 1824, it adorned the clasp of Charles X's coronation mantle, and around 1853 it was remounted onto this brooch for Empress Eugénie, which has been preserved. Photo by Peter Semrád; courtesy of the National Museum of Natural History in Paris (inventory no. MNHN 87.44).

See end of article for About the Author and Acknowledgments.
Gems & Gemology, Vol. 59, No. 4, pp. 466–483,
http://dx.doi.org/10.5741/GEMS.59.4.466

Slovakia, a landlocked country in Central Europe, covers an area of 49,000 km^2 and has a population of 5.4 million. Its terrain is mostly mountainous, especially in the north and central regions, while the remaining areas are more or less flat with occasional hills that break through the landscape. Slovakia is a small country but rich in mineral resources. These resources were exploited extensively in the past, when present-day Slovakia was part of the Kingdom of Hungary. Since 1918, when this multiethnic kingdom collapsed and Slovakia transitioned to Czechoslovakia and later became an independent state in 1993, the Slovakian mining industry has changed significantly. Depleted mineral sources have been abandoned and new ones discovered and developed. Some localities that were once active and then vacated have seen attempts at revival. That is exactly the case with opal from the Slovakian village of Červenica-Dubník (figure 1).

Due to the geopolitical situation in the past, opal from this source was once known as Hungarian opal. Mining efforts expanded dramatically over the course of the nineteenth century, when there was private entrepreneurship in the locality. The "golden era" of 1845–1880 saw opal mines leased to the Goldschmidt family. Starting on November 1, 1896, gem mining was carried out by the state, which owned the deposits. Unfortunately, the state did not send the extracted stones to the market but to the treasury of the Ministry of Finance in Budapest (Butkovič, 1970). During that same period, the bountiful Australian deposits emerged as a formidable competitor to Hungarian opal (Cram, 1998). After World War I, Czechoslovakia could not afford to continue mining operations, which ceased in 1922. Today, these formerly Hungarian opals—now considered Slovak—are poised to regain their popularity.

SOURCE LOCATION

The opal region is situated in eastern Slovakia, in the Prešov region, largely in the Prešov district and the Červenica and Zlatá Baňa villages (figure 2). The area is accessible by vehicle on local road no. 3440 connecting the city of Prešov and the village of Rozhanovce, which is near the city of Košice.

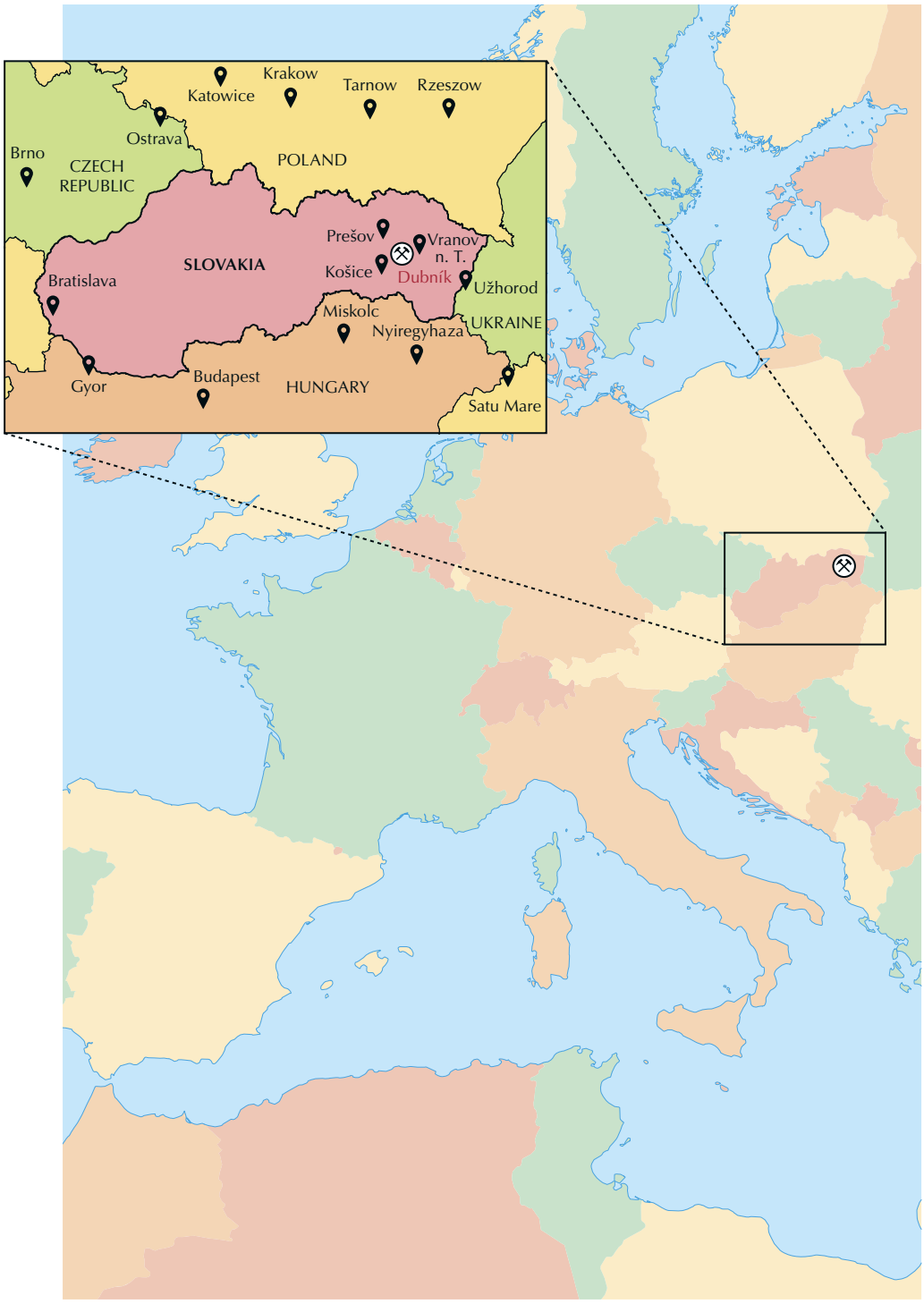

Figure 2. Maps of Europe and Slovakia showing the location of the Červenica-Dubník site.

Whether starting in Prešov or Košice, the drive across the rural area is over slightly hilly terrain. The scenery eventually turns into the Slanské vrchy Mountains. From Prešov, one can admire a picturesque caldera (cauldron-like hollow) where Zlatá Baňa was founded in connection with exploration and subsequent small-scale, intermittent mining focused on antimony ore (stibnite) as well as polymetallic ores containing silver and gold. Starting from Košice, the traveler will not miss the Červenica village, which remains most associated with opal (figure 3) even though it likely had its beginnings

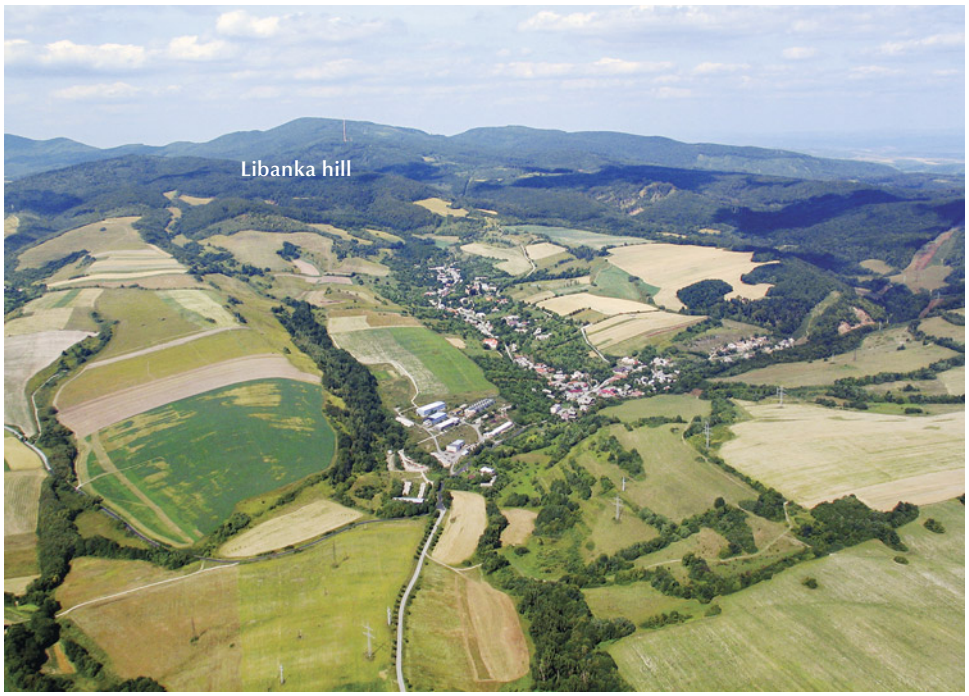

Figure 3. Aerial view of Červenica village. Photo by Igor Pap.

with cinnabar mining circa 1400. Nevertheless, opal took the lead during the sixteenth century and made the place widely known.

The historical and prospective opal region extends several kilometers north-northeast from Červenica. The nearly defunct settlement of Dubník, which once served as lodging for the high-ranking staff of the opal mining enterprise, was a thriving place throughout the nineteenth century. It also housed an opal cutting workshop. Mining was carried out in various locations within and around the settlement. The most productive of the mines until the end of operations in 1922 (Butkovič, 1970) was located at Libanka Hill (figure 4). An operational center consisting of buildings for residential, industrial, and administrative purposes once stood on the eastern foothills,

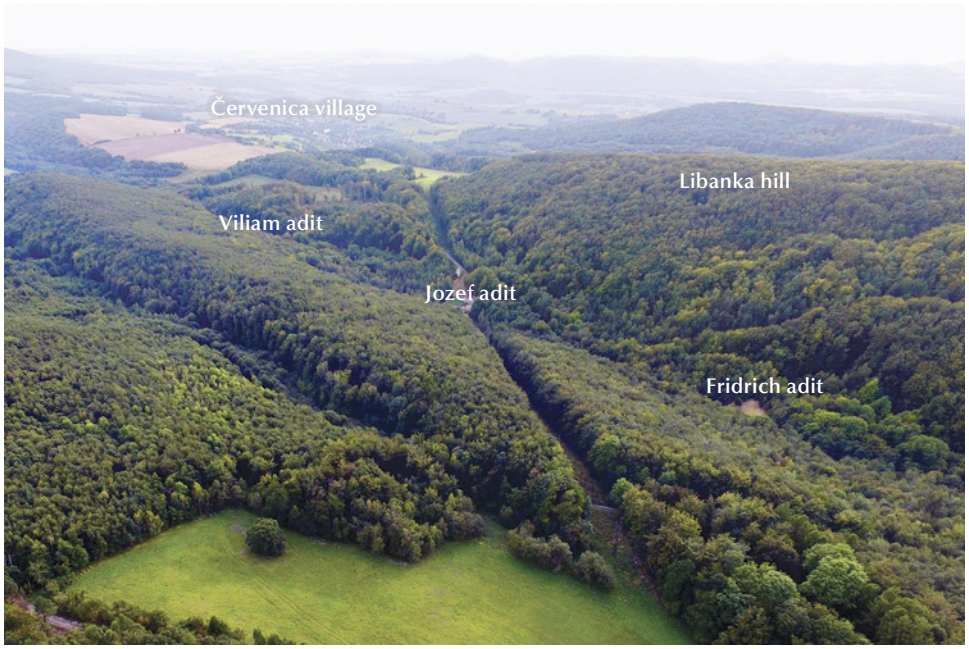

Figure 4. Aerial view of the south section of Libanka Hill. Photo by Milan Goš.

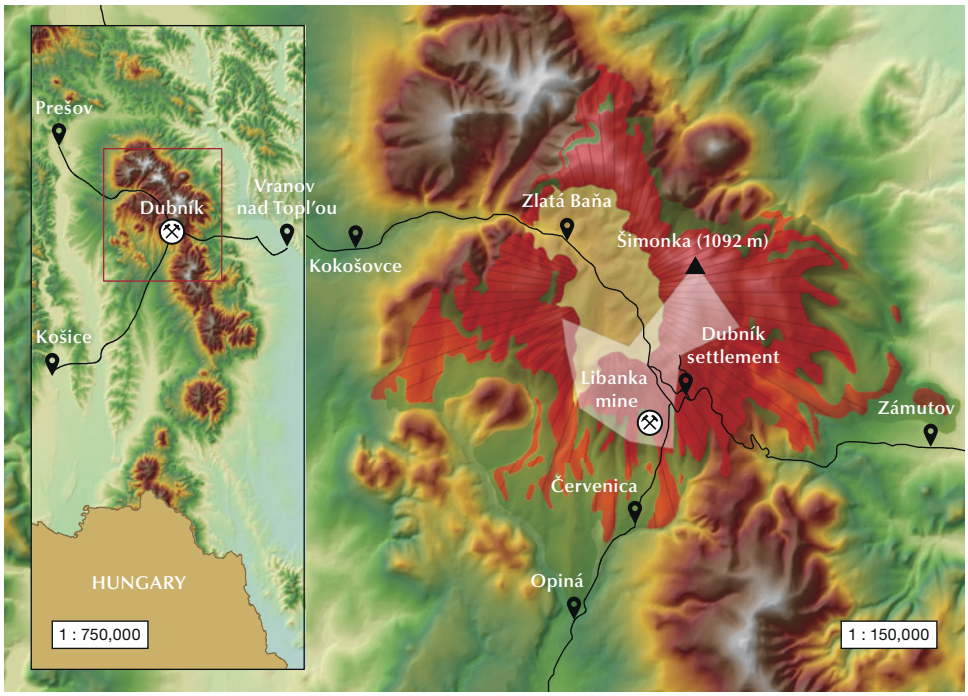

Figure 5. Maps of the Slanské vrchy Mountains and the Zlatá Baňa stratovolcano showing the position of the locality. The translucent white shape represents the Červenica I protected deposit area for opal.

though time and development have removed the evidence. Recent activities are focused on this area and will be discussed further in this field report.

GEOLOGY AND MINERALOGY

Based on the geological environment, experts differentiate between "sedimentary-type" opal (found in numerous Australian deposits within the Great Artesian Basin) and "volcanic-type" opal (located around Tintenbar in New South Wales in Australia, as well as additional localities in the United States, Mexico, Honduras, Ethiopia, and Indonesia, among others) (Rondeau et al., 2004). Nevertheless, it is sometimes difficult to decide which "opal type" a specific site belongs to. At the Boi Morto mine in Brazil, for instance, opal can be found in both volcanic and sedimentary rocks (Farrar, 2007). Červenica-Dubník is also peculiar but in another respect. Rondeau et al. (2004) reported that opal from this locality shows all the physical properties typical of a "sedimentary-type" deposit but is found in a volcanic host rock (andesite). Some recent research has led to similar conclusions (Semrád, 2017). However, the genesis of precious opal is quite complex and beyond the scope of this report.

As previously mentioned, the home of Slovak opal is the Slanské vrchy Mountains, where the host environment for opal mineralization is of volcanic origin. This volcanic mountain range is approximately 10–14 million years old (Lower Pannonian to Upper Badenian, respectively) (Kaličiak and Repčok, 1987). The main segment running north to south bends slightly toward the east and consists of large adjacent relics of stratovolcanic structures: the Zlatá Baňa, Makovica, Strechový vrch, Bogota, and Veľký Milič stratovolcanoes. The range is 50 km long and varies in width from 20 km in the north to 12 km in the south. The Červenica-Dubník opal deposits are situated in the northern part of the mountains, specifically in the southeastern section of the Zlatá Baňa stratovolcano transitional zone (figure 5).

The geology of the deposits comprises four distinct lithologies. They differ in spatial orientation, and thus in age, as well as in petrographic composition (Kaličiak et al., 1976): two-pyroxene andesite ("Libanka" type), pyroxene andesite ("Ošvárska" type), pyroxene-amphibole andesite, and pyroxene-amphibole-biotite andesite. The old opal mining fields are situated close to two major tectonic zones of a northwest-southeast direction where petrographic varieties of andesite and their pyroclastics converge (figure 6). This suggests that lithological-petrographic and structural-tectonic "traps" played an essential role in the formation and distribution of opal mineralization (Kaličiak and Jacko, 1995). Major tectonic structures of a northwest-southeast direction are accompanied by minor pinnated and possibly parallel (synthetic) faults, shrinkage cracks, and cavities. These features and their surroundings are potential hosts for accumulations of opal. The high-

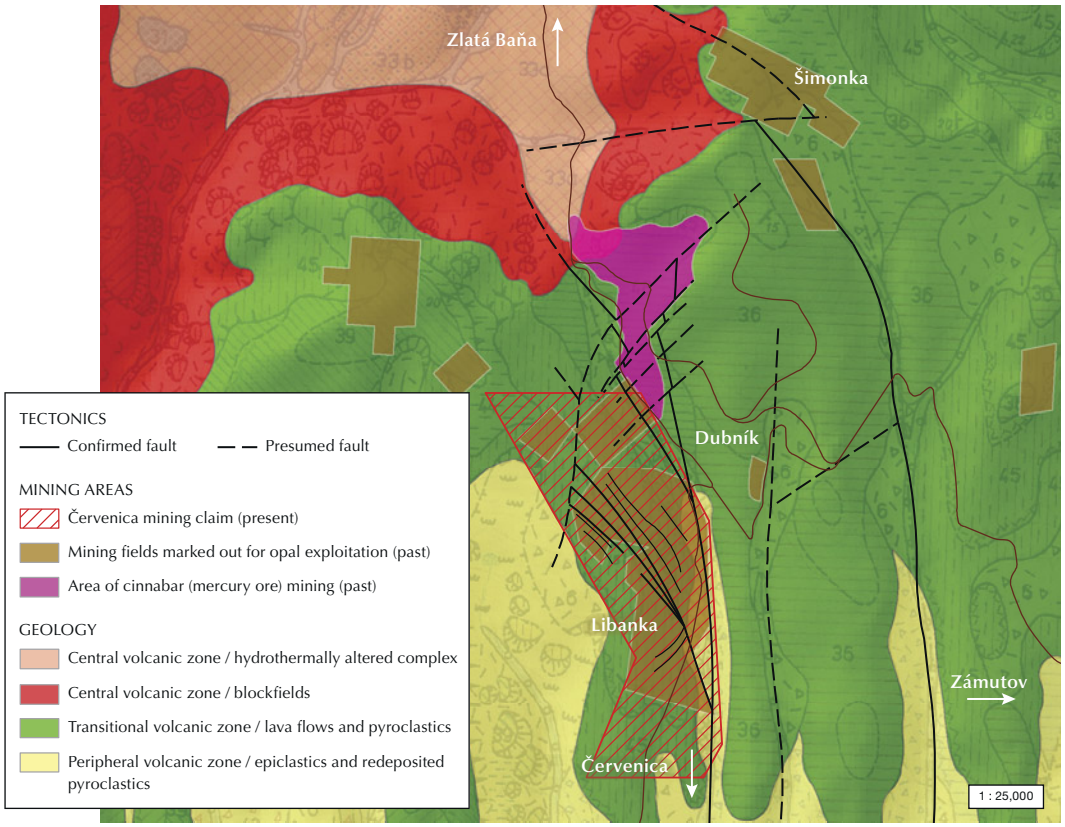

Figure 6. Geological map of the area where opal mineralization occurs.

est opal concentrations were found and mined at fault intersections (Kaličiak et al., 1976).

In terms of mineralogy, the Červenica-Dubník opal deposits contain mostly opal and sulfides. The former comprises a few macroscopically distinct varieties of A_G-opal (specifically precious opal, glassy opal, and milky opal; figures 7 and 8) and A_N-opal (hyalite). X-ray diffraction analysis sometimes reveals minor admixtures of CT-opal, however (Semrád, 2017). The most abundant of the sulfides is iron disulfide, including both pyrite and marcasite (Slavík, 1920). Besides these two species, stibnite is also found in the deposits, though much less frequently. Interestingly, the Natural History Museum in London has one specimen from the locality that features precious opal and macroscopic flecks of native gold (Semrád, 2022a,b). Some clay minerals are also present in these deposits. Visitors touring the old mining works with a guide can marvel at places where walls and ceilings are covered with secondary sulfates.

RECENT DEVELOPMENTS

Because the Libanka mine was the largest and most bountiful in the area, it is not surprising that subsequent prospectors decided to continue mining activities in this region. During the peak decades (from the 1840s through the 1880s), this mine likely yielded tens of thousands of carats of cut precious opal annually. More accurate production data is available only from 1880 (tables 1 and 2). At the time the mining ceased, it was suggested that the future of opal from the Červenica-Dubník locality was not a question of reserves and production but one of sales (Slavík, 1920). Unfortunately, no one stepped forward during the interwar period to resume operations, and World War II further hampered the possibility.

Post-war Czechoslovakia saw exclusive state ownership of enterprises, and the economy was centrally managed. This meant that only the state could breathe life into the abandoned mines at Dubník. Mineral resources were surveyed (including the cinnabar deposit at nearby Libanka Hill) and extracted on a large scale in various localities. Economic planners, however, gave preference to industrially attractive commodities such as ores for the production of iron, copper, manganese, magnesium, and antimony, as well as coal and salt. Only when the transition from communism to democracy and a free-market

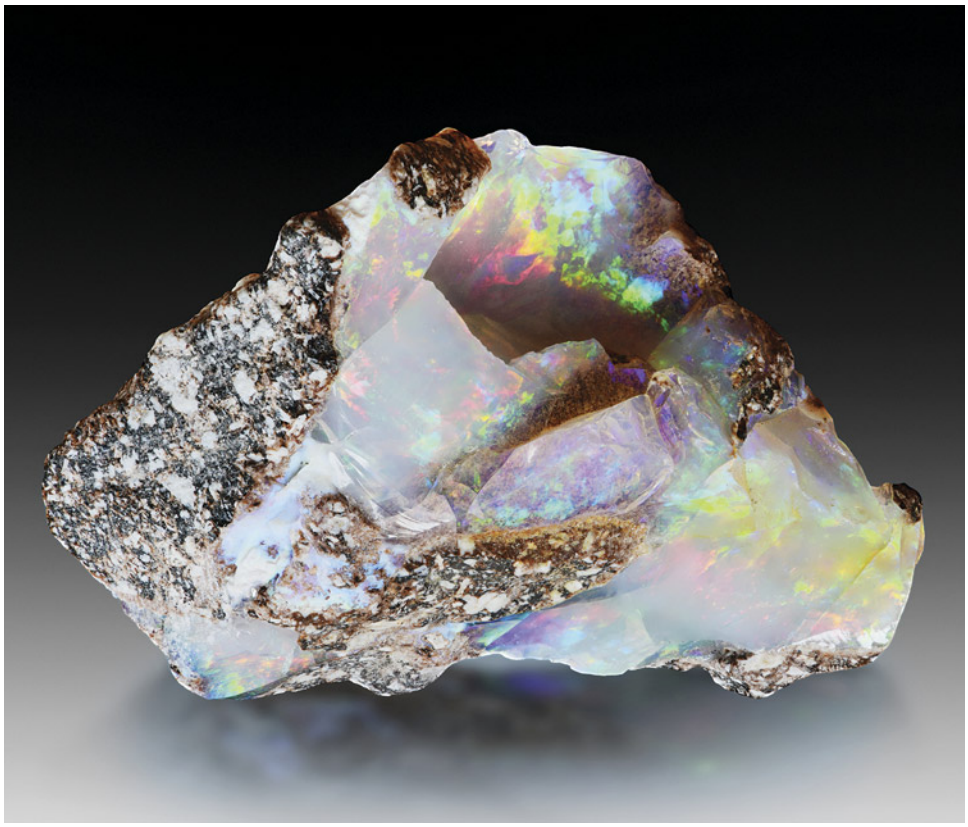

Figure 7. Precious opal in andesite host rock (28 × 22 × 14 mm). Photo by Albert Russ; courtesy of Great Rent JSC.

economy brought private entities back to the stage during the late 1980s and early 1990s was there a chance to revive the opal mining operation.

Between 1991 and 2001, the companies Jozef Jančok - SAVARNA and Slovenský opál Ltd, surveyed all historical mining sites and adjacent areas

Figure 8. Glassy and milky common opal (42 × 28 × 17 mm). Photo by Albert Russ; courtesy of Great Rent JSC.

TABLE 1. Cut opal production, 1880–1896.[a]

Date	Pieces	Carats	Date	Pieces	Carats
August 12, 1881[b]	21,047	5,738	August 12, 1889	125,026	20,976
August 12, 1882	19,351	10,706	August 12, 1890	207,447	27,990
August 12, 1883	22,712	12,026	August 12, 1891	243,747	24,272
August 12, 1884	30,957	14,793	August 12, 1892	146,822	10,373
August 12, 1885	25,181	10,152	October 9, 1893	82,376	13,344
August 12, 1886	26,468	9,646	October 13, 1894	71,593	12,401
August 12, 1887	82,268	12,061	October 10, 1895	67,246	10,060
August 12, 1888	174,783	21,017	February 7, 1896[c]	3,955	459

[a]*Source: Slovenský banský archív (Slovak Mining Archives), Banská Štiavnica (file HKG: 639/1896)*
[b]*The first period started on August 12, 1880.*
[c]*The last period was significantly shorter than the others.*

TABLE 2. Cut opal production, 1897–1922.[a]

Year	Pieces	Carats	Year	Pieces	Carats
1897	46,687	6,853	1910	8,561	2,406
1898	28,862	2,177	1911	10,566	2,468
1899	23,695	3,328	1912	10,322	2,636
1900	22,609	3,553	1913	11,034	2,259
1901	24,876	4,095	1914	11,287	2,380
1902	26,300	3,113	1915	10,108	1,726
1903	8,569	1,248	1916	7,622	1,580
1904	6,366	1,058	1917	6,058	769
1905	11,856	2,020	1918	9,703	1,752
1906	10,537	2,422	1919	5,365	750
1907	10,557	1,172	1920	5,522	1,101
1908	13,211	2,270	1921	6,506	1,224
1909	10,127	2,641	1922[b]	106	170

[a]*Source: Pelikán (1923)*
[b]*The production figures for 1922 only cover the first half of the year (Semrád, 2022a).*

with the hope of finding new opal-bearing structures (Jančok, 2001; table 3). Since October 2000, following the survey, Slovenský opál Ltd has held the Červenica mining claim, which overlaps considerably with the Libanka mining field from the past. On the basis of a preliminary agreement with an investor, the company Opálové bane Dubník JSC (Joint Stock Company) was founded in 2001. Subsequently, Slovenský opál Ltd applied to the regional mining authority to transfer the claim to Opálové bane Dubník JSC. This never materialized, however. A call aimed at regranting the claim was launched instead.

ObaB Ltd held the Červenica mining claim from September 2005 until July 2007, when it was transferred onto Opálové bane a brusiarne Ltd and in June 2010 further onto Opálové bane Libanka Ltd. Actual mining activity did not take place until 2012, however, and has since been intermittent. Finally, a new commercial name for opal from this area was introduced to sever any historical promotional ties. On October 11, 2016, the certified geographic designation "Slovak Opal" was registered with the Industrial Property Office of the Slovak Republic (Opálové bane Libanka Ltd, 2016). On November 10, 2016, it was subsequently registered with the International System of Appellations of Origin and Geographical Indications (Opálové bane Libanka Ltd, 2017). In accordance with the national and international registrations, the "Slovak Opal" designation is applicable exclusively to precious opal originating from the Červenica I protected deposit area (approximately 11 km^2) and the Červenica mining claim (approximately 1 km^2) (State Geological Institute of Dionýz Štúr, n.d.).

Currently, the Červenica claim is held by Slovenské opálové bane Ltd, the successor to Opálové bane Libanka Ltd since November 2021. Considerable time has passed since 2001, when Jozef Jančok provided the most recent calculation of opal reserves and resources. To gain up-to-date insight into the current production chain, the author interviewed Maroš Turek and Igor Kromka, executive directors of Slovenské opálové bane Ltd and Great Rent JSC, respectively.

OPAL EXTRACTION

Recent production relies exclusively on collecting and extracting the raw material from secondary deposits, specifically anthropogenic deposits. These include heaps of opal-bearing rock on the surface and underground backfilling in stopes (figures 9 and 10). According to Jančok (2001), the yield from these sources is substantial. In fact, opal miners left behind a considerable amount of gemmy material as they worked under challenging conditions. First was the poor lighting at underground excavation sites, with the use of very simple lighting tools. Second,

TABLE 3. Opal reserves in the Libanka deposit as of December 2001.[a]

Specification of reserves	Category	Free or blocked[b]	Opal-bearing rock (m^3)	Reserves (ct)
Excavated material on the surface: heap of the Viliam drainage adit	Proven	Free	25,737	311,900
Excavated material underground: backfilling in stopes	Probable	Free	18,590	796,371
Excavated material underground: backfilling in stopes	Inferred	Free	28,819	1,082,231
Opal-bearing rock in the primary position (safety pillar of the Fedö central shaft)	Inferred	Blocked	1,638	118,700
Total reserves			**74,784**	**2,309,202**

[a]*Source: Jančok (2001)*
[b]*Blocked reserves are safety pillars in mining works for operational safety and protected interests, while free reserves are all other reserves.*


Figure 9. Left: The author opal hunting (with Jozef Čurík in the blue parka) on the heap of the Viliam drainage adit (Libanka mine). Right: Part of the heap of the Viliam drainage adit. Photos by Slavomír Krestian; courtesy of Slovenské opálové bane Ltd.

the opal mineralization within the host rock environment occurred extremely irregularly in the form of either clusters or dendritic nests, veinlets or veins, breccia "cement," and impregnations. Third, the

Figure 10. Opal hunting with Miroslav Kravec (blue parka) in the stope around the Jozef adit of the Libanka mine. Photo by Slavomír Krestian; courtesy of Slovenské opálové bane Ltd.

Figure 11. A precious opal specimen found in the stope around the Jozef adit (Libanka mine). Photo by Slavomír Krestian.

presence of sticky clay from decomposed andesite, as well as hydrated iron oxide-hydroxides (possibly iron-oxyhydroxysulfate) from decomposed iron disulfide, made it difficult to spot gems. Nevertheless, it is still possible to find some modest opal specimens without picking through old rubble for hours (figure 11).

Larger pieces, unfortunately, are rarely found today. No wonder: Miners in the old days, despite all the aforementioned difficulties, did their best to extract as many "opal chunkies" as possible. Even when they failed, there was still a chance that unnoticed gems would be retrieved. Coincidentally, the author recently heard a story from a descendant living in the United States whose ancestors, a husband and wife, both worked in the opal mines at Červenica-Dubník. According to family recollections, the husband's daily task was to search for the gems underground while his wife sifted through the material brought up to the surface. During this activity, she once managed to find a very large piece of opal (L. Lane, pers. comm., 2022).

Anyone searching for opal today must have permission from Slovenské opálové bane Ltd and use only hand tools. The company obtains its raw material in the same way because of the Červenica mining claim's overlap with the Dubnícke bane Protected Site, declared in accordance with the SRNC (Slovak Republic National Council) Nature and Landscape Protection Act, and the Dubnícke bane Special Area of Conservation designated by the European Union's Habitats Directive, also known as the Directive on the Conservation of Natural Habitats and of Wild Fauna and Flora (Štátna ochrana prírody Slovenskej republiky, n.d.; figure 12). Under the circumstances, any mechanized underground mining in this locality would very likely be rejected. As reported by Turek, the company's priority is maintaining the safety of the old mining works for organized guided tours (figure 13). While finding opals during maintenance is considered a bonus, Turek noted that company workers sometimes look for them intentionally.

On the surface, the most promising place for opal reserves is the heap at the Viliam drainage adit. Besides casually picking through the excavated material by hand and possibly with hand tools, systematic and even to some extent mechanized mining would be feasible here, as it lies beyond the boundaries of the Dubnícke bane Protected Site. Knowing that this heap area is permitted by the regional mining authority for opal extraction until at least December 2030 (with the possibility of extension to December 2045),

Figure 12. Over time, the old mining works have become a hibernation site for bats. Photo by Miloš Greisel; courtesy of Slovenské opálové bane Ltd.

the author asked Turek whether they planned to start mining. He sounded somewhat skeptical and expressed doubt about the economic benefits compared to the project's costs.

Figure 13. Some parts of the Libanka opal mine have been adapted for geotourism. Visitors can choose between a family-friendly tour or a more adventurous opal hunting experience. Photo by Peter Semrád; courtesy of Slovenské opálové bane Ltd.

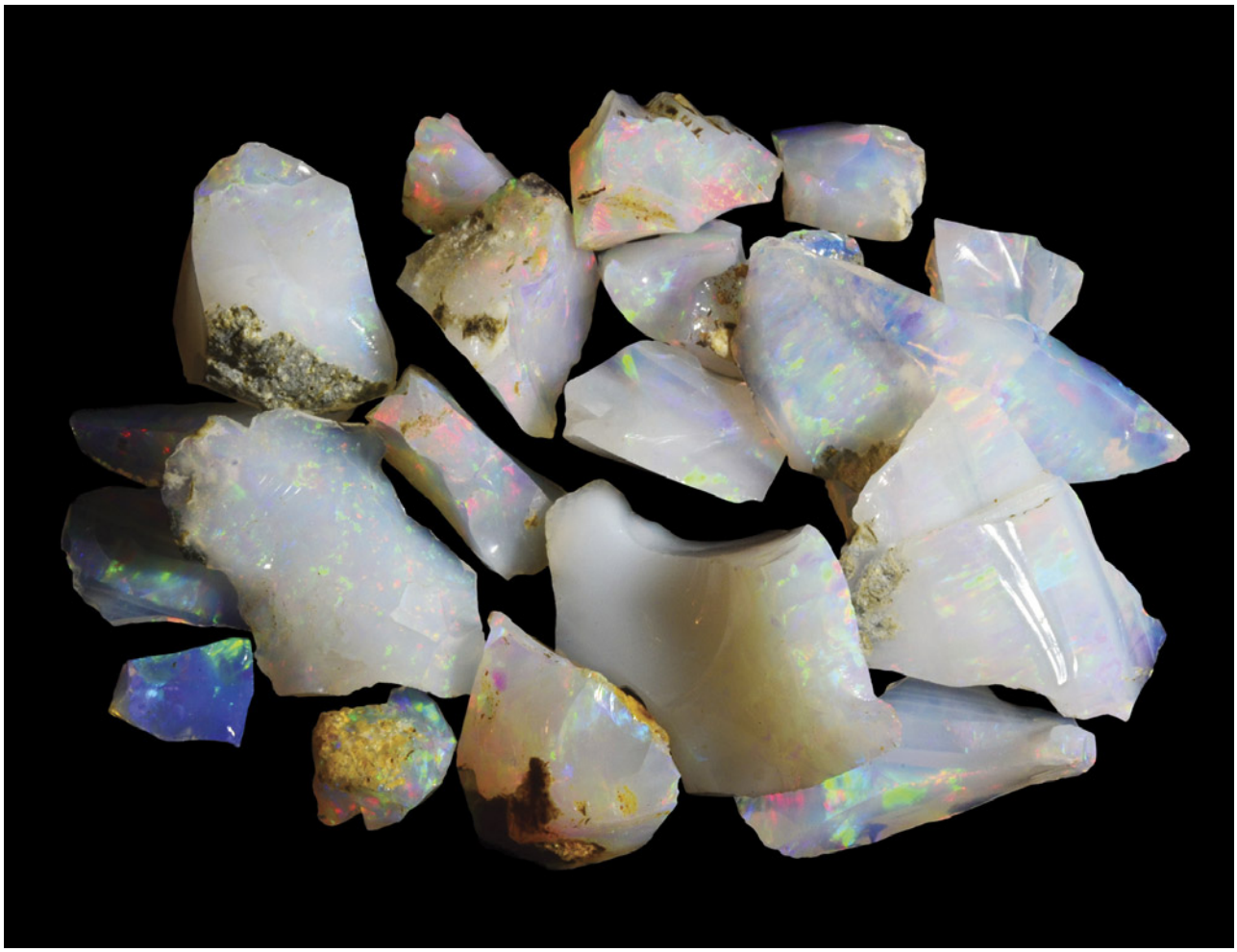

Figure 14. Rough Slovak Opal (0.52–5.54 ct). Photo by Peter Semrád; courtesy of Great Rent JSC.

SORTING, CUTTING, AND FINISHING

For the first step of the production chain at Slovenské opálové bane Ltd, all the material obtained is thoroughly rinsed. The second step entails the separation of potential mineralogical specimens from potential rough material for cutting. The latter is sifted through a series of sieves (25, 20, 14, 10, 5, 4, and 2 mm^2). During the third stage, both potential mineralogical specimens and rough material for cutting undergo a "stabilizing process," as Turek called it. In this process, the material is deposited for a specific period under controlled temperature and humidity (further details were not disclosed). Given the description provided, it would be more accurate to call this a test of structural integrity under changing conditions. The material that does not pass the "stabilizing" process—meaning it has degraded considerably due to cracking, crazing, or loss of water—is excluded from further processing.

The mineralogical specimens that do pass are prepared for sale without any further treatment. The "stabilized" rough for cutting is sorted by hand. This process includes separation of precious opal (figure 14) as well as a highly transparent variety of common opal known as glassy opal (figure 15) from other varieties such as hazy glassy opal, milky opal, and hydrophane. The vast majority of the material is sold to Great Rent JSC, which purchases nearly all of the mineralogical specimens containing precious opal as well as compact pieces of precious opal and high-quality glassy opal for cutting purposes. The low-quality material that remains with Slovenské opálové bane Ltd is sold at the locality in the form of various souvenirs.

Great Rent JSC markets and sells Slovak Opal under the trademark Yophine. Kromka explained that the name is an allusion to Joséphine de Beauharnais, who possessed a beautiful opal parure given to

Figure 15. Rough Slovak Ice Opal (3.36–25.42 ct). Photo by Peter Semrád; courtesy of Great Rent JSC.

her by Napoleon Bonaparte. Kromka added that the mineralogical specimens are first registered, with a unique identifier assigned and a specimen "passport" issued before being offered for sale. The opal pieces intended for cutting undergo an additional stabilizing process that is very similar to the previous one and again serves as a test of structural integrity. If an opal piece passes this test, a temporary identifier is assigned and it is either sent directly to a cutter or put in inventory (figure 16). Any piece that does not pass this process is returned to Slovenské opálové bane Ltd for reimbursement.

Figure 16. A rough piece of Slovak Opal (7.66 ct) as an investment stone. A client would decide whether to keep it in this form or cut it. Photo by Slavomír Krestian; courtesy of Great Rent JSC.

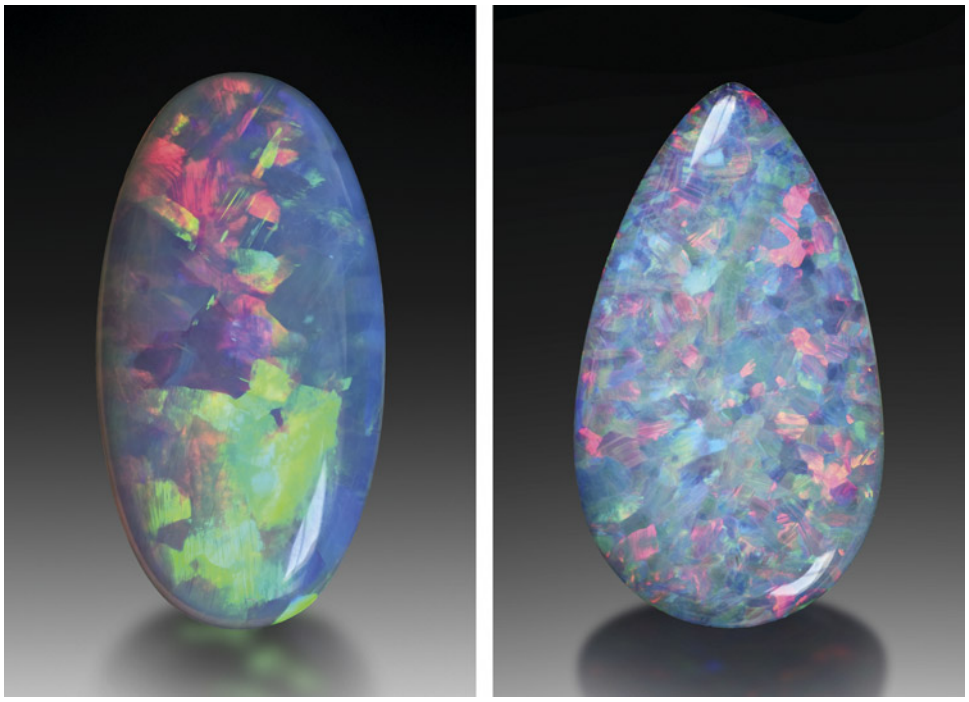

Figure 17. Slovak Opal cabochons weighing 1.58 ct (11 × 5 mm, left) and 2.67 ct (12 × 8 mm, right). Photos by Albert Russ; courtesy of Great Rent JSC.

Most of the Červenica-Dubník precious opal, commercially known as Slovak Opal, can be classified as light opal (with a white and translucent to opaque body) or crystal opal (with a colorless, transparent body). Precious opal with a chromatic body hue, specifically within a range of yellow to orange to brown, occur rarely and are showcased as historical specimens in galleries at the Natural History Museum in Vienna, the Victoria and Albert Museum in London, and the Natural History Museum in London (Semrád, 2015, 2022a,b). In addition to precious opal, Great Rent JSC supplies the market with glassy opal under the trade name Slovak Ice Opal, named for its distinctive blue hue. This color is produced by the material's microstructure. As with precious opal, specimens with an unusual chromatic hue appear from time to time. Conversely, this variation is a compositional color, and inclusions of goethite seem to play a role in it (Semrád, 2017).

Figure 18. A 0.68 ct faceted Slovak Ice Opal measuring 6 mm. Photo by Albert Russ; courtesy of Great Rent JSC.

As for the cutting, Kromka explained that Great Rent JSC chooses skilled cutters who specialize in opal to maximize the recovery from each stone. Precious opals are mostly cut as cabochons (figure 17), while gem-quality glassy opal (i.e., Slovak Ice Opal) is usually faceted (figure 18). After cutting, every opal piece receives a unique identifier and is registered in a custom-developed software that is also used to generate gem certificates. Kromka graciously provided recent data on the processing of Slovak Opal and Slovak Ice Opal (table 4). Since the table shows statistics for both rough and cut material, it is possible to calculate cut yields ranging from 18.23% to 26.22%.

TABLE 4. Gem-quality Slovak Opal processed from May 2021 to February 2023.[a]

		With play-of-color				Without play-of-color	
		Crystal Opal		Light Opal		Ice Opal	
		Pieces	Weight (ct)	Pieces	Weight (ct)	Pieces	Weight (ct)
Rough	<0.5	58	18.30	1	0.35	4	1.42
	0.5–0.99	55	39.49	8	5.53	12	10.25
	1–1.99	30	42.50	11	16.16	68	101.75
	2–4.99	55	161.33	13	36.79	106	355.06
	5–9.99	15	100.45	1	9.37	77	521.66
	10–19.99	5	58.75	2	26.75	26	325.66
	20–49.99	0	0	1	24.45	14	391.49
	>50	0	0	0	0	4	369.30
	Total	218	420.82	37	119.40	311	2,076.59
	Min–max	—	0.09–16.00	—	0.35–24.45	—	0.29–165.80
	Average	—	1.93	—	3.23	—	7.40
Cut	<0.5	162	29.54	20	5.10	159	44.31
	0.5–0.99	40	27.57	12	9.32	66	47.40
	1–1.99	14	19.92	4	6.28	56	85.22
	2–2.99	10	24.06	0	0	21	54.36
	3–3.99	0	0	1	3.87	10	34.79
	4–4.99	2	9.26	0	0	7	32.64
	5–9.99	0	0	1	5.17	4	25.90
	10–19.99	0	0	0	0	2	22.13
	20–49.99	0	0	0	0	1	31.81
	Total	228	110.35	38	29.74	326	378.58
	Min–max	—	0.03–4.88	—	0.10–5.17	—	0.11–31.83
	Average	—	0.50	—	0.80	—	1.62

[a]*Source: Great Rent JSC, 2023*

The minimum and maximum opal weights provided are also interesting because they indicate the size of gemstones available for sale.

Once an opal cut is finalized, it is put either in inventory or directly into the production process and crafted into jewelry, Kromka noted. Each product commissioned by Great Rent JSC or a client of the company is unique (figures 19 and 20). In addition to selling jewelry and excluding mineralogical specimens, Great Rent JSC offers three services:

Figure 19. White gold earrings containing Slovak Opal (0.72 ct total) and diamonds. Photo by Albert Russ; courtesy of Great Rent JSC.

1. Selling a rough opal piece accompanied by a certificate. The client decides how to use the opal, and Great Rent JSC assumes no further responsibility.
2. Selling a rough opal piece with options for either cutting alone or cutting and crafting into jewelry. In these situations, Great Rent supervises the process and issues a certificate upon completion.
3. Selling a cut opal with a certificate.

Figure 20. White gold ring containing Slovak Ice Opal (7.65 ct) and diamonds. Photo by Albert Russ; courtesy of Great Rent JSC.

Great Rent JSC prefers doing business face-to-face with customers. The company provides a venue (either their own sales events or participation in others' events), or they can visit the client if preferred. According to the most recent information provided, the company is developing an e-commerce platform.

SUSTAINABLE MODEL

Bringing a historical gem back to life is no easy feat. Today, the Červenica-Dubník locality certainly cannot supply the market with opal on a large scale. There are, however, some advantages that the stakeholders can capitalize on. In particular, the Červenica-Dubník locality is very likely the world's oldest known commercial source of precious opal, with a long, rich history. Even its apparent disadvantages of limited access to reserves and a yield of mostly small cut stones could be an asset due to scarcity driving up demand and price. The market has plenty of opal and large cut opal from various sources, but some consumers will want to possess a Slovakian stone.

During the author's interview with Turek and Kromka, the two directors described their business model. Collaboration between Slovenské opálové bane Ltd and Great Rent JSC is rational and mutually beneficial. By focusing on specific activities rather than operating individually across a broad spectrum, the two companies are able to deliver high-quality results. The former manages on-site activities, such as conventional medium-size group tours or more adventurous small-group tours that include opal hunting and occasional collecting of opal for sale. The latter company handles off-site operations such as processing, jewelry making, and sales, tasks that require expertise and mobility.

Both parties share a common goal. By supporting each other in various ways, they seek to revive the historical gem under a new name, Slovak Opal, while preserving and developing a unique historical site. The hope is that this cooperation will build on the successful past of this opal source and continue it for as long as possible.

ABOUT THE AUTHOR

Dr. Peter Semrád is an independent researcher originally from Slovakia but residing in Bergen in the province of North Holland, the Netherlands. He has specialized in opal and in particular the Červenica-Dubník opal locality in Slovakia for more than 25 years.

ACKNOWLEDGMENTS

The author gratefully acknowledges the assistance provided by Slovenské opálové bane Ltd and Great Rent JSC. He would also like to thank photographers Milan Goš, Miloš Greisel, Slavomír Krestian, Igor Pap, and Albert Russ. Lisa Lane (Excelsior, Minnesota) shared stories of ancestors who worked at the mines.

REFERENCES

Butkovič Š. (1970) *História slovenského drahého opálu z Dubníka (History of Slovak Precious Opal from Dubník)*. Alfa, Bratislava.

Cram L. (1998) *A Journey with Colour: A History of Queensland Opal 1869–1979*. Published by the author, Lightning Ridge, Australia.

Farrar B. (2007) Brazilian opal and the Boi Morto mine. In J. Clifford et al., Eds., *Opal: The Phenomenal Gemstone*. Lithographie, LLC, East Hampton, Connecticut, pp. 70–74.

Jančok J. (2001) *Záverečná správa o výsledkoch geologických prác úlohy Červenica – drahý opál: vyhľadávací prieskum I etapa; Časť B: Výpočet zásob* (Final report on the results of the geological works of the Červenica - precious opal task: Prospecting survey I stage; Part B: Resources calculation). Štátny geologický ústav Dionýza Štúra, Bratislava (Sign. 86077).

Kaličiak M., Jacko S. (1995) *Zhodnotenie doterajších poznatkov a možnosti prieskumu drahého opálu – Dubník* (Evaluation of existing knowledge and possibilities of exploration of precious opal – Dubník). Štátny geologický ústav Dionýza Štúra, Bratislava (Sign. 82494).

Kaličiak M., Repčok I. (1987) Rekonštrukcia časového vývoja vulkánov severnej časti Slanských vrchov (Reconstruction of time evolution of volcanoes in the northern part of the Slanské vrchy Mountains). *Mineralia slovaca*, Vol. 19, No. 5, pp. 401–416.

Kaličiak M., Ďuďa R., Burda R., Kaličiaková E. (1976) Geologicko-štruktúrna charakteristika dubníckych opálových ložísk (Geological-structural characteristics of opal deposits in Dubník). In S. Kipikašová, Ed., *Zborník Východoslovenského múzea v Košiciach (Séria AB – prírodné vedy)*. Východoslovenské vydavateľstvo n.p. pre Východoslovenské múzeum v Košiciach, pp. 7–21.

Opálové bane Libanka Ltd. (2016) Zemepisné označenia výrobkov:

Slovenský opál (Geographical designations of products: Slovak Opal). In *Vestník Úradu priemyselného vlastníctva Slovenskej republiky*, No. 11, pp. 251–253, https://www.indprop.gov.sk/swift_data/source/pdf/vestnik_upv_sr/2016/201611_v.pdf

——— (2017) Registration No 1061/Appelation of origin: SLOVENSKÝ OPÁL. In *Appellations of Origin* (Publication of the International Bureau of the World Intellectual Property Organization), No. 45, pp. 163–165, https://www.wipo.int/export/sites/www/lisbon/en/docs/bulletin_2017_45.pdf

Pelikán J. (1923) Státní opálové doly na Slovensku (State opal mines in Slovakia). In Spolek československých inženýrů a architektů, *Památník třetího valného sjezdu československých inženýrů a architektů v Košicích*, pp. 113–116.

Rondeau B., Fritsch E., Guiraud M., Renac C. (2004) Opals from Slovakia ("Hungarian" opals): A re-assessment of the conditions of formation. *European Journal of Mineralogy*, Vol. 16, No. 5, pp. 789–799, http://dx.doi.org/10.1127/0935-1221/2004/0016-0789

Semrád P. (2015) *Krása drahokamu: Európsky drahý opál z Dubníka (The Beauty of the Gem: European Precious Opal from Dubník)*. Granit Ltd, Prague.

——— (2017) *Svet minerálov: Európske drahoopálové ložiská v Dubníku (The World of Minerals: European Precious Opal Deposits at Dubník)*. Granit Ltd, Prague.

——— (2022a) *Zrkadlo minulosti: Európske drahoopálové bane v Dubníku (Mirror of the Past: European Precious Opal Mines at Dubník)*. Published by the author, Košice.

——— (2022b) Three outstanding "Hungarian" opal pieces in the Natural History Museum, London. *Jewellery History Today*, Vol. 45, No. 3, pp. 3–5.

Slavík F. (1920) *Zpráva o nalezišti drahého opálu u Dubníka* (Report on the precious opal locality at Dubník). Česká geologická služba, Prague (Sign. P 2394).

State Geological Institute of Dionýz Štúr (n.d.) Chránené ložiskové územia a dobývacie priestory (Protected deposit areas and permitted mining areas [claims]), http://apl.geology.sk/geofond/loziska2/

Štátna ochrana prírody Slovenskej republiky (n.d.) Zoznam osobitne chránených častí prírody SR (Register of particularly protected natural areas of the Slovak Republic), https://data.sopsr.sk/chranene-objekty/chranene-uzemia/detail/525 and https://data.sopsr.sk/chranene-objekty/chranene-uzemia/detail/SKUEV0401

Thank You, Reviewers

GEMS & GEMOLOGY requires each manuscript submitted for publication to undergo a rigorous peer review process, in which each paper is evaluated by at least three experts in the field prior to acceptance. This is essential to the accuracy, integrity, and readability of *G&G* content. In addition to our dedicated Editorial Review Board, we extend many thanks to the following individuals who devoted their valuable time to reviewing manuscripts in 2023.

Non-Editorial Board Reviewers

Alessandra Altieri • Sebouh Aslanian • Philippe Belley • Richard Berg • Troy Blodgett • Thanh Nhan Bui • Gagan Choudhary • James Conant • Aurélien Delaunay • Dona Dirlam • Elliot Entin • Alexander Falster • Hans Albert Gilg • Rhiana Henry • Shiyun Jin • Paul Johnson • Yusuke Katsurada • Yan Li • Edward Liu • George Mustoe

MICRO-FEATURES OF BERYL

Nathan Renfro, Tyler Smith, John I. Koivula, Shane F. McClure, Kevin Schumacher, and James E. Shigley

The beryl group of beryllium silicate minerals currently contains six member species, all of which have a hexagonal crystal structure: beryl, pezzottaite, bazzite, avdeevite, stoppaniite, and the most recent member, johnkoivulaite, which was named as a new mineral in 2019 (Palke et al., 2019) after GIA's analytical microscopist, John Koivula. As faceted gems, beryl and pezzottaite are the most commonly encountered species. Beryl is the most common beryllium-containing mineral (London, 2008) and often forms in pegmatitic environments or as a product of metasomatism. Also possible is a unique set of conditions in which beryl can crystallize from magma-derived gases and groundwater, as in the case of the red beryl deposit in the state of Utah (Shigley et al., 2003). Beryl gems include blue aquamarine (figure 1), golden beryl, red beryl, pink morganite, colorless goshenite, as well as Maxixe beryl, which is commonly dark blue with an unstable color. Emerald is the green variety of beryl colored by chromium and/or vanadium. Pezzottaite was first discovered in a granitic pegmatite in Madagascar in 2002 (Laurs et al., 2003). This unique bright pink beryl mineral has high cesium and lithium contents, which differentiate it as a unique beryl-group mineral.

Many of the beryl examples in the accompanying wall chart crystallized from a pegmatitic environment in which there is a high enough beryllium concentration for these gems to crystallize, which require the element as it is a bulk part of the crystal structure. These pegmatitic environments often contain fluids that get trapped along with other pegmatitic minerals, leaving a signature of their geologic formation within the gem's interior. The minerals most likely to be observed in these pegmatitic gems include albite, apatite, muscovite, garnet, tourmaline, and quartz (Gübelin and Koivula, 1986), while rare minerals such as stibiotantalite and monazite are only occasionally encountered.

This chart will focus on the members of the beryl group commonly seen as gems but will exclude emerald, which already has its own inclusions chart.

Figure 1. This 9.885 kg specimen of aquamarine on albite with a quartz cathedral center, measuring 31 × 23 × 28 cm, is from Pakistan's Shigar Valley. Courtesy of GIA Museum, collection no. 43068. Photo by Robert Weldon.

While synthetic and treated beryl gems do exist, they are relatively uncommon, so this chart only deals with natural beryl. These include fluids and solid minerals, as well as surface features and structural inclusions. As with past charts, the images presented are not meant to be all-encompassing but

GEMS & GEMOLOGY, Vol. 59, No. 4, pp. 484–485,
http://dx.doi.org/10.5741/GEMS.59.4.484

offer a wide range of the possible types of inclusions found in beryl gems.

For more on beryl inclusions, please see the Additional Reading list.

ABOUT THE AUTHORS

Nathan Renfro is senior manager of colored stone identification, John Koivula is analytical microscopist, Shane McClure is global director of colored stone services, Kevin Schumacher is photo/video producer for Gems & Gemology*, and James Shigley is distinguished research fellow, at GIA in Carlsbad, California. Tyler Smith is a senior staff gemologist at GIA in New York.*

REFERENCES

Gübelin E.J., Koivula J.I. (1986) *Photoatlas of Inclusions in Gemstones, Volume 1*. Opinio Verlag, Basel, Switzerland.

Laurs B.M., Simmons W.B., Rossman G.R., Quinn E.P., McClure S.F., Peretti A., Armbruster T., Hawthorne F.C., Falster A.U., Günther D., Cooper M.A., Grobéty B. (2003) Pezzottaite from Ambatovita, Madagascar: A new gem mineral. *G&G*, Vol. 39, No. 4, pp. 284–301.

London D. (2008) *Pegmatites*. Canadian Mineralogist, Special Publication No. 10, Mineralogical Association of Canada, Québec, 347 pp.

Palke A.C., Sun Z., Renfro N., Henling L.M., Ma C., Rossman G.R., Thu K., Myo N., Wongrawang P., Weeramonkhonlert V. (2019) Gem News International: Johnkoivulaite: A new gem mineral. *G&G*, Vol. 55, No. 3, pp. 454–455.

Shigley J.E., Thompson T.J., Keith J.D. (2003) Red beryl from Utah: A review and update. *G&G*, Vol. 39, No. 4, pp. 302–313.

ADDITIONAL READING

Adamo I., Pavese A., Prosperi L., Diella V., Ajò D., Diego Gatta G., Smith C.P. (2008) Aquamarine, Maxixe-type beryl, and hydrothermal synthetic blue beryl: Analysis and identification. *G&G*, Vol. 44, No. 3, pp. 214–226.

Bocchio R., Adamo I., Caucia F. (2009) Aquamarine from the Masino-Bregaglia Massif, Central Alps, Italy. *G&G*, Vol. 45, No. 3, pp. 204–207.

Cairncross B., Campbell I.C., Huizenga J.M. (1998) Topaz, aquamarine, and other beryls from Klein Spitzkoppe, Namibia. *G&G*, Vol. 34, No. 2, pp. 114–125.

Danet F., Schoor M., Boulliard J.-C., Neuville D.R., Beyssac O., Bourgoin V. (2012) Inclusions in aquamarine from Ambatofotsikely, Madagascar. *G&G*, Vol. 48, No. 3, pp. 205–208.

Gübelin E.J. (1960) More light on beryls and rubies with synthetic overgrowth. *G&G*, Vol. 10, No. 4, pp. 105–113.

Hu Y., Lu R. (2020) Color characteristics of blue to yellow beryl from multiple origins. *G&G*, Vol. 56, No. 1, pp. 54–65.

Huong L.T.-T., Hofmeister W., Häger T., Khoi N.N., Nhung N.T., Atichat W., Pisutha-Arnond V. (2011) Aquamarine from the Thuong Xuan District, Thanh Hoa Province, Vietnam. *G&G*, Vol. 47, No. 1, pp. 42–48.

Jennings R.H., Kammerling R.C., Kovaltchouk A., Calderon G.P., El Baz M.K., Koivula J.I. (1993) Emeralds and green beryls of upper Egypt. *G&G*, Vol. 29, No. 2, pp. 100–115.

Kampf A.R., Francis C.A. (1989) Beryl gem nodules from the Bananal mine, Minas Gerais, Brazil. *G&G*, Vol. 25, No. 1, pp. 25–29.

Koivula J.I., Renfro N. (2022) Micro-World: Quarterly Crystal: Hillocks on beryl. *G&G*, Vol. 58, No. 1, pp. 70–71.

——— (2023) Micro-World: Quarterly Crystal: Columbite(?) in beryl. *G&G*, Vol. 59, No. 1, pp. 90–91.

Lahti S.I., Kinnunen K.A. (1993) A new gem beryl locality: Luumäki, Finland. *G&G*, Vol. 29, No. 1, pp. 30–37.

Li J., Sun Y., Hao W., Luo H., Cheng Y., Liu H., Liu Y., Ye H., Fan C. (2009) Polymer-filled aquamarine. *G&G*, Vol. 45, No. 3, pp. 197–199.

Miley F. (1980) An examination of red beryl. *G&G*, Vol. 16, No. 12, pp. 405–408.

Nassau K., Prescott B.E. (1981) Nonfading Maxixe-type beryl? *G&G*, Vol. 17, No. 4, pp. 217–219.

Nassau K., Wood D.L. (1973) Examination of Maxixe-type blue and green beryl. *G&G*, Vol. 14, No. 5, pp. 130–133.

Schmetzer K. (1990) Hydrothermally grown synthetic aquamarine manufactured in Novosibirsk, USSR. *G&G*, Vol. 26, No. 3, pp. 206–211.

——— (1996) Growth method and growth-related properties of a new type of Russian hydrothermal synthetic emerald. *G&G*, Vol. 32, No. 1, pp. 40–43.

——— (2014) Letters: Analysis of three-phase inclusions in emerald. *G&G*, Vol. 50, No. 4, pp. 316–319.

——— (2021) History of emerald mining in the Habachtal deposit of Austria, Part I. *G&G*, Vol. 57, No. 4, pp. 338–371.

——— (2022) History of emerald mining in the Habachtal deposit of Austria, Part II. *G&G*, Vol. 58, No. 1, pp. 18–46.

Shigley J.E., Foord E.E. (1984) Gem-quality red beryl from the Wah Wah Mountains, Utah. *G&G*, Vol. 20, No. 4, pp. 208–221.

Shigley J.E., McClure S.F., Cole J.E., Koivula J.I., Lu T., Elen S., Demianets L.N. (2001) Hydrothermal synthetic red beryl from the Institute of Crystallography, Moscow. *G&G*, Vol. 37, No. 1, pp. 42–55.

Sun Z., Renfro N., Muyal J., Steenbock A. (2015) Micro-World: Blue gahnite inclusions in cat's-eye heliodor. *G&G*, Vol. 51, No. 3, pp. 325–326.

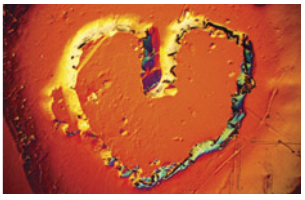

Lab Notes

Editors
Thomas M. Moses | Shane F. McClure | Sally Eaton-Magaña

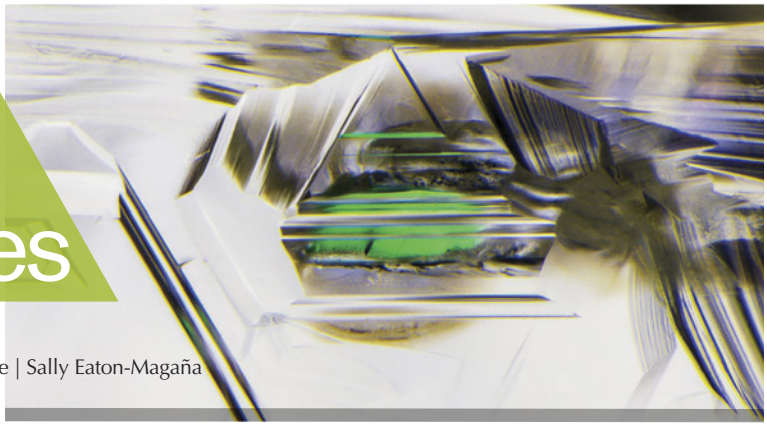

DIAMOND

Rare Natural Bicolor Diamond

A 0.63 ct bicolor diamond was submitted to GIA at the 2023 Tucson gem show for scientific examination. Previously submitted to GIA in 2008 for a colored diamond grading report, this tapered baguette-cut natural diamond had two major color zones: Fancy Dark orangy brown and Fancy Dark brown greenish yellow (figure 1). The brown greenish yellow zone had chameleon properties, including a temporary color change upon heating or when left in darkness for an extended period of time (possibly days). Visible narrow bands with darker color were observed within the brown greenish yellow zone (figure 1). Fourier-transform infrared spectra collected from the two color zones indicated that both were type Ia with comparable nitrogen concentrations. No amber centers or carbon dioxide absorption were detected in either color zone.

Bicolor diamonds are very uncommon, and the colors likely result from a combination of lattice defects. The major causes for yellow coloration in diamond include N3 centers, C centers, H3 centers, and the 480 nm absorption band (C.M. Breeding et al., "Naturally colored yellow and orange gem diamonds: The nitrogen factor," Summer 2020 *G&G*, pp. 194–219), whereas brown coloration is typically associated with vacancy clusters produced during plastic deformation (D. Fisher, "Brown diamonds and high pressure high temperature treatment," *Lithos*, Vol. 112, Supplement 2, 2009, pp. 619–624). It has been reported that diamonds rich in carbon dioxide might also have a brown color (T. Hainschwang et al., "HPHT treatment of CO_2 containing and CO_2-related brown diamonds," *Diamond and Related Materials*, Vol. 17, 2008, pp. 340–351). Ultraviolet/visible/near-infrared spectra collected separately from the two color zones to determine their color origins indicated that both color zones contained the 480 nm absorption band. In addition to this 480 nm absorption band, the brown color zone also showed enhanced absorption extending from the near-infrared region toward the UV region of the spectrum.

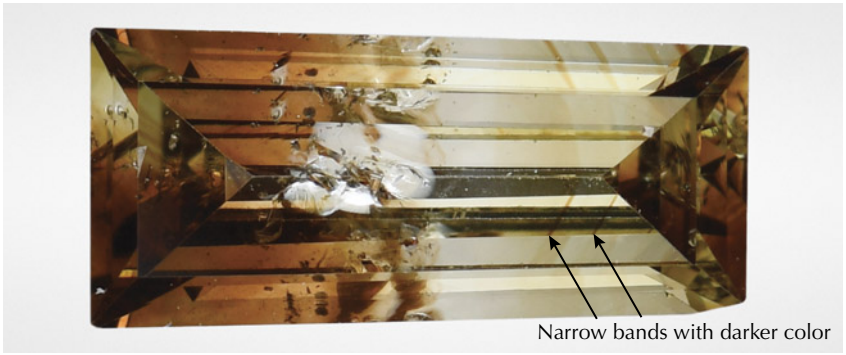

Figure 1. This 0.63 ct tapered baguette-cut diamond showed two major color zones.

Diamonds colored by the 480 nm absorption band generally have multiple growth zones with distinct fluorescence colors excited by deep UV (<230 nm), due to their complex multi-stage growth under changing conditions in the earth's mantle (Breeding et al., 2020). This bicolor diamond had alternating blue and greenish yellow fluorescence zones (figure 2), similar to the fluorescence patterns in other diamonds with the 480 nm absorption band. The fluorescence zones did not correlate with the major color zoning (i.e., orangy brown and brown greenish yellow) in this diamond. However, the greenish yellow fluorescence bands (figure 2) appeared to correspond to the narrow bands with darker color in the brown greenish yellow color zone (figure 1).

A cluster of orange mineral inclusions was observed beneath the table facet, where the largest inclusion measured 180 µm in maximum dimension (figure 3). The Raman spectrum of the largest inclusion showed the characteristic peaks of pyrope-almandine-grossular garnet, $(Mg,Fe,Ca)_3Al_2(SiO_4)_3$, at

Editors' note: All items were written by staff members of GIA laboratories.

Gems & Gemology, Vol. 59, No. 4, pp. 486–498.

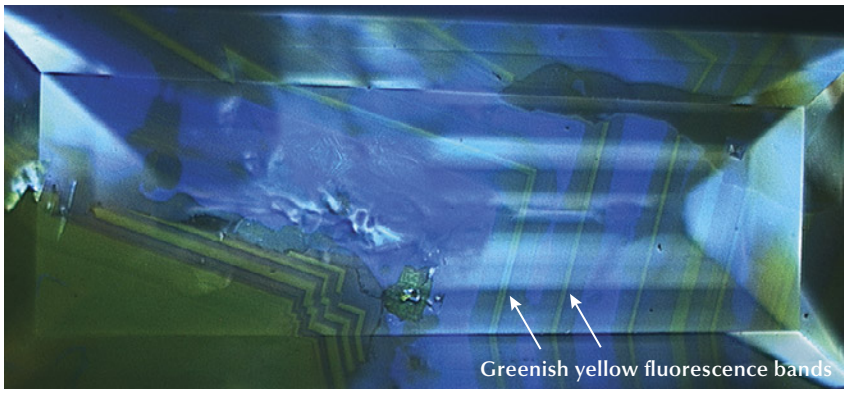

Figure 2. Alternating blue and greenish yellow fluorescence zones were observed with deep-UV excitation. This fluorescence pattern is typical for diamonds colored by the 480 nm visible absorption band.

358, 558, and 917 cm^{-1} (e.g., E.M. Smith et al., "Raman identification of inclusions in diamond," *Reviews in Mineralogy and Geochemistry*, Vol. 88, 2022, pp. 451–473), indicating the diamond was associated with eclogite host rocks having pyrope-almandine-grossular garnet as a major constituent mineral.

This unique bicolor diamond exhibiting two distinctly different colors demonstrates the variety possible within the natural world.

Mei Yan Lai and Sally Eaton-Magaña

Carbon Dioxide in a Brown Diamond

The Carlsbad laboratory recently examined a 1.03 ct natural Fancy Dark brown diamond with uneven color zoning and abundant black inclusions (figure 4). The diamond had infrared absorption features at 2370 and 659 cm^{-1}, corresponding to the asymmetric stretching mode and bending mode of carbon dioxide, respectively (E. Barannik et al., "Shift of CO_2-I absorption bands in diamond: A pressure or compositional effect? A FTIR mapping study," *Diamond and Related Materials*, Vol. 113, 2021, article no. 108280). Diamonds containing carbon dioxide are rarely submitted for diamond grading reports, and this brown diamond is one of the few GIA has encountered. Carbon dioxide likely exists as submicroscopic solid inclusions in natural diamond (M. Schrauder and O. Navon, "Solid carbon dioxide in a natural diamond," *Nature*, Vol. 365, 1993, pp. 42–44). The major infrared absorption peaks observed are shifted from the peak positions of atmospheric carbon dioxide (2350 and 667 cm^{-1}), and the peak shift depends on pressure and the presence of impurities such as water and nitrogen in the trapped carbon dioxide inclusions (Barannik et al., 2021).

Carbonate-related absorptions at 1433 and 870 cm^{-1} were also detected. These absorptions have previously been reported in some natural diamonds containing solid carbon dioxide inclusions (e.g., Summer 2005 Lab Notes, pp. 165–167; Barannik et al., 2021). Clusters of black hexagonal inclusions were observed in the diamond

Figure 3. Multiple orange inclusions were observed in this bicolor diamond. The largest was identified as pyrope-almandine-grossular garnet. Field of view 1.76 mm.

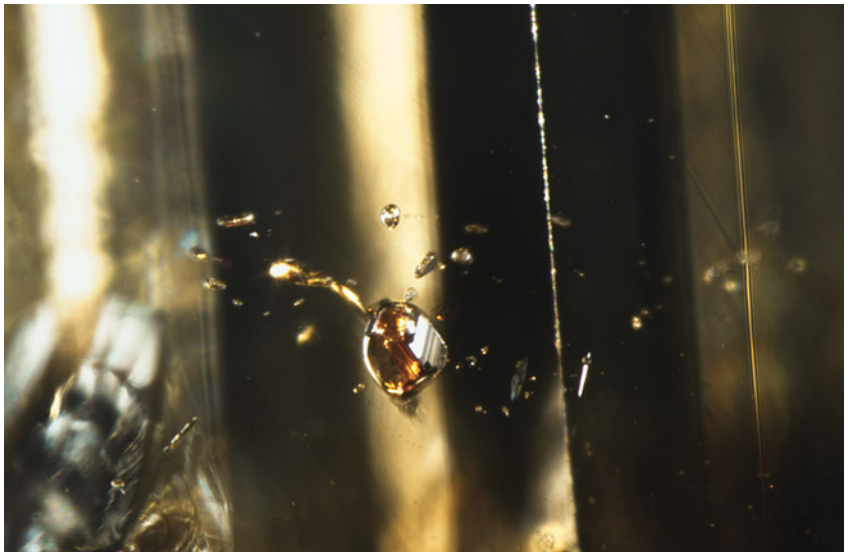

Figure 4. This 1.03 ct natural Fancy Dark brown diamond has uneven color zoning and abundant black inclusions. Infrared absorptions corresponding to carbon dioxide (2370 and 659 cm^{-1}) and carbonate (1433 and 870 cm^{-1}) were detected.

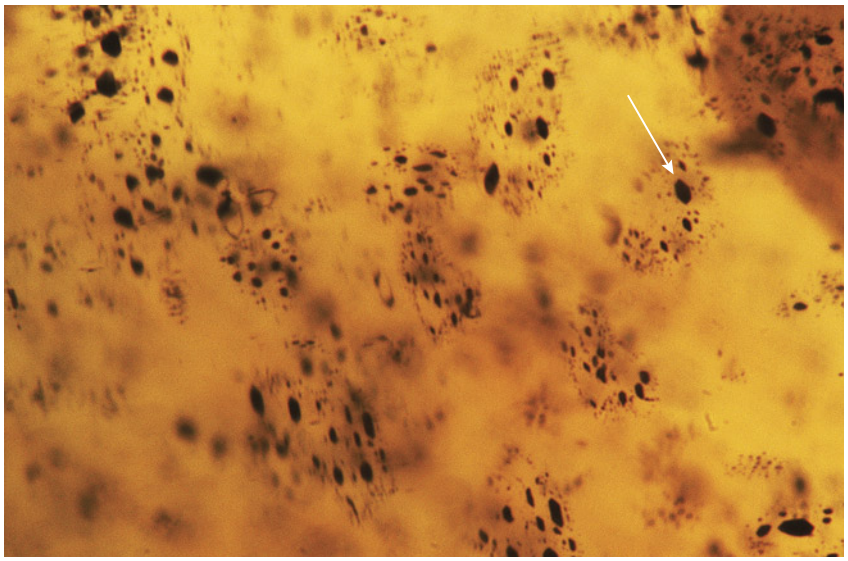

Figure 5. Microscopic examination under high magnification revealed the hexagonal shape of the black inclusions. Field of view 1.26 mm.

(figure 5), and the individual inclusions ranged in size from <1 to ~50 µm. Similar inclusions have been documented in some carbon dioxide–bearing natural diamonds and identified as graphite platelets (A. Shiryaev et al., "Exsolution of oxygen impurity from diamond lattice and formation of pressurized CO_2-I precipitates," *Carbon Trends*, Vol. 11, 2023, article no. 100270).

This brown diamond containing carbon dioxide displayed yellow fluorescence when exposed to long-wave UV. When exposed to deep UV (<230 nm), the diamond exhibited irregular surface fluorescence zoning with yellowish green, bright green, and blue colors caused by distinct lattice defects. The yellow fluorescence to long-wave UV, heterogeneous distribution of lattice defects, and irregular surface fluorescence zoning under deep-UV excitation are commonly observed in diamonds colored by the 480 nm absorption band (known as "480 nm band diamonds" in the trade; C.M. Breeding et al., "Naturally colored yellow and orange gem diamonds: The nitrogen factor," Summer 2020 *G&G*, pp. 194–219). In fact, the photoluminescence (PL) spectra of this brown diamond closely resembled those of 480 nm band diamonds. The most notable PL feature detected was the broad band centered at ~680 nm, which is attributed to the vibronic emission associated with the 480 nm absorption band (A. Collins and K. Mohammed, "Optical studies of vibronic bands in yellow luminescing natural diamonds," *Journal of Physics C: Solid State Physics*, Vol. 15, 1982, pp. 147–158). The similarity in spectroscopic features between carbon dioxide–bearing brown diamonds and 480 nm band diamonds has been previously reported, and a genetic relationship between the two has been suggested (T. Hainschwang et al., "HPHT treatment of CO_2 containing and CO_2-related brown diamonds," *Diamond and Related Materials*, Vol. 17, 2008, pp. 340–351).

Mei Yan Lai and Virginia Schwartz

Cricket Bat Diamond

As early as the seventeenth century, the British introduced the sport of cricket to the Indian subcontinent, where it is now the most popular sport. Recently, a diamond shaped like a cricket bat (figure 6) was submitted to GIA's Mumbai laboratory for testing. In cricket, a bat is a wooden piece of equipment with a long handle attached to a flat-fronted blade, used to hit the ball. This diamond weighed 1.04 ct and measured 14.20 × 4.12 × 2.13 mm. It had a Light brown color. The bat-shaped diamond was partially polished with a rough texture retained on the tip of the handle and the front part of the bat. According to the diamond manufacturer, the original rough skin is intentionally kept in a few parts to authenticate its natural origin.

Based on spectroscopic features, it was confirmed to be type IIa with a very weak peak at 3107 cm^{-1} (hydrogen-related infrared absorption peak). Photoluminescence spectra collected at liquid nitrogen temperature with varying laser excitations revealed its natural origin; no color treatment was detected. A crosshatched "tatami" strain pattern was clearly observed between crossed polarizers when viewed under a microscope.

In photoluminescence spectra collected at room temperature with 405 nm excitation, this diamond also showed the presence of N3, a defect wherein a vacancy is surrounded by three nitrogen atoms.

Figure 6. A 1.04 ct diamond in the shape of a cricket bat, measuring 14.20 mm long.

Figure 7. The cricketer's name and signature inscribed on the diamond.

As shown in figure 7, this special diamond is inscribed with the name and signature of Virat Kohli, who is widely regarded as one of the greatest players in the history of the sport. The owner of the diamond intends to gift it to Kohli.

Manisha Bhoir, Shoko Odake, and Wuyi Wang

Treated HPHT LABORATORY-GROWN DIAMOND with Dramatic Color Zoning

Recently, the Carlsbad laboratory examined a 2.20 ct laboratory-grown diamond that received a color grade of Fancy Deep brownish orange (figure 8). Spectroscopic analysis indicated high-pressure, high-temperature (HPHT) growth methods and subsequent irradiation and annealing to create nitrogen vacancy centers. Infrared absorption spectra collected from the entire stone identified it as type Ib with a concentration of ~5 ppm of single isolated nitrogen. The diamond was distinctive because of a pronounced pink square under the table facet within the cubic {100} sector. The other major growth sectors (e.g., {110}, {111}) surrounding the central cubic sector appeared yellow due to single isolated nitrogen. The pink growth sector displayed pronounced reflections when viewed through the pavilion facets and had more of a purple color (figure 9).

Figure 8. This 2.20 ct Fancy Deep brownish orange treated HPHT-grown diamond owes its distinctive appearance to multiple defect concentrations created within the various growth sectors.

Visible/near-infrared (Vis-NIR) absorption spectra were collected from the center of the table using a reflectance probe positioned to show pink fluorescence. The probe was then repositioned toward the crown facets that did not show pink fluorescence (figure 10). The spectra from both areas indicated type Ib-related absorption at low wavelengths. Additionally, the pink color region was dominated by the NV^- center (zero-phonon line, or ZPL, at 637 nm) and its associated sidebands, while the surrounding yellow regions had minor absorption from NV^0 (ZPL at 575 nm). This difference in NV-related absorption shifts the transmission window from pink to yellow.

The uptake of single nitrogen is generally lower in {100} growth sectors than in {111} sectors (R.C. Burns et al., "Growth-sector dependence of optical features in large synthetic diamonds," *Journal of Crystal Growth*, Vol. 104, 1990, pp. 257–279). However, the concentration of single nitrogen (necessary to ultimately create NV centers) can be increased within the cubic sector through lower growth temperatures (S. Satoh et al., "Differences in nitrogen concentration and aggregation among {111} and {100} growth sectors of large synthetic diamonds," *Science and Technology of New Diamond*, KTK Scientific Publishers/Terra Scientific Publishing Co., Tokyo, 1990, pp. 351–355). It is possible that such growth conditions were used with this diamond in order to incorporate sufficient nitrogen within the cubic sectors, which were subsequently transformed to NV centers with treatment.

Within the cubic sector, photoluminescence (PL) mapping showed a significantly higher concentration of NV^- compared with the other major growth sectors (e.g., {110} and {111}), while the concentration of NV^0 was lower (figure 11). The presence of donors, such as single nitrogen, can often shift the balance between neutral and negative NV centers so that NV^- is enhanced in diamonds with single nitrogen (I.A. Dobrinets et al., *HPHT-Treated Diamonds: Diamonds Forever*, 2013,

Figure 9. The square-shaped cubic {100} growth sector appears pink when viewed through the table (left) and more of a purple color when viewed through the pavilion (right). The surrounding regions appear predominantly yellow due to the presence of single nitrogen. Fields of view 4.23 mm and 4.50 mm.

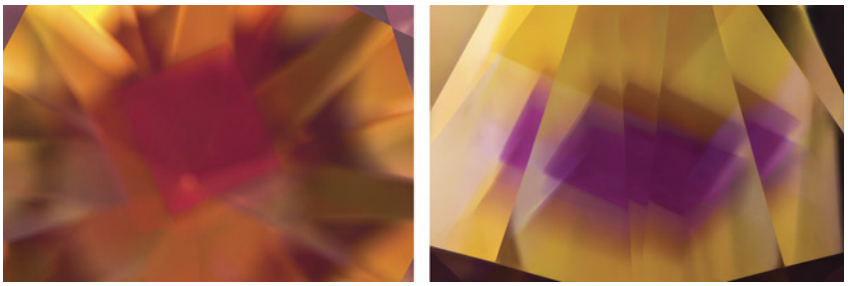

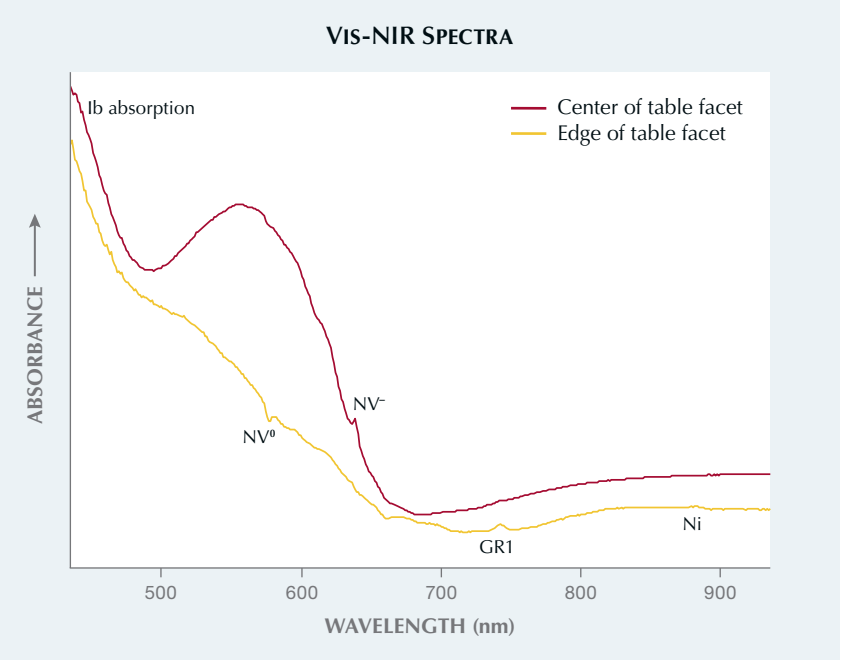

Figure 10. Room-temperature Vis-NIR absorption spectra were collected using a reflectance probe to document the absorption differences between the pink central region and the surrounding areas. The red trace shows a pronounced absorption associated with NV^- along with Ib (i.e., single nitrogen) absorption. The yellow trace also shows Ib absorption along with a minor contribution of NV^0 and small peaks associated with GR1 (741.2 nm) and nickel (883/884 nm). Spectra are offset vertically for clarity.

Springer-Verlag, Berlin). The presence of single nitrogen can be related to an elevated concentration of NV^- within the cubic sector; however, in the {111} sectors, NV^0 dominates over NV^- despite the appreciable concentrations of single nitrogen. This can likely be attributed to the {111} sectors also preferentially incorporating boron. Although boron was not detected within the infrared absorption spectra for this stone, it is often present in HPHT-grown diamond, even at low concentrations. Since boron preferentially incorporates within {111} sectors (U.F.S. D'Haenens-Johansson et al., "Synthesis of diamonds and their identification," *Reviews in Mineralogy and Geochemistry*, Vol. 88, No. 1, 2022, pp. 689–753), these acceptors could shift the charge balance within those areas, thus causing the preferential creation of NV^0 over NV^-.

PL mapping highlighted other pronounced differences between the growth sectors. The GR1 defect (V^0) and TR12, an irradiation-related defect with ZPL at 469.9 nm, was highest in {110} and negligible in {100}. The nickel-related doublet at 883/884 nm was extremely high in {111} and negligible in {110} and {100}.

This HPHT-grown diamond is a notable example of growth techniques and treatment engineering producing a combination of defects that is visually interesting. The faceting approach, in which the pink growth sector was positioned under the table facet, served to enhance the dramatic appearance.

Sally Eaton-Magaña and Taryn Linzmeyer

Figure 11. PL mapping using 532 nm excitation at liquid nitrogen temperature shows pronounced differences in defect concentrations based on growth sector. The NV^- intensity (left, normalized to the diamond Raman line) is highest within {100} and much lower within the other regions. The normalized NV^0 defect intensity (right) was detected throughout the diamond but was noticeably higher within {111} sectors.

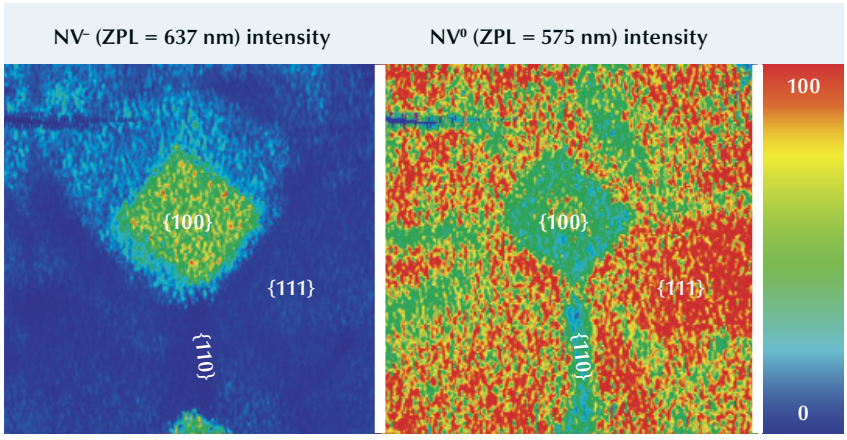

PEARLS

Two Foraminifera-Like Objects Found in a Natural Saltwater Pearl

GIA's Hong Kong laboratory recently received a brown nacreous pearl weighing 1.57 ct and measuring 11.06 × 9.15 × 7.20 mm (figure 12). It had a baroque shape and exhibited a soft luster with an unaltered surface. Despite its size, the pearl felt relatively lightweight, indicating the possibility of a hollow or partially hollow internal structure. Viewed under 40× magnification, the surface displayed overlapping nacre platelets

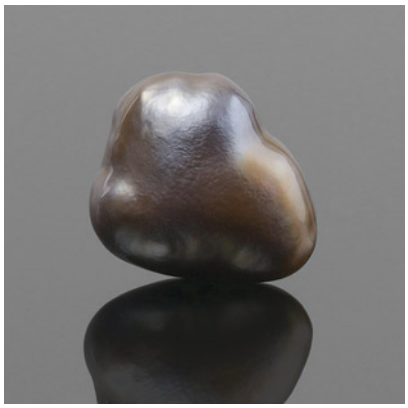

Figure 12. The 1.57 ct brown nacreous pearl measuring 11.06 × 9.15 × 7.20 mm.

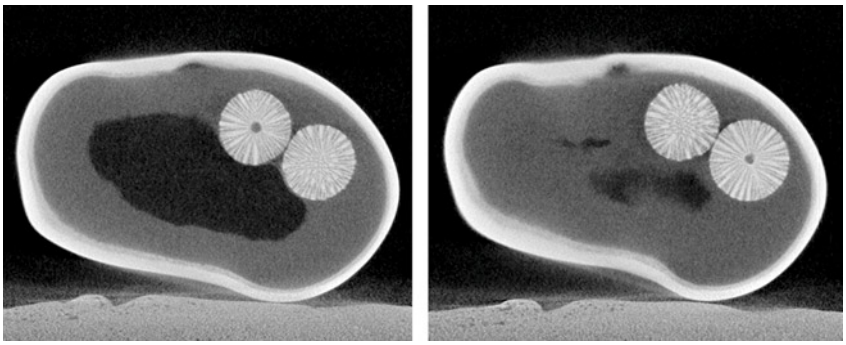

Figure 14. µ-CT images revealed more details of the foraminifera-like spheres. Both consisted of a radiating structure that extended from an empty core.

in a spiral pattern, similar to that observed in pearls produced by *Pteria* species mollusks (L. Kiefert et al., "Cultured pearls from the Gulf of California, Mexico," Spring 2004 *G&G*, pp. 26–39).

The sample exhibited the typical brownish surface tint of pearls produced by the *Pteria* mollusk species. Its ultraviolet/visible spectrum showed the characteristic reflectance features of naturally colored pearls formed in this mollusk, with identifiable absorptions at 405 and 495 nm (S. Karampelas et al., "Spectral differentiation of natural-color saltwater cultured pearls from *Pinctada margaritifera* and *Pteria sterna*," Summer 2011 *G&G*, p. 117). Under long-wave UV radiation, the pearl also displayed moderate red fluorescence, a reaction linked to a type of porphyrin pigment found in pearls originating from the *Pteria* species (Kiefert et al., 2004). Energy-dispersive X-ray fluorescence analysis showed no traces of manganese and 1150 ppm of strontium, confirming its saltwater origin.

Real-time microradiography revealed a fascinating internal structure (figure 13). A large central void, composed of light and dark gray areas associated with the presence of organic matter, occupied almost the entire interior of the pearl, which explained the lighter than expected heft. Surrounding the void, a few distinct growth arcs were observed, following the outline of the pearl's shape—a typical feature seen in natural pearls. In addition, two intriguing foreign materials were trapped within the inner wall of the light gray organic-rich area of the void.

Further analysis via X-ray computed microtomography (µ-CT) imaging revealed the porous nature of these two materials. Resembling foraminifera, a marine micro-skeleton member of a phylum of amoeboid protists, they consisted of radial structures extending from the center of empty cores (figure 14). The pair of near-spherical objects measured 1.50 × 1.25 mm and 1.53 × 1.33 mm, respectively, and appeared to be separate entities while sharing a homogeneous formation. The pearl's structure was judged to be natural due to the appearance of the natural-looking void, which consisted of a flowy outline, and the presence of the foraminifera-like entities. It is worth noting that most cultured pearls from the *Pteria* species available in the market are bead cultured pearls. Non-bead cultured "keshi" *Pteria* pearls are normally of smaller sizes and distinguishable internal structures.

GIA has received numerous pearl submissions in the past with interesting internal structures related to foreign materials. In fact, the skeletal composition of the foreign material observed looked exceedingly similar to that found in a natural pearl examined by GIA's Bangkok laboratory in 2015 (Winter 2015 Lab Notes, pp. 434–435). However, this pearl stands out for the presence of paired foraminifera-like spheres. No two pearls are the same, and it is always rewarding when advanced testing reveals such captivating features.

Cheryl Ying Wai Au

Figure 13. Real-time microradiographs showing the overall internal structure of the pearl (left) and greater detail of the foreign materials (right).

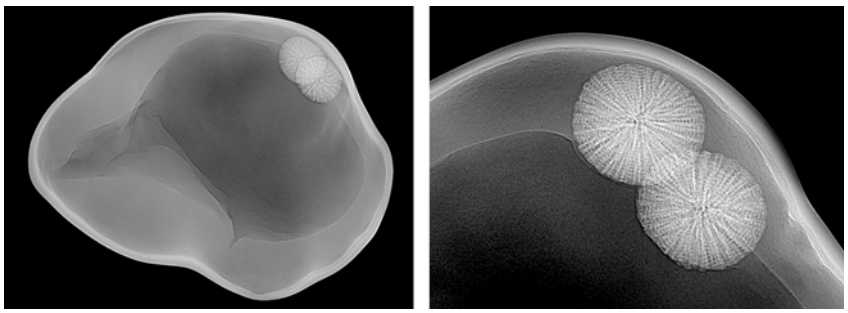

Figure 15. Strands of freshwater bead cultured pearls acquired at the Hong Kong show (top) and freshwater BC pearls submitted for identification (middle) are shown with a strand of 6.60 mm akoya bead cultured pearls (bottom) for comparison.

Small Freshwater Bead Cultured Pearls

Recently, the Carlsbad laboratory received a strand of 78 light bluish gray near-round pearls for identification. The strand (figure 15, middle) weighed 16.75 g (gross), and the pearls measured approximately 5.45 mm in diameter. Upon first impression, they looked like akoya bead cultured (BC) pearls due to their small size and shell bead nuclei observed down the drill holes with a 10× loupe. Their light bluish gray bodycolor also resembled the unprocessed and untreated akoya BC pearls that have become more popular in the market. However, microscopic observation revealed light blue color concentrations under the surface of many pearls (figure 16, left) and blue dye around a surface-reaching feature on one sample (figure 16, right), suggesting that the colors had been artificially modified.

Energy-dispersive X-ray fluorescence chemical analysis showed high levels of manganese, indicating a freshwater origin, as opposed to the saltwater origin of akoya. In 2023, at the AGTA GemFair in Tucson and the Hong Kong International Jewellery show, we saw small near-round to round Chinese freshwater BC pearls around 2–4 mm gaining popularity in the market (Spring 2023 Gem News International, pp. 109–110). These Chinese cultured pearls were available in various colors that were either natural or modified. A strand consisting of 126 small light gray freshwater BC pearls approximately 3.50 mm in diameter (figure 15, top) was acquired at the Hong Kong show to study the internal structures. The light gray bodycolor, likely caused by irradiation considering the dark gray bead nuclei seen in the drill holes, was atypical for natural colored freshwater pearls.

Real-time microradiography (RTX) revealed a distinct bead nucleus in each pearl in both the strand submitted for identification (figure 17, top) and the strand obtained from the Hong Kong show (figure 17, bottom), confirming they were bead cultured. All the pearls displayed relatively thick nacre, averaging about 1 mm for the larger strand and 0.8 mm for the smaller strand. The bead nuclei measured approximately 3.5 mm and 2.7 mm in diameter, respectively.

Although this type of small freshwater BC pearl is generally smaller than typical akoya BC pearls, there are

Figure 16. Left: Multiple blue color concentrations under the surface of one pearl; field of view 19.27 mm. Right: Blue dye concentration inside a fracture; field of view 2.34 mm.

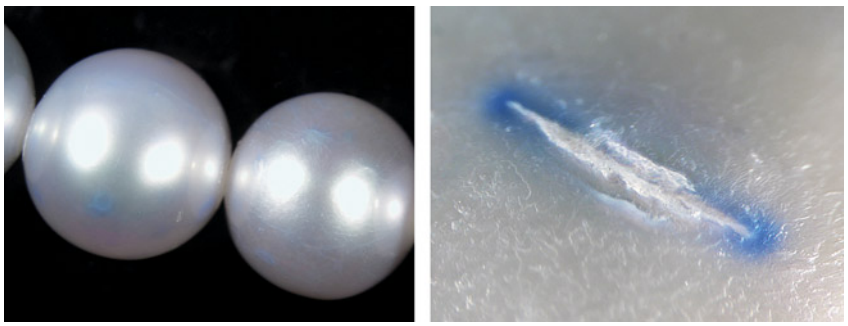

Figure 17. RTX image of freshwater BC pearls. The top strand, submitted for identification, has an average nacre thickness of 1 mm and an average bead diameter of 3.5 mm. The bottom strand, from the Hong Kong show, has an average nacre thickness of 0.8 mm and an average bead diameter of 2.7 mm.

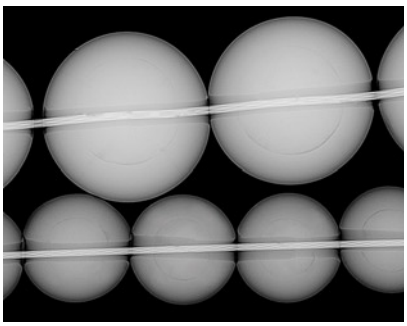

also very small akoya BC pearls below 3 mm in the market (Spring 2018 Gem News International, pp. 103–105). Due to the popularity of very small round BC pearls, the size range of these types of freshwater and akoya pearls can be very similar. It could be difficult to separate them through visual inspection, and more advanced methods are likely needed to verify the environmental origin. The slightly flat surface feature previously encountered on white freshwater BC pearls was not present on the samples studied here (Spring 2023 Gem News International, pp. 109–110). Moreover, our freshwater BC pearl samples showed thicker nacre compared with the very small akoya pearls previously reported, with a nacre that was above the usual commercially accepted range (0.15–0.50 mm) for akoya.

Chinese freshwater cultured pearls are widely available in various sizes, shapes, colors, and qualities and have become a major part of the global market. This was GIA's first examination of such small freshwater BC pearls, demonstrating the versatility of Chinese freshwater culturing methods in adapting to consumer demands.

Amiroh Steen, Joyce Wing Yan Ho, and Artitaya Homkrajae

Unusual Large Nacreous Pen Pearls

GIA's Mumbai laboratory has received a wide variety of interesting pearls for identification since opening its pearl testing department in May 2022. One recent submission included three baroque pearls weighing 24.47 ct, 36.58 ct, and 36.70 ct and measuring 28.22 × 18.04 × 9.84 mm, 28.79 × 19.48 × 10.40 mm, and 32.49 × 20.50 × 18.35 mm, respectively (figure 18).

Visual observation revealed a combination of nacreous and non-nacreous surface structures. The pearls were white to light gray and brown and exhibited a strong orient with variations in saturation and tone. In some areas, their surface quality was poor to slightly damaged. Viewed under 40× magnification, the white to light gray areas displayed a striated and much finer form of nacre growth structure than observed in most nacreous pearls from *Pinctada* and *Pteria* mollusks (figure 19, left). The dark brown areas showed a characteristic non-nacreous cellular structure consisting of a network of closely packed cells (figure 19, right). These observations were consistent with previous studies (N. Sturman et al., "Observations on pearls reportedly from the Pinnidae family (pen pearls)," Fall 2014 *G&G*, pp. 202–215).

Figure 18. Left to right: Three large nacreous pearls weighing 24.47 ct (pearl 1), 36.58 ct (pearl 2), and 36.70 ct (pearl 3).

Raman analysis using a 514 nm and 830 nm laser excitation was performed on different surface areas. The nacreous areas on all three pearls showed a doublet at 701 and 704 cm^{-1} and a peak at 1085 cm^{-1} indicative of aragonite. However, the brown non-nacreous areas on pearls 1 and 2 showed a peak at 712 cm^{-1} indicative of calcite. Photoluminescence analysis for all pearls revealed weak bands at 620, 650, and 680 nm, suggesting natural coloration (S. Karampelas et al., "Raman spectroscopy of natural and cultured pearls and pearl producing mollusc shells," *Journal of Raman Spectroscopy*, Vol. 51, No. 9, 2020, pp. 1–9).

Despite the possibility of these three being large blister pearls, closer examination of them did not reveal any indications of previous attach-

Figure 19. Features characteristic of pen pearls shown on pearl 1. Left: Striated nacre on the white and light gray areas; field of view 3 mm. Right: Non-nacreous structure consisting of a network of cells observed on the dark brown region; field of view 1.3 mm.

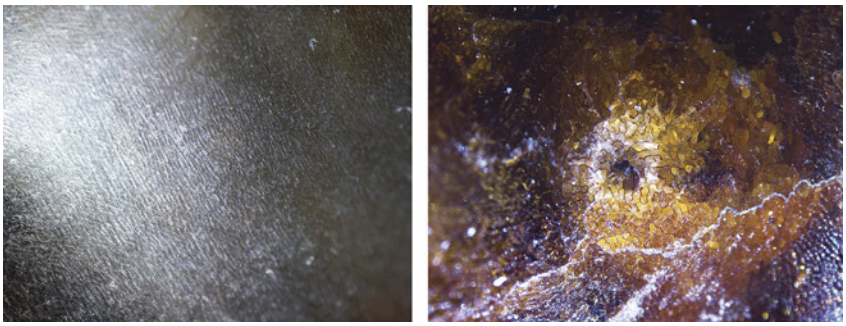

ment to the shell such as signs of heavily worked or sawn areas ("Natural shell blisters and blister pearls: What's the difference?" *GIA Research News*, August 26, 2019). The lack of such features indicated they were whole pearls. The few small organic-rich areas visible on the pearls' surfaces (figure 20), along with the non-nacreous and nacreous surfaces, were possibly damaged because the organic-rich material weakened over time.

X-ray fluorescence analysis revealed an inert reaction for all the samples. Energy-dispersive X-ray fluorescence spectrometry showed very low manganese levels (below detection limit in both pearls 1 and 2 and 9.9 ppm in pearl 3) and high strontium levels (1535 ppm, 1682 ppm, and 1250 ppm, respectively). Both analytical results were indicative of a saltwater origin.

Real-time microradiography (RTX) and X-ray computed microtomography (μ-CT) revealed a combination of large voids with some dark organic-rich material surrounded by white walls and fine growth arcs (figure 20). A chambered effect was notable in all three samples. The complex appearance of the voids differed from those observed in most non-bead cultured pearls from the *Pinctada* species, yet they were similar to nacreous and non-nacreous pen pearls reported in Sturman et al. (2014). The outline of the voids was consistent and followed the shape of the pearls' surfaces, unlike the irregular and inconsistent voids found in the non-bead cultured pearls. In addition, μ-CT imaging revealed light gray and dark gray areas associated with the presence of organic matter within the voids, a characteristic commonly observed in natural pearls ("Non-bead cultured pearls from *Pinctada margaritifera*," *GIA Research News*, April 27, 2018).

Based on the external and internal structure analysis, the samples were identified as natural pearls from the *Pinnidae* family (pen pearls). Visual observation, combined with the absence of any evidence of commercial culturing, played a crucial role in their identification. Their size and appearance further supported their classification as natural whole pearls.

Karan Rajguru, Abeer Al-Alawi, and Roxane Bhot Jain

Figure 20. RTX images, μ-CT images, and photomicrographs of the three pearls. The dark organic-rich voids are marked with red arrows, and the external weakened organic-rich areas on the surface are marked with blue arrows. Fields of view 9 mm (pearl 1) and 16.3 mm (pearls 2 and 3).

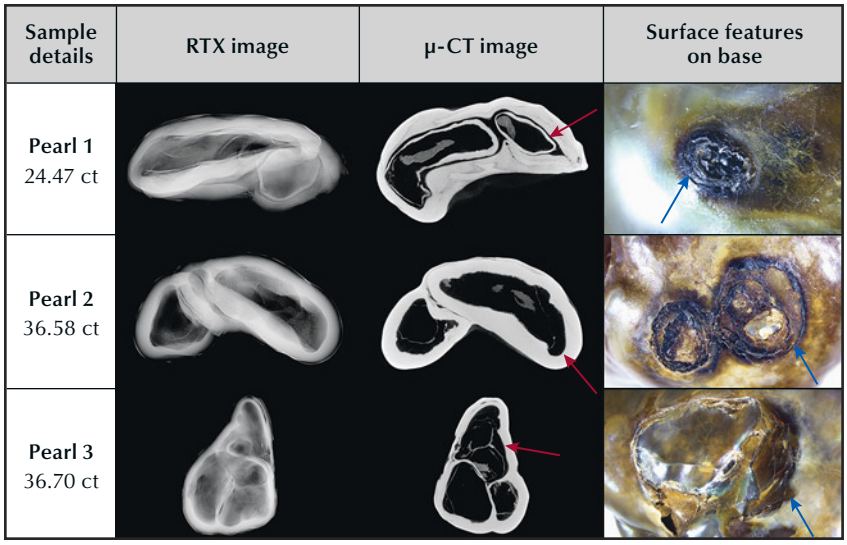

Seed Pearls in an Antique Indian-Style Headdress

Identification of seed pearls often poses a challenge to gemologists. Seed pearls are typically smaller than 3 mm and can be of either saltwater or freshwater origin (*The Pearl Blue Book*, CIBJO, 2022). These tiny pearls have long been used for adornment on clothing, jewelry, and various decorative items.

Recently, GIA's Mumbai laboratory examined an antique headdress (figure 21) submitted for pearl identification service. The exquisite headdress, which according to the client dates back several decades, featured intricate embroidery on a red velvet base. It incorporated approximately 7,000 light cream and cream-colored pearls, most of which displayed a strong orient. These pearls, ranging from semi-baroque to baroque in shape, were meticulously hand-woven onto the headdress using white silk thread and further secured by a surrounding framework of twisted white metal wire. The headdress itself weighed 240 g, and most of the pearls measured around 2.10 mm, with some larger ones reaching up to 3.40 mm.

Under a 10× loupe, some of the pearls displayed slight wear around the drill hole, while maintaining an overall intact nacre condition with a medium to high surface luster. The pearls embroidered on top of the headdress displayed nacreous overlapping aragonite platelets (platy structure) patterns, which are typically observed in pearls from a saltwater environment. Those on the side portion exhibited slightly broader platy patterns, which are common in freshwater pearls. Under long-wave ultraviolet radiation (figure 22, top), most of the pearl samples showed weak greenish yellow fluorescence, with a small percentage showing yellowish brown. A similar weaker reaction was observed under short-wave ultraviolet radiation (not shown).

When exposed to X-ray fluorescence, the pearls on top of the headdress were inert, indicating their

Figure 21. This antique Indian-style headdress is decorated with hand-woven light cream and cream-colored seed pearls.

saltwater origin. In contrast, the pearls on the side portion showed a strong yellowish green fluorescence due to high manganese contents, indicating a freshwater origin (figure 22, bottom). Interestingly, some freshwater pearls also displayed an orangy red fluorescence, suggesting the presence of vaterite, a less commonly observed form of calcium carbonate ($CaCO_3$) compared to aragonite or calcite (Winter 2021 Lab Notes, pp. 377–378). Due to the size and delicate nature of the headdress, further analysis of chemical composition using energy-dispersive X-ray fluorescence spectrometry was not feasible.

To study the internal structures, the authors performed random sampling using real-time microradiography (RTX) imaging (figure 23). Internally, most of the saltwater pearls exhibited small organic-rich cores with fine growth arcs, while other samples displayed tight to minimal structures with a few fine growth arcs toward the outer nacre. These internal structures were similar to those observed in natural pearls from the *Pinctada* species. Similarly, the freshwater pearls displayed natural structures with growth arcs throughout the pearl, consistent with natural freshwater pearls from GIA's research database (Summer 2021 Gem News International, pp. 167–171). Twisted linear structures or voids, which are commonly found in non-bead cultured Chinese freshwater pearls, were also observed in a minority of the tested samples (K. Scarratt et al., "Characteristics of nuclei in Chinese freshwater cultured pearls," Spring 2000 *G&G*, pp. 98–109).

Although the identification of seed pearls has always presented challenges and limitations, advancements in equipment and instrumentation available at GIA laboratories enable the detailed analysis of even the most minute structures and features in pearls, whether natural or cultured.

Roxane Bhot Jain, Jayesh Surve, Abeer Al-Alawi, and Chunhui Zhou

Figure 22. Top: Long-wave ultraviolet reaction displaying a greenish yellow reaction and an occasional yellowish brown reaction. Bottom: Freshwater pearls emitting a strong yellowish green XRF reaction; some orangy red fluorescence suggesting vaterite.

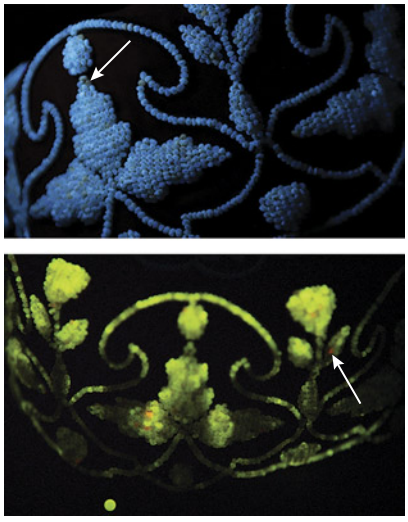

Figure 23. Left: RTX image of pearls from the top portion of the headdress (saltwater environment). Right: RTX image of pearls from the side portion (freshwater environment).

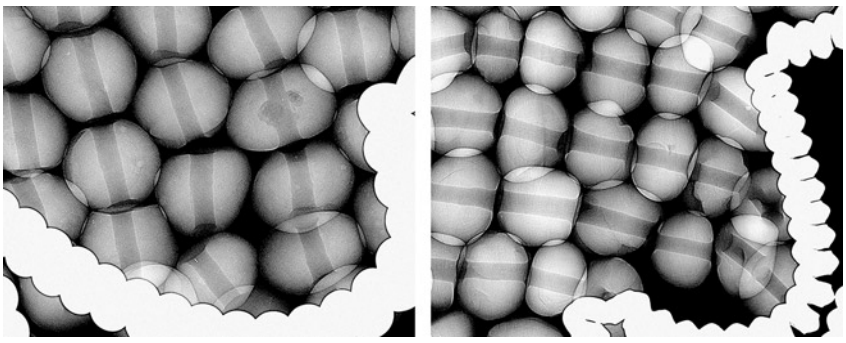

Figure 24. This 1.27 ct white semi-baroque pearl exhibited a typical platy structure when examined under magnification.

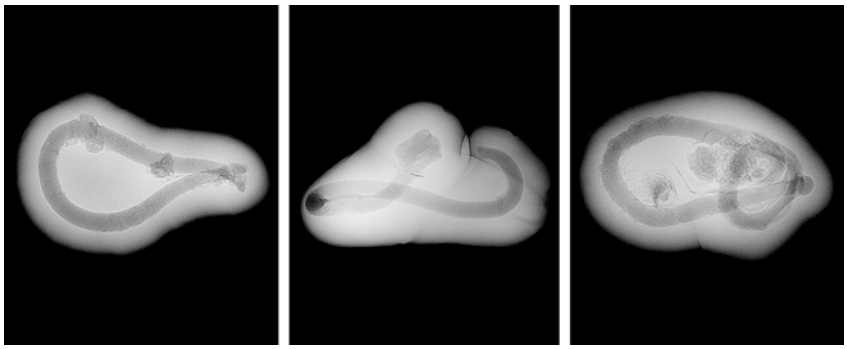

Figure 26. Similar tubular features observed in three reportedly natural saltwater pearls weighing 0.25, 0.34, and 0.44 ct, respectively, sourced from Pinctada radiata *mollusks from the waters of Bahrain.*

Tubular Feature in a Natural Pearl

Recently, GIA's Bangkok laboratory received a 1.27 ct white semi-baroque pearl for pearl identification service (figure 24). Under 40× magnification, the surface exhibited typical nacreous overlapping aragonite platelets (platy structure).

Real-time microradiography (RTX) revealed a tubular feature like a twisted tunnel at the center of the pearl, surrounded by fine growth arcs. When observed along the pearl's thickest direction, the feature resembled a void or cavity-like structure (figure 25, left), similar to those found in non-bead cultured pearls ("The microradiographic structures of non-bead cultured pearls," *GIA Research News*, November 20, 2009). However, when viewed from its flat direction (figure 25, center), the elongated tubular nature of the feature was inconsistent with the voids observed in non-bead cultured pearls. This inconsistency was further supported by X-ray computed microtomography (μ-CT), which showed multiple interconnected rounded voids (figure 25, right). When exposed to X-ray fluorescence, the pearl displayed an inert reaction indicative of a saltwater environment.

While this was the first time the lab had encountered a client submission with such a structure, similar structures were previously documented in three reference pearl samples from GIA's research database. The three were reported to be natural *Pinctada radiata* pearls sourced from the waters of Bahrain; they were baroque and weighed 0.25, 0.34, and 0.44 ct (figure 26). Those samples showed a similar elongated twisted tubular feature at their center in RTX and μ-CT scan imaging, which helped confirm the natural origin of the examined pearl.

To further study this tubular feature, three-dimensional models were created using specialized software to render the μ-CT scan images ("New 3-D software expands GIA's pearl identification capabilities," *GIA Research News*, May 13, 2016). The results from these models clearly showed that the central structure consisted of an elongated twisted tube. Based on the tubular formation presented, the feature is suspected to be formed by a burrowing parasite trapped in the center of the pearl (figure 27; see video of the 3D model at www.gia.edu/gems-gemology/winter-2023-lab-notes-tubular-feature-natural-pearl). Parasites of various types have been observed in both saltwater and freshwater bivalves, and certain worms have been known to use bivalve mollusks as their hosts. Notably, marine bivalve mollusks tend to be more prone to parasitic intrusions than freshwater mussels (E. Strack, *Pearls*, Rühle-Diebener-Verlag, Stuttgart, 2006, p. 116). Therefore, the presence of such tubular features in saltwater pearls indicates the potential

Figure 25. Left: RTX image taken along the pearl's thickest direction showing a stacked internal structure that could be misinterpreted as a void typically observed in non-bead cultured pearls. Center: RTX image from the flat direction revealing a tubular feature in the center. Right: μ-CT image revealing multiple interconnected rounded voids.

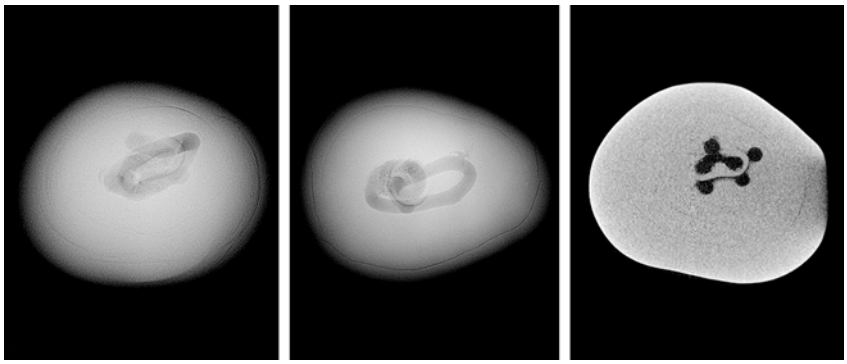

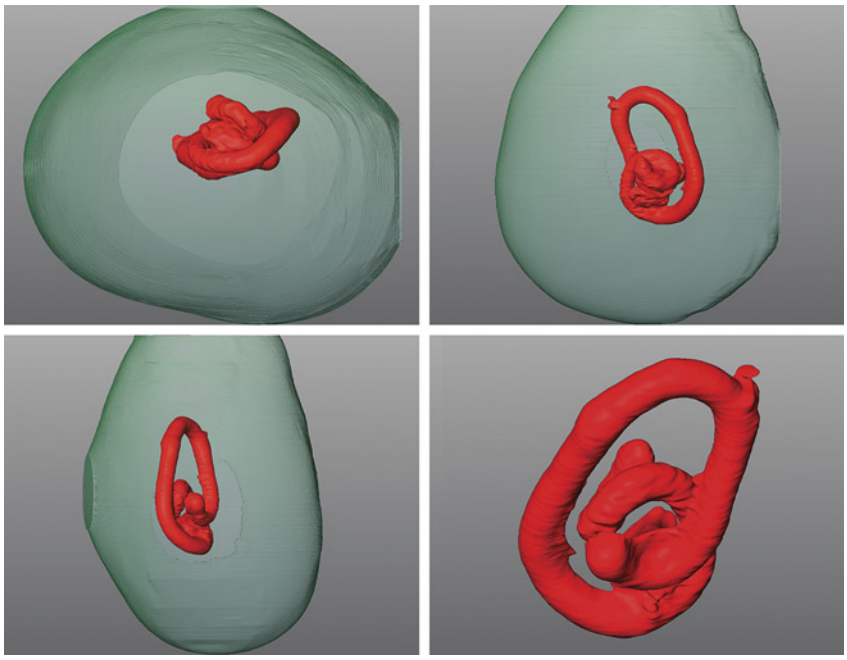

Figure 27. The 3D models generated using µ-CT scans revealed the tunnel-like feature (red) suspected of being parasite remnants or evidence of parasitic activity within the pearl.

infiltration of worm larvae into the mollusks' mantle. These larvae—either dead, alive, or hibernating—may have subsequently become encapsulated by the mantle epithelial cells, leading to the formation of a pearl sac and eventually the creation of a pearl.

Ravenya Atchalak and Emiko Yazawa

A Remarkable 16.71 ct Transparent Orange-Yellow SODALITE

GIA's Bangkok laboratory recently examined the 16.71 ct transparent orange-yellow faceted oval shown in figure 28. Standard gemological testing revealed the stone to be singly refractive with a refractive index of 1.484 and a hydrostatic specific gravity of 2.28. The stone showed strong orange fluorescence under long-wave ultraviolet light and weak orange with chalky white fluorescence under short-wave UV. Microscopic examination revealed internal features such as a fingerprint-like plane of two-phase fluid inclusions and numerous tiny transparent crystals. Raman spectroscopy analysis using 514 nm laser excitation showed several distinct peaks at 263, 294, 464, 969, 986, and 1058 cm^{-1}, which are characteristic features of sodalite (B. Lafuente et al., 2015, http://rruff.info/about/downloads/HMC1-30.pdf). Energy-dispersive X-ray fluorescence also identified the main chemical composition as sodium, aluminum, silicon, and chlorine, consistent with sodalite, which falls into the feldspathoid mineral group $Na_8(Al_6Si_6O_{24})Cl_2$.

Figure 28. A 16.71 ct transparent orange-yellow oval sodalite measuring 17.61 × 15.74 × 12.88 mm.

Sodalite is typically a semitransparent to opaque blue stone with calcite veining resembling lapis lazuli. However, it can occasionally exhibit other colors. The orange-yellow variety of sodalite is rare, and its color may be related to the presence of sulfide ions (F. Seel, "Sulfur in artwork: Lapis lazuli and ultramarine pigments," *Studies in Inorganic Chemistry*, Vol. 5, 1984, pp. 67–89). Ultraviolet/visible spectroscopy showed an absorption band centered at approximately 480 nm, likely caused by heavy radioactive elements creating an unstable color center substituting for Cl^- in a tetrahedron of Na^+ ions (H. Annerstein and A. Hassib, "Blue sodalite," *Canadian Mineralogist*, Vol. 17, 1979, pp. 39–46; P.S. Pizani et al., "Color centers in sodalite," *American Mineralogist*, Vol. 70, 1985, pp. 1186–1192). This sodalite is exceptional for its color, transparency, and 16.71 ct size. To the author's knowledge, this is GIA's first encounter with a large faceted orange-yellow sodalite.

Narint Jaisanit

Rare Faceted THOMSONITE

The Carlsbad laboratory recently examined a colorless semitransparent 1.04 ct oval modified brilliant (figure 29). Standard gemological testing gave a specific gravity (SG) of 2.47 and a refractive index of 1.520–1.538. These properties suggested the stone was a rare faceted thomsonite, which was confirmed by Raman spectroscopy. There are two types of thomsonite: the more common thomsonite-Ca with the chemical formula $NaCa_2Al_5Si_5O_{20} \cdot 6(H_2O)$ and the less common thomsonite-Sr with the chemical formula of $Sr_{1.4}Ca_{0.6}NaAl_5Si_5O_{20} \cdot 7.1(H_2O)$. X-ray fluorescence was not run on this stone to determine which, for fear of damag-

Figure 29. A rare 1.04 ct semitransparent thomsonite measuring 7.53 × 6.15 × 4.67 mm. The inset shows the typical appearance of thomsonite.

ing the potentially fragile stone. The SG reading was slightly higher than the expected value of 2.35 (+0.05/–0.10). Multiple surface scratches and abrasions indicated a relatively soft material, consistent with thomsonite's hardness of 5.0–5.5 on the Mohs scale. This specimen featured a radiating fibrous inclusion resembling a snowflake (figure 30). Although the identity of the inclusion could not be confirmed with Raman spectroscopy, it was likely a member of the zeolite group.

Thomsonite is a rare member of the zeolite group named for Scottish chemist and mineralogist Thomas Thomson (1773–1852). While the source of this specimen is unknown, thomsonite is typically found in Minnesota along Lake Superior. It usually occurs as semitranslucent to opaque rounded crystal aggregates (figure 29, inset) with a fibrous structure. Thomsonite has also been known to appear as part of a rock aggregate (B.M. Laurs et al., "Benitoite from the New Idria District, San Benito, County, California," Fall 1997 *G&G*, figure 13) or as rare needle inclusions in Canadian sapphires (Winter 2004 Gem News International, pp. 344–345). Semitransparent and faceted thomsonite is very unusual. To the best of our knowledge, this is the first faceted thomsonite examined by GIA.

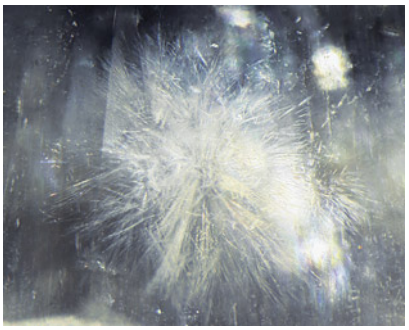

Figure 30. A fibrous snowflake-like inclusion found within the semitransparent thomsonite. Field of view 3.57 mm.

Michaela Damba

PHOTO CREDITS
Adriana Robinson—1, 15, 29; Stephanie Shaw—2; Mei Yan Lai—3–5; Priyanka Kadam—6; Diego Sanchez—8; Nathan Renfro—9; Tony Leung—12; Artitaya Homkrajae—16; Joyce Wing Yan Ho—17; Gaurav Bera—18, 21; Karan Rajguru—19, 20; Lhapsin Nillapat—24, 28; Scott Lewis—29 (inset); Michaela Damba—30

The Science of Colored Stone Identification and Origin.

GIA

GIA research and reports are the benchmark of colored stone analysis. Those who buy, sell, or curate the world's most important gems rely on GIA's expertise, precision, objectivity, and integrity.

Learn more.

GIA.edu/ColoredStones

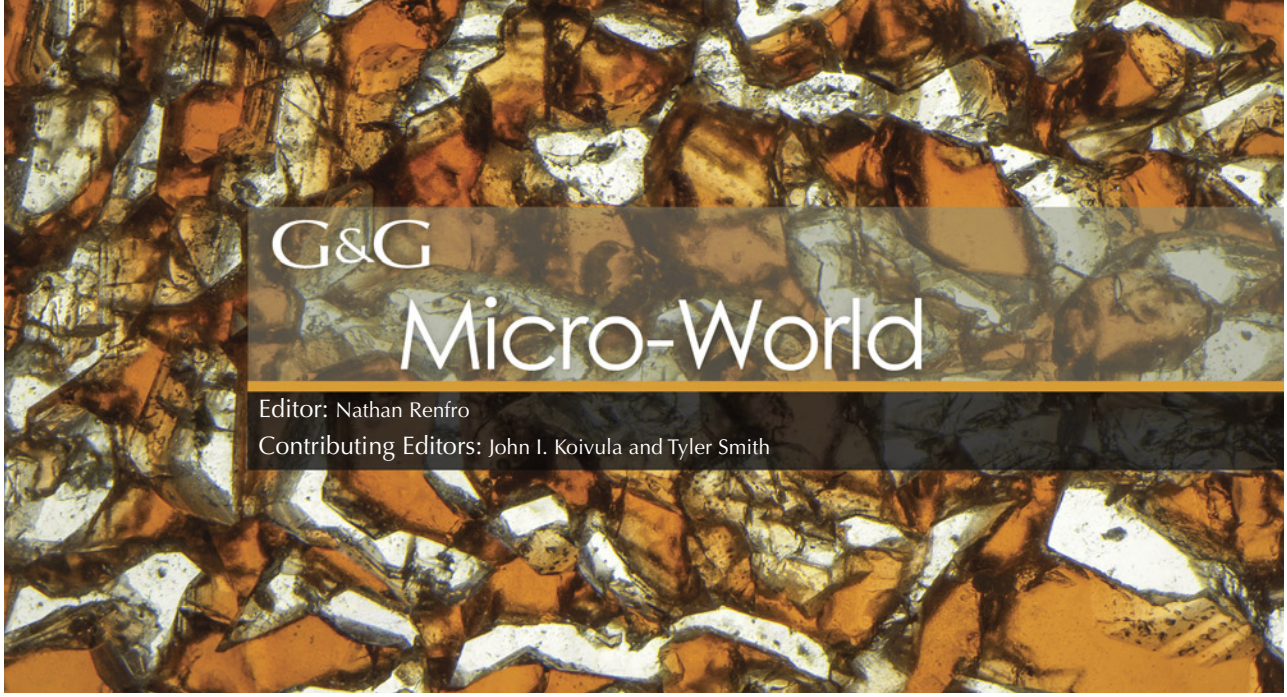

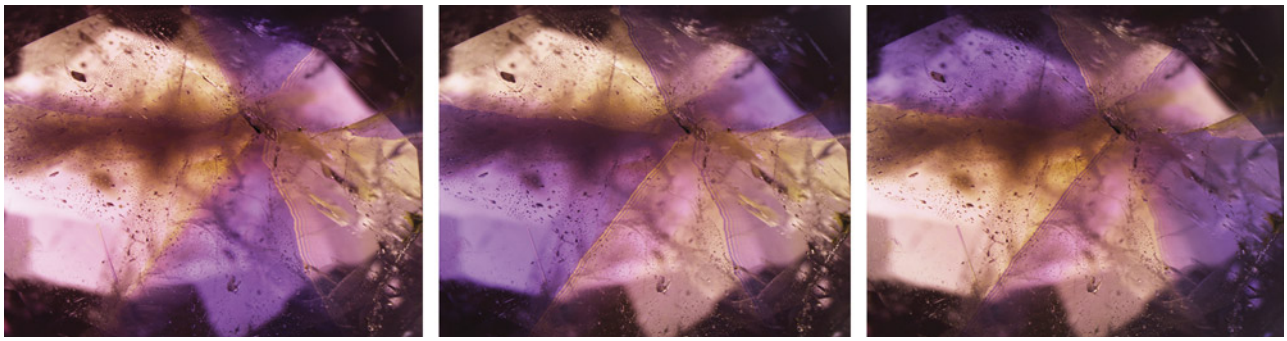

Figure 1. This 0.69 ct alexandrite showed a stellate structure due to cyclic crystal twinning and pleochroism, producing a kaleidoscope effect when rotated. These photomicrographs were taken with a single polarizer placed above the stone and a white diffuser below the stone to highlight the color. Photomicrographs by Makoto Miura; field of view 9.80 mm.

"Kaleidoscope" in Alexandrite

Recently, the author examined an interesting 0.69 ct alexandrite measuring 6.22 × 5.21 × 2.51 mm. This stone displayed a color change from greenish blue in fluorescent light to purple in incandescent light. Its trace element chemistry along with the presence of characteristic inclusions suggested a Russian origin.

Under the microscope, this alexandrite showed a unique stellate structure that was divided into six sections of purple, pink, and yellow color. Chrysoberyl occasionally shows a stellate structure due to cyclic crystal twinning (trilling), with triplets oriented at 120° to one another (e.g., K. Schmetzer, *Russian Alexandrites*, Schweizerbart Science Publishers, Stuttgart, Germany, 2010). Each section showed a different face-up color, and the colors were changed by rotating the stone. This observation suggested that the stone was cut from a cyclic twin rough crystal and the various colors were due to pleochroism, not color zoning. When rotating a single polarizer between the stone and objective lens (analyzer), opposite areas showed the same pleochroic colors (figure 1). This feature indicated that the alexandrite consisted of three penetration twins (again, see Schmetzer, 2010). The unique pleochroic colors caused by cyclic twinning were reminiscent of a kaleidoscope.

Makoto Miura
GIA, Tokyo

About the banner: The component minerals of this rock crystal quartz and spessartine garnet rock have intergrown, resulting in a rare graphic texture. Photomicrograph by Nathan Renfro; field of view 19.12 mm. Courtesy of the John Koivula inclusion collection.

Gems & Gemology, Vol. 59, No. 4, pp. 500–509.

"Sun Spangle" in Amber

Fractures often diminish a gemstone's beauty and appeal. To reduce the detrimental effects caused by fractures and to enhance appearance, many gemstones undergo treatment. But not all fractures are undesirable. One such example is the circular stress fracture in amber (figure 2) recently encountered by the author.

Minute gas bubbles in amber cause cloudiness, which can be removed by heating the material. If the amber cools too rapidly, it may develop internal circular stress cracks called "sun spangles." Sun spangles are considered desirable and are often created deliberately, such as the attractive example shown here. The concept can be likened to the Japanese art of *kintsukuroi* or *kintsugi*, in which broken pottery is repaired with gold undisguised, embracing the piece as more beautiful for having been broken.

Aamir Sayed
Al Zain Jewellery, Manama, Bahrain

Distinctive Feather in Diamond

Recently, the authors examined a 0.30 ct type Ia diamond with D color and I_1 clarity. The diamond displayed a grade-setting feather resembling an alligator (figure 3), which was best observed through the pavilion facets. This unusual clarity characteristic is a charming find that adds distinction to this colorless diamond.

Bhavya Maniar
GIA, Surat

Sally Eaton-Magaña
GIA, Carlsbad

Figure 3. A feather in a 0.30 ct diamond with I_1 clarity resembled an alligator. Photomicrograph by Raju Jain; field of view ~3 mm.

Exquisite Butterfly in Diamond

Examination of a 1.01 ct triangular portrait-cut diamond with E color and I_2 clarity revealed an inclusion in the center of the table resembling a butterfly (figure 4; see video at www.gia.edu/gems-gemology/winter-2023-micro-world-butterfly-in-diamond). The butterfly inclusion was composed of a crystal with a stress halo. The crystal did not break the surface and was completely enclosed within the diamond. The rough was skillfully cut in such a way that this crystal was positioned on the center of the table when polished. The play of light reflects artistically on the stress halo, creating the appearance of a colorful butterfly.

Tejas Jhaveri
GIA, Mumbai

Figure 2. A "sun spangle" created in amber as a result of rapid cooling. Photomicrograph by Aamir Sayed; field of view 1.5 mm.

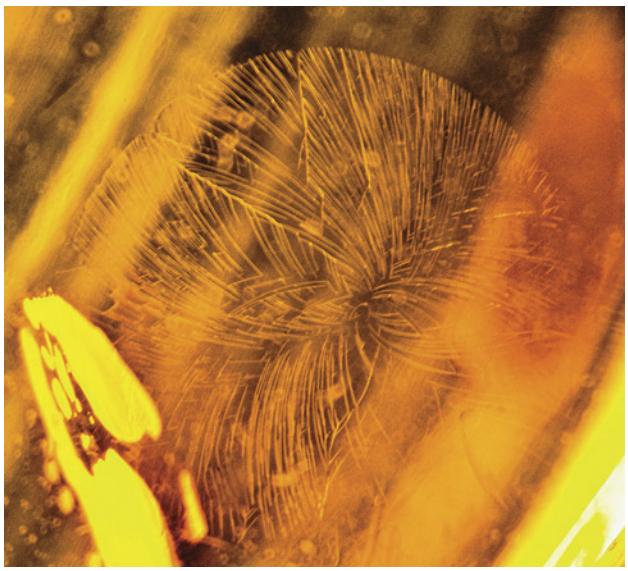

Figure 4. When light reflects from this crystal in a 1.01 ct diamond, the halo resembles a colorful butterfly. Photomicrograph by Tejas Jhaveri; field of view 2.90 mm.

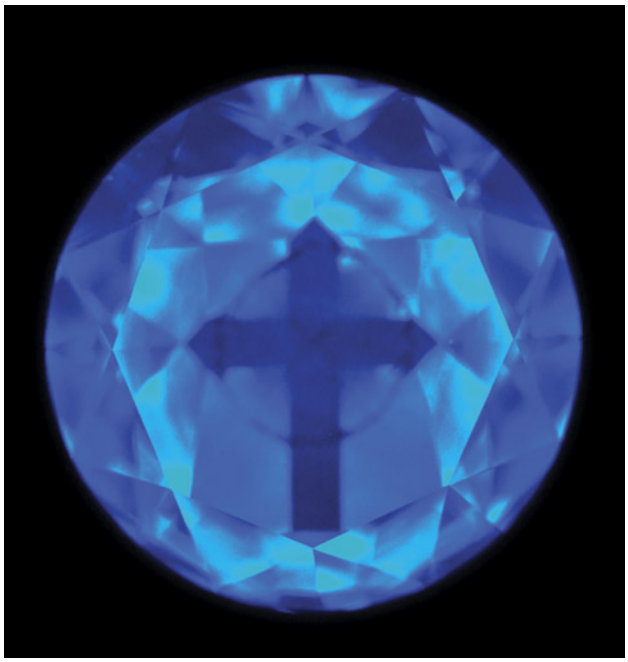

Figure 5. A cross pattern observed in this DiamondView image of a 0.31 ct D-color type IIa diamond. Image by Priyanka Kadam.

Cross in Natural Diamond

DiamondView imaging of the 0.31 ct D-color type IIa modified round brilliant diamond shown in figure 5 revealed an interesting fluorescence pattern. The image displayed blue fluorescence as well as a darker pattern in the shape of a cross. One of the pavilion main facets was longer than the other three, producing this distinct cross pattern when the diamond was viewed through the table. Depending on the specific angle of the pavilion main facets, such a distinct pattern might not be visible in the DiamondView.

Priyanka Kadam
GIA, Mumbai

Shoko Odake
GIA, Tokyo

Spotted Diamond

The author recently examined a large 3.05 ct Fancy Light gray diamond featuring dark crystals scattered throughout (figure 6). It had a clarity of I_3, the lowest grade for gem-quality diamond, but demonstrated that low-clarity diamonds can sometimes be more intriguing than their higher-clarity cousins. Stones with numerous eye-visible crystal inclusions such as this are sometimes referred to in the trade as "salt and pepper" diamonds.

Numerous attempts to identify the dark crystals using Raman spectroscopy proved unsuccessful. X-ray fluorescence revealed high levels of iron, leading the author to conclude that they were likely metal sulfides rather than graphite. This presumption has not been confirmed with Raman spectroscopy.

Michaela Damba
GIA, Carlsbad

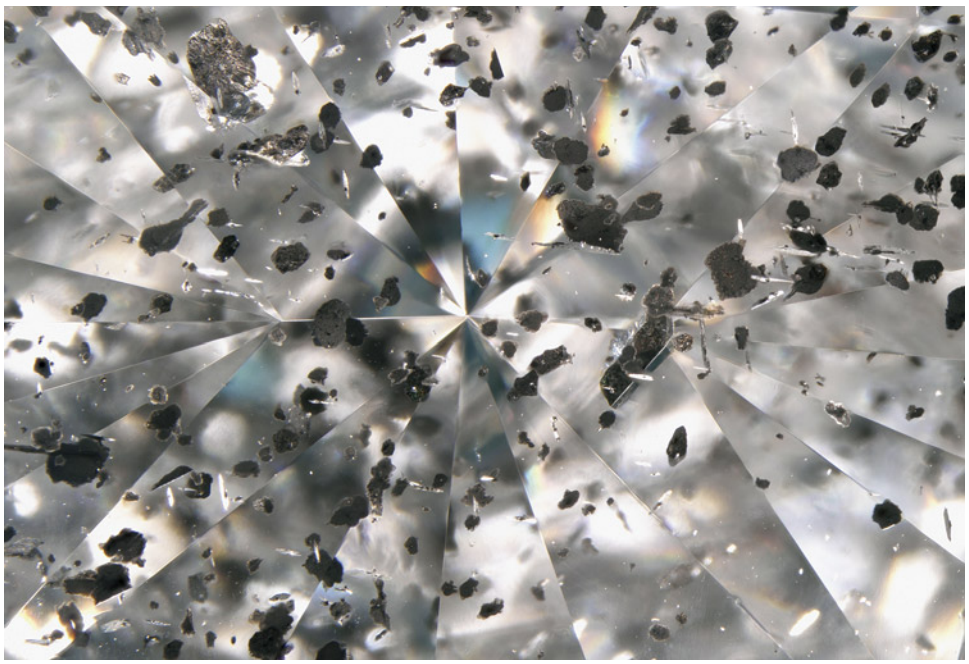

Figure 6. Numerous metal sulfide crystals scattered throughout a 3.05 ct Fancy Light gray diamond. Photomicrograph by Michaela Damba; field of view 14.52 mm.

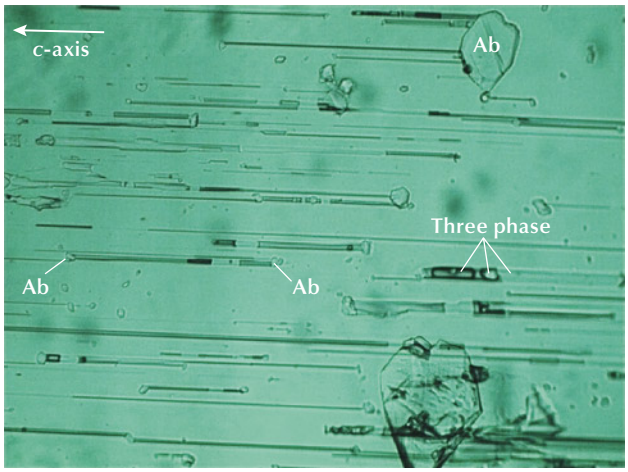

Figure 7. Tubular three-phase inclusions with albite (Ab) at each end in a natural Colombian emerald. These inclusions are oriented parallel to the c*-axis of the crystal. Photomicrograph by Javier Toloza; field of view 0.95 mm.*

Unusual Inclusions in Natural Emerald from Chivor

Nailhead inclusions are commonly associated with hydrothermal synthetic emeralds and occasionally found in flux-grown emeralds as well (G. Choudhary and C. Golecha, "A study of nail-head spicule inclusions in natural gemstones," Fall 2007 *G&G*, pp. 228–235; N. Renfro et al., "Inclusions in natural, synthetic, and treated emerald," Winter 2016 *G&G*, pp. 402–403). Interestingly, similar inclusions have also been observed in natural emeralds. These inclusions occur when a tiny particle or platelet of a foreign substance becomes trapped within the host mineral during crystal growth. As the crystal continues growing, a conical void develops behind the particle, which typically captures various forms of matter, including liquids and gases (Choudhary and Golecha, 2007).

While examining a 1.40 ct rough Colombian emerald sourced from the Chivor district in Boyacá, the authors encountered growth blockage inclusions resembling nailhead inclusions. Unlike the jagged shape typical in Colombian emeralds, these three-phase inclusions exhibited a tubular form and were oriented parallel to the *c*-axis of the crystal. Using Raman spectroscopy, euhedral albite crystals were identified at both ends of the inclusion (figure 7), suggesting a strong interaction between the mineralizing fluids and the host rock, where the fluids may have dissolved albite from the rock and become enriched with its constituents. This could be due to previous alteration processes within the host rock resulting in the replacement of preexisting minerals by albite, known as albitites (A. Cheilletz and G. Giuliani, "The genesis of Colombian emeralds: A restatement," *Mineralium Deposita*, Vol. 31, No. 5, 1996, pp. 359–364).

Javier Toloza, Luis Gabriel Angarita, Holman Alvarado, and Camilo Andrés Betancur
CDTEC Gemlab
Bogotá

Octahedral Gahnospinel Crystal in Sri Lankan Blue Sapphire

Recently, the authors encountered a greenish blue octahedral crystal inclusion in a Sri Lankan blue sapphire (figure 8). Visual features, such as the greenish blue color and octahedral shape, and Raman spectroscopy identified the inclusion as gahnospinel, with the formula $(Mg,Zn)Al_2O_4$.

Gahnospinel inclusions in sapphire often suggest a Sri Lankan origin (A.C. Palke et al., "Geographic origin determination of blue sapphire," Winter 2019 *G&G*, pp. 536–579). In addition, gahnospinel inclusions with euhedral crystal shape have been reported previously (E.J. Gübelin and J.I. Koivula, *Photoatlas of Inclusions in Gemstones, Volume 3*, Opinio Verlag, Basel, Switzerland, 2008). This crystal, however, shows large and beautiful octahedral features.

Yusuke Takamura
GIA, Tokyo

Hollandite in Amethyst

We are used to seeing groups of dark hollandite crystals that resemble sea urchins, but this time Mother Nature offered up a completely different and evocative vision. Crystals of hollandite, with the chemical formula

Figure 8. A greenish blue octahedral crystal of gahnospinel found in Sri Lankan blue sapphire. Photomicrograph by Yusuke Takamura; field of view 3.81 mm.

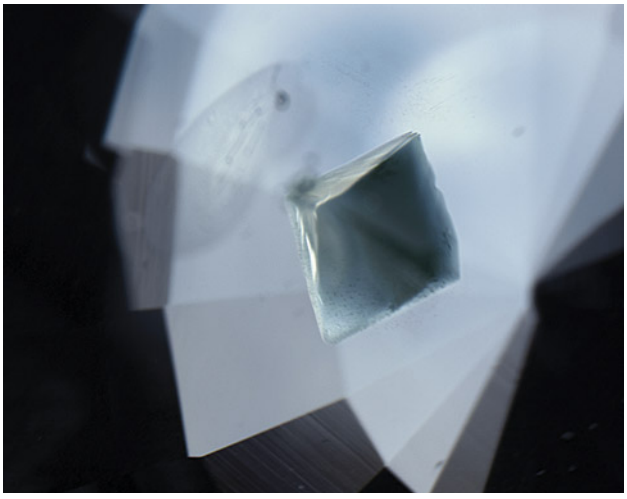

Figure 9. Hollandite crystals inside a natural amethyst from Bahia, Brazil. Photomicrograph by Liviano Soprani; field of view 2.20 mm.

$Ba(Mn^{4+}_{6}Mn^{3+}_{2})O_{16}$, were observed inside a 15.00 ct amethyst cabochon. The arrangement of the acicular crystals created a shape resembling ears of barley (figure 9), making this photomicrograph look more like a botanical image. It was taken in darkfield illumination and oblique fiber-optic illumination with the use of image stacking. To obtain a good focus, the author took multiple photos on different focal planes and then used specific software to reconstruct the image—in this case, 67 stacked images.

Liviano Soprani
Ravenna, Italy

Figure 10. A view through the girdle displayed one of the lighter violet pleochroic colors of the iolite host, revealing a mix of monazite and zircon inclusions surrounded by yellow radiation halos. Note the colorless cores in the larger halos. Photomicrograph by Emily Jones; field of view 3.64 mm.

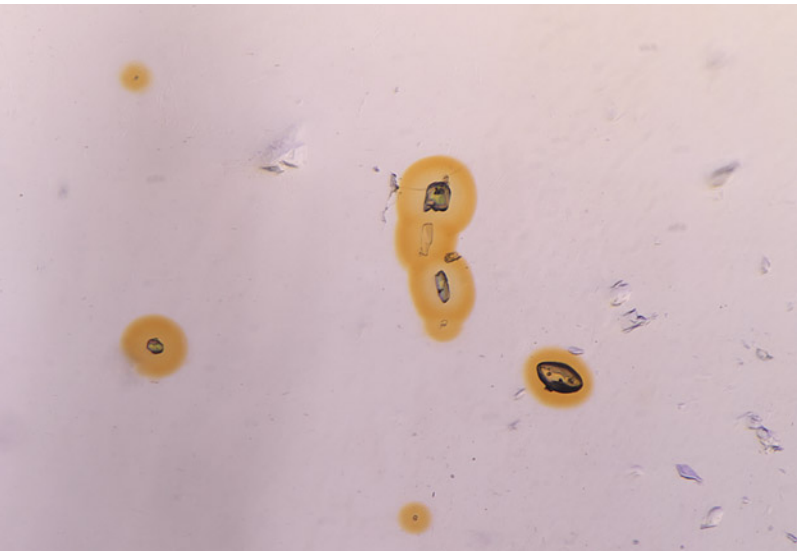

Yellow Radiation Halos in Iolite (Cordierite)

A mounted violet oval cabochon was recently examined by the authors. The stone was identified as iolite through standard gemological testing and confirmed by Raman spectroscopy. Iolite, the gem-quality variety of the mineral cordierite, $(Mg,Fe)_2Al_3(AlSi_5O_{18})$, is known for its vibrant coloration and dramatic pleochroism but is rarely the subject of photomicrography because of its tendency to be either clean or heavily fissured. Under the microscope, small colorless and yellow crystal inclusions were observed, most of which were surrounded by yellow halos (figures 10 and 11) reminiscent of blue internal diffusion observed in heat-treated sapphire. Some of the inclusions were identified via Raman spectroscopy as zircon, monazite, and apatite, although not all were reachable due to their size or depth.

Interestingly, the size of the yellow halos varied across the species. For example, the large apatite shown in figure 11 possessed a much thinner halo than the relatively smaller monazites, likely due to the relative concentrations of radioactive trace elements in the inclusions. Alpha particles are known to cause yellow radiation damage in cordierite, both naturally and artificially (R. Krickl et al., "Radio-induced alteration in cordierite—Implications for petrology, gemmology and material science," *Geophysical Research Abstracts*, Vol. 11, 2009). This yellow coloration fades at

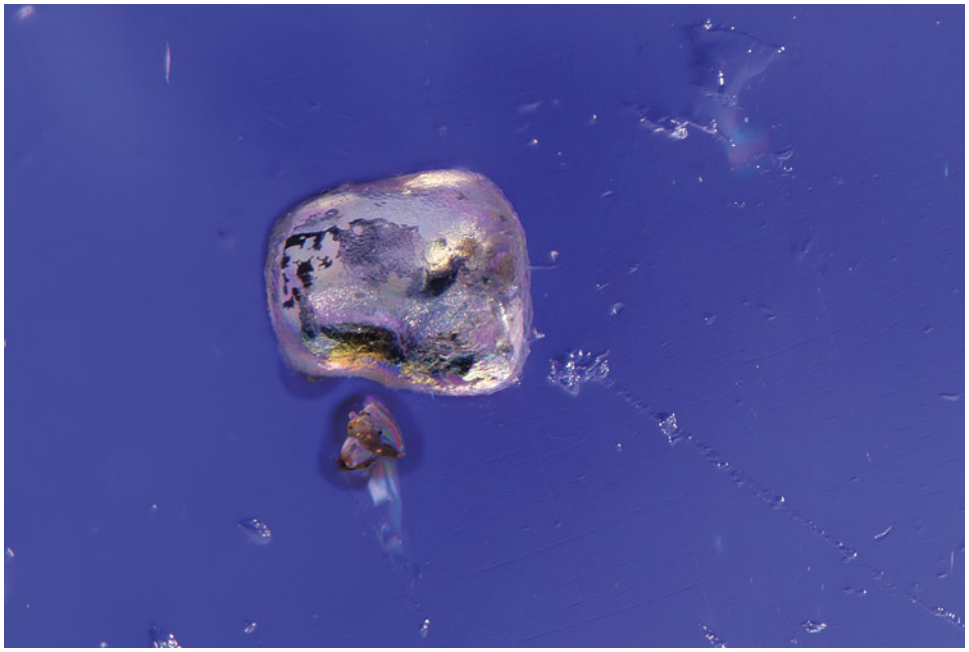

Figure 11. The dark violet background of the iolite shown through a polarizer creates a stunning backdrop for the large apatite and smaller monazite inclusions. The yellow radiation stains surrounding the monazite crystals are much thicker than the thin rim around the apatite. Photomicrograph by Tyler Smith; field of view 1.99 mm.

higher levels of radiation, perhaps due to degradation of the crystal structure through a process known as metamictization, which could explain the colorless core displayed by some of the inclusions (figure 10). Inclusions are often used to detect color-altering treatments, making it quite ironic that these inclusions were the source of the alteration.

Tyler Smith and Emily Jones
GIA, New York

Pseudo-Icosahedral Pyrite in Colombian Emerald

The author recently examined a 2.88 ct emerald containing a beautiful metallic yellow pseudo-icosahedral pyrite crystal with truncated edges (figure 12). The emerald was identified as Colombian based on its jagged three-phase inclusions and trace element analysis using X-ray fluorescence. The included crystal's color, luster, and shape were characteristic of pyrite, which is sometimes found in em-

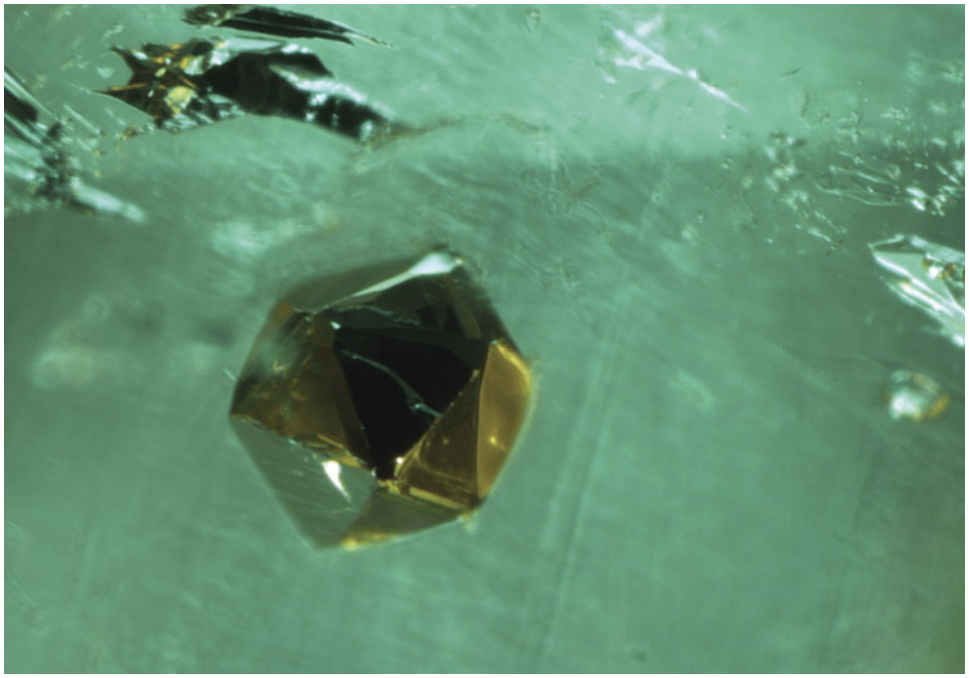

Figure 12. A pseudo-icosahedral crystal of pyrite in a 2.88 ct Colombian emerald. Photomicrograph by Taku Okada; field of view 1.01 mm.

Figure 13. A rock crystal pendant measuring 48.5 × 31.2 × 8.8 mm with a white cross inclusion. Photo by Tsung-Ying Yang.

eralds from various countries (S. Saeseaw et al., "Geographic origin determination of emerald," Winter 2019 *G&G*, pp. 614–646). Pyrite, also known as "fool's gold," belongs to the isometric crystal system and has an ideal chemical composition of FeS_2.

Like other isometric or cubic minerals, including diamonds and garnets, pyrites exhibit various morphologies depending on growth parameters such as temperature and/or degree of supersaturation (J.B. Murowchick and H.L. Barnes, "Effects of temperature and supersaturation on pyrite morphology," *American Mineralogist*, Vol. 72, 1987, pp. 1241–1250). A regular icosahedron is one of the five classic Platonic solids, but it cannot exist in a crystal because it contradicts Haüy's law of rational indices, which states that the intercepts of any crystal face along the crystallographic axes are either equal to the lattice constant lengths or some simple whole number multiples of them. Goniometric studies by Romé de L'Isle from 1783 showed that a pseudo-icosahedral form, often found in pyrite, is a combination of a regular octahedron and an irregular pentagonal dodecahedron known as a pyritohedron.

This pyrite crystal in Colombian emerald would be a welcome sight for any gemologist.

Taku Okada
GIA, Tokyo

Rock Crystal with Cross Inclusion Exhibiting Brownian Motion

Recently, the authors encountered a transparent faint yellow pendant with a striking white cross inclusion (figure 13). Raman and Fourier-transform infrared spectroscopy identified the pendant as rock crystal. Microscopic observation revealed that the white cross was composed of numerous two-phase inclusions measuring less than 20 µm. One of the two-phase inclusions contained a gas bubble with a diameter of approximately 2 µm (figure 14) that was found to exhibit Brownian motion due to the influence of water molecules (see video at www.gia.edu/gems-gemology/winter-2023-microworld-rock-crystal-cross). Brownian motion refers to the unstable random movement of microscopic particles in a fluid, caused by continuous bombardment from molecules of the surrounding medium. This motion becomes more pronounced as the particle size decreases, fluid viscosity lowers, and temperature increases. Brightfield illumination, polarized light, and optical zoom techniques were used to obtain the photomicrographs.

Shu-Hong Lin
Institute of Earth Sciences,
National Taiwan Ocean University
Taiwan Union Lab of Gem Research, Taipei

Tsung-Ying Yang, Kai-Yun Huang, and Yu-Shan Chou
Taiwan Union Lab of Gem Research, Taipei

Spiky Inclusion in Padparadscha Sapphire

A peculiar inclusion with metallic luster (figure 15) was observed in a 5.31 ct faceted pinkish orange padparadscha sapphire. Though reminiscent of an inclusion previously observed in garnet (Summer 2023 *G&G* Micro-World, p.

Figure 14. The white cross inclusion in the rock crystal contained this two-phase inclusion, in which the bubble had a diameter of approximately 2 µm and exhibited Brownian motion. Photo by Shu-Hong Lin; field of view 65 µm.

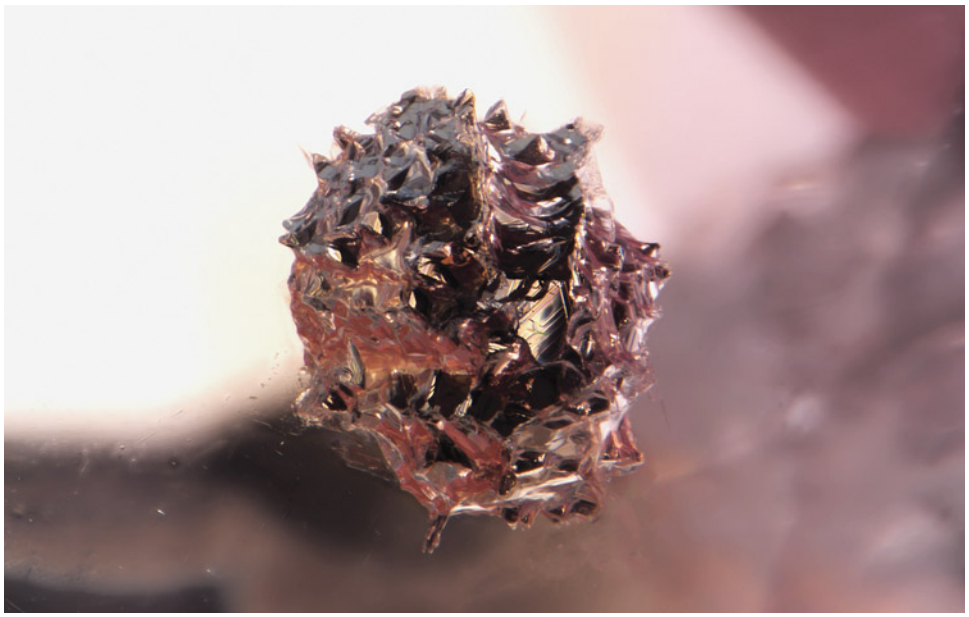

Figure 15. A view through the table of a padparadscha sapphire displayed this jagged suspended crystal, likely a metal sulfide, featuring a rare texture. Photomicrograph by Courtney Robb; field of view 2.90 mm.

226), this occurrence in sapphire displayed a more irregular and pronounced spiky texture. The combination of nearly pyramidal protrusions and sloped valleys gives this inclusion a fascinating and unique topography. While neither inclusion was conclusively identified, the opacity and dark metallic appearance suggest a metal sulfide.

Courtney Robb
GIA, New York

Suspended Crystal in Red Spinel

The sharp outline of a tabular included crystal in a 0.44 ct red spinel (figure 16) appeared suspended when viewed with darkfield illumination. Under fiber-optic lighting, the body of the crystal darkened and displayed a flash of rainbow colors caused by thin-film interference between the host spinel and the inclusion.

Not all included crystals display such drastically different appearances with different light sources. This particular well-formed crystal was the only notable inclusion in the red spinel. The surprising "rainbow" effect made it stand out from other crystal inclusions observed in similar material.

Isabelle Corvin
Olympia, Washington

Quarterly Crystal: Hiddenite from Idaho

Not every day do we encounter a known but rare gem mineral from a previously unknown locality for the species. But that is exactly what happened when we examined the doubly terminated, heavily etched green crystal shown in figure 17. This slightly yellowish green crystal, weighing 20.57 ct and measuring 37.10 × 10.00 × 8.50 mm, is from

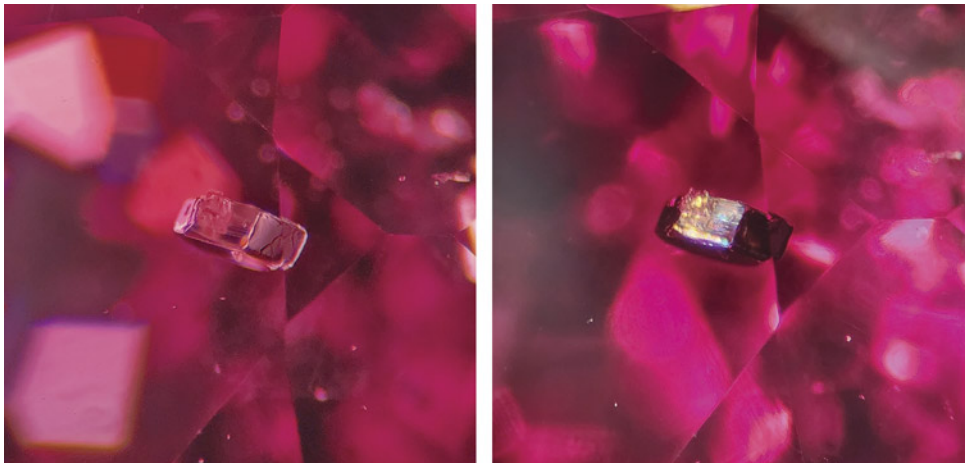

Figure 16. A crystal inclusion in red spinel shown in darkfield illumination (left) and fiber-optic lighting (right). Photomicrographs by Isabelle Corvin; field of view 1.78 mm.

Figure 17. Weighing 20.57 ct and measuring 37.10 mm in length, this doubly terminated, heavily etched spodumene crystal contains chromium as its coloring agent or chromophore. Photo by Adriana Robinson.

Sawtooth National Forest in Elmore County, Idaho. It came to us from the mineral collection of Jack Lowell of Tempe, Arizona.

Mined by Geary Murdoch in the 1990s, the crystal was sold to Lowell as an etched aquamarine. Lowell suspected that it was a spodumene crystal due to the very distinctive

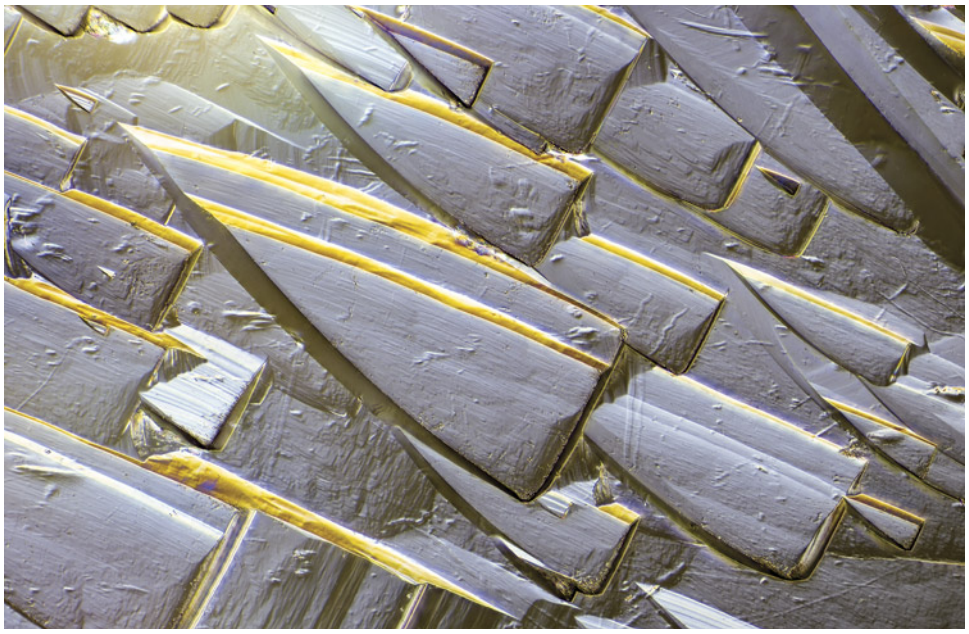

Figure 18. Found on the surface of the heavily etched crystal, these sail-shaped etch features captured with differential interference contrast photomicrography provide definitive proof of the mineral spodumene. Photomicrograph by Nathan Renfro; field of view 1.44 mm.

and diagnostic etching on its surfaces (figure 18). The authors examined the crystal with Raman analysis to confirm its identity as spodumene. Energy-dispersive X-ray fluorescence identified its chromophore as chromium, indicating the specimen was the rare green variety known as hiddenite.

Idaho is only the second known hiddenite source. The first to yield gem crystals (figure 19) was the Adams hiddenite and emerald mine in Alexander County, North Carolina.

John Koivula, Nathan Renfro, and Maxwell Hain
GIA, Carlsbad

Figure 19. This 2.30 ct doubly terminated hiddenite crystal comes from the Adams mine in North Carolina, the first known locality for the gem. Photo by Annie Haynes.

Gems Recovered from Sedimentary Rocks

James E. Shigley, Roy Bassoo, and Aaron C. Palke

Sedimentary rocks such as shale, limestone, and sandstone are among the most common rocks exposed on the earth's surface (figure 1). In actuality they represent only a thin covering of the crust, which mainly consists of igneous and metamorphic rocks. Despite their relatively insignificant volume, many of the major geologic events in the earth's history are more accurately documented and age-dated by their scientific study. In addition to having economic deposits of oil, natural gas, coal, and certain heavy minerals such as gold and platinum, sedimentary rocks also host important primary and secondary occurrences of many gemstones (Dill, 2018).

The occurrences of gems in sedimentary rocks result from two different geological processes. Opal and turquoise, for example, can form in voids or empty spaces by precipitation from water or mineralized solutions, respectively (figure 2). In contrast, other gems such as diamond and sapphire were weathered out of their original igneous or metamorphic host rocks and then carried away by erosion to be later trapped in sediments. Their hardness and resistance to mechanical abrasion allowed these minerals to be transported and then deposited by moving water to create alluvial or placer gem deposits (figures 3 and 4). Both categories of gems in sediments will be discussed in this column.

Editors' note: Questions or topics of interest should be directed to Aaron Palke (apalke@gia.edu) or James Shigley (jshigley@gia.edu).

Gems & Gemology, Vol. 59, No. 4, pp. 510–523.

Sedimentary Rock Formation

A three-step sequence of geologic processes results in sedimentary rocks forming on or near the earth's surface. The first step is termed *weathering*—the physical, chemical, and biological decomposition of preexisting rocks of all kinds to form finer-sized particles. These particles accumulate and compact in geological basins over time to form new sedimentary rocks. Weathering involves the combined actions of air, water, chemical salts and/or solutions, freezing and thawing temperature cycles, and the effects of plants and animals on rocks.

The change in relative abundance of the various minerals from the original rock to the final sedimentary products is a measure of their comparative resistance to weathering. In our Winter 2022 column, titled "Gems Formed in Magmatic Rocks," we discussed the concept of "Bowen's reaction series" (figure 7 in Palke and Shigley, 2022). Based on field observations of rock relationships and experimental studies of their formation, this concept describes the sequence of formation of the common rock-forming silicate minerals at specific decreasing temperatures from a cooling magma.

In a similar way, geologists have recognized a "mineral dissolution series" of the relative stability (or "resistance to weathering") of common minerals at the earth's surface (figure 5). This dissolution series is also based on several other factors, including the extent of bonding of silica tetrahedra in the mineral's crystal structures, as well as the relative resistance of their chemical elements to leaching by water. Minerals that are more resistant to weathering and dissolution are more likely to be retained in sedimentary environments and concentrated in alluvial deposits.

The next step is *erosion*—the process by which solid or dissolved products are transported various distances

Figure 1. Sedimentary rocks are among the most common rocks exposed on the earth's surface. This image shows multicolored sandstone layers known as "The Wave" that have been eroded and sculpted by winds to form a swirling pattern of rock strata in the Coyotes Buttes North wilderness area along a portion of the Arizona/Utah border. Photo by Greg Bulla.

from the weathering site and are eventually deposited elsewhere as loose, unconsolidated sediments. Erosion acts to lower the overall topography of the land surface. Flowing water is the most important transporting agent for sedi-

Figure 2. The gems shown here formed in sediments by the evaporation of water or from mineralized solutions (amber is solidified tree resin). From left to right and top to bottom: 59.88 ct turquoise, Turkey; 75.30 ct chrysoprase, Queensland, Australia; 67.79 ct malachite, Democratic Republic of Congo; 19.56 ct opal, Brazil; 14.67 ct amber, Poland; and 28.14 ct rhodochrosite, Argentina. Composite image by Robert Weldon.

Figure 3. Alluvial gems that can more commonly be found in sediments. From left to right and top to bottom: 16.94 ct grossular, Tanzania; 9.72 ct jadeite, Myanmar; 13.52 ct spinel, Sri Lanka; 4.86 ct sapphire, Myanmar; 4.43 ct rhodolite, Tanzania; 2.53 ct rhodolite, Tanzania; and 2.21 ct ruby, Myanmar. Composite image by Robert Weldon.

Figure 4. Alluvial gems that are less often found loose in sediments. From left to right and top to bottom: 14.41 ct andalusite, Brazil; 18.50 ct sinhalite, Sri Lanka; 13.00 ct sphene, Madagascar; 11.19 ct kornerupine, Sri Lanka; 2.62 ct sillimanite, Sri Lanka; 3.20 ct zoisite, Tanzania; 2.77 ct kyanite, Madagascar; 1.68 ct sapphirine, Sri Lanka; 0.29 ct grandidierite, Sri Lanka; and 1.23 ct taaffeite, Sri Lanka. Composite image by Robert Weldon.

ments, which can result in the breakage, abrasion, chemical alteration or dissolution, and sorting by size and/or shape of rock fragments and particles. This transport occurs when the velocity of the water overcomes the downward pull of gravity, and the water moves the suspended material. Sediments can also be transported by winds (as volcanic ash or fine-grained sand), by the movement of glacial ice, and by gravity (downslope sliding)—these situations, however, are less important for the creation of alluvial gem deposits.

After the deposition of sediments, the final step is termed *lithification*. Sedimentary rocks form when layers or accumulations of clay, silt, sand, and other deposited materials are compacted and cemented by the weight of overlying rocks (figure 6). Before, during, and after lithification, sedimentary rocks undergo physical and chemical changes due to heating, compaction, and reaction with groundwater. Biological agents, including small animals or microbial bacteria, can also be important, as can chemical agents brought in by flowing water or heated hydrothermal solutions. These changes are collectively called *diagenesis*, and they can be described as grading into a low temperature and pressure form of metamorphism. Textural changes, including compaction and loss of pore space and trapped water, recrystallization, and the changing of fine-grained rocks into coarser ones, are all forms of diagenesis. During recrystallization, secondary minerals may precipitate in open spaces, and mineral cements such as calcite,

Figure 5. A listing of various primary and secondary minerals and their relative resistance to weathering when exposed at or near the earth's surface. Resistant minerals toward the top of the list are more likely to be preserved in sedimentary rocks. From Birkeland (1999).

RESISTANCE OF MINERALS TO WEATHERING

	Primary minerals	Secondary minerals
Most weathering resistant	Zircon	Anatase
	Rutile	Gibbsite
	Tourmaline	Hematite
	Ilmenite	Goethite
	Garnet	Kaolinite
	Quartz	Clay minerals
	Epidote	Calcite
	Titanite	Gypsum
	Muscovite	Pyrite
	K-feldspar	Halite
	Plagioclase	
	Hornblende	
	Chlorite	
	Augite	
	Biotite	
	Serpentine	
	Volcanic glass	
	Apatite	
Least weathering resistant	Olivine	

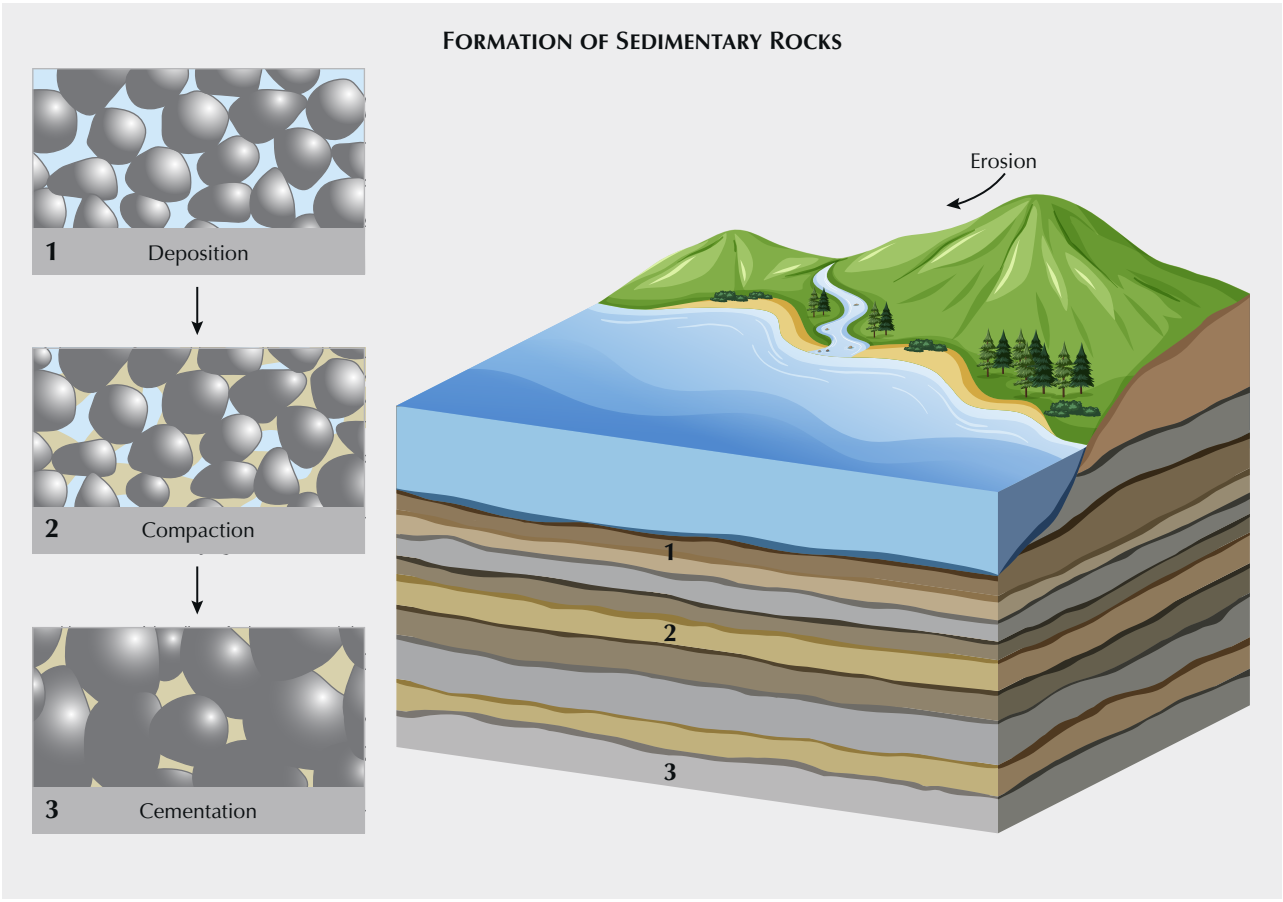

Figure 6. Weathering and erosion of preexisting rocks produces rock particles and fragments which can be carried into bodies of water where they undergo deposition, compaction, and cementation to form new sedimentary rocks.

silica, and hematite may develop—consequently, rocks become more resistant to erosion. With increasing burial conditions, sedimentary rocks become even more compacted as they are exposed to higher temperatures and pressures, which also results in the solid-state precipitation of low-grade metamorphic minerals such as chlorite. This sequence of changes by which sedimentary rocks form are described here as separate geological processes, but in actuality they merge into one another with no sharp boundaries between them.

Sandstone forms from quartz-rich sediments, whereas shale forms from those rich in clays. Limestone forms when calcite and aragonite precipitate out of water containing dissolved calcium, or it forms from the accumulation of corals and shells on the sea floor. Compaction of mixtures of pebbles or fragments results in a conglomerate. Most sedimentary rocks contain predominantly quartz, calcite, and/or various clay minerals. Fossil plants and animals are found in sedimentary rocks which have experienced conditions favorable for their long-term preservation.

Sedimentary Rock Classification

The nature of a sedimentary rock depends both on the source supply of the sediment as well as the depositional environment in which it formed (including continental, marine, and transitional settings involving water) (figure 7). Most sedimentary rocks can be divided into several groups based on mineral compositions and geologic formation mechanisms.

Clastic rocks are composed of rock fragments of varying sizes that are cemented together. When transported by moving agents such as water or wind, sediments often become sorted by particle size before lithification. These rocks include shale, claystone, mudstone, siltstone, sandstone, and conglomerate, with the difference between them being the increasing size of the particles from less than a millimeter to larger than a few centimeters. Most gem minerals discussed here occur in clastic rocks.

Biogenic rocks are formed by accumulations of skeletons of large or microscopic organisms or decomposed plant material. These rocks include limestone, dolostone, chert, diatomite, and coal.

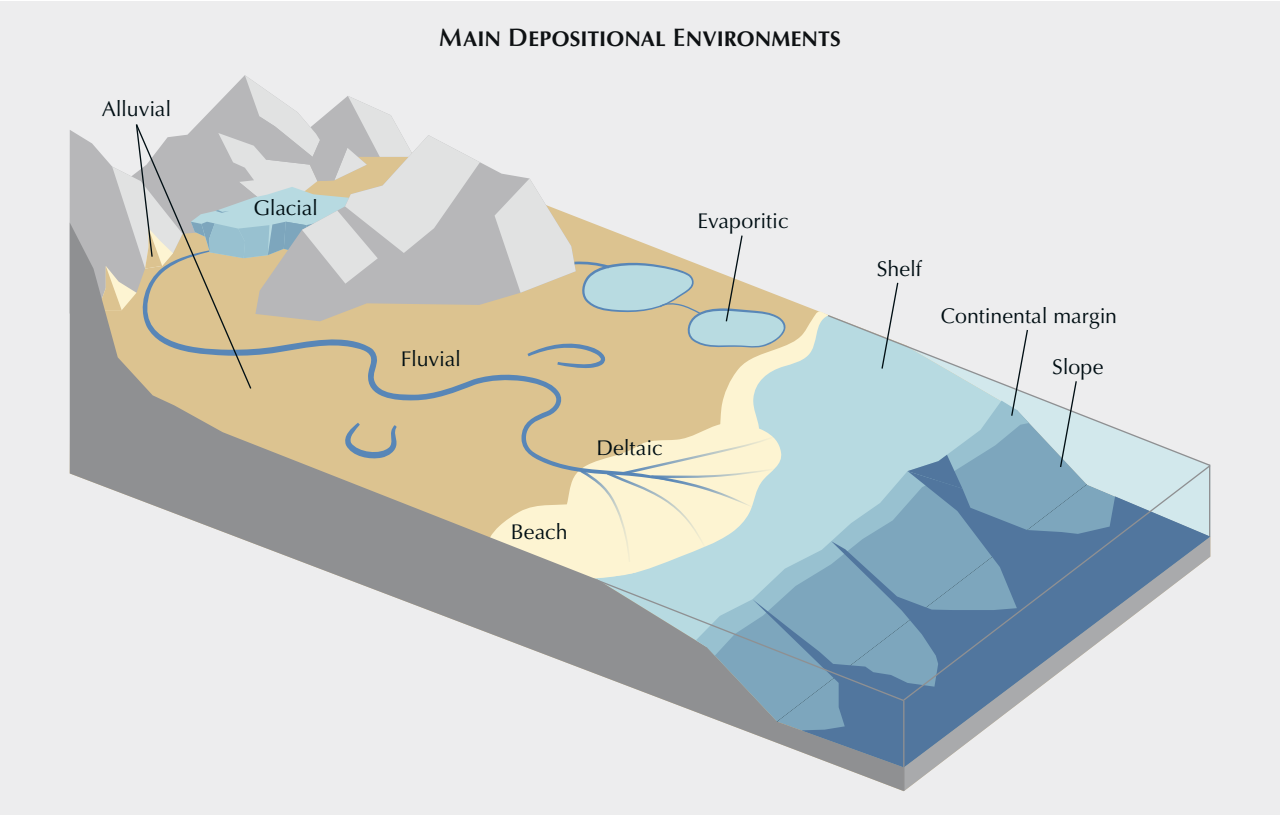

Figure 7. Common geological environments where sedimentary rocks form and where alluvial gem minerals can be concentrated.

Chemical sedimentary rocks are formed by inorganic constituents dissolved in and later precipitated from solution when it evaporates at normal surface temperatures. They include some limestone and dolostone (e.g., travertine), phosphorite, evaporates (such as halite), and banded iron-oxide formations.

Sedimentary Rock Textures

Sedimentary rock formations often display features related to their deposition environment, such as along a river channel or coastline where sediments are deposited. These conditions can result in coarse- or fine-scale layering, banding, or bedding structures. The rocks may also exhibit cross or graded bedding, ripple marks, and mud cracks. Layering, banding, or bedding structures are due to preferential particle orientation and packing, or to the concentration of mineral particles into distinct layers. Folding and faulting of rock layers resulting from local or large-scale deformation can occur after sediment deposition and before or after rock consolidation.

Sedimentary rocks themselves display various textures resulting from the size, shape, and arrangement (packing and orientation) of the constituent particles. Particle size is of particular importance for geologic field studies because it provides information on both the conditions of transportation, sorting, and deposition of the sediment, and the geologic conditions at the deposition site. Particle shape involves the overall shape, roundness or angularity, and surface texture.

Gems Formed in Sedimentary Environments

The formation of gem minerals in sedimentary rocks (table 1, left column; again, see figure 2) can be summarized as follows:

Opal is a hydrated form of amorphous silica produced by the deposition of spherical particles from silica-rich water flowing through cracks, pores, and voids in sedimentary rocks during hotter months as the water itself evaporates. The process is repeated over long periods of time, with the silica particles settling out over time by gravity. These tiny particles arrange themselves into regular layered structures, and they range from about 150 to 400 nanometers in diameter. Opal can produce a "play of colors" appearance by light diffraction. Both gem and non-gem opal occur widely, with the most important sedimentary deposits being in Australia (Rey, 2013; Liesegang and Milke, 2014; Hsu et al., 2015). Fire opal forms by leaching followed by deposition of silica from water moving through cavities in porous volcanic rocks. Other opal sources include Ethiopia, Hungary, Mexico, and Nevada in the United States.

Turquoise is a hydrated copper phosphate that can form in more than one way. One process begins with copper sulfide ore minerals (such as chalcopyrite or bornite) being deposited by higher-temperature hydrothermal solutions to form a mineralized rock. The turquoise forms later when meteoric waters percolate through this rock, and dissolved oxygen in the water reacts with sulfide minerals to produce soluble copper sulfates. The resulting acidic, copper-containing solution reacts with aluminum and potassium minerals in a host rock to produce turquoise that fills veins, seams, or fractures, sometimes forming nodular masses. It was among the first gem minerals to be mined, beginning more than 2000 years ago in Egypt (Ovissi et al., 2017; Ardekani et al., 2020; Shirdam et al., 2021). Important current sources include Argentina, Armenia, Australia, China, Iran, Mexico, and the United States.

Chalcedony forms in volcanic rocks that contain gas cavities, which can then be partially or completely filled with cryptocrystalline silica material that precipitates from volcanic fluids from the walls of the cavity inward. Thus, most chalcedony is not considered a gem that forms in sediments. The one exception is the green chrysoprase variety, which forms as veins, fracture fillings, and nodules in sediments due to the weathering at shallow depths of nickel-bearing serpentinite rocks that are rich in iron and magnesium (Shigley et al., 2009; Sachanbiński et al., 2023). Chalcedony occurrences are found in many localities.

Malachite and azurite are copper carbonate hydroxides that precipitate from hydrothermal fluids in fractures or underground spaces as secondary gems, followed by surface weathering and oxidation of a copper ore body. The two mineral aggregations form botryoidal, reniform, fibrous, or stalagmitic masses, with azurite sometimes also occurring as crystals. Malachite can display internal banding patterns. Both minerals have been used since antiquity as mineral pigments for decorative purposes, and both are mined by open pit and from underground workings. The major current source of malachite is the Democratic Republic of the Congo, while the less common azurite comes from various localities (Cook, 2001; Kampunzu et al., 2009; El Desouky et al., 2010; De Putter et al., 2010; Papineau, 2020).

Rhodochrosite is a less common manganese carbonate mineral that is found as distinct crystals or massive fracture- or vein-fillings associated with some ore deposits. Larger transparent crystals are sometimes faceted as gems. In a few localities, the mineral forms from dripping water which creates stalactites and stalagmites (Marquez-Zavalia and Craig, 2022).

Amber is not a mineral but an organic fossilized resin that was exuded as a sticky substance from the bark of certain trees. Pieces of resin that dropped to the ground became covered by soil. When the trees fell, the resin-containing logs were carried by rivers and tides to coastal regions where they were buried by sediments. Due to the compression pressures and elevated temperatures from the overlying sediments, the pieces of resin were compacted and transformed over geologic time, first to copal and then to amber. While long used as a gem material, amber is important for the science of paleontology since it preserves a wide variety of animal and plant matter (Grimaldi, 2003; Penny, 2010; Ross, 2010). Amber is widely distributed in rocks of Cretaceous age or younger. Historically, the southern coast of the Baltic Sea extending from Poland to Latvia has been the world's leading source of this material. Myanmar and the Dominican Republic are other current amber sources (Wolfe et al., 2009; Weitschat and Wichard, 2010; Leelawatanasuk et al., 2013; Sun et al., 2015; Zhang et al., 2020).

While being described here as "forming" in sediments, the occurrence of these gem minerals is not directly the result of sedimentation. Instead, it involved physical and chemical changes associated with diagenesis and possibly the action of circulating hydrothermal solutions to introduce the necessary components for gem mineral formation.

Gems Found in, but Not Formed in, Sedimentary Deposits

The second category of gems occurring in sedimentary environments are those that formed originally in igneous and metamorphic rocks (again, see figures 3 and 4). After these host rocks weathered, their abrasion-resistant gems were transported and are found deposited along current and

TABLE 1. Examples of gems found in sedimentary environments.

Gems that formed in sedimentary environments	Gems found in sedimentary environments that formed elsewhere
Amber, chalcedony (agate), chrysocolla, chrysoprase, malachite, opal, rhodochrosite, smithsonite, turquoise	Apatite; beryl (aquamarine, morganite); chrysoberyl (alexandrite); corundum (ruby, sapphire); diamond; garnet (almandine, demantoid, hessonite, pyrope, rhodolite, spessartine, tsavorite); jade (nephrite, jadeite); kornerupine; olivine (peridot); pyroxene (diopside, enstatite); quartz (amethyst, citrine, chalcedony, agate, rose quartz, smoky quartz); sphene; spinel; topaz; tourmaline

former stream and river channels, either in loose or more compacted sediments. These gem minerals were formed elsewhere and were transported and concentrated by moving water and other geological processes. A placer deposit is a natural concentration of heavy minerals in secondary sediments caused by the effect of gravity on moving particles.

Alluvial or placer mineral deposits have been mined since ancient times. Because they occur at the earth's surface, they were likely one of the earliest known types of economic ore deposit. They could be worked using simple traditional tools, and the deposits would provide an almost immediate economic reward to the miners. They continue to be significant sources of valuable metals such as gold and platinum (Ibrahim et al., 2020; Nikiforova, 2021; Cabri et al., 2022; Torvela et al., 2022).

Placer deposits form as the result of the concentrations of "heavy minerals" in secondary sediments (Patyk-Kara, 2002; Garnett and Bassett, 2005; Stanaway, 2012; Nikiforova, 2021). These deposits are masses of unconsolidated or semi-consolidated clastic sediments, formed by surface weathering and erosion of primary rocks and subsequently transported by gravity, water, wind, or ice from their original source. The heavy gem minerals must be hard, durable, resistant to weathering and breakage during water transportation, have a high specific gravity (>2.58), and possess chemical stability to be hosted in placer deposits (Joshi et al., 2021).

During water transport, fractured or other poor-quality mineral crystals are often broken up and removed, so the final alluvial deposits often contain better-quality gem material. In some instances, the gem fragments being transported become water-worn or rounded by mechanical abrasion. All of these factors can result in economically valuable mineral concentrations. Such deposits are among the most important sources of a variety of gems including diamond, corundum, spinel, garnet, and quartz, as well as nephrite and jadeite jade (table 1, right column). Such deposits often occur along current or former river channels in unconsolidated or poorly consolidated sediments. In some cases, loose gem diamonds have been carried along by glaciers, which transport but do not sort or separate the placer minerals.

Types of Placer Gem Deposits

Placer deposits are classified by Dill (2018) based on the geological factors such as weathering, erosion, and local surface topography that created them (again, see figure 6).

Retained Deposits. Eluvial placer deposits are not transported and are located near the point of original gem formation in igneous or metamorphic host rocks. They are found on weathered hillslopes where lighter material has been weathered and/or carried away, but they are often not economically significant enough to support large-scale gem mining.

Transient Deposits. Colluvial deposits result from short-distance transport of material by gravity action downslope from the original gem host rock. These deposits can form at the base of steep hillsides, for example.

Alluvial deposits involve longer-distance transport mainly by water. The most significant alluvial deposits are located along bends in rivers, natural hollows, breaks in the slope of hillsides, or at the base of an escarpment or other natural barrier, and involve short- or long-distance transport of minerals by moving water. Because the transport ability varies approximately as the square of the velocity, the speed of the moving water plays an important role in deposit formation and the travel distance from the original source of the placer minerals. Thus, when the water velocity decreases, heavy minerals are deposited more quickly than the light ones. Placers can form whenever and wherever the water velocity remains below that required to transport the gems further, including bends in meandering streams, at the base of waterfalls, behind obstacles, and along eroded or hollowed-out depressions at the base of riverbeds. Over time, stream flow can remove larger and lighter minerals thereby concentrating the heavier minerals. During transport by moving water, mineral crystals or rock fragments can become abraded and waterworn.

Terminal Deposits. Beach or delta deposits form along the edge of water bodies by wave action (such as sand deposits). Continent shelf deposits occur further offshore in shallow coastal environments. Examples of the latter include diamond deposits along the southern coast of South Africa and Namibia.

Each of these three types of placer gem deposits can reside long enough to be termed a "paleoplacer," or an ancient sediment deposit that has been buried and/or lithified to rock. Examples include the extensive Witwatersrand in Southern Africa, and the Roraima Supergroup in northern South America, which are both known to host significant amounts of diamonds and gold, and the extensive sapphire and colored stone alluvial deposits at Ilakaka, Madagascar. It should also be mentioned that in many places there are no longer any geological signs of the ancient river systems that deposited the gem gravels.

The mining of gems from natural caves is another type of occurrence that does not fit into the above classification, with the best example being the recovery of ruby and spinel from caves found in marbles. In this case, caves act as a trap for gem minerals weathered out of the marbles during karstic processes forming the caves, as well as gem-bearing sediments that may be introduced from surface-reaching openings in the cave systems.

Examples of Important Alluvial Gem Deposits

Montepuez Ruby Deposit in Mozambique. The regional geology of the countries located along the east and southeast

Figure 8. Local people washing for sapphires in 2010 near the village of Ambalavy 50 km southwest of Ilakaka in south-central Madagascar. Photo by Vincent Pardieu.

portions of Africa is dominated by the rocks of the East African orogeny. Ruby deposits are hosted in the Montepuez metamorphic complex, consisting of Mesoproterozoic to Neoproterozoic granitic to amphibolitic orthogneisses (Boyd et al., 2010). Rubies are mined from both the host metamorphic rocks and in predominantly eluvial and colluvial type deposits derived from them. In this area, the primary ruby deposits are curiously easier to mine than secondary deposits because the metamorphic rocks have weathered predominantly to clays (Vertriest and Saeseaw, 2019).

Ilakaka Sapphire Deposit in Madagascar. Secondary deposits of sapphire and other gem minerals in the Ilakaka region include extensive buried paleoplacers of the Triassic Isalo sandstones (figure 8). These alluvial deposits have concentrated highly productive gem-bearing, poorly consolidated terraces that contain cobble- to pebble-sized rounded lithic fragments of laterite, sandstone, quartzite, and schist. They are exploited using shafts extending down about 20 m, and sometimes in open pits which target potholes or meanders in current or former rivers (Rakontondrazafy et al., 2008).

Gem Occurrences in Sri Lanka. Sri Lanka is underlain by Archean metamorphic to Proterozoic migmatites and granitoid rocks. This assemblage is overlain by loosely consolidated alluvial sediments which have accumulated over millions of years. Concentrated deposits of many types of colored gemstones derived from the basement rocks occur in sediments in various areas of the central and southern portions of the island (Dissanayake and Rupasinghe, 1993; Gunatilaka, 2007) (figure 9).

Historical Diamond Deposits in Brazil. Alluvial diamonds in Brazil are recovered from rivers and streams or in nearby unconsolidated sediments. The most productive of regions in Brazil have been the states of Minas Gerais, Bahia, and Mato Grosso. These deposits are part of a complex network of alluvial, colluvial, and eluvial deposits which vary in time and space. Compositionally, deposits are a mix of clay to sand-sized sediments, containing rounded to angular pebbles and cobbles from the surrounding bedrock including kimberlites and diamondiferous conglomerates (Farrar, 2009; Svisero et al., 2017).

Figure 9. Washing sediments to recover fragments of gems in 2011 near Ratnapura, Sri Lanka. Photo by Vincent Pardieu.

Alluvial Diamond Deposits along the Vaal and Orange Rivers, and Related Continental Shelf Marine Deposits along the Atlantic Coast of Southern Africa. Diamonds from restricted kimberlite sources in the interior of Southern Africa were transported westward so that they are found along the Vaal and Orange River channels as well as underwater along an extended length of the continental shelf (Maree, 1987; Jacob et al., 1999; Moore and Moore, 2004; Wilson et al., 2006). The coastal diamond deposits of Namibia and South Africa are host to excellent gem-quality diamonds because most of the inferior stones would have been lost due to comminution during transport (Sutherland, 1982; Gurney et al., 1991; Corbett and Burrell, 2001; Bluck et al., 2005; Nakashole et al., 2018; Phillips et al., 2018; Jacob and Grobbelaar, 2019).

Sapphire Deposits in Montana. Sapphires are mined from secondary deposits in Montana at three locales: Rock Creek,

Figure 10. Artisanal miners removing alluvial sediments to reach a deeply buried gravel layer containing gem fragments near Ilakaka in Madagascar. Photo courtesy of Toby Smith.

the Missouri River, and Dry Cottonwood Creek (Zwaan et al., 2015; Hsu et al., 2017; Palke et al., 2023). These deposits are all related to Cenozoic volcanism, although the volcanic source rocks have not been clearly identified in all cases. The Rock Creek locality appears to be an eluvial or a colluvial deposit possibly related to rhyolitic volcanism and related ash or mudflows. Along the Missouri River, sapphires are found concentrated in gravel bars along the river banks. There is a large mining operation at Rock Creek as well as smaller artisanal operations along the Missouri River, all utilizing heavy machinery to enhance the volume processing of gravels and sapphire recovery.

Amber Deposits along the Baltic Sea Coastline. Baltic amber occurs in late Eocene to Oligocene glauconite-rich sediments (approximately 23–48 Ma in age) along the Baltic Sea coastline extending from Poland, Kaliningrad, Lithuania, and Latvia (Kasiński and Kramarska, 2008; Standke, 2008). Detailed study of the flora preserved in Baltic amber suggests a warm and temperate climate in the past. Glacial activity coincident with a marine transgression deposited amber into Pleistocene glacial tills, which are continuously eroded and deposited unto the Baltic Sea coastline (Weitschat and Wichard, 2010; Sadowski et al., 2017). Since ancient times, amber has been recovered by picking it up along the beaches (especially after storms), or by using nets and other tools to obtain it from shallow water.

Locating Alluvial Gem Deposits

Finding an alluvial gem deposit is no small task, and such occurrences are often just the result of a serendipitous discovery by an individual spotting a gem crystal fragment lying loose in the dirt along a path or exposed in a rock outcrop. Such an event often results in many local people swarming the area and digging up the ground hoping to "strike it rich." Historic examples include the gold rushes in California in 1848 (Kelley, 1954; Eifler, 2016; Mountford and Tuffnell, 2018; Baumgardner, 2020), in Australia in 1851 (Mudd, 2007), and more recently the extensive alluvial gem deposits found in the Ilakaka region of Madagascar in the mid-1990s (figure 10; see Guerin and Moreau, 2000).

Figure 11. Artisanal miners washing sediments along the Njuga River to recover fancy sapphires and other gem fragments in 2016 near Amani Makoro, a few kilometers from Songea in southern Tanzania. Photo by Wim Vertriest.

Alluvial gem deposit formation is due collectively to geological, geomorphological, and sedimentological processes. Ideally, one tries to first establish whether the geological conditions in the area would allow for the formation of certain gemstones in original host rocks (such as the presence of pegmatites which can host beryl, tourmaline, and topaz). The geomorphology of a prospective secondary location must also be conducive to collecting and storing gem crystals over geologic time through "structural traps" such as valleys, scours, dike margins, fractures, large changes in elevation, and river splays onto a floodplain. Rivers and streams must have enough water velocity and volume to move gemstone-bearing sediments into structural traps where the reduced velocity causes the gem crystals to settle out. Similarly, they settle out along the inner bends of river meanders where the water velocity is also reduced. Geologic time is also another important consideration. Alluvial sediments are constantly in flux, so the most productive alluvial deposits are those that have had enough time to remove fine clays and sands and those that have also been buried to protect them from further erosion.

Mining Alluvial Gem Deposits

As described above, alluvial deposits of gems and other valuable heavy minerals vary widely in their geologic occurrence, extent, and accessibility. The host sediments can also vary in their degree of compaction from unconsolidated to more cemented sedimentary rocks. In some cases, the gemstones themselves are not contained within any sediments, but they lie loose along the bottoms of bodies of water. All these factors influence the mining techniques and types of equipment used for mineral recovery (Griffith, 2013).

Both placer gems and industrial minerals are often recovered by artisanal miners (both men and women) working in the informal sector. Alluvial deposits are prospective because they typically have higher quality gem crystals, since over time inferior stones tend to be mostly destroyed by comminution, the geologic process where large particles are reduced to a smaller size. In addition, the deposits are often easier to mine with simple hand tools because the sediments are exposed near the surface, they are only partly consolidated, and the loose gems can often be recovered by washing and/or panning (figure 11).

Artisanal miners usually target alluvial gem deposits that are typically impractical in economic terms for mining companies. A few placer deposits are exploited on a larger scale by companies using more modern mining equipment and techniques (figure 12). Among these are diamond deposits on the Atlantic continental shelf and beaches of South Africa and Namibia, the ruby deposits near Montepuez in Mozambique, and the deposits of volcanic sapphire in sediments near Chanthanaburi in Thailand.

Summary

Sedimentary rocks host important deposits of numerous gem minerals that either formed or have been found in these rocks. This edition of Colored Stones Unearthed summarizes the characteristic features of sedimentary rocks and describes the sedimentary geological environments where gem minerals can become concentrated. Although often limited in lateral extent, surface exposures of secondary gem deposits can often be worked with simple tools, so they are exploited by artisanal miners in many parts of the world.

A final comment is necessary. The previous two installments of this column covered gems found in igneous and in metamorphic rocks. The present entry on gems in sedimentary rocks completes the main categories of rocks exposed at the earth's surface as would be discussed in any geology textbook. The three installments present these subjects as separate rock categories, when geological field observations sometimes produce a less clear picture. Since the environments of mineral formation among these three rock types lack distinct and accepted boundary conditions of temperature, pressure, time, and chemical composition, some surface rocks display evidence of having formed under conditions along the borders between rock categories. As mentioned earlier, for example, sediments being heated and compacted by burial undergo the process of diagenesis, whose conditions with even deeper burial can evolve into metamorphism. Therefore, mineral and gem formation can sometimes take place more along a continuum of geological conditions than might be inferred by the organization of the installments of this series.

Figure 12. Mining of eluvial gem-bearing sediments from very weathered lava flows with mechanical equipment including a mechanical excavator, a rotating trammel cage to separate large rock pieces from the sediments, and a long sluice box to wash the sediments. This photo was taken in November 2020 at Khao Ploy Waen, an eroded volcano where sapphire is mined near Chanthaburi in eastern Thailand. Photo by Wim Vertriest.

REFERENCES

Ardekani S.J., Mackizadeh M.A., Ayati F. (2020) Mineralogy and formation conditions of turquoise in Ali Abad copper porphyry deposit. *Journal of Economic Geology*, Vol. 12, No. 1, pp. 93–109.

Baumgardner F. (2020) *Golden Dreams: True Stories of Adventure in the California Gold Rush*. Author Solutions, Bloomington, Indiana, 218 pp.

Birkeland P.W. (1999) *Soils and Geomorphology*, 3rd ed. Oxford University Press, New York.

Bluck B.J., Ward J.D., De Wit M.C.J. (2005) Diamond mega-placers: Southern Africa and the Kaapvaal craton in a global context. *Geological Society of London Special Paper*, Vol. 248, pp. 213–245.

Boyd R., Nordgulen O., Thomas B., Bingen B. (2010) The geology and geochemistry of the East African orogen in northeastern Mozambique. *South African Journal of Geology*, Vol. 113, No. 1, pp. 87–129, http://dx.doi.org/10.2113/gssajg.113.1.87

Cabri L.I., Oberthur T., Keays R.R. (2022) Origin and depositional history of platinum-group minerals in placers – A critical review of facts and fiction. *Ore Geology Reviews*, Vol. 144, article no. 104733, http://dx.doi.org/10.1016/j.oregeorev.2022.104733

Cook R.B. (2001) Connoisseur's choice: Malachite - Shaba Region, Democratic Republic of Congo. *Rocks and Minerals*, Vol. 76, No. 5, pp. 326–330, http://dx.doi.org/10.1080/00357520109603236

Corbett I., Burrell B. (2001) The earliest Pleistocene (?) Orange River fan-delta: An example of successful exploration delivery aided by applied Quaternary research in diamond placer sedimentology and palaeontology. *Quaternary International*, Vol. 82, No. 1, pp. 63–73, http://dx.doi.org/10.1016/S1040-6182(01)00009-X

De Putter T., Mees F., Decree S., Dewaele S. (2010) Malachite, an indicator of major Pliocene copper remobilization in a karstic environment (Katanga, Democratic Republic of Congo). *Ore Geology Reviews*, Vol. 38, No. 1/2, pp. 90–100.

Dill H.G. (2018) Gems and placers – A genetic relationship par excellence. *Minerals*, Vol. 8, No. 10, article no. 470.

Dissanayake C.B., Rupasinghe M.S. (1993) A prospectors' guide map to the gem deposits of Sri Lanka. *G&G*, Vol. 29, No. 3, pp. 173–181, http://dx.doi.org/10.5741/GEMS.29.3.173

Eifler M.A. (2016) *The California Gold Rush - The Stampede that Changed the World*. Routledge Publishers, Milton Park, United Kingdom, 234 pp.

El Desouky H.A., Muchez P., Boyce A.J., Schneider J., Cailteux J.L.M., Dewaele S., von Quadt A. (2010) Genesis of sediment-hosted stratiform copper-cobalt mineralization at Luiswishi and Kamoto, Katanga Copperbelt (Democratic Republic of Congo). *Mineralium Deposita*, Vol. 45, No. 8, pp. 735–763, http://dx.doi.org/10.1007/s00126-010-0298-3

Farrar B. (2009) Three centuries of diamonds: Preserving a tradition in Brazil. *Rock and Gem*, Vol. 39, No. 3, pp. 37–40.

Garnett R.H.T., Bassett N.C. (2005) Placer deposits. *Economic Geology*, Vol. 100, pp. 813–843.

Griffith S.V. (2013) *Alluvial Prospecting and Mining*. Elsevier Publishers, Amsterdam, Netherlands, 256 pp.

Grimaldi D.A. (2003) *Amber: Window to the Past*. Harry N. Abrams Publishers, New York, 216 pp.

Guerin C., Moreau S. (2000) Ilakaka (Madagascar): La ruée vers le saphir. *Les Cahiers d'Outre-Mer*, Vol. 53, No. 211, pp. 253–272, http://dx.doi.org/10.3406/caoum.2000.3769

Gunatilaka A. (2007) Role of basin-wide landslides in the formation of extensive alluvial gemstone deposits in Sri Lanka. *Earth Surface Processes and Landforms*, Vol. 32, No. 12, pp. 1863–1873, http://dx.doi.org/10.1002/esp.1498

Gurney J.J., Levinson A.A., Smith H.S. (1991) Marine mining of diamonds off the west coast of southern Africa. *G&G*, Vol. 27, No. 4, pp. 206–219, http://dx.doi.org/10.5741/GEMS.27.4.206

Hsu T., Lucas A., Pardieu V. (2015) Splendor in the outback: A visit to Australia's opal fields. *G&G*, Vol. 51, No. 4, pp. 418–427, http://dx.doi.org/10.5741/GEMS.51.4.418

Hsu T., Lucas A., Kane R.E., McClure S.F., Renfro N.D. (2017) Big Sky country sapphire: Visiting Montana's alluvial deposits. *G&G*, Vol. 53, No. 2, pp. 215–227, http://dx.doi.org/10.5741/GEMS.53.2.215

Ibrahim E., Lema L., Barnabe P., Lacroix P., Pirard E. (2020) Small-scale surface mining of gold placers: Detection, mapping, and temporal analysis through the use of free satellite imagery. *International Journal of Applied Earth Observation and Geoinformation*, Vol. 93, article no. 102194, http://dx.doi.org/10.1016/j.jag.2020.102194

Jacob J., Grobbelaar, G. (2019) Onshore and nearshore diamond mining on the south-western coast of Namibia: Recent activities and future exploration techniques. *Journal of Gemmology*, Vol. 36, No. 6, pp. 524–532.

Jacob R.J., Bluck B.J., Ward J.D. (1999) Tertiary-age diamondiferous fluvial deposits of the Lower Orange River Valley, Southwestern Africa. *Economic Geology*, Vol. 94, No. 5, pp. 749–758.

Joshi K.B., Banerji U.S., Dubey C.P., Oliveira E.P. (2021) Heavy minerals in provenance studies: An overview. *Arabian Journal of Geosciences*, Vol. 14, No. 14, article no. 1330, http://dx.doi.org/10.1007/s12517-021-07687-y

Kampunzu A.B., Cailteux J.L.H., Kamona A.F., Intiomale M.M., Melcher F. (2009) Sediment-hosted Zn–Pb–Cu deposits in the Central African Copperbelt. *Ore Geology Reviews*, Vol. 35, No. 3/4, pp. 263–297, http://dx.doi.org/10.1016/j.oregeorev.2009.02.003

Kasiński J.R., Kramarska R. (2008) Sedimentary environment of amber-bearing association along the Polish-Russian Baltic coastline. In J. Rascher et al., Eds., *Bitterfeld Amber versus Baltic Amber - Hypotheses, Facts, Questions*. Excursion Guide and Publications of the German Society for Geosciences, Vol. 236, pp. 46–57.

Kelley R.L. (1954) Forgotten giant: The hydraulic gold mining industry in California. *Pacific Historical Review*, Vol. 23, No. 4, pp. 343–356, http://dx.doi.org/10.2307/3634653

Leelawatanasuk T., Wathanakul P., Paramita S., Sutthirat C., Sriprasert B., Bupparenoo P. (2013) The characteristics of amber from Indonesia. *Australian Gemmologist*, Vol. 25, No. 4, pp. 142–145.

Liesegang M., Milke R. (2014) Australian sedimentary opal-A and its associated minerals: Implications for natural silica sphere formation. *American Mineralogist*, Vol. 99, No. 7, pp. 1488–1499, http://dx.doi.org/10.2138/am.2014.4791

Maree B.D. (1987) The deposition and distribution of alluvial diamonds in South Africa. *South African Journal of Geology*, Vol. 90, No. 4, pp. 428–447.

Marquez-Zavalia M.F., Craig J.R. (2022) Stalactitic rhodochrosite from the 25 de Mayo and Nueve veins, Capillitas, Catamarca, Argentina: Physical and chemical variations. *Journal of Geosciences*, Vol. 67, No. 3, pp. 223–241, http://dx.doi.org/10.3190/jgeosci.354

Moore J.M., Moore A.E. (2004) The roles of primary kimberlitic and secondary Dwyka glacial sources in the development of alluvial and marine diamond deposits in Southern Africa. *Journal of African Earth Sciences*, Vol. 38, No. 2, pp. 115–134, http://dx.doi.org/10.1016/j.jafrearsci.2003.11.001

Mountford B., Tuffnell S., Eds. (2018) *A Global History of Gold Rushes*. University of California Press, Oakland, California, 336 pp.

Mudd G.M. (2007) Gold mining in Australia: Linking historical trends and environmental and resource sustainability. *Environmental Science and Policy*, Vol. 10, No. 7/8, pp. 629–644, http://dx.doi.org/10.1016/j.envsci.2007.04.006

Nakashole A.N., Hodgson D.M., Chapman R.J., Morgan D.J., Jacob R.J. (2018) Long-term controls on continental-scale bedrock river terrace deposition from integrated clast and heavy mineral assemblage analysis: An example from the lower Orange River, Namibia. *Sedimentary Geology*, Vol. 364, pp. 103–120,

http://dx.doi.org/10.1016/j.sedgeo.2017.12.010
Nikiforova Z.S. (2021) Criteria for determining the genesis of placers and their different sources based on the morphological features of placer gold. *Minerals*, Vol. 11, No. 4, article no. 381, http://dx.doi.org/10.3390/min11040381
Ovissi M., Yazdi M., Ghorbani M. (2017) The Persian turquoise mining at [the] Neyshabur mine in historical times. *Geography*, Vol. 14, No. 51, pp. 87–99.
Palke A.C., Shigley J.E. (2022) Colored Stones Unearthed: Gems formed in magmatic rocks. *G&G*, Vol. 58, No. 4, pp. 494–506.
Palke A.C., Renfro N.D., Hapeman J.R., Berg R.B. (2023) Gemological characterization of Montana sapphire from the secondary deposits at Rock Creek, Missouri River, and Dry Cottonwood Creek. *G&G*, Vol. 59, No. 1, pp. 2–45, http://dx.doi.org/10.5741/GEMS.59.1.2
Papineau D. (2020) Chemically oscillating reactions in the formation of botryoidal malachite. *American Mineralogist*, Vol. 105, No. 4, pp. 447–454, http://dx.doi.org/10.2138/am-2020-7029
Patyk-Kara N.G. (2002) Placers in the system of sedimentogenesis. *Lithology and Mineral Resources*, Vol. 37, No. 5, pp. 429–441.
Penny D. (Ed) (2010) *Biodiversity of Fossils in Amber from Major World Deposits*. Siri Scientific Press, Rochdale, United Kingdom, 304 pp.
Phillips D., Harris J.W., de Wit M.C.J., Matchan E.L. (2018) Provenance history of detrital diamond deposits, west coast of Namaqualand, South Africa. *Mineralogy and Petrology*, Vol. 112, Supp. 1, pp. 259–273, http://dx.doi.org/10.1007/s00710-018-0568-9
Rakontondrazafy A.F.M., Giuliani G., Ohnenstetter D., Fallick A.E., Rakotosamizanany S., Andriamamonjy A., Ralantoarison T., Razanatseheno M., Offant Y., Garnier V., Maluski H., Dunaigre C., Schwarz D., Ratrimo V. (2008) Gem corundum deposits of Madagascar: A review. *Ore Geology Reviews*, Vol. 34, No. 1/2, pp. 134–154.
Rey P.F. (2013) Opalisation of the Great Artesian Basin (central Australia): An Australian story with a Martian twist. *Australian Journal of Earth Sciences*, Vol. 60, No. 3, pp. 291–314, http://dx.doi.org/10.1080/08120099.2013.784219
Ross A. (2010) *Amber: The Natural Time Capsule*. Firefly Books Publishers, Richmond Hill, Canada, 112 pp.
Sachanbiński M., Kuleba M., Natkaniec-Nowak L. (2023) Chrysoprase – History and present. *Mineralogia*, Vol. 54, No. 1, pp. 1–10, http://dx.doi.org/10.2478/mipo-2023-0001
Sadowski E-M., Schmidt A.R., Seyfullah L.J., Kunzmann L. (2017) Conifers of the "Baltic amber forest" and their palaeoecological significance. *Stapfia*, Vol. 106, pp. 1–73.
Shigley J.E., Laurs B.M., Renfro N.D. (2009) Chrysoprase and prase opal from Haneti, central Tanzania. *G&G*, Vol. 45, No. 4, pp. 271–279, http://dx.doi.org/10.5741/GEMS.45.4.271
Shirdam B., Shen A.H., Yang M.X., Moktari Z., Fazliani H. (2021) Persian turquoise: The ancient treasure of Neyshabur. *G&G*, Vol. 57, No. 3, pp. 240–257, http://dx.doi.org/10.5741/GEMS.57.3.240
Stanaway K.J. (2012) Ten placer deposit models from five sedimentary environments. *Applied Earth Science*, Vol. 121, No. 1, pp. 43–51, http://dx.doi.org/10.1179/1743275812Y.0000000020
Standke H. (2008) Bitterfeld amber equal to Baltic amber? - A geological space-time consideration and genetic conclusions. In J. Rascher et al., Eds., *Bitterfeld Amber versus Baltic Amber - Hypotheses, Facts, Questions*. Excursion Guide and Publications of the German Society for Geosciences, Vol. 236, pp. 11–33.
Sun T.T., Kleišmantas A., Nyunt T.T., Minrui Z., Krishnaswamy M., Ying L.H. (2015) Burmese amber from Hti Lin. *Journal of Gemmology*, Vol. 34, No. 7, pp. 606–615.
Sutherland D.G. (1982) The transport and sorting of diamonds by fluvial and marine processes. *Economic Geology*, Vol. 77, No. 7, pp. 1613–1620, http://dx.doi.org/10.2113/gsecongeo.77.7.1613
Svisero D.P., Shigley J.E., Weldon R. (2017) Brazilian diamonds: A historical and recent perspective. *G&G*, Vol. 53, No. 1, pp. 2–33, http://dx.doi.org/10.5741/GEMS.53.1.2
Torvela T., Lambert-Smith J.S., Chapman R.J., Eds. (2022) *Recent Advances in Understanding Gold Deposits – from Orogeny to Alluvium*. Geological Society of London Special Publication, Vol. 516, 440 pp.
Vertriest W., Saeseaw S. (2019) A decade of ruby from Mozambique: A review. *G&G*, Vol. 55, No. 2, pp. 162–183, http://dx.doi.org/10.5741/GEMS.55.2.162
Weitschat W., Wichard W. (2010) Baltic amber. In D. Penny, Ed., *Biodiversity of Fossils in Amber from the Major World Deposits*, Siri Scientific Press, Rochdale, United Kingdom, pp. 81–116.
Wilson M.G.C., Henry G., Marshall T.R. (2006) A review of the alluvial diamond industry and the gravels of the North West Province, South Africa. *South African Journal of Geology*, Vol. 109, No. 3, pp. 301–314, http://dx.doi.org/10.2113/gssajg.109.3.301
Wolfe A.P., Tappert R., Muehlenbachs K., Boudreau M., McKellar R.C., Basinger J.F., Garrett A. (2009) A new proposal concerning the botanical origin of Baltic amber. *Proceedings of the Royal Society B*, Vol. 276, No. 1672, pp. 3403–3412, http://dx.doi.org/10.1098/rspb.2009.0806
Zhang Z., Jiang X., Wang Y., Kong F., Shen A.H. (2020) Fluorescence characteristics of blue amber from the Dominican Republic, Mexico, and Myanmar. *G&G*, Vol. 56, No. 4, pp. 484–496, http://dx.doi.org/10.5741/GEMS.56.4.484
Zwaan J.C., Buter E., Mertz-Kraus R., Kane R.E. (2015) Alluvial sapphires from Montana: Inclusions, geochemistry, and indications of a metasomatic origin. *G&G*, Vol. 51, No. 4, pp. 370–391, http://dx.doi.org/10.5741/GEMS.51.4.370

GEM NEWS INTERNATIONAL

Contributing Editors
Gagan Choudhary, *IIGJ-Research & Laboratories Centre, Jaipur, India* (gagan.choudhary@iigjrlc.org)
Christopher M. Breeding, *GIA, Carlsbad* (christopher.breeding@gia.edu)
Guanghai Shi, *School of Gemmology, China University of Geosciences, Beijing* (shigh@cugb.edu.cn)

COLORED STONES AND ORGANIC MATERIALS

Blue amblygonite-montebrasite from Rwanda. Amblygonite-montebrasite, with the formula $LiAlPO_4(F,OH)$, is a fluorophosphate mineral series found in granitic pegmatites and pegmatite-related environments. The Pala district in California and the Black Hills in South Dakota are historic U.S. sources of amblygonite-montebrasite for industrial use, but most of the world's well-known pegmatite districts have also produced considerable quantities of amblygonite-montebrasite.

A relatively common rock-forming mineral in these specific environments, the mineral is typically opaque and contains abundant fractures. Its color is often an unremarkable creamy white, causing it to blend in with associated feldspars. All of these factors limit its use as a gemstone. When used as a gem material, it is often colorless to yellow-green.

Figure 1. The newly discovered variety of amblygonite-montebrasite is unique for its blue color. It often has a mottled appearance with alternating blue and creamy white patches. The faceted stone weighs 0.83 ct. Photo by Lhapsin Nillapat.

Geologists are interested in this mineral because of its high lithium content (up to 10%), which often suggests the presence of other (and easier to process) lithium minerals nearby. With increasing demand for lithium ores, exploration teams around the world are paying closer attention to amblygonite-montebrasite as an indicator of high lithium content in geological environments. This was the case in western Rwanda, an area known for its pegmatite-related tin deposits, where local geologists discovered an unusual variety of amblygonite-montebrasite in multiple pegmatites and sent it to mineral traders in Bangkok.

The new material (figure 1) differs from classic varieties in that its color is bright blue, sometimes associated with creamy white patches in a mottled pattern. All other characteristics match the known properties of amblygonite-montebrasite.

Confocal Raman spectroscopy showed a perfect match with amblygonite for several of the whitish and all of the bright blue patches. The position of certain peaks is related to the fluorine concentration in the mineral and can help to estimate the distribution between both end members (B. Rondeau et al., "A Raman investigation of the amblygonite-montebrasite series," *Canadian Mineralogist*, Vol. 44, No. 5, 2006, pp. 1109–1117). The position of the peak around 1060 cm^{-1} was in the lower range (1052 cm^{-1} or lower), which points to a very fluorine-poor composition, near pure montebrasite. Raman spectroscopy performed at

Editors' note: Interested contributors should send information and illustrations to Stuart Overlin at soverlin@gia.edu.

Gems & Gemology, Vol. 59, No. 4, pp. 524–542.

GIA's Bangkok laboratory also revealed the presence of other minerals in the creamy white matrix. This included a mix of complex phosphates that share mineralogical and chemical similarities (e.g., berlinite, souzalite, and trolleite, confirmed by Raman spectroscopy) as well as feldspar. The only exception in terms of coloration consisted of small dark blue spots of the mineral scorzalite, with the formula $(Fe^{2+},Mg)Al_2(OH,PO_4)_2$, a common secondary phase in complex, phosphate-rich pegmatites.

Despite advanced techniques indicating that this newly discovered variety, as well as the majority of previously documented gems, are closer to montebrasite (the OH-rich end member), the gemological community keeps referring to these materials as amblygonite. Amblygonite-montebrasite remains a rare gem that is unfamiliar to the general consumer. It requires considerable care due to its perfect cleavage and hardness of approximately 6, making it less suitable for daily wear. With this new addition to its color range, amblygonite-montebrasite might gain more recognition.

Wim Vertriest
GIA, Bangkok
Gil Yuda
Gil Yuda Mogok Minerals Ltd.
Bangkok
Joe Henley
Joe Henley Rough & Gemstones, LLC
Portland, Oregon

FTIR identification of carbon dioxide fluids in sapphire. Carbon dioxide is well known as a trapped fluid in negative crystals in sapphire. From room temperature to cooler temperatures, the negative crystals change from a single supercritical fluid phase to two phases of gas and liquid. This feature is fascinating to observe under the microscope (e.g., Spring 2016 *G&G* Micro-World, pp. 78–79). These fluid inclusions are considered proof that a sapphire has not undergone thermal treatment (e.g., J.I. Koivula, "Carbon dioxide fluid inclusions as proof of natural-colored corundum," Fall 1986 *G&G*, pp. 152–155).

However, the Summer 2020 issue of *G&G* reported on a sapphire heated with pressure that contained a carbon dioxide gas bubble even after treatment (N. Ng-Pooresatien, "Lab Notes: Negative crystal containing a mobile CO_2 bubble in blue sapphire heated with pressure," pp. 287–288). Most previous reports about carbon dioxide fluid inclusions were based on microscopic observation, but this one addressed the presence of carbon dioxide fluid using Fourier-transform infrared (FTIR) spectroscopy.

Figure 2 shows two sapphires from Sri Lanka and Myanmar with fluid inclusions of primary and secondary negative crystals. FTIR spectra of these two sapphires are presented in figure 3. The two peaks at 3601 and 3705 cm^{-1} are easily confused with kaolinite-related peaks at 3619 and 3698 cm^{-1}. All of the spectra show several peaks assigned to dense carbon dioxide vibration and combination overtone bands. The 2342 cm^{-1} peak is C=O asymmet-

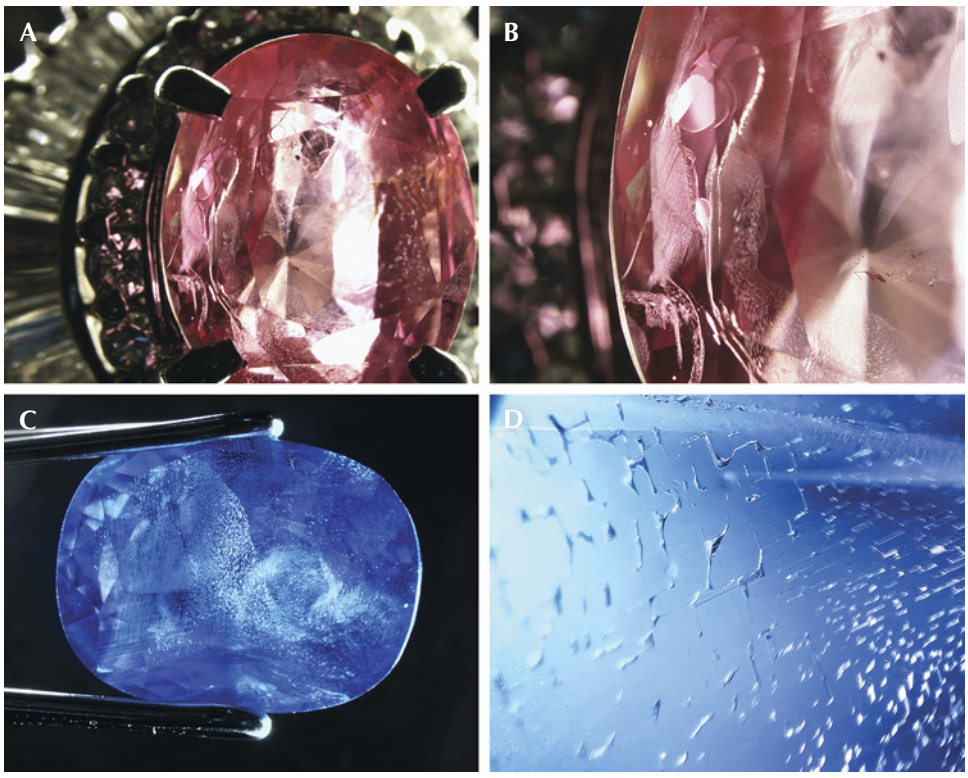

Figure 2. Various negative crystals in pink sapphire from Sri Lanka (A, enlarged in B) and fingerprints in blue sapphire from Myanmar (C, enlarged in D). Image B shows bubbles in flat negative crystals, and the center negative crystal in D has a bubble. Photomicrographs by Momo Matsumura (A and B) and Shunsuke Nagai (C and D); fields of view 4.05 mm (A), 8.15 mm (B), 8.47 mm (C), and 1.71 mm (D).

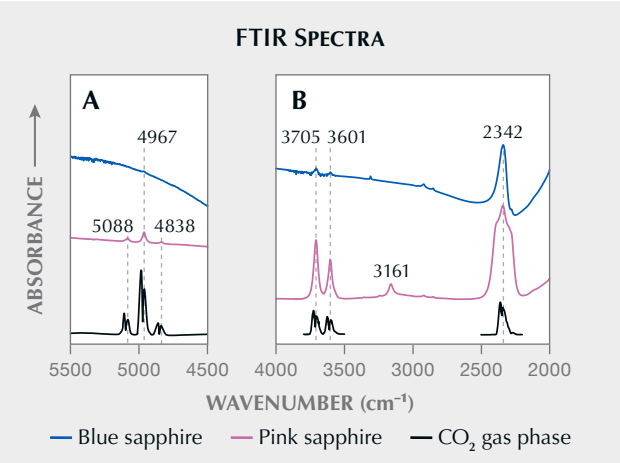

Figure 3. FTIR spectra of the two sapphires from figure 2 indicate dense carbon dioxide–assigned peaks from 2000 to 4000 cm^{-1} and 4500 to 5500 cm^{-1}. The two peaks at 3601 and 3705 cm^{-1} are easily mistaken for kaolinite peaks at 3619 and 3698 cm^{-1}.

ric stretching vibration ν_3. The 3601 and 3705 cm^{-1} peaks are $2\nu_2 + \nu_3$ and $\nu_1 + \nu_3$ first Fermi resonance, respectively. The 4838, 4967, and 5088 cm^{-1} peaks are $4\nu_2 + \nu_3$, $\nu_1 + 2\nu_2 + \nu_3$, and $2\nu_1 + \nu_3$ second Fermi resonance peaks, respectively, where ν_1 is a symmetric stretching and ν_2 is a doubly degenerate bending (table 1). Those peaks generally present double absorption bands, P- and R-contour, under atmospheric pressure and temperature due to the rotational transitions that occur for the stretching band, as seen in the bottom spectrum of figure 3. The double peaks change to a single peak, increasing the carbon dioxide fluid density by more than ~0.4 g/cm^3 (M. Buback et al., "Near infrared absorption of pure carbon dioxide up to 3100 bar and 500 K. I. Wavenumber range 3200 cm^{-1} to 5600 cm^{-1}," *Zeitschrift für Naturforschung A*, Vol. 41, 1986, pp. 505–511; A. Oancea et al., "Laboratory infrared reflection spectrum of carbon dioxide clathrate hydrates for astrophysical remote sensing applications," *Icarus*, Vol. 221, No. 2, 2012, pp. 900–910).

In order to prove the high density of carbon dioxide fluids, this author used micro-Raman spectroscopy. Raman spectra of carbon dioxide in fluid inclusions show a Fermi diad (or doublet) (figure 4), which is useful in estimating carbon dioxide fluid pressure and density in negative crystals (e.g., J. Yamamoto et al., "Paleo-Moho depth determined from the pressure of CO_2 fluid inclusions: Raman spectroscopic barometry of mantle- and crust-derived rocks," *Earth and Planetary Science Letters*, Vol. 253, 2007, pp. 369–377; H.M. Lamadrid et al., "Reassessment of the Raman CO_2 densimeter," *Chemical Geology*, Vol. 450, 2016, pp. 201–222). Using the equations reported by Lamadrid et al. (2016), carbon dioxide fluid densities in sapphires measured by FTIR spectra were estimated at 0.54–0.74 g/cm^3. This density is consistent with the results derived from FTIR spectra in figure 3.

TABLE 1. Carbon dioxide vibration band position (Buback et al., 1986; Oancea et al., 2012).[a]

Wavenumber (cm^{-1})	Mode/assignment
2342	C=O asymmetric stretching vibration ν_3
3601	$2\nu_2 + \nu_3$ (first Fermi resonance)
3705	$\nu_1 + \nu_3$ (first Fermi resonance)
4838	$4\nu_2 + \nu_3$ (second Fermi resonance)
4967	$\nu_1 + 2\nu_2 + \nu_3$ (second Fermi resonance)
5088	$2\nu_1 + \nu_3$ (second Fermi resonance)

[a] *ν_1 is a symmetric stretching, and ν_2 is a doubly degenerate bending.*

According to the Summer 2020 Lab Notes entry, sapphire with heat and pressure showed a strong broad peak at 3047 cm^{-1} with C=O asymmetric stretching vibration ν_3 at 2342 cm^{-1} and no other peaks at wavenumbers higher than 3600 cm^{-1}. The Raman spectra also revealed a carbon dioxide Fermi diad (N. Ng-Pooresatien, pers. comm., 2023), and the density was estimated to be 0.11–0.18 g/cm^3, which is about one-fifth lower. The existence of carbon dioxide bubbles in a negative crystal is therefore no longer definitive proof of the absence of thermal

Figure 4. Raman spectrum of carbon dioxide showing the Fermi diad (or doublet) from a negative crystal inclusion in a sapphire.

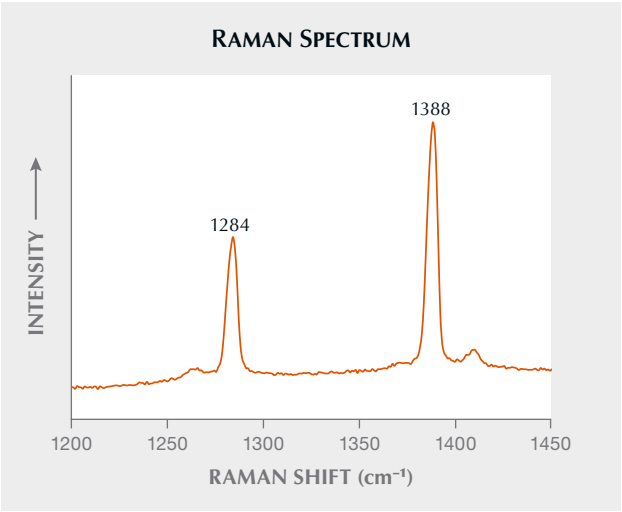

Figure 5. Demantoid garnet (0.84 ct on the left and 0.28 ct on the right) and an orange grossular garnet (0.55 ct) from Sonora, Mexico. Photo by Diego Sanchez.

treatment. This investigation also showed that FTIR analysis is a useful method for detecting the high density of carbon dioxide fluid in sapphire, and the resulting FTIR peaks above 3600 cm^{-1} could indicate the absence of heat treatment.

Kazuko Saruwatari
GIA, Tokyo

Demantoid, andradite, and grossular from Mexico. Iridescent andradite garnet is an interesting phenomenal stone that was initially produced in Nevada but has also been found in Mexico, Japan, and New Mexico. A small parcel consisting of three stones (figure 5) was recently submitted to GIA's Carlsbad laboratory and contained some new gem material from the iridescent andradite deposit in Mexico. The deposit is located high in the Sonoran Sierra in the Mexican state of Sonora about 145 km northeast of the city of Hermosillo. The stones were provided by Marion Alberto Márquez Suárez, who works with the mine owner, Salvador Barba.

Figure 6. Mineral inclusions in a Mexican demantoid. Photomicrograph by Aaron Palke; field of view 1.26 mm.

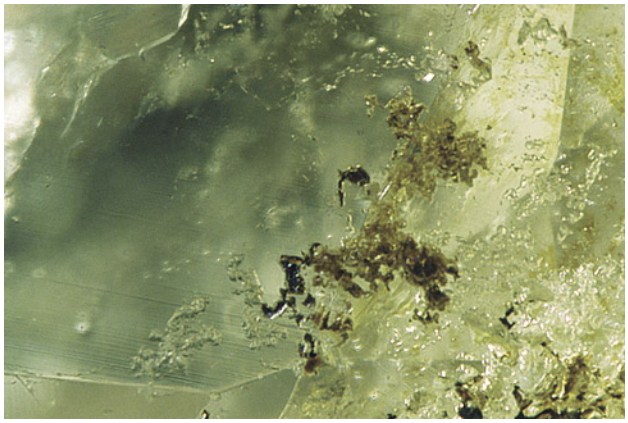

Standard gemological testing gave a refractive index of 1.740 for the grossular garnet and over-the-limit readings for the demantoid garnets. All three samples were inert to both long-wave and short-wave ultraviolet light. Fingerprints and fields of fluid inclusions as well as colorless and dark crystal inclusions were observed (figure 6). The inclusion scenes were reminiscent of skarn-related demantoid garnet from Namibia and Madagascar rather than the horsetail inclusion scenes noted in serpentinite-related demantoid from Russia. Trace element chemistry was collected as part of an ongoing project for demantoid origin determination. Curiously, the demantoid garnets had low gallium levels ranging from 0.45 to 1.96 ppm. This is more in line with serpentine-related demantoid, with gallium less than 1 ppm, than with skarn-related demantoid, which always has gallium levels above 2 ppm. Chromium was also below detection limits, which is consistent with iron-colored demantoid from skarn-related deposits. While these Sonoran demantoid and other garnets are not currently on the market, the miners have produced up to 7 kg of the material over the last 10 years.

Aaron Palke
GIA, Carlsbad

An unusual partially non-nacreous *Pinctada radiata* natural blister pearl. The vast majority of pearls produced by the different *Pinctada* species display a lustrous nacreous surface structure. However, a small percentage of these pearls exhibit non-nacreous surfaces. GIA's Mumbai laboratory received one very interesting example for scientific examination: a partially non-nacreous natural blister pearl, obtained from the waters of Bahrain by a noted pearl diver in March 2023.

The shell weighed 21 g and measured approximately 64.55 × 63.90 × 7.72 mm. The back of the shell showed fine layered striations toward one end and areas of massive parasite holes toward the center and hinge area. The inner surface was silvery cream in color with strong orient and held a large light cream and brownish black baroque pearl, measuring approximately 11.39 × 9.31 × 8.69 mm, attached close

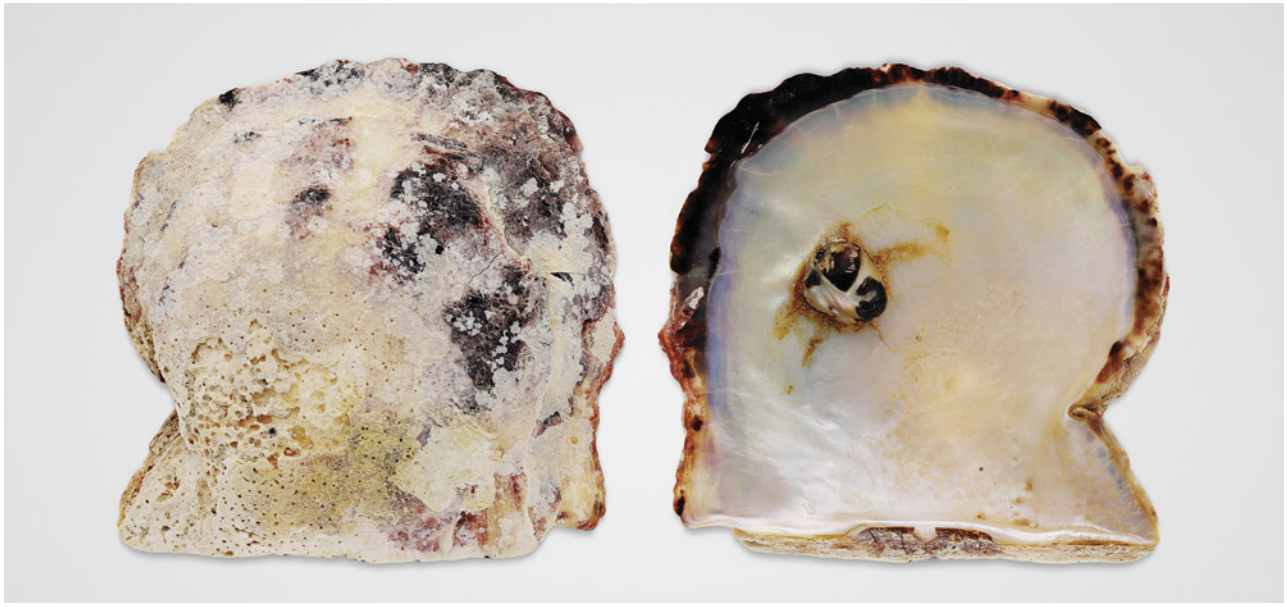

Figure 7. Pinctada radiata *shell with a natural blister pearl measuring approximately 11.39 × 9.31 × 8.69 mm. Photo by Gaurav Bera.*

to the upper mantle-lip area (figure 7). This blister pearl was very unusual compared to those typically found in the *Pinctada radiata* mollusk. Viewed under 40× magnification, the inner shell's brown edges exhibited columnar calcite honeycomb-like structures, while the white portion displayed the typical platy structure of fine nacreous overlapping aragonite platelets, presenting a chalky appearance near the hinge. Surrounding the central blister pearl was a yellowish brown region consisting of desiccated organic matter.

A closer look at the light cream, strongly iridescent section of the blister pearl with the distinctive platy structure looked more like "fingerprints," distinctly separated by a delineated step feature from the adjacent black area. The black region was noticeably dull and matte and covered by a translucent layer revealing circular botryoidal surface spirals with a calcitic columnar pattern. Additionally, significant surface-reaching cracks were present in the translucent black area along the columnar structures (figure 8, left). Within the non-nacreous "cellular" structure, a layer had peeled off, accentuating the light cream calcitic step feature (figure 8, right).

Real-time microradiography imaging of the blister pearl and its host shell revealed a distinct outline showing the point of attachment of the pearl to the shell. An organic-rich

Figure 8. Left: Partially non-nacreous blister pearl showing significant surface-reaching cracks (blue arrow) and a distinct delineated step feature separating the light cream area from the adjacent black area (red arrow). Right: A columnar honeycomb-like calcite structure was observed at the edge of the step feature; field of view 14.40 mm. Photos by Karan Rajguru.

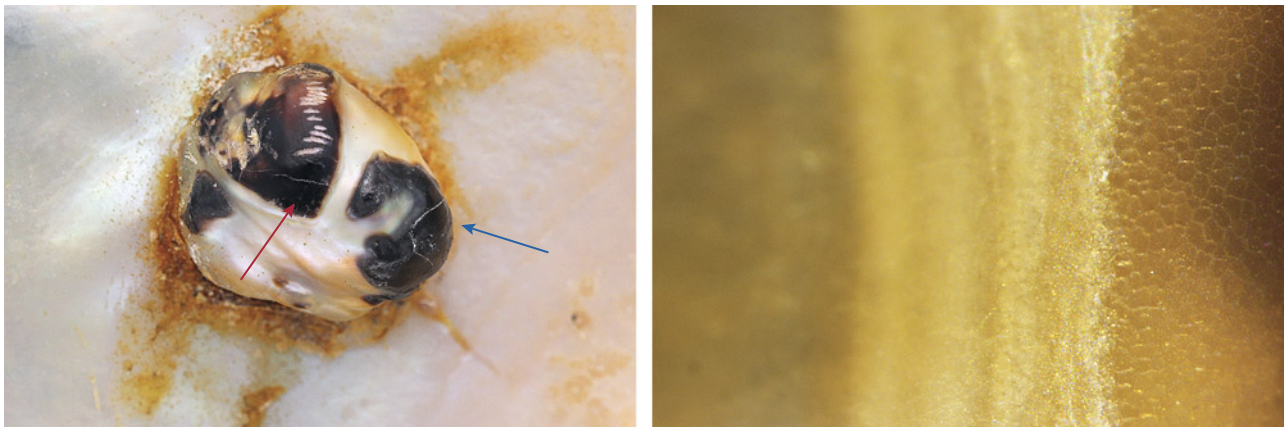

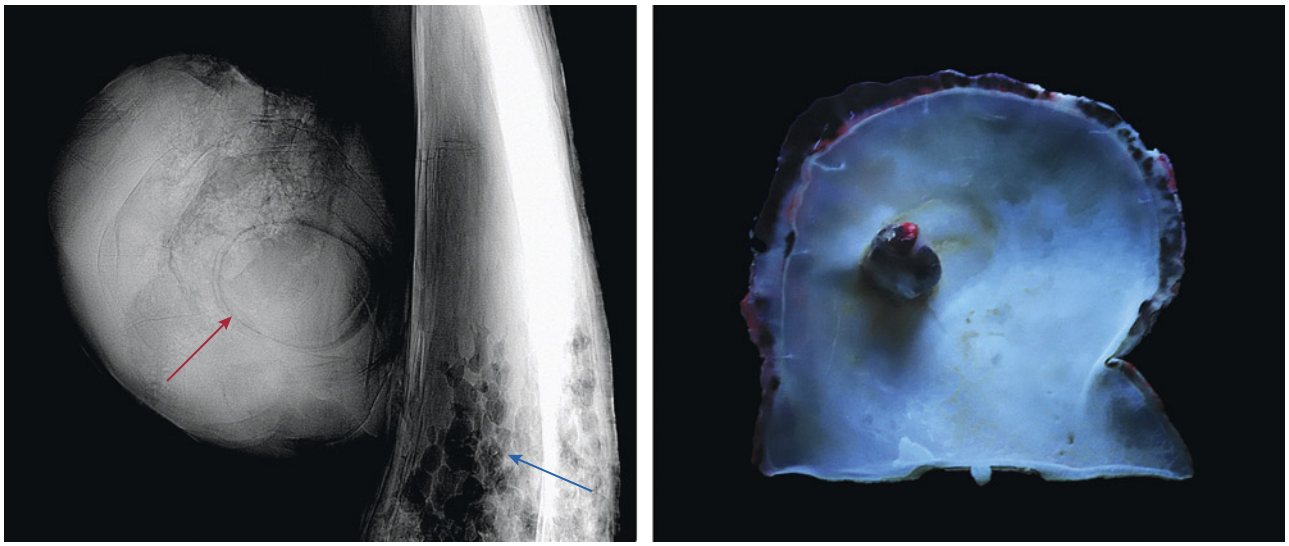

Figure 9. Left: A real-time microradiograph image showing the internal structure of the blister pearl consisting of an organic-rich core surrounded by concentric growth arcs (red arrow) with parasite holes in the host shell (blue arrow). Right: Strong orangy red reaction under long-wave UV light, observed on the edge of the shell and part of the black area on the blister pearl. Photos by Lubna Sahani (left) and Gaurav Bera (right).

core with contrasting patchy light and dark gray areas occupied almost half of the pearl's internal structure (figure 9, left). This was surrounded by concentric growth arcs, which are classic features of natural pearl structures, similar to those observed in known *Pinctada radiata* pearls from GIA's research database. In addition, significant cracks extending from the pearl to the shell and parasite tubes forming a dendritic pattern in the host shell were seen when the pearl was X-rayed in other directions. The structure indicated a natural whole pearl that had attached itself to the host shell ("Natural shell blisters and blister pearls: What's the difference?" *GIA Research News*, August 26, 2019).

Due to the limitations imposed by the size of the shell, it was not possible to collect chemical data on the pearl using energy-dispersive X-ray fluorescence spectrometry. However, both shell and pearl showed an inert reaction when exposed to X-ray fluorescence, indicative of its saltwater origin. An interesting reaction was observed under long-wave ultraviolet light. The edge of the shell and part of the black area on the pearl showed a strong orangy red fluorescence, while the inner part of the shell displayed a weak blue reaction (figure 9, right). The shell was inert under short-wave UV. Similar reactions linked to a type of porphyrin pigment have been observed in partially non-nacreous and nacreous pearls from the *Pteria* species (S. Karampelas, "Black non-nacreous natural pearls from *Pteria* species," *Journal of Gemmology*, Vol. 35, No. 7, 2017, pp. 590–592). Raman spectroscopy using 514 nm and 814 nm laser excitation revealed peaks at 701/704 cm^{-1} and 1086 cm^{-1}, indicative of aragonite. Due to high fluorescence, no calcitic peaks were observed in the non-nacreous area. Photoluminescence spectra collected from both the shell and the blister pearl revealed three broad peaks centered at 620, 650, and 680 nm, which are characteristic of some naturally colored pearls.

Formation of natural blister pearls in the wild has always been an interesting topic of research for gemological laboratories. The studied sample is certainly noteworthy due to its size, partially non-nacreous structure, and unique reaction under long-wave ultraviolet light.

Abeer Al-Alawi, Lubna Sahani, Karan Rajguru, and Roxane Bhot Jain
GIA, Mumbai

A unique omphacite jade pendant. In the past decade, omphacite jade with strong to vivid green color has increased in popularity. Especially noteworthy is the high-quality omphacite jade now coming from Guatemala. There are generally two types of omphacite jade. The first, commonly known as "black omphacite jade" (*mo cui* in Chinese), is typically opaque to semitranslucent and black to dark green. The second type contains higher chromium content and is usually made into cabochons, tablets, and pendants of 2–3 mm thickness to produce a strong green color and semitransparent appearance.

Recently, a carved pendant measuring 68.4 × 39.9 × 6.4 mm was submitted to the Taiwan Union Lab of Gem Research (TULAB) for identification (figure 10). The pendant was semitranslucent; its color appeared black when viewed under reflected light but dark green and yellow when viewed with transmitted light. Due to the pendant's uneven surface, its refractive indexes were challenging to measure. The dark

Figure 10. An omphacite jade pendant measuring 68.4 mm tall, shown in reflected light (left) and transmitted light (right). Photo by Tsung-Ying Yang.

green part showed a refractive index of approximately 1.67, and that of the yellow part was around 1.71 (both by spot reading). To further confirm the mineral composition, Raman spectroscopy with 785 nm excitation was performed on the yellow and dark green areas. The spectra were compared with the RRUFF database (Lafuente et al., 2015, https://rruff.info/about/downloads/HMC1-30.pdf) in figure 11, and the results indicated that the main component of the dark green portion of this pendant was omphacite. However, the yellow regions were identified as vesuvianite, constituting approximately 30% of the entire piece. Omphacite jade displaying both dark green omphacite and paragenetic yellow vesuvianite are not common.

From a gemological perspective, this green and yellow pendant is undoubtedly an exceptional case, given the rarity of omphacite jade coexisting with vesuvianite. However, precisely calculating the amounts of omphacite and vesuvianite with destructive X-ray diffraction analysis was not possible.

Shu-Hong Lin
Institute of Earth Sciences,
National Taiwan Ocean University
Taiwan Union Lab of Gem Research, Taipei

Tsung-Ying Yang, Kai-Yun Huang, and Yu-Shan Chou
Taiwan Union Lab of Gem Research, Taipei

Star beryl. Asterism is not a common phenomenon in beryl species, but it has previously been reported in emerald and aquamarine (K. Schmetzer et al., "Asterism in beryl, aquamarine and emerald – an update," *Journal of Gemmology*, Vol. 29, No. 2, 2004, pp. 65–71; Fall 2015 Gem News International, pp. 334–335). Recently, the author observed several star black beryl bead bracelets purchased from a Chinese e-commerce platform. For this report, four beads with noticeable asterism were collected for testing. The material was called "Devil Blue" aquamarine. The beads ranged from 9.11 to 9.47 mm in diameter and displayed a star phenomenon.

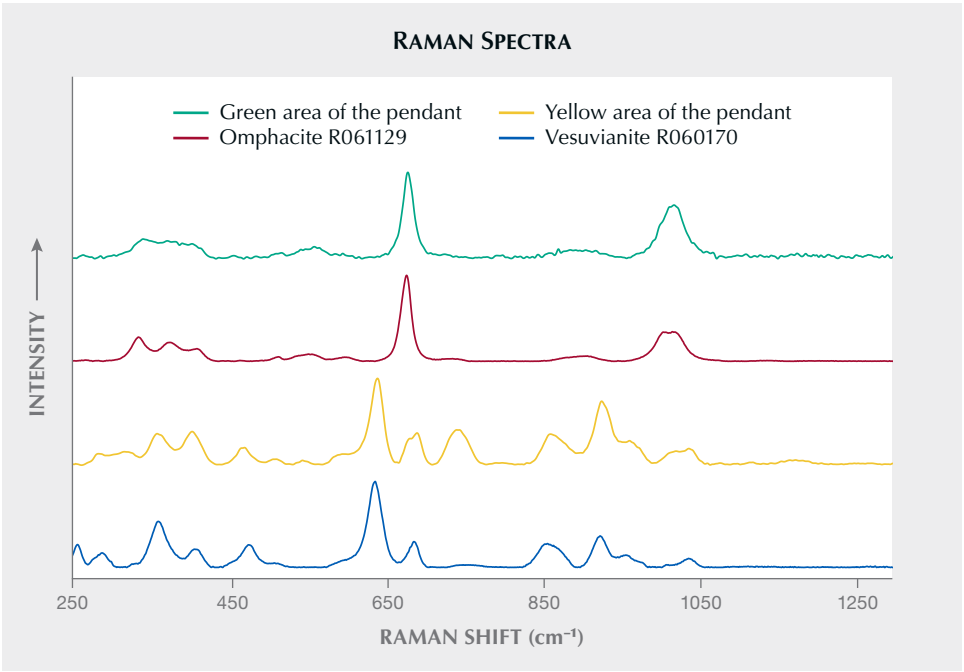

Figure 11. Comparisons between the Raman spectra of the jade pendant and the spectra of RRUFF database. The results confirmed that the green part of the jade pendant is omphacite and the yellow part is vesuvianite. The stacked spectra are baseline-corrected and normalized.

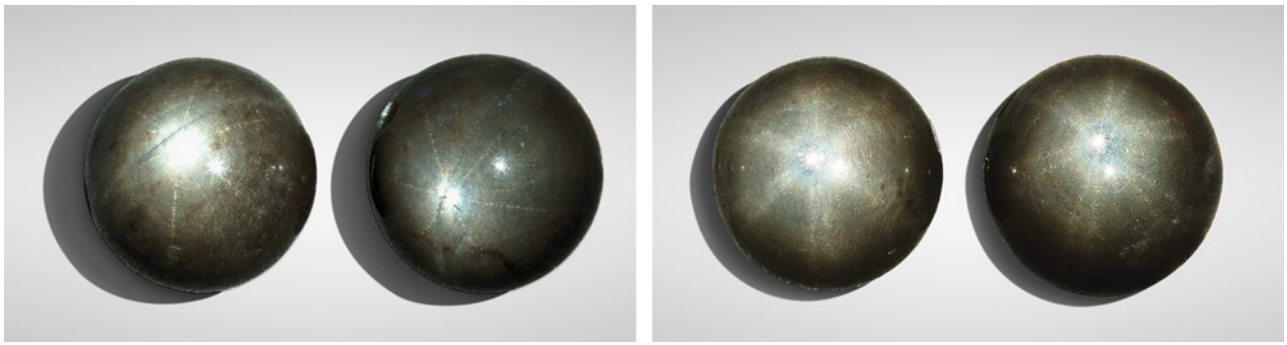

Figure 12. Left: Black beryl beads displaying six-rayed stars. Right: Black beryl beads displaying twelve-rayed stars. Photos by Tinh Xuan Nguyen.

Of the four beads, two had six-rayed stars with arms intersecting at 60° angles (figure 12, left) and two had twelve-rayed stars with two sets of six-rayed stars located in the same concentric point but with different orientations—the two stars were offset by approximately 10° (figure 12, right). Gemological testing of the beads provided the following characteristics: a hydrostatic specific gravity varying from 2.67 to 2.73, a spot refractive index of 1.57, an inert reaction under long-wave and short-wave UV, and no diagnostic absorption spectrum. These properties were consistent with beryl. Raman analysis confirmed the material was beryl.

Figure 13. The observed asterism was due to oriented iridescent needle inclusions. Several dark intersecting lines with lower relief are from the hexagonal growth structure of beryl. Photomicrograph by Tinh Xuan Nguyen; field of view 0.5 mm.

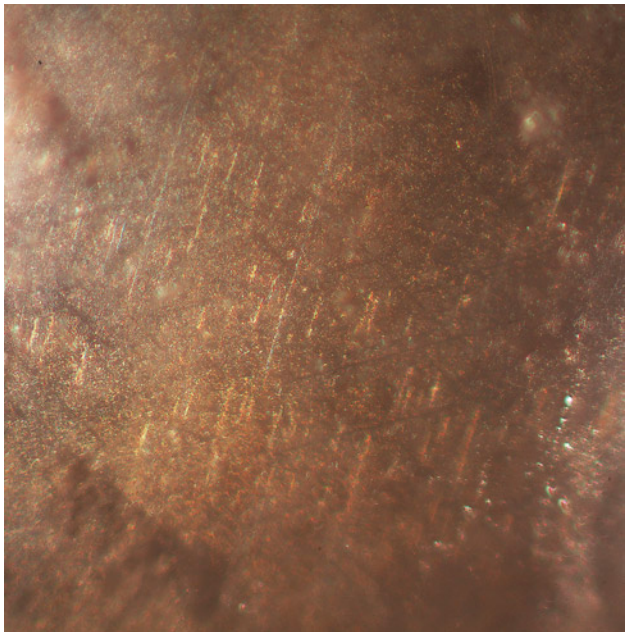

Under the microscope, we observed numerous needle inclusions oriented perpendicular to the *c*-axis and parallel to the three *a*-axes, which caused the asterism (figure 13). Moreover, the needles were concentrated as layers, forming multiple parting planes (figure 14) parallel to the basal pinacoid plane in all beads. This parting, combined with the presence of twelve-rayed stars, suggested that the growth orientation of this beryl was changing during the growth process. Additionally, the samples also showed an intersecting structure (figure 13) with angles of 120°/60° that resembled part of the hexagonal growth structure previously observed on the pinacoid of an aquamarine (Spring 2022 *G&G* Micro-World, pp. 70–71). This structure highlights that the asterism is oriented perpendicular to the *c*-axis, allowing the easy determination of this direction in translucent to opaque beryl.

Tinh Xuan Nguyen
PNJ Laboratory Company Ltd.
Ho Chi Minh City

Figure 14. Multiple parting planes, illustrated by parallel lines lying perpendicular to the c*-axis, represent the differing concentrations of oriented needle inclusions occurring during growth. Photomicrograph by Tinh Xuan Nguyen; field of view 0.5 mm.*

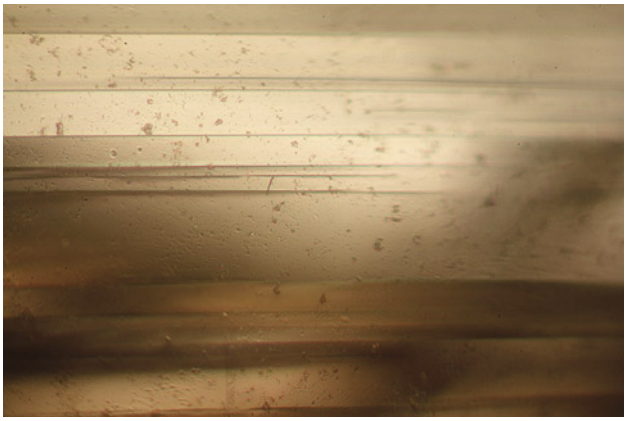

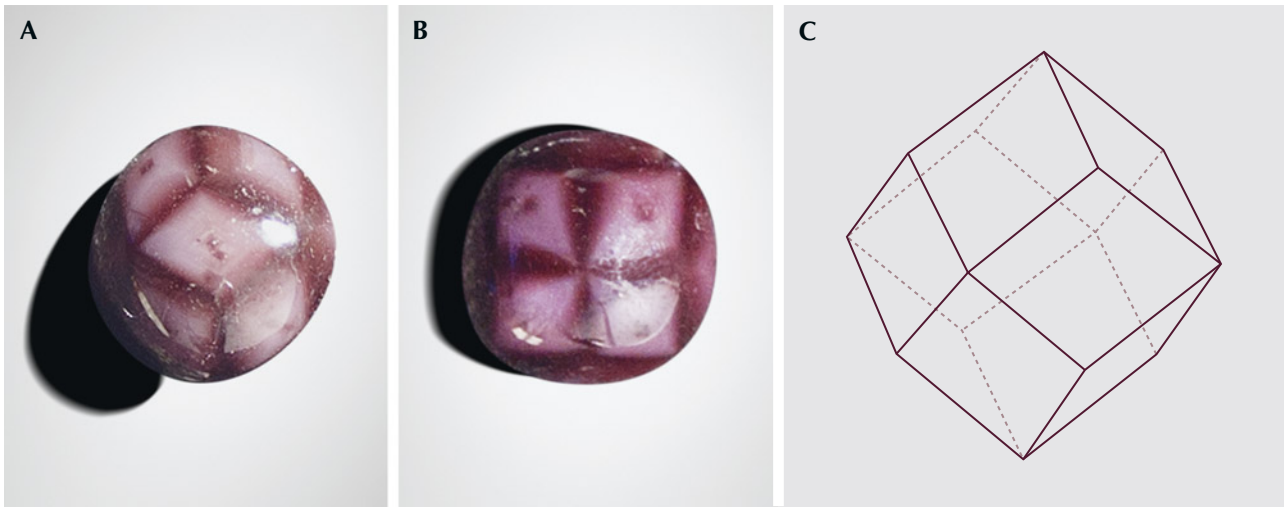

Figure 15. The color zoning in this 3.57 ct almandine garnet creates a cross structure that forms three-arm (top of A) and four-arm trapiche patterns (B) at every intersecting point of the crystal. These color zones are arranged along the edges of the dodecahedron (C). Photos by Le Ngoc Nang.

Trapiche garnet from Vietnam. The garnet group contains the most gem-quality species for jewelry manufacturing. Phenomenal garnets such as almandine and pyrope species are also known for their four- and six-rayed asterism. Nevertheless, the trapiche structure found in emerald, ruby, sapphire, tourmaline, and quartz is extremely rare in garnet. This structure can be considered an immobile star phenomenon. Inclusions and color zoning are responsible for the formation of two-, four-, or six-arm trapiche patterns.

Recently, the authors received a garnet sample originating from Thac Ba Lake in the Yen Bai province of Vietnam, obtained by a local miner. The 3.57 ct polished gem was pinkish white and reddish brown, translucent to opaque, and measured 7.11 × 6.90 × 6.40 mm. The diamond-shaped pinkish white portions were surrounded by reddish brown color zones, creating three-arm and four-arm trapiche patterns (see the video clip at www.gia.edu/gems-gemology/winter-2023-gemnews-trapiche-garnet).

Gemological testing revealed the sample's specific gravity of 4.16 and refractive index of 1.78. The stone displayed absorption spectra with distinct bands at 504, 520, and 573 nm, and it was inert under ultraviolet light for both long-wave and short-wave. All the data confirmed the almandine garnet species.

Observing all sides of the stone, we identified 14 trapiche patterns, including 6 four-arm and 8 three-arm patterns, surrounding 12 diagonal faces (figure 15). The arms grew outward from the center of the four-arm trapiches and inward for the three-arm trapiches. While the reddish brown portions extended along the edges of the garnet crystal, the diagonal lines formed the faces of the rhombic dodecahedron crystal, a typical crystal habit of almandine originating from metamorphic rock. Interestingly, when illuminated with a flashlight, the trapiche patterns glowed a fascinating vivid red and outlined the diamond-shaped portions in sharp contrast (figure 16).

Using the gemological microscope, we found that the reddish brown color zones were not colored by inclusions. In contrast, we hypothesized that the reddish hue might be induced by the dispersion of metal ions—in this case, iron (E. Fritsch and G.R. Rossman, "An update on color in gems. Part 1: Introduction and colors caused by dispersed metal ions," Fall 1987 *G&G*, pp. 126–139). The position of the color zoning along the edges of the crystal might be explained by the concentration of coloration elements in the crystal's symmetrical planes. The reddish brown zones had higher transparency than the crystal planes, producing a "glowing net" when shining a light through the stone.

Figure 16. This 3.57 ct garnet emits vivid red through the trapiche patterns when shining a flashlight through the gem. Photo by Le Ngoc Nang.

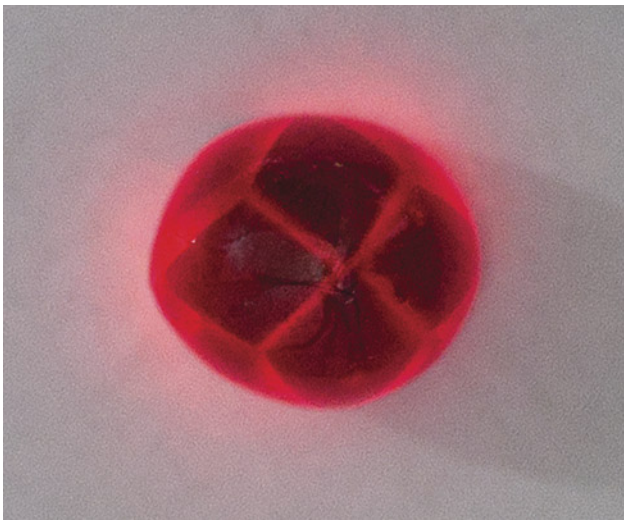

Although the trapiche pattern has been observed in several gems, it is rarely seen in garnet. The 14 trapiche patterns together in one specimen make this garnet unique.

Le Ngoc Nang, Ho Nguyen Tri Man, and Pham Minh Tien
Liu Gemological Research and Application Center
Ho Chi Minh City

Pyritized triceratops fossils from South Dakota. In recent years, the Hell Creek Formation spanning the Dakotas, Montana, and Wyoming has been extensively studied by paleontologists. This rock formation is home to fossils of various vertebrates, including dinosaurs such as *Tyrannosaurus rex* and triceratops. The author, an amateur paleontologist, recently unearthed a new dinosaur fossil site on privately owned land in Perkins County, on the northern edge of South Dakota.

Although multiple creatures are being uncovered at the site, closer examination of these fossils recovered revealed that they were from triceratops (figure 17). In addition, the fossils contained pyrite, an iron sulfide also known as "fool's gold" that forms in sedimentary rocks, giving the fossils a striking metallic appearance. This discovery of pyrite inspired the author to cut and polish the fossils into pieces for collectors to display (figure 18). Sixteen pieces have been cut so far.

Only water was used for cutting, to avoid dust inhalation and to keep the specimens from turning black. A cerium oxide polishing compound was used for the finish, followed by a drying process. The pieces were then treated with an epoxy adhesive to prevent pyrite decay.

The newfound dinosaur site in the Hell Creek Formation of South Dakota holds the promise of unveiling more treasures from the past. As the author's team and others dive deeper into the site, they hope to uncover additional fossils, providing insight into the long-lost world of dinosaurs.

Deven Fisher
Rapid City, South Dakota

Figure 17. Triceratops fossils recovered from the Hell Creek Formation in South Dakota. Photo by SD Gem & Fossil.

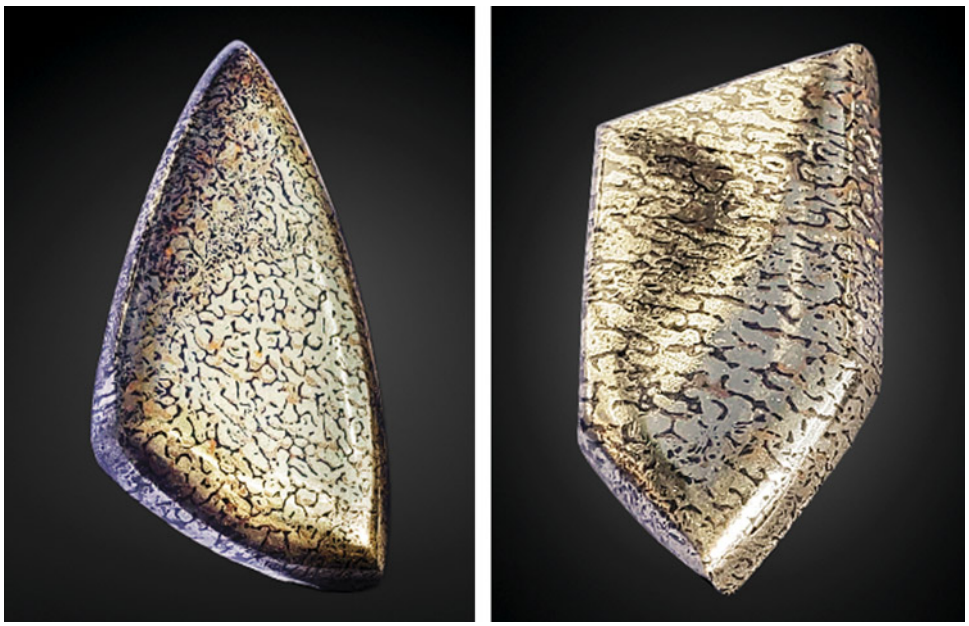

Figure 18. The cut and polished piece of pyritized triceratops fossil on the left weighs 50.5 ct and measures 41.28 × 22.23 mm. The piece on the right weighs 22.5 ct and measures 31.75 × 15.88 mm. Photos by SD Gem & Fossil.

Figure 19. The "Infinite Blue," an 11.28 ct Fancy Vivid blue diamond, sold for $25.3 million in Hong Kong. Courtesy of Sotheby's.

Figure 20. Selling for $44 million, the 17.61 ct Internally Flawless "Bleu Royal" became the most expensive auction jewel of 2023. Courtesy of Christie's Images Ltd. 2023.

AUCTION REPORT

Fall 2023 auction highlights. Following the controversial three-part sale of Heidi Horten's jewels in the spring (Summer 2023 GNI, pp. 254–256), Christie's announced the cancellation of the fourth sale ahead of the fall auction season. The late Austrian billionaire's estate made headlines earlier in the year because of her husband's connection to Nazi Germany, resulting in considerable backlash against Christie's despite their pledge to donate part of commissions to Holocaust-related charities.

In early October, Sotheby's kicked off the season with a single-lot sale of the 11.28 ct "Infinite Blue" (figure 19) in Hong Kong. Celebrating its 50th year in Asia, the auction house offered the Fancy Vivid blue type IIb diamond from the Cullinan mine in South Africa set in a ring with a pink diamond halo and colorless diamond side stones. With GIA's highest color grade for a blue diamond, the ring sold for $25.3 million, just below the low end of its presale estimate.

Another blue diamond achieved better results in early November. The pear-shaped "Bleu Royal" (figure 20), a 17.61 ct Internally Flawless Fancy Vivid blue, was offered by Christie's in Geneva as the largest diamond of its color to ever appear at auction. Set in a ring that also featured two pear-shaped colorless diamonds of approximately 3 ct each, the piece became the most expensive auction jewel of 2023. After seven minutes of bidding, the ring featuring the GIA-graded type IIb diamond sold for $44 million, near the higher end of its presale estimate.

The "Pink Supreme" (figure 21), a 15.48 ct Internally Flawless Fancy Intense pink diamond and the largest of its kind ever offered at auction, sold for $10.8 million at

Figure 21. A ring featuring the "Pink Supreme," a 15.48 ct Internally Flawless Fancy Intense pink diamond, sold in Hong Kong for almost $11 million. Courtesy of Christie's Images Ltd. 2023.

Christie's Magnificent Jewels sale in Hong Kong on November 27. Set in a gold ring with pear-shaped and round colorless diamonds, the GIA-graded type IIa gem belonging to a private collector sold within its presale estimate.

In a season filled with plot twists, some highly advertised and anticipated pieces did not go under the hammer on auction day. The "Blue Lagoon," a 93.94 ct blue Paraíba tourmaline and the top lot for Sotheby's Magnificent Jewels in Geneva, was withdrawn before the auction went live. In the final Magnificent Jewels auction of the season in New York, Christie's promoted the "California Sunset" diamond earrings as their top lot. Featuring a stunning pair of Fancy Vivid orange-yellow diamonds weighing approximately 12 ct each, the earrings, estimated to fetch up to $12 million, were also a no-show.

Erica Zaidman
GIA, Carlsbad

RESPONSIBLE PRACTICES

Artisanal diamond mining: Addressing the knowledge gap. In the developed world, the word *diamond* immediately evokes the allure and sparkle of a polished brilliant. What does the word mean, however, for an artisanal diamond miner living in poverty?

Artisanal diamond mining accounts for 20% of global production and significantly impacts millions of lives in the developing world, particularly in Africa. "Artisanal" simply implies that the tools and equipment used by the miners are rudimentary. This type of mining is conducted predominantly by individuals, small groups, or families, who frequently migrate in search of the next deposit. The work is subsistence labor, and the miners typically sell to anyone willing to buy (often without the luxury of a legal transaction). Despite its numerous challenges, which also include smuggling and human rights abuses, artisanal mining is their principal form of income. But beyond the fact that diamonds can be exchanged for subsistence money, what do these miners know about them?

In many countries where artisanal mining is prevalent, miners often have an innate and comprehensive understanding of the material. For example, Sri Lankan gem miners can expertly locate and sort through the *illam* (gem gravel) and differentiate between the fine-quality and lesser-quality material. They have been doing this for thousands of years. But diamond mining is different, particularly in Africa, where the first known primary deposit was discovered less than 200 years ago. In the twentieth century, the system of grading based on the Four *C*s (color, cut, clarity, and carat weight) established a framework for price setting in the diamond trade. This pricing system for polished material underlies the value of rough material and determines its selling price. Therefore, understanding the Four *C*s is vital to the effective trade of diamond rough.

However, the majority of artisanal miners in Africa do not yet have a strong working knowledge of rough diamond, placing them at a significant disadvantage when negotiating the price of rough with buyers. In 2022, the NGO Diamonds for Peace conducted basic training on rough diamond grading for Liberian miners (figures 22 and 23), a project funded by the World Bank and operating in collaboration with Empowerment Works Incorporated.

Liberia's first major diamond deposit was discovered in 1957 along the Lofa River, close to the border of Sierra Leone to the north, which has much higher diamond pro-

Figure 22. Artisanal mining in Liberia. Courtesy of Diamonds for Peace.

Figure 23. Miners sorting through gem gravel. Courtesy of Diamonds for Peace.

duction. Currently, figures stand at around 50,000 carats per annum. Production peaked at 600,000 carats annually in the 1970s (although most of that figure could be attributed to smuggled material coming in from bordering countries). Two civil wars, starting with a military coup in 1980, resulted in export sanctions imposed by the United Nations. Since 2007, when the country joined the Kimberley Process, diamond has been reestablished as an important mineral resource, particularly with the recent discovery of diamond-bearing kimberlites. These deposits have not been commercially exploited. Instead, the mining remains artisanal and the material is found primarily in alluvial placers along the Lofa River.

In pre-training interviews given to establish each miner's level of knowledge, numerous misconceptions became evident. For instance, they valued a diamond based on carat weight alone, regardless of quality, color, and potential yield. They had also been told that colored diamonds have no value. Such diamond "myths" have disseminated over the past fifty years, and buyers are often quick to exploit the miners' lack of knowledge.

For artisanal diamond mining to benefit the future of Liberian communities, the diamonds need to be traded for a price that reflects their real-time value according to their potential polished price (figure 24). The diamonds must be fed into the supply chain correctly, and the economic gain

Figure 24. A parcel of rough diamonds, collected over a month by a Liberian artisanal miner. The diamond indicated by the arrow weighs 0.80 ct. Photo by Beth West.

needs to find its way back into these rural communities. This boomerang-back of benefit is no easy feat in West Africa.

Yet small steps toward progress can be made by adjusting the information asymmetry. These artisanal miners need to understand the material they are working with. At the very least, it will give them a little more cash in their pocket and a slightly more comfortable standard of living. Regardless of the big picture, a simple win on that level is easily achievable.

Knowledge—and the sharing of it—is the key to building a stronger and more equitable supply chain. It is one thing for the supply chain to be traceable, but quite another for it to be equitable and ethical. To level the playing field, each player must be equally empowered. One thing that allows for such empowerment is knowledge. It is a simple right.

Diamonds for Peace, in collaboration with the author, is currently working on a next-stage "train to teach" program for the miners.

Beth West
Diamonds for Peace
London

More on Virtu Gem's ethical supply chain practices. We first covered Virtu Gem at the 2023 Ethical Gem Fair in Tucson (see Spring 2023 GNI, pp. 122–125). Virtu Gem gives artisanal and small-scale miners, traders, and cutters in Kenya, Malawi, and Zambia formal access to the international market and offers training in cutting, basic gemology, and mine safety.

The gems Virtu Gem sells (see figure 25) are cut in the source country and tracked with Provenance Proof Blockchain. One of Virtu Gem's efforts is training artisans in cutting and polishing standards to meet international market expectations. Percy Maleta, Virtu Gem's country exporter and ambassador in Malawi, said the training has attracted many cutters there and allowed them to sell gems at premium prices.

In 2022, Virtu Gem launched the National Gem Cut Course in the three countries. In online workshops led by Adriano Mol from the University of Minas Gerais State, cutters learned facet development and brainstormed to design gem cuts to represent their nations. The resulting cuts (figure 26) resembled a cheetah head for Kenya, the *mbuna* (cichlid) fish for Malawi, and the eagle for Zambia. Buyers can order gemstones from each country in its respective cut.

Virtu Gem has received two grants from the World Bank as well as assistance from other organizations. Rio Grande donated a GemLightbox, and Virtu Gem purchased more for its three country coordinators. The GemLightboxes allow traders to upload photos and videos of gems to the online sales platform rather than export stones on consignment. In addition, Gemworld donated its *World of Color* books to each country coordinator, which help traders evaluate color and cut and set prices.

The donations have also been instrumental in Virtu Gem's work with the National Gem Cutting School in Zambia, where students use the books and GemLightboxes. Virtu Gem cofounder Susan Wheeler said there are many gem cutters in Kenya, and she would like to establish a gem cutting program for women in Malawi.

Figure 25. These indicolite tourmalines (9.27 and 6.16 ct) from Zambia are among the variety of gems Virtu Gem offers. Photo by Robert Weldon.

Figure 26. Gemstone cutters in Kenya, Malawi, and Zambia developed cuts to represent their countries in Virtu Gem's National Gem Cut Course. Left to right: the Kenya Cheetah Head, Zambia Eagle, and Malawi Mbuna *Fish cuts in aquamarine, amethyst, and rhodolite garnet. Photo courtesy of Virtu Gem.*

Wheeler said gemology students should understand the ethical issues inherent in the traditional gemstone supply chain and the importance of cutting in the source country. She emphasized the importance of knowing that prices are based on not only the gemstones but also the labor of the miner and the jewelry manufacturer and other costs.

Virtu Gem's country coordinator for Kenya, Caroline Muchira (figure 27), is a gem cutter by trade. While working full-time in logistics, she was inspired to travel more than 300 km by bus every weekend from Nairobi to Voi to visit the mines and talk to traders. "I was fascinated by the gemstones and how the miners could tell the difference between green garnet, green tourmaline, and pieces of green glass," Muchira said. She planned to study gemology in retirement, but in 2009, after the company she worked for was sold, she sold all of her belongings to earn her Graduate Gemologist diploma at GIA's Thailand school. During Muchira's visits to Voi, she saw the issues the miners faced, especially women and youth. "Often they are unable to sell their stones at a fair price to middlemen, whose aim is to strike the lowest possible deal, leaving miners barely able to eke out a living," she said. Virtu Gem's system focuses on fair pricing, and Muchira now runs the organization's pricing workshops.

Muchira's ability to earn a GG is not the norm. Maleta said many in Malawi's gem trade are interested in taking

Figure 27. Virtu Gem's Kenya country coordinator, Caroline Muchira, with Nadan tsavorite mine manager Daniel Chege (left) and owner John Kimuyu (right). Photo courtesy of Virtu Gem.

Figure 28. Participants at the 37th International Gemmological Conference, held in October 2023 in Tokyo. Photo by Masayuki Itokazu.

GIA courses but can't afford it. "In a country with more than 60,000 artisanal and small-scale miners, Malawi probably only has two or three GIA graduates," he said.

The communities Virtu Gem works with produce a wide variety of gemstones, but they have yet to access some resources. While some artisanal and small-scale mining (ASM) of emeralds occurs in Zambia, Wheeler pointed out, the miners are largely unable to access the more than 400 ASM emerald concessions in Zambia, in the same area as Gemfields. Two women they work with in Zambia have a digger but can't afford the fuel to run it. "They could be producing the same quality emerald as Gemfields," Wheeler said. "They can't afford to do it on a regular basis, and loans are very expensive. We want to support the emerald mining. So we're trying to work on how to go forward with sourcing and getting more supply with emeralds."

Virtu Gem is part of the United Nations Conscious Fashion and Lifestyle Network, which highlights collaborations that further the UN's Sustainable Development Goals (SDGs). Virtu Gem's efforts are associated with six of the SDGs: ending poverty, ending hunger, gender equality, decent work, inclusive and sustainable industrialization, and reducing inequality. "We're going to continue to align everything that we do in Virtu Gem with the Sustainable Development Goals so people can see that framework and what gemstones can do to make progress," Wheeler said.

Erin Hogarth
GIA, Carlsbad

CONFERENCE REPORTS

37th International Gemmological Conference. The 37th International Gemmological Conference (IGC) was held October 23–27 in Tokyo, with more than 80 delegates, observers, and special guests from 24 countries attending (figure 28). The IGC, which started in 1951 and takes place every two years, brings together international gemologists,

Figure 29. Left: IGC participants viewed a 102-ton jadeite boulder at the Oyashirazu jade museum in Itoigawa. Right: During a field trip to Ago Bay, participants observed the implanting of a bead nucleus in a Pinctada fucata *oyster. Photos by Ahmadjan Abduriyim.*

scholars, and researchers to present their work on natural and synthetic diamonds, colored gemstones, pearls, gem treatments, geological and geographical study of gem deposits, and more. This year, IGC delegates had the opportunity to meet with researchers from various earth science disciplines as well as Japanese laboratory gemologists and gem traders at specially organized events.

The opening ceremony began with a welcome from the Japan Jewellery Association, the Japan Gem Society, the Gemmological Society of Japan, and the IGC. Six keynote presentations followed. IGC executive secretary **Dr. Jayshree Panjikar** discussed the past, present, and future of the conference, beginning with its formation, followed by advancements in gemological science and the latest developments in instrumentation. Dr. Panjikar announced the IGC's goal of recruiting more young gemologists and scientists by its 100th anniversary in 2052, bringing greater knowledge to the general public and consumers. **Professor Hisao Kanda** (National Institute for Materials Science, Japan) described the activities of Japanese researchers from 1980 to 2000, particularly in the area of diamond synthesis. **Dr. Hanco Zwaan** (Netherlands Gem Laboratory/Naturalis Biodiversity Center, Leiden) discussed the differences between natural and laboratory-grown diamond in terms of growth history and conditions and properties. **Yuichi Nakamura** (Mie Prefecture Pearl Promotion Council) reviewed the status quo of the akoya pearl industry and initiatives for sustainable pearl cultivation in Japan. **Professor Pornsawat Watanakul** (Kasetsart University) emphasized the importance of research for the gem and jewelry industry, noting examples of in-depth research and advanced technology that are yielding applicable knowledge. **Dr. Michael Krzemnicki** (Swiss Gemmological Institute SSEF) addressed the issue of classifying colored gems into their respective varieties and presented a number of case studies to illustrate the topic from a gemological laboratory perspective.

At the main conference venue, the National Museum of Nature and Science, participants attended oral and poster presentations, along with the IGC exhibition booth and a demonstration booth showcasing recent advances. Many high-quality scientific talks were presented by IGC members, and some of the presenters were elected as new delegates. Abstracts of the 48 presentations covering topics ranging from diamonds and colored stones to technology and techniques can be viewed on the conference website at www.igc-gemmology.org/s/IGC2023_webfinal.pdf.

In addition to the academic program, the IGC Japan committee organized pre-conference and post-conference excursions (figure 29). Before the conference, 32 participants visited the jadeite gorge in the Itoigawa region of Niigata Prefecture and learned about its geological setting and formation and observed the jadeite deposit's location in serpentinite lenses within a high-pressure metamorphosed complex. After the conference, 25 participants visited the akoya cultured pearl farm at Ago Bay, where they witnessed the bead implantation process and pearl harvesting. In addition to these conference excursions, a tour of Mount Fuji and a visit to the jewelry city of Kofu were organized.

Ahmadjan Abduriyim
Tokyo Gem Science and GSTV Gemological Laboratory

ANNOUNCEMENTS

***G&G* contributors awarded for best geoscience research.** Several *G&G* authors and editorial board members are among those honored for their contributions to a recent volume in the *Reviews in Mineralogy and Geochemistry* series (figure 30). The Geoscience Information Society's annual Mary B. Ansari Best Geoscience Research Resource Award recognizes the year's outstanding reference publication or website. The 88th volume in the *Reviews* series, *Diamond: Genesis, Mineralogy and Geochemistry* is a comprehensive resource covering a wide range of diamond-related subjects. The publication is available for download at geoscienceworld.org and minsocam.org.

Congratulations to volume editors Karen Smit, Steve Shirey, Graham Pearson, Thomas Stachel, Fabrizio Nestola, and Thomas Moses, as well as *G&G* contributors Christopher M. Breeding, Jim Butler, Alan Collins, Ulrika D'Haenens-Johansson, Dorrit Jacob, Mandy Krebs, and Evan Smith for their chapters in the volume.

GIA Alumni Collective. The GIA Alumni Collective offers an exciting networking platform for GIA graduates. The online community at collective.gia.edu allows a diverse group of users to access both live and self-paced Continuing Education seminars, join virtual chapters, connect with global alumni, and more. The site also puts GIA alums in the spotlight (figure 31), celebrating those who uphold the highest standards of GIA's consumer protection mission.

Winning a 40-pound tub of historical jewelry at auction led sisters Laura Mae and Amanda Jean (last names withheld) to launch their online jewelry resale business, Maejean Vintage, in 2010. New to the industry, they both pursued Graduate Gemologist diplomas at GIA. Today they use their expertise to salvage rare and valuable historical pieces and sell them all over the world.

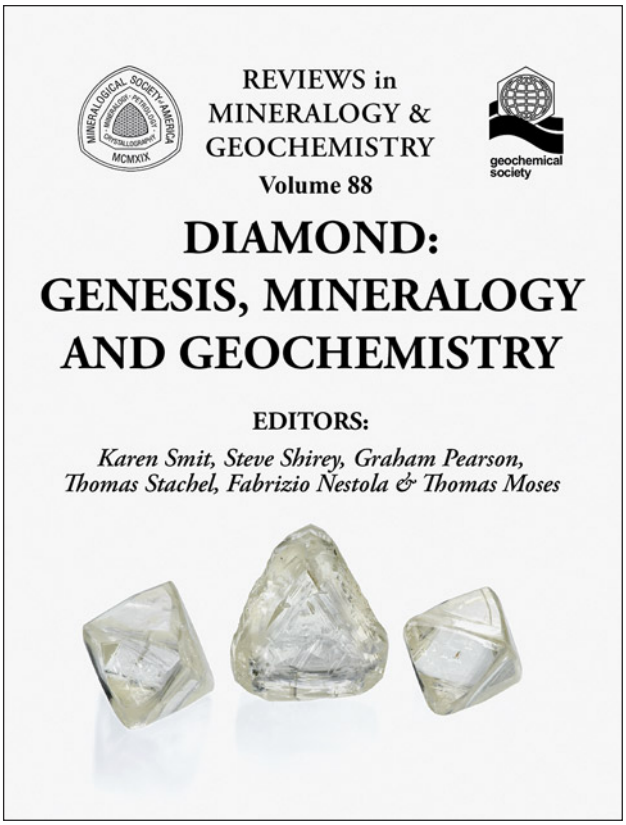

Figure 30. Diamond: Genesis, Mineralogy and Geochemistry, *Volume 88 in the* Reviews in Mineralogy and Geochemistry *series, received this year's Mary B. Ansari Best Geoscience Research Resource Award.*

Ilan Portugali's journey took him from Israel to Madagascar to Mozambique and finally to the U.S., where he worked for a diamond dealer and completed his Graduate

Figure 31. Laura Mae, Amanda Jean, and Ilan Portugali are some of GIA's featured graduates on the Alumni Collective website.

Figure 32. Heitor Barbosa discovered Paraíba tourmaline in 1989 after almost a decade of mining. Photo by Duncan Pay.

Diamonds diploma at GIA. After positions with Van Cleef & Arpels and Harry Winston, Portugali started his own business, Beverly Hills Diamonds, which sources conflict-free and fair-trade diamonds.

Visit https://collective.gia.edu/meet-the-collective.html to read stories from these alumni and more.

IN MEMORIAM

Heitor Barbosa. The discoverer of Paraíba tourmaline, Heitor Barbosa (figure 32), died September 23, 2023, at the age of 90. Driven by intuition, Barbosa began his quest in the early 1980s at an old pegmatite mine in the Brazilian state of Paraíba. After several unsuccessful years and considerable skepticism from others, Barbosa prevailed and unearthed one of the world's rarest gems—cuprian elbaite tourmaline—in 1989. Over the next two years, using simple hand tools and candles for lighting, Barbosa and his team recovered between 10 and 15 kg of the tourmaline characterized by its vivid blue and blue-green hues. Production slowed significantly in the years that followed, but Barbosa continued to work the mine, remaining hopeful that more tourmaline would be uncovered. Today, Barbosa's son Sergio maintains the mine.

Barbosa is survived by his wife, four children, and two grandchildren. We extend our condolences to his family and friends.

Micro-Features of Beryl

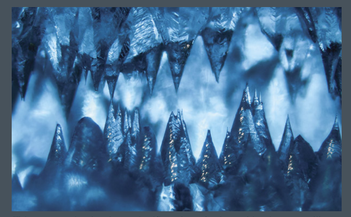

This aquamarine has been significantly etched, resulting in a cave-like cavity filled with sharp spires of beryl. Field of view 3.28 mm.

This morganite crystal shows a heart-shaped etch feature on the pinacoid face, as seen using differential interference contrast microscopy. Field of view 1.5 mm.

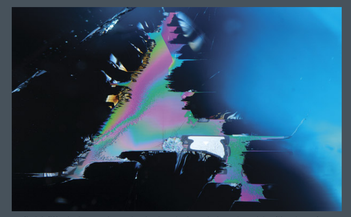

A fluid-filled, three-phase inclusion in beryl showing thin-film interference under oblique fiber-optic lighting. Field of view 3.52 mm.

A complex three-phase inclusion in aquamarine is observed using polarized light, revealing a variety of birefringent interference colors in the multitude of daughter crystals. Field of view 0.25 mm.

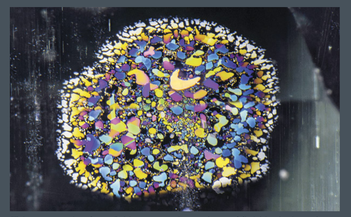

This aquamarine from Pakistan contains a plane of fluid inclusions that display colorful thin-film interference when examined with reflected light. Field of view 5.63 mm.

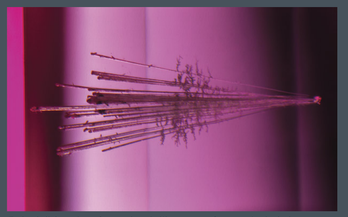

Etched dislocations form a brush-like pattern from an included quartz crystal in this red beryl from Utah. Field of view 1.30 mm.

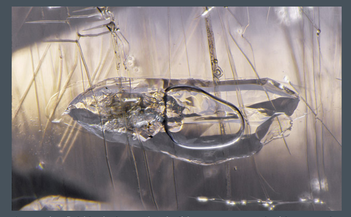

A complex fluid inclusion and etch ribbons are present in this morganite from Minas Gerais, Brazil. Field of view 2.78 mm.

A goshenite beryl from Pakistan is host to pinkish orange crystals of the rare mineral zwieselite. Field of view 7.61 mm.

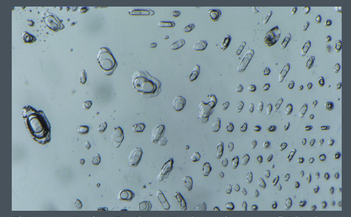

This aquamarine from Brazil contains planes of numerous fluid inclusions that show a "bubble in bubble" effect resulting from the immiscibility of an aqueous liquid and carbon dioxide liquid and gas phases. Field of view 1.79 mm.

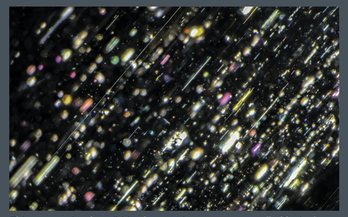

This aquamarine from Sri Lanka contains numerous needle-like inclusions of hematite and ilmenite, which result in aventurescence. Field of view 7.72 mm.

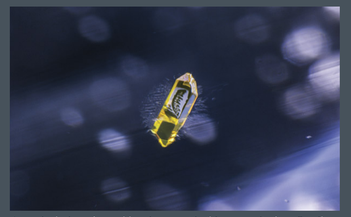

A rare inclusion of pyrochlore is present in this morganite from Brazil. Field of view 3.35 mm.

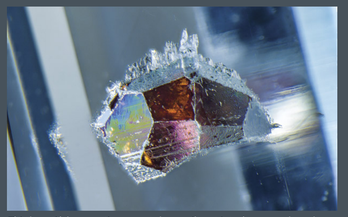

This beautiful spessartine garnet shows vibrant interference colors along its interface with the aquamarine host. Field of view 5.63 mm.

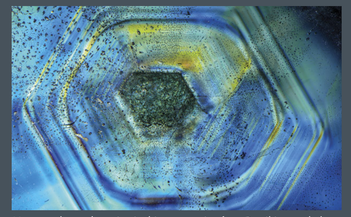

Hexagonal growth zoning in this aquamarine from Brazil is revealed using polarized light. Field of view 15.67 mm.

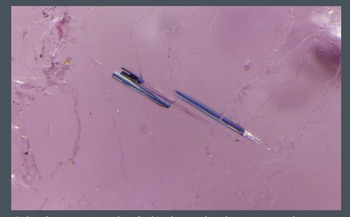

Galenobismutite was identified in the rare beryl-group mineral pezzottaite. Field of view 0.91 mm.

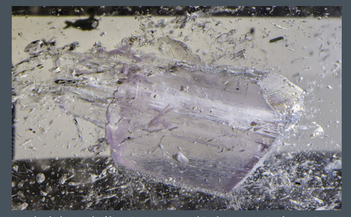

A euhedral crystal of kunzite is preserved in this morganite from Minas Gerais, Brazil. Field of view 8.81 mm.

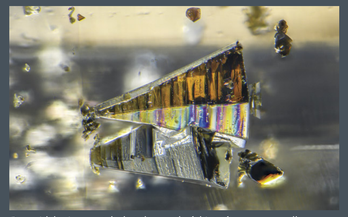

Pyramidal mica crystals that show colorful interference are well preserved in this aquamarine from Brazil. Field of view 2.71 mm.

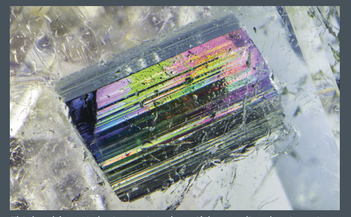

This beryl from Kashmir contains a beautiful tourmaline showing striated faces and thin-film interference colors along the interface with the host. Field of view 11.52 mm.

A crystal cluster of what is probably columbite (Mn) is present in this aquamarine from Pakistan. Field of view 10.28 mm.

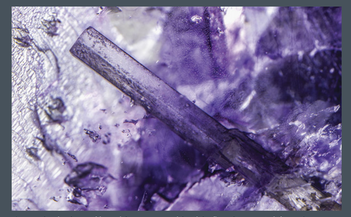

A rare inclusion of beryl is preserved in this fluorite crystal from Inyo, California. Field of view 8.6 mm.

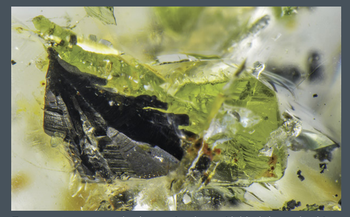

Transparent green crystals of monazite along with black ferrocolumbite crystals are seen in this goshenite from Pakistan. Field of view 4.49 mm.

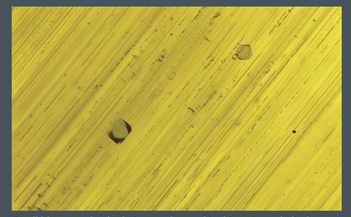

Small blue crystals of gahnite are observed in this cat's-eye heliodor reportedly from Brazil. Field of view 1.10 mm.

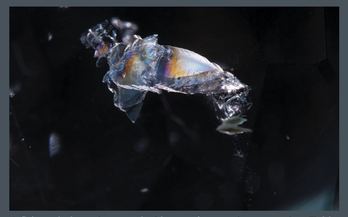

A flaky, colorless mica crystal with stress fractures in aquamarine. Field of view 4.79 mm.

This goshenite from the Himalaya mine in California contains dark yellow crystals of stibiotantalite. Field of view 4.09 mm.

This beryl from Brazil features a prominent display of purplish pink lepidolite. Field of view 16.00 mm.

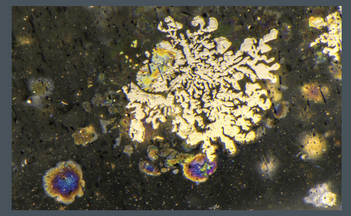

Skeletal dendritic inclusions of ilmenite are the cause of silvery aventurescence in this aquamarine from Brazil. Field of view 2.59 mm.

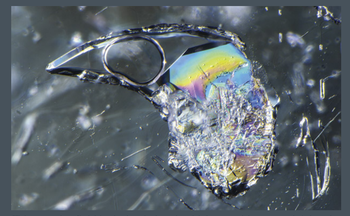

This complex fluid inclusion in beryl, which resembles an eagle's head, contains a liquid, gas, and numerous solid crystals that show birefringence using polarized light. Field of view 3.55 mm.

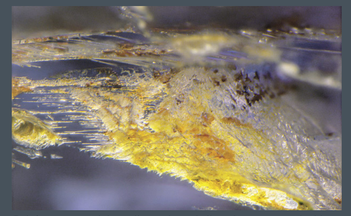

Etch features containing yellow epigenetic limonite are present in this rare example of johnkoivulaite, recognized as a beryl-group mineral in 2019. Field of view 1.88 mm.

A morganite from Brazil contains elongate crystals of muscovite mica that show parallel cleavage cracks. Field of view 4.21 mm.

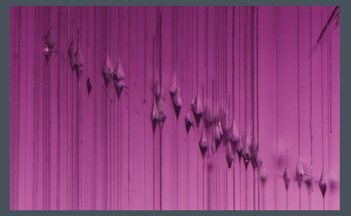

Numerous etch tubes are the cause of chatoyancy in this cat's-eye pezzottaite. Field of view 1.16 mm.

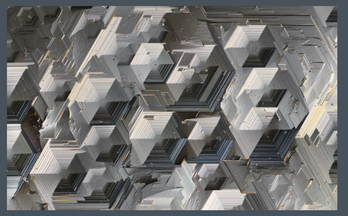

Growth hillocks reveal the hexagonal crystal structure on the pinacoid face of this aquamarine from Pakistan using differential interference contrast microscopy. Field of view 2.32 mm.

This chart contains a selection of photomicrographs of natural beryl. It is by no means comprehensive. The images show the appearance of numerous features a gemologist might observe when viewing beryl with a microscope.

Published in conjunction with Nathan Renfro, Tyler Smith, John I. Koivula, Shane F. McClure, Kevin Schumacher, and James E. Shigley (2023), "Micro-Features of Beryl," *Gems & Gemology*, Vol. 59, No. 4, pp. 484–485. Photomicrographs by Nathan Renfro and Tyler Smith. Stones courtesy of GIA and the John Koivula Inclusion Collection.

GIA®